Modeling capillarity and two-phase flow in granular media : from pore-scale to network scale

Eduard Puig Montellà

To cite this version:

Eduard Puig Montellà. Modeling capillarity and two-phase flow in granular media : from pore-scale to network scale. Fluid mechanics [physics.class-ph]. Université Grenoble Alpes; Universitat politècnica de Catalunya - BarcelonaTech, 2019. English. NNT : 2019GREAI046 . tel-02317802

HAL Id: tel-02317802
https://theses.hal.science/tel-02317802

Submitted on 16 Oct 2019

Communauté
UNIVERSITÉ Grenoble Alpes

UNIVERSITAT POLITÈCNICA
DE CATALUNYA
BARCELONATECH

THÈSE

Pour obtenir le grade de

DOCTEUR DE LA COMMUNAUTÉ UNIVERSITÉ GRENOBLE ALPES

préparée dans le cadre d'une cotutelle *entre la Communauté Université Grenoble Alpes* et *Universitat Politècnica de Catalunya*

Spécialité: **IMEP2/Matériaux, Mécanique, Génie civil, Electrochimie**

Arrêté ministériel: le 6 janvier 2005 – 25 mai 2016

Présentée par

Eduard PUIG MONTELLÀ

Thèse dirigée par **Bruno CHAREYRE** et
codirigée par **Antonio GENS**

préparée au sein du **Laboratoire 3SR -** Grenoble
dans **l'École Doctorale IMEP2**
et **Departament Enginyeria Civil i Ambiental** – Barcelone
dans l'**Escola de Doctorat de l'UPC**

Modeling capillarity and two-phase flow in granular media: from pore-scale to network scale

Thèse soutenue publiquement le **16/07/2019**
devant le jury composé de:

M Hugues BODIGUEL
Professeur à l'INP Grenoble, Président
M S. Majid HASSANIZADEH
Professeur à Utrecht University, Rapporteur
M Jean-Yves DELENNE
Directeur de Recherche à l'INRA, Rapporteur
Mme Vanessa MAGNANIMO
Professeur associé à University of Twente, Examinatrice
M Bruno CHAREYRE
Maître de conférences (HDR) à l'INP Grenoble, Directeur de thèse

Acknowledgements

First and foremost I want to thank my supervisor Bruno Chareyre. He has been supportive since the days I began working in Laboratoire 3SR. I appreciate all his contributions of time and ideas that made my PhD experience productive and stimulating. I started my PhD journey with little knowledge of geomechanics and coding and he guided me over all these years giving me countless advices, motivational support and the freedom I needed to move on.

I am also grateful to Simon Salager, who initially co-supervised my thesis but left academia at the end of my first year. I thank him for his enthusiasm and scientific advice from a non-numerical perspective.

I want to thank my co-director Antonio Gens. He helped me to complete a Joint PhD with the Universitat Politècnica de Catalunya. He also provided experience, refreshing insight and critical questions that improved the development of the thesis.

During my PhD I decided to teach some courses. At the beginning I felt completely lost, but eventually, it turned out to be an incredible and enriching experience. I want to thank professors Damien Ricotier, Eric Charpentier, Emmanuel Godde and Jean-Martial Cohard for their patience and advices at the early stages of my teaching time.

The members of Laboratoire 3SR have contributed immensely to my personal and professional time at Grenoble. The lab has been a source of friendships as well as good advice and collaboration. I am especially grateful to Cyrille, Olga, Marta, Fabio, and Ivan. You were always there for a fast coffee or a chat to break the routine at work. We spent countless enjoyable lunches, endless discussions and fast races to get out of the Galilée building before the alarm went off.

My time at Grenoble was enjoyable in large part due to the many friends and groups that became part of my life. I am grateful for the time spent with flatmates, to my climbing and hiking buddies and the memorable trips around France.

I have also been fortunate to come across very interesting and nice people during my time at Universitat Politècnica de Catalunya. Special thanks go to Luigi and Chiara with whom I enjoyed lunches while sunbathing in the park.

Lastly, I would like to thank my family for all their love and encouragement. And most of all, to my loving, encouraging and patient girlfriend Alba whose faithful support during all the stages of this PhD was highly appreciated. Her ever-present support and laughs helped me from the first day of the thesis. Thank you.

Contents

List of Figures

List of symbols

α	parameter related to the portion of liquid included in the cell, [-]
A^{eff}	effective entry pore throat area, [m^2]
a^{nw}	specific area of the fluid-fluid interface per unit volume, [m]
a^*	ratio between grains, [-]
Bo	Bond number, [-]
Ca	Capillary number, [-]
c_s	speed of sound, [m/s]
Δ_{ij}	equivalent pressure drop between i and j, [Pa]
Δt	time step, [s]
Δx	distance between nodes, [m]
δ_c	normal particle displacement, [m]
δ_{ij}	Kronecker delta, [-]
D	displacement of a grain moved away from the rest, [m]
d	separation between the spherical grains, [m]
E	solid particle elastic modulus, [Pa]
ε	geometrical correction parameter, [-]
ε_v	volumetric strain, [-]
$\varepsilon_{yy}, \varepsilon_{xx}$	vertical and horizontal strains, [-]
e_k	discrete velocity with direction k in the lattice, [m/s]
$\mathbf{f}$	sources/sinks matrix, [m^3/s]
f_k^{σ}	particle distribution function of phase σ with direction k in the lattice, [kg/m^3]
$f_k^{\sigma,eq}$	equilibrium distribution function of phase σ with direction k in the lattice, [kg/m^3]
$\mathbf{F}_{\sigma}$	non-local volume force responsible for the fluid-fluid interaction, [N/m^3]
$\mathbf{F_c}$	capillary force vector acting on the grains, [N]
F_c	capillary force acting on the grains, [N]
F_c^*	dimensionless capillary force, [N]
$\mathbf{F_k^f}$	total fluid force vector acting on particle k, [N]
$\mathbf{F_k^c}$	contribution of the contact forces on particle k, [N]
$\mathbf{F_k^g}$	gravitational force on particle k, [N]
$\mathbf{F^p}$	pressure force vector acting on the interface, [N]
$\mathbf{F_k^p}$	pressure force vector acting on particle k, [N]
$\mathbf{F^t}$	tension force vector acting on the fluids-solid contact lines, [N]
$\mathbf{F_k^t}$	surface tension force vector acting on particle k, [N]
$\mathbf{F_c}$	total capillary force, [N]
$\mathbf{F_n}$	normal contact force, [N]
$\mathbf{F_s}$	tangential contact force, [N]
G	interaction strength between phases, [m^3/kg]
γ	interfacial tension between the two fluid phases, [N/m]
γ^{ns}	interfacial tension between the non-wetting and the solid phases, [N/m]
γ^{ws}	interfacial tension between the wetting and the solid phases, [N/m]
H_m	mean curvature of the fluids interface, [m^{-1}]
$\bar{\bar{\mathbf{I}}}$	identity matrix, [-]

I_k	moment of inertia of particle k, [kg ·m^2]
$\bar{\bar{\mathbf{K}}}$	intrinsic permeability tensor, [m^2]
g	gravity, [m/s^2]
g_{ij}	local conductance from cells i to j, [m/s]
κ	intrinsic permeability of the soil, [m^2]
K	hydraulic conductivity, [m/s]
k_n	normal stiffness, [N/m]
k_t	shear stiffness, [N/m]
Λ	inertial number, [-]
λ	bulk viscosity, [Pa·s]
L_c	characteristic length, [m]
L_{ij}	distance between pores i and j, [m]
L_{nw}	total length of fluid-fluid interface, [m]
L_{ns}	total length of non-wetting - solid interfaces, [m]
L_{throat}	length of the pore throat, [m]
l_{ij}	length of the aperture of the throat between pore bodies i and j, [m]
M	viscosity ratio, [-]
m_k	mass of particle k, [kg]
μ	fluid dynamic viscosity, [Pa·s]
ν	kinematic viscosity, [m^2/s]
N_b	number of particles, [-]
Ω	volume element, [m^3]
Ω'	volume element far from the solid-fluid interface, [m^3]
Ω_{ij}	perimeter of solid-fluid interface between pore bodies i and j, [m]
$\delta\Omega$	surface of the particle, [m^2]
$\delta\Omega'$	surface from the intersection between Ω' and the liquid, [m^2]
ω	stress vector, [Pa]
$\bar{\bar{\mathbf{P}}}$	pressure tensor, [Pa]
$\mathbf{P}$	matrix containing the pressure values of the triangular cells, [Pa]
p_c	capillary pressure, [Pa]
p_c^*	dimensionless capillary pressure, [-]
p_c^e	entry capillary pressure, [Pa]
$p_c^{*,e}$	dimensionless entry capillary pressure, [-]
p^i	fluid pressure in cell i, [Pa]
p^{nw}	non-wetting phase pressure, [Pa]
p^w	wetting phase pressure, [Pa]
p_T	transverse component of pressure, [Pa]
p_N	normal component of pressure, [Pa]
Π^σ	momentum of order two of the distribution functions of phase σ, [Pa]
ϕ	porosity, [-]
ϕ_c	inter-particle friction angle, [-]
ϕ_L	level-set function, [-]
ϕ_{ij}	area occupied by the fluid between pore bodies i and j, [m^2]
Ψ	interparticle potential, [kg/m^3]
ψ	angle between the bridge axis and the tangent plane to the solid-liquid

	contact line, [-]
$\mathbf{Q}$	matrix with the information of the conductivities, [m^3/(Pa $\cdot$ s)]
q^*	dimensionless deviatoric stress, [-]
q	total volumetric flux, [m^3/s]
q_{ij}	flux between pore bodies i and j, [m^3/s]
R	radius of the sphere, [m]
R_m	average meniscus radius, [m]
R_{env}	radius of the volume element that enclose a spherical grain, [m]
R_1, R_2	meniscus principal radii of the curvature normal to each other, [m]
R^h_{ij}	hydraulic radius between pore bodies i and j, [m]
r	radius of the bridge neck in a pendular bridge, [m]
r^c	radius of curvature of non-wetting - wetting interface, [m]
r_{ins}	radius of the inscribed circle in a pore throat, [m]
r_s	radius of a spherical meniscus, [m]
Re	Reynolds number, [-]
ρ	local density of the fluid, [kg/m^3]
ρ^w	local density of the wetting phase, [kg/m^3]
ρ^{nw}	local density of the non-wetting phase, [kg/m^3]
σ	phase, [-]
σ_{iso}	isotropic pressure, [Pa]
σ_{yy}, σ_{xx}	vertical and horizontal stresses, [Pa]
σ_{ij}	total stress, [Pa]
σ'_{ij}	effective stress, [Pa]
ς	dimensionless stiffness [-]
S^*	dimensionless separation between the spherical grains, [-]
S^f_{ij}	area occupied by the fluid in the facet between pore bodies i and j, [m^2]
S_{nw}	non-wetting phase saturation, [-]
S_w	wetting phase saturation, [-]
$\bar{\bar{S}}$	deviatoric stress, [Pa]
τ	relaxation time, [s]
θ	contact angle, [-]
Θ	source or a sink flux,[m^3/s]
$\mathbf{T}$	total stress tensor, [Pa]
$\mathbf{u}$	velocity vector, [m/s]
$\mathbf{u}^{'}$	effective velocity, [m/s]
$\mathbf{u}^{\sigma,\mathbf{eq}}$	equilibrium velocity of phase σ, [m/s]
V^*	dimensionless wetting phase volume, [-]
V_t	total or bulk volume of material, [m^3]
V_v	volume of void pore space, [m^3]
w_k	weight factors with direction k in the lattice, [-]
χ	non-dimensional conductance factor, [-]
χ_B	Bishop's effective stress parameter, [-]
$\mathbf{x}$	position coordinates, [m]
ζ	rotation angle, [-]

Abstract

Numerical simulations at the pore scale are a way to study the behavior of multiphase flows encountered in many natural processes and industrial applications. In this work, liquid morphology and capillary action are examined at the pore-scale by means of the multicomponent Shan-Chen lattice Boltzmann method (LBM). The accuracy of the numerical model is first contrasted with theoretical solutions. The numerical results are extended to complex microstructures beyond the pendular regime.

The LBM has been employed to simulate multiphase flow through idealized granular porous media under quasi-static primary drainage conditions. LBM simulations provide an excellent description of the fluid-fluid interface displacement through the grains. Additionally, the receding phase trapped in the granular media in form of pendular bridges or liquid clusters is well captured. Unfortunately, such simulations require a significant computation time. A 2D model (Throat-Network model) based on analytical solutions is proposed to mimic the multiphase flow with very reduced computation cost, therefore, suitable to replace LBM simulations when the computation resources are limited. The approach emphasizes the importance of simulating at the throat scale rather than the pore body scale in order to obtain the local capillary pressure - liquid content relationships. The Throat-Network model is a starting point for a hybrid model proposed to solve 3D problems. The hybrid model combines the efficiency of the pore-network approach and the accuracy of the LBM at the pore scale to optimize the computational resources. The hybrid model is based on the decomposition of the granular assembly into small subsets, in which LBM simulations are performed to determine the main hydrostatic properties (entry capillary pressure, capillary pressure - liquid content relationship and liquid morphology for each pore throat). Despite the reduction of computation time, it is still not negligible and not affordable for large granular packings. Approximations by the Incircle and the MS-P method, which predict hydrostatic properties, are contrasted with the results provided by LBM and the hybrid model. Relatively accurate predictions are given by the approximations.

Key words: wet granular materials, capillary action, throat network, multiphase flow, lattice Boltzmann, pore scale

Résumé

Les simulations numériques à l'échelle du pore sont fréquemment utilisées pour étudier le comportement des écoulements multiphasiques largement rencontrés dans phénomènes naturels et applications industrielles. Dans ce travail, la morphologie des structures liquides et l'action capillaire sont examinées à l'échelle des pores par la méthode de Boltzmann sur réseau (LBM) à plusieurs composants selon le modèle de Shan-Chen. Les résultats numériques obtenus sont en bon accord avec les solutions théoriques. Les simulations numériques sont étendues à microstructures complexes au-delà du régime pendulaire.

La LBM a été utilisée pour modéliser l'écoulement multiphasique à travers un milieu poreux idéalisé dans des conditions de drainage primaire quasi-statique. Les simulations LBM ont fourni une excellente description du déplacement de l'interface fluide-fluide à travers les grains. Pendant le drainage, les simulations LBM sont capables de reproduire la déconnexion d'une phase dans le milieu granulaire sous la forme de ponts pendulaires ou structures liquides complexes. Malheureusement, le temps de calcul nécessaire pour ce type de simulations est assez élevé. Afin d'optimiser les ressources de calcul, nous présentons un modèle 2D (modèle Throat-Network) basé sur des solutions analytiques pour décrire l'écoulement biphasique à travers un ensemble de disques dans un temps de calcul très réduit, donc le modèle 2D est susceptible de remplacer les simulations LBM lorsque les ressources de calcul sont limitées. L'approche souligne l'importance de simuler le problème a l'échelle de la gorge du pore pour obtenir les relations volume - pression capillaire locales. Le modèle Throat-Network est un point de départ pour le modèle hybride proposé pour résoudre les problèmes en 3D. Le modèle hybride combine l'efficacité de l'approche réseau de pores et la précision du LBM à l'échelle des pores. Le modèle hybride est basé sur la décomposition de l'échantillon en petits sous-domaines, dans lesquels des simulations LBM sont effectuées pour déterminer les propriétés hydrostatiques principales (pression capillaire d'entrée, courbe de drainage primaire et morphologie du liquide pour chaque gorge du pore). Malgré la réduction significative des temps de calcul obtenus avec le modèle hybride, le temps n'est pas négligeable et les modélisations numériques d'échantillons de grandes tailles ne sont pas réalistes. Les approximations données par les méthodes Incircle et MS-P, qui prédisent les propriétés hydrostatiques, sont comparées à celles de LBM et du modèle hybride.

Mots clés: matériau granulaire, capillarité, réseau de pores, écoulement multiphasique, drainage, saturation partielle, lattice Boltzmann

Resum

Per tal d'estudiar els fluxos multifàsics presents a molts processos naturals i industrials és indispensable entendre les propietats físiques dels sistemes multifàsics a escala microscòpica. La morfologia dels fluids i les forces capil · lars s'investiguen a l'escala del porus mitjançant el "multicomponent Shan-Chen lattice Boltzmann method (LBM)". La precisió del model numèric ha estat contrastada amb solucions teòriques. Els resultats numèrics s'han estès a microestructures líquides complexes més enllà del règim pendular.

El LBM ha estat emprat per simular fluxos multifàsics a través de medis porosos sota condicions quasi-estàtiques de drenatge. Les simulacions dutes a terme mitjançant el LBM proporcionen una descripció excel · lent del moviment de la interfície entre fluids a través de les partícules sòlides. Durant el drenatge, les simulacions numèriques són capaces de reproduir l'efecte del fluid atrapat dins el medi granular en forma de ponts o estructures líquides complexes. Malauradament, aquestes simulacions requereixen un temps de computació molt elevat. Per tal d'optimitzar els recursos de computació, proposem un model 2D (model Throat-Network) basat en solucions analítiques que permet reproduir fluxos multifàsics a través d'un conjunt de discs amb un temps de computació molt reduït. Per tant, aquest mètode és una alternativa que pot substituir les simulacions LBM quan els recursos de computació són escassos. El model Throat-Network destaca la importància de tractar el problema a l'escala de la gola del porus per tal d'obtenir les relacions pressió capil · lar - volum locals. Aquest enfocament és un punt de partida pel model híbrid que es presenta per resoldre els problemes en 3D. El model híbrid combina l'eficàcia del model "Pore-Network" i la precisió del LBM a l'escala del porus. El model híbrid es basa en la descomposició d'una mostra granular en subdominis més petits, els quals corresponen a les goles dels porus (la gola dels porus és l'espai que connecta dos porus adjacents). Les simulacions LBM s'executen per a cada un dels subdominis per tal de determinar les propietats hidroestàtiques més rellevants (pressió capil · lar d'entrada, la corba de pressió capil · lar - grau de saturació i la morfologia líquida per cada una de les goles del porus). Malgrat la reducció significativa en el cost computacional del model híbrid, els temps de càlcul no són menyspreables i poc realistes per mostres granulars de grans dimensions. Les aproximacions donades pels mètodes de l'"Incircle" i el MS-P, que permeten estimar les propietats hidroestàtiques, han estat contrastades amb els resultats obtinguts amb LBM i el model híbrid.

Mots clau: material granular, capil · laritat, medi porós, flux multifàsic, drenatge, lattice Boltzmann

General Introduction

General context

Multiphase materials cover a wide range of natural phenomena and engineering applications. This includes the rainwater infiltrated into the soil, landslide phenomena, oil recovery, food industry, industrial bed reactors, etc. A better insight into the properties and mechanisms of the flows through porous media is crucial to predict the behavior of the multiphase flows.

Even though multiphase flows are extended to several scientific fields (chemistry, mechanics, pharmacy, geosciences, biology, material science, etc), the present thesis focus on partially saturated soils. Such soils are materials characterized by a solid matrix and voids (pores). The pore space is typically occupied by fluids (for instance, air and water). When the pore space is filled with a single phase (i.e. water), Darcy's law and Navier-Stokes equations describe the motion of the fluid within the porous media. Unfortunately, the description of the flow becomes much more complex in multiphase systems.

Processes like internal erosion, structural damage due to expansive soils and reduction of the bearing capacity of shallow foundations caused by the desaturation cracks above the phreatic level are classical examples of hydro-mechanical problems that evidence the interest in controlling the mechanical behavior of unsaturated soils.

Experiments and macroscopic numerical methods are excellent approaches to obtain the main physical properties. However, some difficulties may arise due to the heterogeneous and discontinuous nature of granular materials. Local properties are unaccessible or inaccurately described by experimental tests or macro-scale-based methods.

Recent advances in computer technology enhanced the development of many powerful and efficient numerical methods capable to reproduce the complex hydro-mechanical interaction between phases at the pore scale. In such context, local properties are employed to recover the processes manifested at the macro-scale.

Furthermore, numerical methods may help to have a better understanding of liquid structures observed in granular media at low liquid saturation (pendular bridges, trimers and other liquid clusters). The hydro-mechanical behavior of pendular bridge has been investigated and implemented in many numerical models (Scholtès et al. (2009); Scholtès et al. (2009)). However, less attention has been devoted to examine the mechanism of wet materials during the funicular regime. Nowadays, three-dimensional images from X-ray tomography are a useful and common tool to characterize the fluid morphology in the porous medium (Scheel et al. (2008);

Turner et al. (2004); Sakellariou et al. (2004)). Despite these advances, very few attempts have been carried out to obtain details of the liquid distribution within the porous media (Melnikov et al. (2015); Yuan et al. (2018)). In this thesis, the hydro-mechanical behavior of liquid microstructures is evaluated in order to have a better understanding of the hydrostatic properties and capillary forces during the funicular and capillary regimes. The study has been possible through lattice Boltzmann simulations (LBM) based on the multicomponent Shan-Chen model. The calibration and validation of the numerical model are described in Chapter 2. Liquid morphology and capillary pressure - saturation relationships are analyzed for typical liquid configurations (pendular bridges, trimers, tetramers, etc) in the latest part of Chapter 2.

A numerical approach based on the integration of the stresses over the grains is considered to compute the capillary forces between solid objects in Chapter 3. Such analysis may shed some light on the path of capillary forces during multiphase flow, thus, we provide new tools to predict the hydro-mechanical phenomena of wet granular materials.

Due to the natural ability to handle complex geometries, LBM is able to accurately describe multiphase flows through porous media. Unfortunately, LBM, like other fully resolved simulations, is computationally expensive. This work explores the possibility of a hybrid model based on a decomposition of the granular assembly to evaluate the hydro-mechanical properties within acceptable computation time and maintain the geometrical discretization unaltered. Chapter 4 describes a 2D model (Throat-Network model) inspired in previous pore-network models. The representation of the pore space in the 2D Throat-Network model (TN hereinafter) is based on a regular triangulation of a disk assembly. Regarding the flow of the fluid phases within the granular medium, pressure field and fluxes are evaluated by means of the continuity equation for incompressible fluids. Details about the local conductances and fluid-fluid interface location are found in Chapter 4. Some of the analytical solutions employed in the TN model are not valid when the model is extended to the third dimension. Therefore, multiphase algorithms need to be reformulated to overcome the complexities of the pore geometry. In Chapters 5 and 6 we propose a hybrid model that takes advantage of both the efficiency of the pore-network models and the accuracy of direct fluid dynamics solutions obtained with LBM. In other words, we rely on LBM simulations to determine the hydrostatic properties (capillary forces, entry capillary pressure, capillary pressure - saturation curves, etc) at the pore-scale to be further integrated in a pore-network model based on a regular triangulation of the pore space. The multiscale approach provides an alternative to a large LBM simulation by decomposing the granular assembly into small LBM problems. Even though the hybrid model benefits from the pore-network approach by optimizing the computational resources, the computation cost is not negligible. Hence, Chapters 5 and 6 include a revision of approximations and empirical solutions found in previous literature in order to improve and validate the local rules that govern the multiphase flow.

Chapter 1

Multiphase flow in granular porous media

1.1 Introduction

Multiphase fluid flows in porous media occur in many natural and industrial processes. Indeed, the study of the physics of multiphase flow through porous media plays a crucial role in several scientific disciplines, such as soil mechanics, ground water hydrology, oil engineering, industrial applications, etc. This thesis is carried out in the field of soil mechanics, thus, the mechanical behavior and properties are investigated in partially saturated soils (typically, air, water and solid particles). The process of excavating, recompacting and other human actions on the soil result in unsaturated granular materials. Another interesting type of wet material are the swelling soils. These contain clays that are capable of absorbing water. The volume of the soil can significantly change as a consequence of the penetration of water in the pore space. The expansion of these soils may cause damage on foundations, pavements and retaining walls. The last example of this brief introduction concerns the partially saturated soils located over the water table. Due to capillary, water rises to a certain height above the phreatic level (water table). During dry periods, evaporation and evapotranspiration mechanism produce a gradual desaturation of the soil that eventually shrink the soil. Therefore, cracks (desaturation fissures) appear as the soils dry out.

Previous examples of partially saturated soils illustrate the hydro-mechanical impact of the soil when the water content is changed. The macroscopic behavior of unsaturated soils is not restricted to the amount of water and air, instead, mechanical and hydraulic properties are susceptible to temperature changes, chemical reactions, fluid flow, etc. All these phenomena evidence the need for exhaustive studies that will help understand which parameters control the mechanical behavior of unsaturated materials.

Overall, this chapter aims to review the previous work on the analysis of unsaturated soils and multiphase flow. In the first part, we introduce the physics and mechanics of partially saturated granular material. The second part of the chapter summarizes several numerical methods employed to explore the nature of multiphase flow in porous media. Even though, current techniques allow micro- and macro-scale analysis of the multiphase flow, we will emphasize the pore-scale methods. Indeed, microscopic analysis are essential to understand the capillary phenomena observed at the pore scale and, therefore, determine the origin of many macroscopic behaviors.

1.2 Physics of multiphase flow

Many natural and industrial processes involve the flow of immiscible phases in porous media. Some examples include environmental hydrogeology, storage in underground reservoirs, riser reactors, crude oil recovery, gas-liquid flows in evaporators and condensers, fluidized beds, dryers, etc (Abriola (1988); Young (1993); Wang and Cheng (1997); Blunt (2001); Pruess and Garcia (2002)).

In the last decades, experimental, theoretical and numerical approaches have been used to study the intricate phenomena observed at the pore space (Lenormand et al. (1983); Kueper et al. (1989); Helba et al. (1992)). A better understanding of the processes at the micro-scale results in a better prediction of fluid flow and phase distribution in porous media at the macro-scale.

In order to predict the behavior of multiphase flow, it is crucial to know the governing equations that describe the physical phenomena. Unfortunately, the complexity of multiphase flows and the difficulties encountered when solving the ruling equations and closure laws of multiphase flows hinder a complete study of such flows.

1.2.1 Solid and fluid properties of single-phase flow

At the macro-scale, multiphase flow through porous media are characterized by two important quantities: the porosity ϕ and the permeability κ.

Porosity is defined as the ratio between the void pore space (V_v) to the bulk volume of a certain material (V_t):

$$\phi = \frac{V_v}{V_t} \tag{1.1}$$

Permeability refers to the flow conductance of the solid matrix. It is related to the geometrical features of the solid phase including particle size and shape, pore size, and pore distribution. Hence, permeability is a characteristic of the porous media, not the fluid. Fluid properties are included in the hydraulic conductivity $K = \frac{\kappa \rho g}{\mu}$, where ρ is the density of the fluid, g is gravity, μ the dynamic viscosity and κ the intrinsic permeability of the soil. The hydraulic conductivity describes the ability of fluid to flow through the porous media. Besides, the flow can be formulated by Darcy's law:

$$\mathbf{q} = -\frac{\kappa}{\mu}(\nabla p - \rho \mathbf{g}) \tag{1.2}$$

where $\mathbf{q}$ is the flux and ∇p is the pressure gradient vector. Darcy's law is only valid when fluid flow is laminar ($Re < 1$).

The Navier-Stokes (N-S) equations govern the generic motion of viscous fluids. These equations are obtained from Newton's second law of motion for fluids. The N-S equations under the assumption of isotropic pressure can be written as:

$$\rho\left(\frac{\partial \mathbf{u}}{\partial t}+\mathbf{u}\cdot\nabla\mathbf{u}\right)=-\nabla p+\nabla\cdot[\mu(\nabla\mathbf{u}+(\nabla\mathbf{u})^T)]+\nabla\cdot[\lambda(\nabla\cdot\mathbf{u})\mathbf{I}]+\mathbf{F} \tag{1.3}$$

where ρ is the fluid density, $\mathbf{u}$ the fluid velocity, μ the dynamic viscosity, λ the bulk viscosity, $\mathbf{F}$ the external forces and p the fluid pressure. The left-side of Eq. 1.5 corresponds to the inertial forces, whereas the right-side of Eq. 1.5 stands for the sum of pressure forces, viscous forces, and external forces applied to the fluid.

N-S equations are solved alongside the continuity equation:

$$\frac{\partial \rho}{\partial t}+\nabla\cdot(\rho\mathbf{u})=0 \tag{1.4}$$

Eq. 1.4 states that an increase of density in a volume element must be balanced by a mass influx into the element. N-S and continuity equations represent the conservation of momentum and mass, respectively. It is worth noting that N-S equations are usually too complex to be solved in a closed form. However, special (but common) cases are considered to simplify the previous equations. For instance, in case of incompressible fluids, Eq. 1.4 and 1.5 reduce to:

$$\rho\left(\frac{\partial \mathbf{u}}{\partial t}+\mathbf{u}\cdot\nabla\mathbf{u}\right)=-\nabla p+\mu\nabla^2\mathbf{u}+\mathbf{F} \tag{1.5}$$

$$\nabla\cdot\ \mathbf{u}=0 \tag{1.6}$$

1.2.2 Multiphase flow

This thesis is focus on partially saturated soils. Such soils are a typical example of multiphase systems, which are distinguished from a single-phase system due to the presence of interfaces separating the fluid phases.

1.2.2.1 Macroscopic behavior

1.2.2.1.1 Dynamic characteristics

In the absence of gravity, muliphase flow is governed by the relative contribution of viscous forces and the action of surface tension. The balance between these effects is controlled by two dimensionless numbers: the viscosity ratio M and the capillary number Ca. Such variables are responsible for the macroscopic pattern fluids adopt inside the porous media (Lenormand (1990)). Capillary number (Ca) expresses the magnitude of the viscous forces relative to the effect of surface tension. Viscosity ratio (M) illustrates the ratio of the invading fluid viscosity to the receding one.

$$C_a=\frac{\mu v}{\gamma},\quad M=\frac{\mu_{inv}}{\mu} \tag{1.7}$$

where μ_{inv} is the viscosity of the invading phase, μ is the viscosity of receding phase, v is the average velocity of the receding phase, and γ is the surface tension between the two fluid phases.

Very small capillary numbers ($Ca < 10^{-5}$) result in a flow dominated by capillary forces whereas high Ca imply capillary forces are negligible compared to the viscous forces. We emphasize that most of the simulations in this thesis are performed under quasi-static conditions, therefore, $Ca \approx 0$ and viscous effects can be neglected. Moreover, Ca is typically evaluated as a macroscopic parameter and not suitable at the pore scale. The reason is the wide range of values the velocity of fluids can have between the macro- and the pore scale (Lu et al. (1995); Joekar-Niasar and Hassanizadeh (2012)). Viscosity ratio is defined as favorable when $M > 1$, while it is referred as unfavorable if $M < 1$.

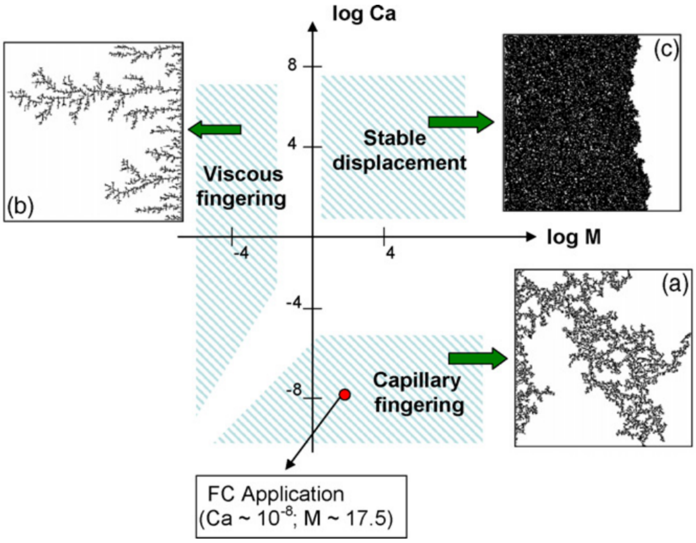

Figure 1.1: Schematic representation of different flow patterns under various viscosity ratios and capillary numbers, after Joekar-Niasar and Hassanizadeh (2012), originally based on Lenormand et al. (1988).

The phase diagram (see figure 1.1) proposed by Lenormand et al. (1988) shows several flow patterns in the absence of gravity at different Ca and M. According to figure 1.1b, viscous fingering takes place when $M << 1$ and Ca is sufficiently large. The fluid invasion front can adopt two different patterns as function of the capillary number for favorable M. If Ca is small, the non-wetting phase is distributed within the porous medium in form of capillary fingering (figure 1.1a). On the contrary, large Ca lead to a stable front displacement (figure 1.1c).

1.2.2.1.2 States of fluid content

In a typical multiphase porous system (i.e., water/air/soil, in which we assume the water is the wetting-phase and the air is the non-wetting phase), the cohesion of the soil strongly depends on the amount of water in the system. A qualitative classification depending on the water content was defined by Newitt and Conway-Jones (1958); Iveson et al. (2001); Mitarai and Nori (2006):

- **Pendular regime**: At low moisture level, solid particles are connected by liquid bridges.

- **Funicular regime**: At this state, pendular bridges around the contact points and liquid-filled pores coexist.
- **Capillary regime**: As the liquid content increases, several clusters are formed after the coalescence of pendular bridges. Most of the pores are filled with liquid in the capillary regime. The tensile strength of a system in the capillary state is three times larger than the pendular regime (Cho et al. (1989)).
- **Slurry regime**: The liquid pressure is equal or higher than the air pressure. The cohesive action vanishes in this state.

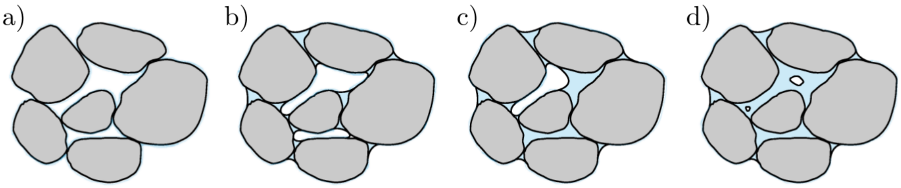

Figure 1.2: Schematic representation of the different states of liquid in a soil: a) Dry material, b) pendular regime, c) funicular regime, d) capillary regime. Image taken from Scholtès (2008).

A better understanding of the liquid structures and the capillary cohesion is crucial to predict landslides or avalanches (Halsey and Levine (1998)). Furthermore, practical applications in wet agglomerates could benefit from a better insight into the behavior of partially saturated systems (Turton (2008)). In this thesis, liquid morphology is studied throughout pendular, funicular and capillary regimes.

1.2.2.2 Influence of the microscopic properties on the macroscopic behavior of soils

The global behavior of a soil strongly depends on the interparticle interactions at the grain scale. Indeed, the macrocopic phenomena of dry, saturated and unsaturated granular media have their origin at the local scale. For this reason, it is common to define macroscopic variables in terms of variables at the microscopic scale, establishing a link between the two scales.

In this section we introduce two microscopic parameters that play a critical role in the dynamics of interface displacement in porous media.

1.2.2.2.1 Wettability

According to Bear (1972), miscible and immiscible fluid displacements are possible in deformable porous media. Miscible displacements refer to fluids in which there are concentration gradients of a dispersed solute, whereas immiscible displacements are the ones in which simultaneous flow of two or more immiscible fluids occur in the porous medium (Martin (1962); Al-Gharbi (2004)). In this work, we focus on immiscible two-phase flow in a porous medium. Additionally, immiscible multiphase flows may not be in a steady-state and change the saturation of the system with respect to the rest of the fluids with time. The phases of the immiscible fluids are separated by a fluid-fluid interface. The tension acting on the interface between the two fluids relates the surface tension of each fluid with the solid phase through the following equation (see figure 1.3):

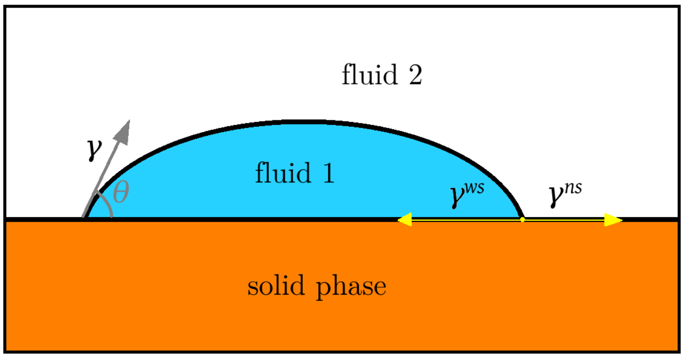

Figure 1.3: Schematic representation of a fluid drop on a solid surface. Contact angle and surface tensions are depicted.

$$\gamma^{ns} - \gamma^{ws} = \gamma cos\theta \tag{1.8}$$

where θ is the contact angle, γ^{ns} is the interfacial tension between the solid phase and the non-wetting phase, γ^{ws} is the surface tension between the solid and the wetting phases, and γ is the surface tension between the wetting and the non-wetting phases.

The contact angle is related to the wettability of a solid by a fluid. Moreover, wettability has a strong influence on the fluid distributions in the porous medium. Following the scheme displayed in figure 1.3, fluid 1 is defined as wetting phase when $\theta < \pi/2$. Otherwise, if $(\theta > \pi/2)$, fluid 1 is referred as non-wetting phase.

The process known as drainage occurs when the non-wetting phase displaces the wetting phase. Imbibition mechanism results after reversing the drainage process, thus, causing the displacement of the non-wetting phase by the wetting phase.

1.2.2.2.2 Capillary pressure

Capillary pressure plays a key role in the description of multiphase flow in porous media. Such flows involve immiscible fluids separated by a common fluid-fluid interface. The thickness of this interface is typically of the nanometer-order. At equilibrium, the curvature of the interface is related to the difference between the non-wetting phase pressure (p^{nw}) and the wetting phase pressure (p^{w}):

$$p_c = p^{nw} - p^{w} = \gamma \left(\frac{1}{R_1} + \frac{1}{R_2} \right) \tag{1.9}$$

where p_c is the pressure differential (also referred as microscopic capillary pressure), γ is the surface tension between the two immiscible fluids and R_1 and R_2 correspond to the principal radii of curvature.

Eq. 1.9 is valid locally for a meniscus of general shape. By assuming a spherical meniscus of radius r_s (for instance, considering the pore radius is equivalent to the radius of the largest inscribed sphere that can be enclosed within the pore) Eq. 1.9 becomes:

$$p_c = \frac{2\gamma}{r_s} \tag{1.10}$$

In the existing literature (Scheidegger et al. (1958); De la Cruz and Spanos (1983)), the equilibrium relation for microscopic capillary pressure is extended to define the macroscopic capillary pressure as follows:

$$p_c = \overline{p^{nw}} - \overline{p^{w}} \tag{1.11}$$

where $\overline{p^{nw}}$ and $\overline{p^{w}}$ are the averaged non-wetting and wetting phase pressures over the representative elementary volume of a porous medium.

Despite the fact that Eq 1.11 is frequently used in quasi-static and dynamic flow, Hassanizadeh and Gray (1993) suggests that capillary pressure should be evaluated on the interface, thus, averaged only over the fluid-fluid interface and not over the volume. As a result, Hassanizadeh and Gray (1993) propose an alternative approach to determine the macro-scale capillary pressure. They found that capillary pressure is related to the change in free energy of the two fluid phases and all three interfaces that results into a change in saturation. Therefore, capillary pressure is determined as a function of the specific area of the fluid-fluid interface per unit volume (a^{nw}) and the wetting phase saturation (S_w):

$$p_c = f(a^{nw}, S_w) \tag{1.12}$$

1.2.2.3 Mechanics of partially saturated soils

For a long time, the difficulties encountered in analyzing the effects of partially saturated granular media prevented a complete study of soil mechanics beyond dry and fully saturated soils.

Terzaghi was the first author to investigate the mechanical response of saturated deformable porous media. Terzaghi (1936) introduced the concept of effective stress stating that "effective constraint (σ'_{ij}) is a function of the total stress (σ_{ij}) and the pore water pressure (p^w)":

$$\sigma'_{ij} = \sigma_{ij} - p^w \tag{1.13}$$

After some years, the previous concept was extended to a more general case by Bishop and Blight (1963) . They proposed the following expression suitable for partially saturated soils:

$$\sigma'_{ij} = (\sigma_{ij} - p^{nw}) + \chi_B(p^{nw} - p^w) = (\sigma_{ij} - p^{nw}) + \chi_B p_c \tag{1.14}$$

where p^{nw} is the pressure of the air and χ_B is the Bishop parameter, which is related to the degree of saturation. χ_B is 1 for a fully saturated material and 0 for a dry soil.

Fredlund et al. (1978) proposed to model the behavior of partially saturated soils through two independent constitutive variables (σ_{ij} and p^w). Accordingly, Alonso et al. (1990) introduced one of the first elastoplastic models capable of describing the mechanical behavior of unsaturated soils. The model is commonly termed Barcelona Basic Model (BBM) and applies for slightly or moderately expansive soils, such as unsaturated sands, silts, and clays of low plasticity.

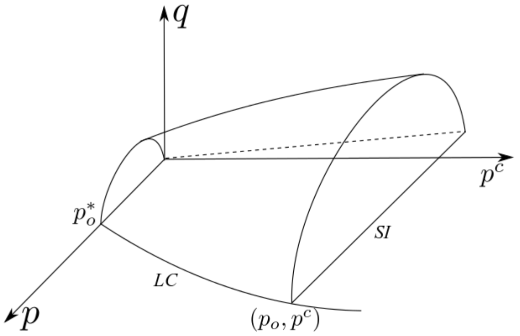

Figure 1.4: Three-dimensional representation of the yield surface in the BBM (after Alonso et al. (1990)).

BBM is based on the modified Cam clay model (MCC), as a matter of fact, the three-dimensional yield surface illustrated in figure 1.4 becomes the MCC ellipse under saturated conditions (i.e., $p_c = 0$), where p is the mean stress and q represents the deviatoric stress.

Due to the simple formulation, BBM is easy to implement in numerical analysis and rapidly became a popular model to describe many mechanical features of unsaturated soils, such as wetting-induced swelling or collapse (Gens et al. (2006)).

Numerous models have been developed inspired by BBM to handle stress–strain relations (Gens and Alonso (1992); Kohgo et al. (1993); Cui et al. (1996)). More recent models incorporate suction-degree of saturation hysteresis into stress–strain relationships (Gallipoli et al. (2003); Sheng et al. (2004); Thu et al. (2007)).

1.3 Numerical Models for multiphase flow - Literature review

The behavior of partially saturated granular media can be studied from an experimental point or view. Due to high cost of some experimental devices and the impossibility to measure some mechanical properties at certain scales, numerical methods arise as an interesting alternative to obtain some insights into the physical mechanisms of the multiphase flow within the porous media. The recent advances in computer technology have created new opportunities to investigate the field of multiphase flow. However, the complex geometry and non-linearity of the problems still hinder the analysis without crude approximations. Accordingly, macroscopic approaches are based on geometrical simplifications and transport properties are taken from laboratory experiments. The main difficulty encountered by researchers to model multiphase flow from a global perspective is related to the local fluctuations induced by the microscopic interactions between the fluids. Such interactions modify the boundary conditions of the other fluid altering the global response. The hydro-mechanical coupling gets even more complex to study when we deal with deformable solid structures.

In contrast to the methods that adopt a macroscopic perspective, some works (Kharaghani et al. (2012); Yuan and Chareyre (2017); Sweijen et al. (2018)) opted for a micro-scale approach. Such models account for the coupling between fluid flow and deformation of the solid phase to investigate the hydro-mechanical behavior at the pore scale. The following subsections provide a literature review of previous works that tackled similar phenomena from different scales.

1.3.1 Scale of observation

Multiphase flow through granular media can be described following a macroscopic continuum approach. The macro-scale continuum based models usually employ empirical relationships or mathematical expressions to evaluate the global behavior. However, the discontinuous and heterogeneous nature of granular materials hinders the macroscopic study of this type of materials.

The need for a greater understanding of the underlying fundamentals and the recent advances of computational fluid dynamics (CFD) enhanced the modeling at a very small scale. Several fully resolved methods are found at this level. For instance, the smoothed particle hydro-dynamics (SPH) has been employed to get microscopic insight of the fluid flow in porous media (Jiang et al. (2007a)). Another popular model is the lattice Boltzmann method (LBM), based upon kinetic formulations of the Boltzmann equation.

Finally, the mesocopic models act like a bridge between the micro- and macro-scale. The discrete nature of granular media suggests that it is reasonable to characterize the global behavior in terms of properties obtained at the pore- or grain-scale instead of relying on mathematical forms based on parameters identified a posteriori from experimental tests. Therefore, numerical modeling based on discrete elements is seen as a promising tool to study the influence of local phenomena on the macroscopic behavior of granular materials.

1.3.2 Macroscopic continuum approach

Macro-scale models are based on continuum descriptions of flow. In particular, the momentum and energy balance are considered in the integral form over finite volumes to reproduce two-phase flow problems. Mechanical variables such as fluid velocity or pressure appear as local mean variables, which are obtained by averaging over large regions compared to the particle spacing but small compared with the whole system. The continuum models based on the local average describe the motion of the fluid and particles, however, the physical quantities of such models appear as formal terms that must be determined empirically through phenomenological laws (Anderson and Jackson (1967); Catalano (2012)). In addition to that, the macroscopic nature of the model results into averaged hydro-mechanical properties that hinder the analysis at the local scale (Catalano et al. (2014)).

According to Joekar-Niasar and Hassanizadeh (2012); Yuan (2016), the following governing equations must be solved to have a continuum description of a two-phase flow. Besides ignoring gravity, the equations below are restricted to a rigid solid matrix and incompressible immiscible fluids:

Mass conservation of fluid phase:

$$\phi \frac{\partial S_\sigma}{\partial t} + \nabla \cdot \mathbf{u}^\sigma = 0, \quad \sigma = nw, w \tag{1.15}$$

where ϕ is the porosity, S_σ the saturation of phase σ, $\mathbf{u}^\sigma$ the velocity of phase σ, and w and nw refer to the wetting and non-wetting phases.

The velocity of the fluid phase ($\mathbf{u}^\sigma$) is the local velocity derived from Darcy's law:

$$\mathbf{u}^\sigma = -\frac{1}{\mu^\sigma} k^\sigma \bar{\bar{\mathbf{K}}}(\nabla p^\sigma), \quad \sigma = nw, w \tag{1.16}$$

where $\mu^\sigma =$ stands for the viscosity of phase σ, k^σ is the relative permeability of phase σ, $\bar{\bar{\mathbf{K}}}$ is the intrinsic permeability tensor and p^σ is the pressure of phase σ.

Moreover, the pore volume conservation is ensured by:

$$S_w + S_{nw} = 1 \tag{1.17}$$

Finally, Buckley-Leverett's assumption is taken into account:

$$p_c = p^{nw} - p^w = f(S_w), \quad \frac{dp_c}{dS_w} = 0 \tag{1.18}$$

1.3.3 Pore-Network models

Pore-network models have been widely used to describe the motion of fluids through porous media (Fatt et al. (1956); Fenwick et al. (1998)). The computation time of pore-network models is significantly reduced after the idealization of the geometry (Øren and Pinczewski (1995); Hilpert et al. (2000)). Thus, pore-network models are frequently employed to simulate large domains that are hardly handleable with micro-continuum models. Pore-network models manage to reduce the high complexity of porous morphology by a discretization of the pore space. However, simplifications taken into the pore network models lead to a detriment of accuracy and make the predictions less credible. Despite the idealization of the geometry, some studies based on the pore-network approach (Blunt (2001)) have been proven successful to simulate multiphase flow and obtain constitutive properties of unsaturated media (such as the hysteresis of saturation curves, the study of the permeability, the effects of wettability on the pore walls or the mass transfer between fluids).

The network topology is described by two characteristics (Joekar-Niasar and Hassanizadeh (2012)): the spatial location of the pore bodies and the connectivity of pore elements. Four different network topologies have been used in previous studies: structured regular (the most common network), structured irregular (Koplik and Lasseter (1985); Mogensen and Stenby (1998)), unstructured regular (King (1987);

Blunt and King (1991)) and unstructured irregular. Early network models were based on square (2D) or cubic (3D) lattices with a constant coordination number of four in 2D or six in 3D (Chandler et al. (1982); Ioannidis and Chatzis (1993)). Recent works (Dong and Blunt (2009); Jivkov et al. (2013)) account for larger coordination numbers by considering connectivity changes within the network.

In addition to the topology, the pore geometry has a strong influence on the flow behavior. The shape of the pore bodies can be assumed as cubical (Joekar-Niasar et al. (2010a); Raoof and Hassanizadeh (2013)) or spherical (Koplik and Lasseter (1985)) nodes. Concerning the pore throats, the shape has been approached using cylinders with different cross-sectional shapes (circular (Dias and Payatakes (1986); Koplik and Lasseter (1985)), square (Singh and Mohanty (2003)), triangular Al-Gharbi and Blunt (2005)), or with angular cross sections (Van Dijke and Sorbie (2006)) to reproduce the phenomena of wetting phase flow in the corner.

Nowadays, it is possible to describe the complex geometry of the pore space more accurately using advanced solutions that include pore throat roughness (Tsakiroglou and Fleury (1999); Tsakiroglou and Payatakes (2000)) and detailed cross-sections extracted from high-resolution 3-dimensional images using X-ray microtomography (Al-Raoush and Willson (2005)). Mapping real granular assemblies yields to irregular lattices (Piri and Blunt (2005); Xiong et al. (2016)). Consequently, reconstruction algorithms are an essential aspect to build the pore-network models. Such algorithms include the multi-orientation scanning method (Zhao et al. (1994)), medial axis algorithms (Lindquist et al. (1996); Sheppard et al. (2005); Prodanović et al. (2006); Jiang et al. (2007b)), Delaunay/Voronoi diagram-based methods (Bryant and Blunt (1992); Øren and Bakke (2003)), or the maximal ball algorithms Silin et al. (2003); Silin and Patzek (2006); Al-Kharusi and Blunt (2007)).

The majority of pore-network models are quasi-static and the pore-scale displacements occur when a threshold capillary pressure is exceeded. More details about the motion of fluids in a pore-network are further explained in section 1.3.5.

1.3.4 Hydro-mechanical studies using the Discrete Element Method

Several approaches have been developed in order to reproduce the physics of multiphase flow through porous media. Fluid flow may have a strong impact on the mechanical behavior of saturated and partially saturated granular systems. Indeed, fluid flowing through porous media exerts forces on the solid grains altering the solid interactions. Additionally, changes in the solid matrix modify the flow field within the granular assembly.

The mechanical behavior of the granular material is frequently based on the popular Discrete Element Method (DEM) introduced by Cundall and Strack (1979). Even though the DEM was conceived to deal with dry granular materials, some works have extended the model to saturated and partially saturated granular media including the fluid effects. Three different coupled DEM-fluid approaches can be adopted depending on the scale:

1.3.4.1 Continuum-based models

The continuum approach (also termed Macroscopic continuum approach) is frequently employed to reproduce the motion of full saturated granular soils. In coupled continuum-discrete models, a complete description of the system is possible by solving the linear and angular momentum for each solid particle and the Navier–Stokes equations to mimic the motion of the interstitial fluid. Some difficulties arise when multiphase flow is considered. These models incorporate the local fluctuations induced by the microscopic interactions between the fluids ensuring mass conservation. As explained in section 1.3.2, macroscopic continuum approaches require empirical laws and information about constitutive properties. Plus, these methods rely on continuum formulations and coarse-grid meshing for the fluid part (Kafui et al. (2002); Zeghal and El Shamy (2004)).

According to Catalano (2012), continuum-based models are incapable to describe the single particle behavior, such limitation may add some difficulties in problems in which heterogeneity plays an important role in the global behavior (shear banding in cohesionless materials, microcracks in cohesive materials, etc). Although this disadvantage constrains the applicability of the model, continuum-discrete couplings perform numerical simulations in reasonable computation times.

1.3.4.2 Micro-scale continuum models

In recent years, several methods have appeared to predict the flow in porous media. Lattice Boltzmann method (LBM) (Pan et al. (2004); Sukop et al. (2008)), volume of fluid (VOF) method (Raeini et al. (2012)) or Lagrangian mesh-free methods (Tartakovsky et al. (2007)) are examples of micro-scale continuum models employed in the analysis of multiphase flow through porous media. Despite the high computational cost, these models have been proven successful to reproduce the physical phenomena at different scales. Besides, the nature of these models make them suitable for complex geometries and benefit from computing parallelism.

Typically, micro-scale continuum models take into account the fluid-grain interactions by a no-slip condition at the fluid–solid interface. We also emphasize that most of the current coupled DEM-fluid models based on fully resolved methods are limited to 2D due to the high computational cost when large granular assemblies are considered, especially with multiphase flows. 2D DEM-LBM coupling is typically used to investigate the behavior of a soil bed subject to a localized injected flow (Cui et al. (2012, 2014)). Regarding the fluid mechanical interactions in full three-dimensional systems, Han and Cundall (2013); Delenne et al. (2011), among others, have developed several 3D DEM-LBM couplings. The Smoothed Particle Hydrodynamics (SPH) has also been coupled with DEM as a promising tool to simulate solid-liquid mixtures as shown by Potapov et al. (2001); Li et al. (2007). However, computations using SPH are usually slower compared with other grid-based models (Crespo (2008)). Furthermore, SPH presents some difficulties to apply the macroscopic viscosity (Li (2013)) and reproduce turbulent flows.

1.3.4.3 Pore-Network approach

In order to have an acceptable computational cost, flow through porous media can be described by means of Pore-Network (PN) models. The idealization of the pore space as a network of connected pores and throats leads to a reduced number of unknowns compared to micro-scale models. Up to now, very few works have been devoted to couple PN models with mechanical models. For single-phase flow, Tarumi and Hakuno (1988) was the first attempt to incorporate the fluid interaction effects into the DEM. Their technique modified the micromechanical DEM to include Darcy's law that takes into account the pore water pressure. Following this approach, Nakase et al. (1999) proposed an alternative strategy where pore pressure was considered in square-cell elements instead of at the pore level. More recently, Jing et al. (2001) analyzed the mechanical behavior of the coupled stress-deformation and fluid flow interaction in rock fracture. Despite the successful results, simulations were restricted to 2D disk assemblies. Extending the approach to 3D spheres packing was a key point to reproduce realistic simulations and predict the macroscopic properties.

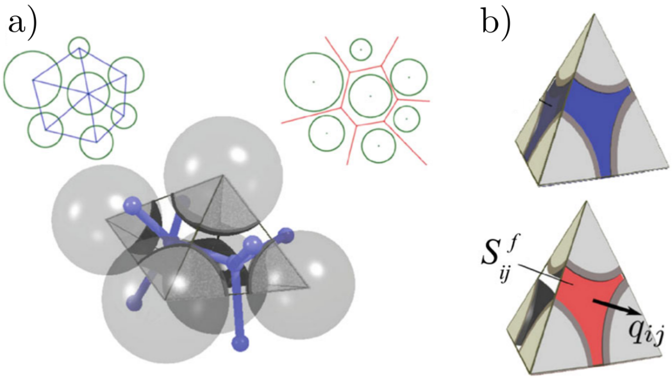

Figure 1.5: a) Regular triangulation and his dual Voronoi's graph in two dimensions and in three dimensions. b) Elementary fluid domain (tetrahedron) in a triangulated sphere assembly. Images taken from Chareyre et al. (2012); Scholtès et al. (2015).

A three-dimensional pore-scale approach worth highlighting is the pore-scale finite volume (PFV) formulation of the viscous flow of an incompressible pore fluid. The technique proposed by Chareyre et al. (2012) is based on a decomposition of the pore space into pore elements and local conductances. The discretization of the pore space is performed by Regular Triangulations and their dual Voronoi graphs applied to the sphere packings as illustrated in figure 1.5a. The implementation of the PFV-DEM has provided successful results in one-phase flow problems (Catalano et al. (2014); Scholtès et al. (2015); Montellà et al. (2016)). Even though the PFV-DEM is capable to study the hydro-mechanical behavior of partially saturated granular materials, its applicability is limited to the saturated regime. Therefore, the PFV-DEM was extended into a model able to reproduce two-phase fluid flows. Such approach is termed ”Two-phase Pore-scale Finite Volume - Discrete Element Method” (2PFV-DEM) and was developed by Yuan et al. (2016). Recent research (Sweijen et al. (2017b); Yuan and Chareyre (2017)) shows that two-phase fluid problems are effectively solved using the 2PFV-DEM (see the example of figure 1.6).

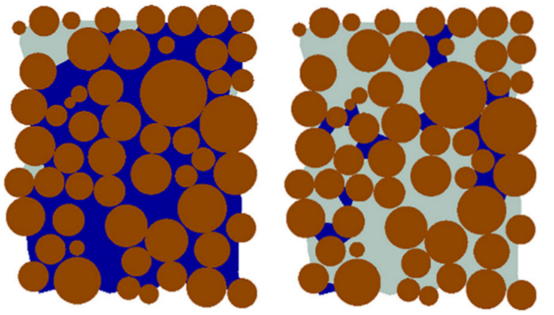

a) p_c^*=7.25 S_w=0.96 b) p_c^*=13.2 S_w=0.18

Figure 1.6: Process of drainage performed with the 2PFV-DEM. Brown spherical bodies are the solid phase, blue represents the wetting phase and grey is the non wetting phase. Non-wetting phase invades the assembly from top. The wetting phase is trapped in the sample in form of clusters after the drainage. Image taken from Yuan and Chareyre (2017).

The governing equations Eq. 1.15 - 1.18 proposed in Buckley-Leverett theory are formulated to describe the fluid dynamics at the macro-scale, thus, not suitable at the pore-scale. A new set of equations is proposed by Joekar-Niasar and Hassanizadeh (2012) adapting the previous governing equations and taking into account the following assumptions:

- Fluids are immiscible and incompressible.
- Rigid solid structure.
- Negligible inertial effects (low Reynolds numbers) in the pore throats.

1.3.4.3.1 Fluid phase

Let's consider a pore unit i. The continuity equation for an incompressible fluid is written as:

$$V_i \frac{\partial S_{w,i}}{\partial t} + \sum_{j=1}^{4} q_{ij} = 0 \tag{1.19}$$

where V_i is the volume of the pore body and q_{ij} are the fluid fluxes from the tetrahedron i to the adjacent tetrahedra j_1 to j_4. Fluxes and pressure gradients are assumed to have linear relation:

$$q_{ij} = g_{ij} \frac{\Delta_{ij}}{L_{ij}} \tag{1.20}$$

where Δ_{ij} is the pressure drop between two adjacent bodies and it is related to the capillary pressure and the fluid pressures at the neighboring pore bodies, L_{ij} is the distance between pores i and j, and g_{ij} is related to the hydraulic conductance across the pore throat ij. The following definition has been proposed with satisfactory results for g_{ij} in the case of a saturated throat (Tong et al. (2012)):

$$g_{ij} = \frac{S_{ij}^{f} R_{ij}^{h}}{L_{ij}^{2}} 2\mu \tag{1.21}$$

where S_{ij}^{f} is the area occupied by the fluid in facet and R_{ij}^{h} is the hydraulic radius (defined as the ratio between the volume occupied by the fluid and the area of solid–fluid interface).

Based on the possible fluid configurations in two neighboring pore bodies and a pore throat (Koplik and Lasseter (1985)), Δ_{ij} can be expressed as:

$$\Delta_{ij} = p_i^{nw} - p_j^{nw} + s_i^{w}(p_{c,ij} - p_{c,i}) - s_j^{w}(p_{c,ij} - p_{c,j}) \tag{1.22}$$

where, $p_{c,i}$ and $p_{c,j}$ are the capillary pressures of elements i and j, respectively, and $p_{c,ij}$ is the entry capillary pressure of pore throat ij. Thus, the volumetric flux (Eq. 1.20) is reformulated as:

$$q_{ij} = g_{ij} \frac{(p_i^{nw} - p_j^{nw} + s_i^{w}(p_{c,ij} - p_{c,i}) - s_j^{w}(p_{c,ij} - p_{c,j}))}{l_{ij}} \tag{1.23}$$

1.3.4.3.2 Solid phase

The total force $\mathbf{F}_k^{f}$ exerted on a solid particle k by two fluid phases includes the contribution of the pressure considering both wetting and non-wetting phases ($\mathbf{F}_k^{p}$) and the effect of surface tension at the solid-wetting-nonwetting interface $\mathbf{F}_k^{t}$.

$$\mathbf{F}_k^{f} = \mathbf{F}_k^{p} + \mathbf{F}_k^{t} \tag{1.24}$$

1.3.5 Local rules for pore-scale models

In order to complete the pore-scale approach to simulate multiphase flow through the porous system, some local rules need to be incorporated into the model. These rules are considered for each pore to have a proper understanding of the phenomena at the pore scale.

1.3.5.1 Entry capillary pressure

Let's assume a pore body filled with the wetting phase. The non-wetting phase will invade the body through the pore throat when the local capillary pressure is larger than the entry capillary pressure of that pore throat. Several approaches can be considered to compute the entry capillary pressure. The most common approximations are the Haines incircle method (Sweijen et al. (2016)) and the Mayer-Stowe-Princen (MS-P) method (Joekar-Niasar et al. (2010b); Yuan et al. (2016)). Haines incircle approximation (Haines (1930)), "Incircle method" hereinafter, proposes that the curvature of the interface passing through the pore throat can be assumed as a sphere in contact with the spherical grains defining the pore throat. On the other hand, the MS-P method is based on a force balance for contact lines during the invasion. MS-P model predicts the capillary pressure of the arc meniscus of a fluid droplet of infinite length inside a cylindrical tube (Princen (1969); Mayer and Stowe (1965); Ma et al. (1996)). The force balance proposed by (Mayer and Stowe, 1965; Princen, 1969) can be written as:

$$\sum \mathbf{F} = \mathbf{F}^p + \mathbf{F}^t = 0 \tag{1.25}$$

where $\mathbf{F}^p$ is the capillary force acting on the area of wetting - nonwetting interface and $\mathbf{F}^t$ is the contribution of the surface tension acting on the contact lines between different phases.

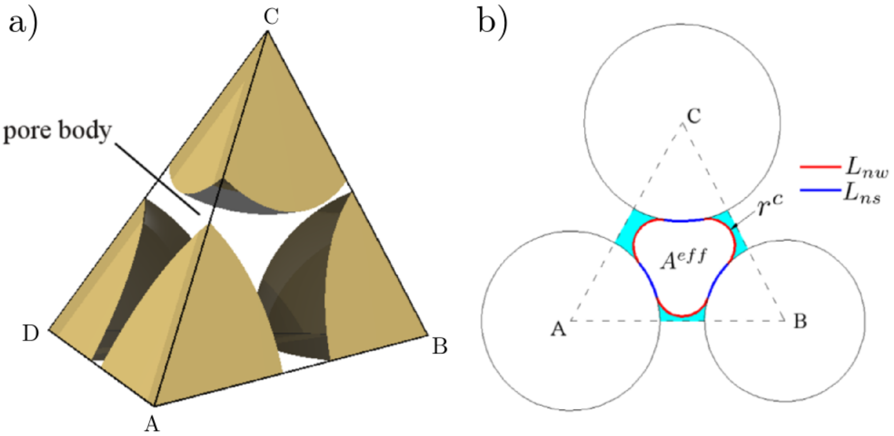

Figure 1.7: Pore geometry. (a) A pore defined by a tetrahedral element of the finite volume decomposition. (b) Definition of a pore throat geometry. r^c is the radius of the meniscus; L_{nw} is the length of contact line between non-wetting and wetting phases; L_{ns} is the length of contact line between non-wetting and solid phases. $L^{eff} = \sum(L_{nw} + L_{ns})$, in which L^{eff} is termed effective entry pore throat perimeter. A^{eff} is the planar project area of non-wetting - wetting interface, and is termed effective entry pore throat area. Image taken from Yuan and Chareyre (2017).

The Regular Triangulation of the pore space leads to a pore subset surrounded by four solid spheres whose centers are the vertices of the corresponding tetrahedron as illustrated in figure 1.7a). Likewise, the shape of the pore throat is defined by each tetrahedral facet (see 1.7b)). Furthermore, figure 1.7b displays the parts occupied by the different phases and interfaces. As the capillary pressure is increased, the interfaces are displaced pushing the wetting phase towards the corners of the throat. When the capillary pressure achieves the entry capillary pressure value, the longitudinal curvature of the fluid-fluid interface is assumed to be zero as suggested by (Joekar-Niasar et al., 2010b), thus, $R_1 \to +\infty$ in Eq.1.9. Following the assumption proposed by Yuan and Chareyre (2017), both fluid phase pressures are uniform around the throat, hence, the transversal cross-sectional curvature $\frac{1}{R_2}$ remains unchanged for the different interfaces. Therefore, Eq 1.9 is rewritten in the following form to obtain the entry capillary pressure:

$$p_c^e = \frac{\gamma}{R_2} = \frac{\gamma}{r^c} \tag{1.26}$$

On the one hand, the capillary action can be determined by projecting the capillary pressure on the pore throat section,

$$\mathbf{F}^p = A^{eff} p_c \tag{1.27}$$

where A^{eff} is the area of the non-wetting phase in the pore throat (see figure .1.7b).

On the other hand, the effect of the surface tension along the interface lines is defined as:

$$\mathbf{F}^t = L_{nw}\gamma + L_{ns}\gamma^{ns} - L_{ns}\gamma^{ws} \tag{1.28}$$

where L_{nw} and L_{ns} are the total lengths of fluid-fluid interfaces and non-wetting - solid interfaces respectively. Additionally, interfacial tensions, γ^{ns}, γ^{ws} and γ are related to the contact angle θ according to Young's equation:

$$\gamma^{ns} = \gamma \cos\theta + \gamma^{ws} \tag{1.29}$$

Under perfectly wetting conditions, ($\theta = 0^o$), Eq. 1.28 can be written as:

$$\mathbf{F}^t = (L_{nw} + L_{ns})\gamma \tag{1.30}$$

Both Eq. 1.27 and 1.30 can be expressed in terms of r^c, thus, Eq. 1.25 is numerically solved to determine the entry capillary radius r^c. Finally, the entry capillary pressure is obtained using Eq 1.26. For more details, the reader can refer to Yuan and Chareyre (2017).

Besides the MS-P and Incircle method, direct simulations using the LBM will be used in this thesis to determine the entry capillary pressure for each pore throat.

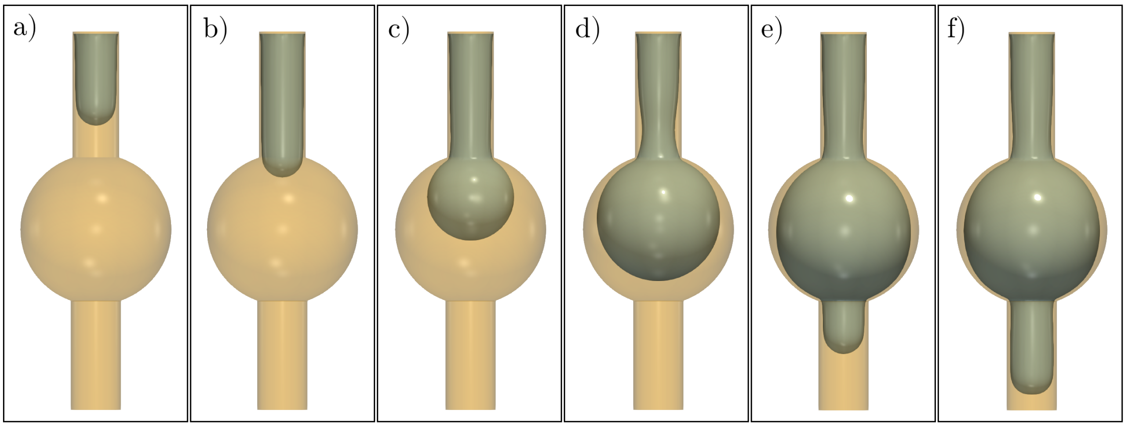

Figure 1.8: Schematic representation of piston-like displacement after a LBM simulation.

1.3.5.2 Interface displacement

The movement of the fluid-fluid interface is possible through snap-off and piston-like displacements. These two mechanisms are well understood, however, previous literature Prodanović and Bryant (2006); Sweijen et al. (2016); Gladkikh and Bryant

(2005) shows that there is still room for improvement in predicting drainage and imbibition in porous media. When the non-wetting phase invades the pore space filled with the wetting phase sweeping the receding fluid in the element (see figure 1.8), the interface displacement is reversible and termed piston-like motion. On the contrary, when the interface menisci exceeds the limits of stability, the configuration becomes unstable and the non-wetting becomes disconnected as displayed in figure 1.9 (Yu and Wardlaw (1986))

Snap-off occurs more frequently with low capillary numbers, whereas piston-like movement becomes dominant as the capillary number is increased. Furthermore, according to Yu and Wardlaw (1986); Blunt et al. (1992), snap-off can only occur under unstable conditions when the piston-like motion is not possible due to topological reasons.

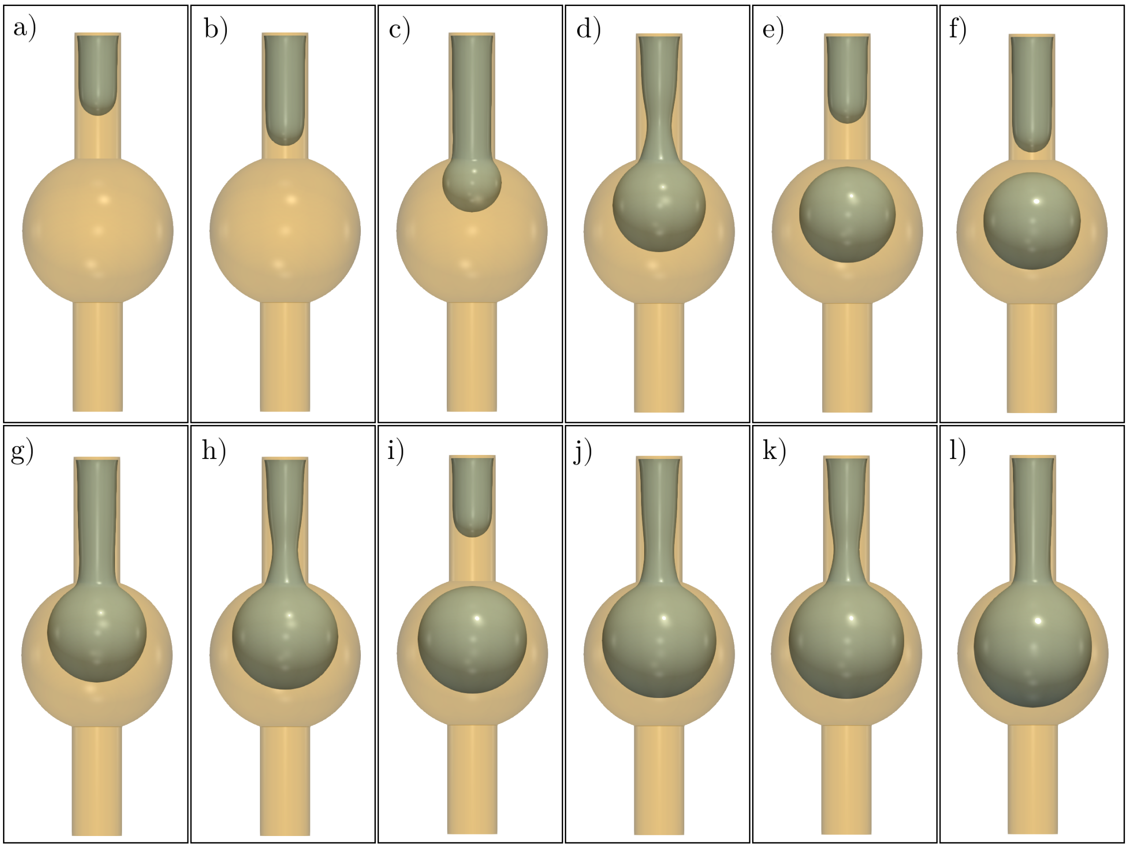

Figure 1.9: Schematic representation of snap-off sequence after a LBM simulation.

Both figures 1.8 and 1.9 illustrate that a capillary pressure increment results into very different phase configurations depending on the capillary number. Additionally, the two mechanisms of fluid motion also reveal discrepancies in terms of capillary pressure - saturation curves as displayed in figure 1.10. In both scenarios, capillary pressure reaches a constant value which corresponds to the entry capillary pressure for a cylindrical pore with a circular cross section (see points "a" in figures 1.8,1.9 and blue and red points "a" in 1.10). The meniscus of the interface increases as the non-wetting phase penetrates the pore body (see points "b" in figures 1.8,1.9 and blue and red points "b" in 1.10). This situation leads to a drastic pressure drop.

In the piston-like displacement case, the non-wetting phase fully occupies the pore body (configuration in between points ”d” and ”e” in figure 1.8), at this moment, capillary pressure reaches a minimum value in figure 1.10. Capillary pressure rapidly builds up until reaching the entry capillary pressure, then, the fluid-fluid interface starts invading the bottom pore throat (see point ”e” in figures 1.8 and red point ”e” in 1.10). On the other hand, the case with relatively low capillary number leads into an unstable interface that gets detached from the rest of the non-wetting phase (see points ”d” and ”e” in figure 1.9 and blue points ”d” and ”e” in 1.10). The new fluid configuration depicted in figure 1.9e shows that the non-wetting phase has receded back to the top pore throat, thus, the meniscus curvature becomes, once again, the one from the cylindrical pore throat. Consequently, the capillary pressure suddenly increases reaching the entry capillary pressure (see point ”e” in figure 1.9 and blue point ”e” in 1.10). The snap-off phenomenon is repeated several times (see points ”h” and ”i” in figure 1.9 and blue points ”h” and ”i” in 1.10) before the pore body and pore throats are completely filled with the non-wetting phase.

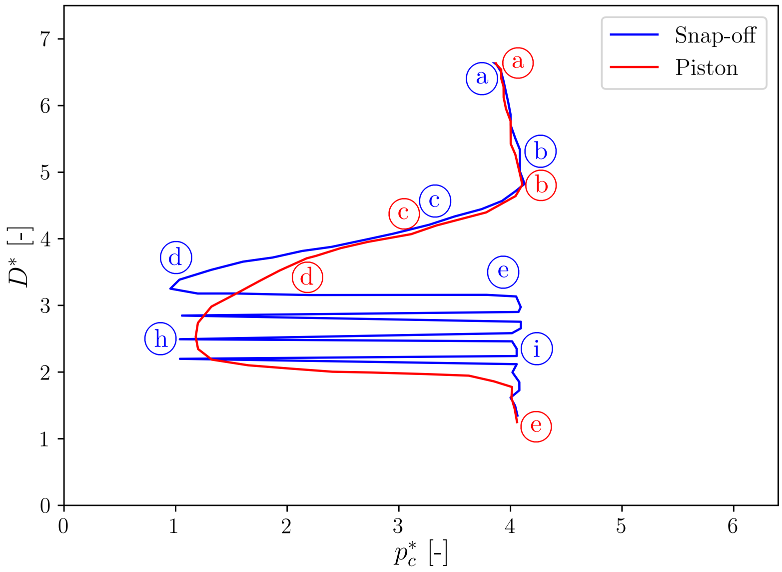

Figure 1.10: Saturation curve during snap-off and piston-like displacement after a LBM simulation. Points indicated in the image correspond to the snapshots illustrated in figure 1.8 and 1.9. Capillary pressure is evaluated as the difference between the inlet (top of the non-wetting phase) and outlet (bottom of the wetting phase) pressures. Viscous effects are subtracted so no pressure loss is depicted in the figure. Dimensionless capillary pressure $p_c^* = \dfrac{2p_c R_{cyl}}{\gamma}$ and distance $D^* = \dfrac{y}{R_{cyl}}$ are considered. R_{cyl} is the radius of the pore throat and y the height of the non-wetting front.

1.3.6 Microscale approach

Even though models based on continuum theory are excellent to mimic the flow in a homogeneous medium, the mechanisms observed at the local scale are crucial to understand the fundamentals of wet granular materials, especially in complex geometries or very heterogeneous media. Several models have been developed at the micro-scale to reproduce such physical phenomena

In addition to the ability to simulate multiphase flow through complex geometries, fully resolved methods do not rely on empirical relations. Moreover, these methods are easy to implement and parallelize. Conversely, high computational cost is associated with fully resolved methods. Consequently, realistic simulations are restricted to small granular assemblies in computer clusters.

1.3.6.1 Lattice Boltzmann Method

Shan and Chen (1993); Swift et al. (1995), among others, showed that the lattice Boltzmann Method (LBM) is a powerful model capable to reproduce the motion of multiphase flow. According to Boltzmann equation, a fluid is composed by many particles. In order to avoid unaffordable calculations, particles are treated within a probabilistic approach. In other words, Boltzmann equation uses particle probability distribution functions $f(\mathbf{x},\mathbf{v},t)$ instead of accounting for every particle's position and velocity. The probability density function describes the probability of finding a particle at position $\mathbf{x}$, at time t with a certain velocity $\mathbf{v}$. In the lattice Boltzmann method, both space and time are discretized into a certain number of velocity vectors. Instead of using a discrete form of macroscopic continuum equations (i.e., mass, momentum, and energy), the discrete Boltzmann equation is solved to simulate the fluid flow in two steps: the streaming step, in which particles move from node to node on a lattice and a collision step in which particles are redistributed at each node towards the equilibrium.

Several LBM models have been developed to describe the interfacial dynamics and simulate multiphase flows in porous media. The following methods are briefly described:

1.3.6.1.1 Color gradient method

Gunstensen et al. (1991) introduced the color gradient model inspired by the Lattice Gas Cellular Automata. Two distribution functions are considered in this model to reproduce the motion of two fluids. The particles of one component are red-colored and the other are blue-colored. Surface tension is incorporated in the model by adding an extra collision term in the model. Furthermore, a recoloring step is introduced in the model to avoid diffusion and ensure the immiscibility of the fluids. Tölke et al. (2006); Ahrenholz et al. (2008) improved the color gradient model using a multiple relaxation time (MRT) collision scheme. The new features increased the numerical stability and allowed the simulation of multiphase systems of higher viscosity ratios. In addition to that, the surface tension can be tuned independently of the viscosity ratio.

1.3.6.1.2 Shan-Chen model

In the Shan and Chen (SC) model, an interaction force between components (or phases) is introduced to describe multiphase flows. This force modifies the collision operator through an equilibrium velocity producing a repulsive effect between the phases. Additionally, the forcing term enhances a consistent treatment of the non-ideal non-monotonic equation of state (EOS). The Shan and Chen model can describe multiphase flows using a single-component (SCMP) (Shan and Chen (1993)) or a multi-component (MCMP) scheme (Shan and Doolen (1995)). In the latter one, different distribution functions are assigned to each component. The simplicity of the Shan–Chen model explain why this is the most popular method to simulate multiphase flow. Despite the encouraging results reported in the field of porous media (Pan et al. (2004); Ahrenholz et al. (2008)), SC model has several drawbacks that restricts its applicability. The main limitation of the Shan-Chen model is the inability to adjust surface tension, density ratio and viscosity ratio independently. Indeed, some parameters must be determined through numerical experiments (Ahrenholz et al. (2008); Huang et al. (2015)). Another problem frequently reported (Wagner (2003)) in the Shan-Chen models are the spurious currents (unphysical velocities near the interfaces). Recent works (Shan (2006)) have successfully reduced the spurious currents adopting multirange pseudopotential forms.

1.3.6.1.3 Free-energy method

The free-energy (FE) model was originally introduced by Swift et al. (1996). FE model includes the phase effects into the collision process through a thermodynamic equilibrium function that incoporates non-ideal pressure tensor terms. Therefore, surface tension is easily adjusted compared to other multiphase models. Unlike the Shan-Chen model, the local momentum conservation is satisfied in the FE model (Gupta and Kumar (2008)). Efforts have been devoted to handle immscible fluids with large density ratios (Inamuro et al. (2004)). Unfortunately, the original FE model is not Galilean invariant for the viscous terms in the Navier-Stokes equations (Luo (1998)). Further improvement was incorporated into FE by Holdych et al. (1998) redefining the stress tensor, consequently, the Galilean invariance was recovered to $O(u^2)$ (Huang et al. (2015)).

1.3.6.1.4 Comparison between the multiphase LBM models

We briefly compare the advantages and drawbacks of multiphase LBM including the color gradient, the Shan–Chen and the free energy model. The comparison in table 1.1 is obtained from the analysis of Yang and Boek (2013); Huang et al. (2015) and simulations performed with the fluid solver Palabos (Latt (2009)). It is worth noting that values in table 1.1 are rather orientative. Indeed, they show the capability of each method in a certain aspect, however, it is important to keep in mind that a feature achieved after the modification of the original model may have a reverse effect on other properties. For instance, Zheng et al. (2006) proposed a Galilean-invariant free-energy lattice Boltzmann model that is much simpler, conversely, the model is only valid for a density ratio of 1.

Without going into excessive detail, the comparisons from previous literature (Hou et al. (1997); Yang and Boek (2013); Huang et al. (2015)) remark the efficiency and simplicity of the Shan-Chen models. In contrast, the large thickness of the diffusive interface may reduce the accuracy of the results in coarse grids compared to the rest of the models. Another important feature associated to the Shan-Chen model is the ability to handle high-density ratio systems.

In the color gradient and the Shan-Chen model, the desired contact angle can be obtained by tuning the density of the solid nodes. On the contrary, the free-energy model relies on density gradients on the solid boundaries to adjust the wetting condition (Liu et al. (2013)). Furthermore, the surface tension in the free-energy and color gradient models can be adjusted much more easily than the Shan-Chen model.

	SCMP	**MCMP**	**Color gradient**	**Free-energy**
Max density ratio	10^9	1000	10	10
Max viscosity ratio	-	5	20	20
Interface thickness	8 lu	8 lu	5 lu	3 lu
Wettability	Easy to adjust	Easy to adjust	Easy to adjust	More difficult to adjust
Efficiency	Very efficient	Very efficient	Not so efficient	Not so efficient
Inherent parallelism	High	Low	High	High

Table 1.1: Features, strengths and limitations of different multiphase models. Information taken from Yang and Boek (2013); Huang et al. (2015) and personal numerical simulations.

1.3.6.2 Volume of fluid

Volume of fluid (VOF) method is an Eulerian method developed by Hirt and Nichols (1981). In the VOF method, the interface is tracked using a scalar function that ranges from 0 (fluid 1) to 1 (fluid 2). The scalar indicator represents the volume fraction between the two fluids. Navier-Stokes equations are solved, alongside the transport equation for the volume fraction to reproduce the motion of the fluids. Advantages of VOF method are its simplicity and the conservation of mass during the interface displacement. On the contrary, the difficulty to determine accurate interface curvatures from the volume fraction function is the main drawback of the model (Balcázar et al. (2016)). Several works (Raeini et al. (2012); Balcázar et al. (2016)) have coupled the VOF method with other flow solvers to simulate two-phase flows.

1.3.6.3 Smoothed particle hydrodynamics method

The smoothed particle hydrodynamics (SPH) is a mesh-free Lagrangian discretization method originally introduced by Lucy (1977) for astrophysical problems. The fluid is treated as a set of discrete particles in the SPH model. Each series of particles has inherent information. Based on these particles, SPH approximates the numerical solutions of the equations of fluid dynamics using kernel and particle approximations (Wang et al. (2016)). The local physical properties (density, velocity, etc) are determined for every group of particles following the governing equations. Consequently, the fluid displacement is represented by the motion of particles. In order to reproduce realistic simulations, SPH requires large numbers of particles that significantly increase the computational cost. Despite this disadvantage, SPH is able to simulate fluid flow through complex solid boundaries and capture the interface with excellent accuracy. Such features are typically needed in multiphase flow systems. Indeed, extensive literature (Monaghan and Kocharyan (1995); Tartakovsky and Meakin (2005); Monaghan (2005)) proves the robustness of SPH for modeling two-phase flows.

1.3.6.4 Level-Set methods

The level-set (LS) method was introduced by Osher and Sethian (1988) as a technique to capture the position of a moving interface. The underlying idea of the LS consists in tracking the fluid interface by means of a smooth function ϕ_L termed "level set" function. Fluid 1 occupies the area in which $\phi_L > 0$ whereas fluid 2 is present in the region where $\phi_L < 0$. The interface is represented by the set of points where $\phi_L = 0$. The motion of the interface is governed by a differential equation for the level-set function. According to Gibou et al. (2007), the main advantage of the level-set method is its ability to handle topological changes. On the other hand, the level-set method is more prone to numerical error than other methods (Balcázar et al. (2016)). The ability to track the fluid interface makes the level-set method suitable for simulations of two-phase flow Sussman et al. (1999); Olsson and Kreiss (2005)).

Chapter 2

Calibration, validation and applications of the Shan Chen - Lattice Boltzmann Method

2.1 Introduction

This work presents case studies to assess the potential of a lattice Boltzmann method (LBM) to analyze the stability and evolution of immiscible phases and their interfaces in generic cases. Such results can help improving pore-network approaches developed in previous works such as Yuan et al. (2016); Sweijen et al. (2017a); Suh and Yun (2018).

The LBM is a mesoscopic model capable of simulating fluid dynamics in complex geometries (Chen and Doolen (1998)). While conventional numerical methods rely on discretizations of macroscopic continuum equations, LBM is based on microscopic models and mesoscopic kinetic equations for fluids. Due to its simplicity and capability to model fluid motion in complex boundaries, the LBM is very suitable to simulate multiphase flow through porous media. Fundamentals of the LBM and Shan-Chen model are briefly reviewed in 2.1.1.

Many works using the LBM have focus on single-phase flow in porous media and proven to be successful (Adrover and Giona (1996); Koponen et al. (1998); Guo and Zhao (2002)). However, multiphase LBM models employed to reproduce partially saturated soils have less satisfactory results due to the complexities and difficulties associated with the coexisting phases. Nevertheless, numerous articles based on multiphase LBM evidence a growing interest in this field. Several multiphase LBM models have been proposed in the literature (see section 1.3.6.1 for more details): the color model (Gunstensen et al. (1991)), the pseudopotential (Shan-Chen) model (Shan and Chen (1993, 1994)) or the free-energy model (Swift et al. (1996)). The so-called Shan-Chen model has single- and multi-component variants which both apply to the problem of immiscible phases. The single-component method is simpler. It has been used to simulate, for instance, flow in porous media with realistic rock geometries (Boek and Venturoli (2010)) or the hysteretic response of idealized sphere-pack systems in drainage-imbibition cycles (Pan et al. (2004)). More recently, Son et al. (2016) investigated with this method the meniscus profile and the effect of contact angle on fluid displacement through polygonal capillary tubes. According to Kamali et al. (2011) however, the gas-liquid interfaces tend to be more diffused in single component simulations, which may hinder the approach of strongly immiscible situations. Moreover, an advantage of the multi-components model is that it allows to accurately simulate the fluids composition (Bao and Schaefer (2013)). Nevertheless, fewer studies (Martys and Chen (1996); Porter et al. (2009)) have applied the multicomponent models to mimic multiphase flow in porous media. In this work, multiphase flow is evaluated by means of the widely extended multicomponent Shan-Chen LBM model using the open-source library Palabos written in C++ (Latt (2009)). The methods and examples presented henceforth, are implemented in Palabos using C++ codes.

This chapter is organized as follows: a brief description of the lattice Boltzmann method is found in section 2.1.1, section 2.2 explains the way to compute and tune surface tension and contact angle. Section 2.2 also includes a method to evaluate the curvature of the fluid-fluid interface; in section 2.3, the model is validated by contrasting analytical solutions and numerical results for the geometry and movement of interfaces in capillary tubes and for pendular bridges between spheres; as an example application, meniscus morphology and stability are studied in three-sphere, four-sphere and seven-sphere systems in section 2.4; finally, conclusions are drawn in section 2.5.

2.1.1 Lattice Boltzmann Method

The LBM has its origin in the lattice gas automata (LGA) (Frisch et al. (1986)), a kinetic model based on discrete space-time field. While LGA method described the evolution of individual particles on a lattice, the LBM solves a discrete kinetic equation (Boltzmann's equation) for a particle distribution function $f^{\sigma}(\mathbf{x},t)$. Where the superscript σ indicates the fluid component, $\mathbf{x}$ refers to the lattice node and t is the time. In the LBM, the motion of fluid is described by the lattice Boltzmann equation. Based on the simple and popular Bhatnagar-Gross-Krook (BGK) collision operator (Bhatnagar et al. (1954)), the standard lattice Boltzmann equation can be expressed as follows:

$$f_k^{\sigma}(\mathbf{x_k}+\mathbf{e_k}\Delta t, t+\Delta t) - f_k^{\sigma}(\mathbf{x_k},t) = \frac{-\Delta t}{\tau^{\sigma}}(f_k^{\sigma}(\mathbf{x_k},t) - f_k^{\sigma,eq}(\mathbf{x_k},t)) \tag{2.1}$$

where τ^{σ} is the rate of relaxation towards local equilibrium, $f_k^{\sigma,eq}$ is the equilibrium distribution function, Δt is the time increment, $\mathbf{e_k}$ are the discrete velocities which depend on the particular velocity model, in this work, D3Q19 (three-dimensional space and 19 velocities) model is used, and k varies from 0 to $Q-1$ representing the directions in the lattice. The left-hand side of Eq. 2.1 describes the streaming step (particles move to the nearest node following its velocity direction) whereas the right-hand side stands for the collision operator (particles arriving to the nearest node modify their velocity towards a local equilibrium). The collision operator corresponds to the viscous term in the Navier-Stokes equation.

For the D3Q19 model, the discrete velocity set $\mathbf{e_k}$ is written as:

$$\mathbf{e_k} = \left\{ \begin{array}{c} (0,0,0) \\ (\pm 1,\ 0,\ 0),\ (0,\ \pm 1,\ 0),\ (0,\ 0,\ \pm 1) \\ (\pm 1,\ \pm 1,\ \pm 1) \end{array} \right\} \quad w_k = \left\{ \begin{array}{c} 1/3 \\ 1/18 \\ 1/36 \end{array} \right\} \quad \begin{array}{c} \text{k=0} \\ \text{k=1, ... , 6} \\ \text{k=7, ... , 18} \end{array} \tag{2.2}$$

where w_k are the weight factors.

The local equilibrium $f_k^{\sigma,eq}$ depends on the lattice type, the density and the momentum (Latt et al. (2008)). Macroscopic variables at each node of the lattice are recovered as the moments of the distribution functions:

- Density (moment of order 0):

$$\rho^\sigma = \sum_k f_k^\sigma \tag{2.3}$$

- Momentum (moment of order 1):

$$\rho^\sigma \mathbf{u}^\sigma = \sum_k f_k^\sigma \mathbf{e_k} \tag{2.4}$$

- Moment of order 2:

$$\Pi^\sigma = \sum_k f_k^\sigma \mathbf{e_k}\mathbf{e_k} \tag{2.5}$$

The equilibrium distribution can be seen as an expansion of the Maxwell-Boltzmann's distribution function for low Mach numbers:

$$f_k^{\sigma,eq} = \rho^\sigma w_k \left[1 + \frac{1}{c_s^2}(\mathbf{e_k} \cdot \mathbf{u}^{\sigma,\mathbf{eq}}) - \frac{1}{2c_s^2}(\mathbf{u}^{\sigma,\mathbf{eq}} \cdot \mathbf{u}^{\sigma,\mathbf{eq}}) + \frac{1}{2c_s^4}(\mathbf{e_k} \cdot \mathbf{u}^{\sigma,\mathbf{eq}})^2 \right] \tag{2.6}$$

where $c_s = \frac{1}{\sqrt{3}}$ is the speed of sound and $\mathbf{u}^{\sigma,\mathbf{eq}}$ is the equilibrium velocity defined as (Shan and Chen (1993, 1994)):

$$\mathbf{u}^{\sigma,\mathbf{eq}} = \mathbf{u}^{'} + \frac{\tau^\sigma \mathbf{F}_\sigma}{\rho^\sigma} \tag{2.7}$$

where $\mathbf{u}^{'} = \frac{\sum_\sigma \frac{\rho^\sigma \mathbf{u}^\sigma}{\tau^\sigma}}{\sum_\sigma \frac{\rho^\sigma}{\tau^\sigma}}$ is an effective velocity and $\mathbf{F}_\sigma$ is the total force (including body forces and the fluid-fluid interactions that will be presented in section 2.1.1.1) acting on each component.

2.1.1.1 Pseudopotential model

In the Shan and Chen model, a pairwise interaction force between components (or phases) is introduced to describe multiphase flows. This force modifies the collision operator through an equilibrium velocity producing a repulsive effect between the phases.

In this work, we focus on biphasic mixtures (i.e., $\sigma = 2$). Thus, two $f_k^{\sigma}(\mathbf{x},t)$ are considered to model a fluid mixture containing two fluid components. Hereinafter, ρ^{w} and ρ^{nw} will refer to the wetting and non-wetting phases. ρ_o is defined as the reference density which is set to $\rho_o = 1$.

In the Shan-Chen model, the non-local force responsible for the fluid-fluid interaction can be expressed as:

$$\mathbf{F}_{\sigma}(\mathbf{x}) = -\Psi(\mathbf{x}) \sum_{\bar{\sigma}} G_{\sigma\bar{\sigma}} \sum_{k} \Psi_{\bar{k}}(\mathbf{x}+\mathbf{e_k})\mathbf{e_k} \tag{2.8}$$

where Ψ_k is the interparticle potential that induces phase separation and $G_{\sigma\bar{\sigma}}$ is the interaction strength between components σ, $\bar{\sigma}$.

Previous works (Shan and Chen (1994); Yuan and Schaefer (2006); Huang et al. (2011); Porter et al. (2012)) have employed several interparticle potentials. For simplicity, we consider $\Psi_k = \rho_k$, as done by Pan et al. (2004). The interactions within each component, G_{11} and G_{22}, are set equal to zero for biphasic mixtures. On the other hand, the interactions between components, $G_{12} = G_{21}$, are set positive in order to induce a repulsive force between the phases. Low values of G_{12} lead to dissolution processes seen in typical miscible mixtures. On the contrary, significantly high values of G_{12} result in almost immiscibile binary mixtures with sharp interfaces prone to numerical instability. Thus, special attention must be paid when choosing the interaction strength as it controls the surface tension and immiscibility of the mixture.

According to Benzi et al. (2006); Sbragaglia and Belardinelli (2013), the interaction force given by Eq. 2.8 leads to a non-spherical pressure tensor $\bar{\bar{\mathbf{P}}}$ deduced from the condition: $-\nabla\bar{\bar{\mathbf{P}}} + \nabla\bar{\bar{\mathbf{P}}}_{\mathbf{o}} = \mathbf{F}_{\sigma}(\mathbf{x}) + \mathbf{F}_{\bar{\sigma}}(\mathbf{x})$, where $\bar{\bar{\mathbf{P}}}_{\mathbf{o}} = \bar{\bar{\mathbf{I}}} c_s^2(\rho^{\sigma} + \rho^{\bar{\sigma}})$ is the ideal pressure tensor. Components of the pressure tensor can be computed as:

$$P_{ij}(\mathbf{x}) = c_s^2[\rho^{\sigma}(\mathbf{x}) + \rho^{\bar{\sigma}}(\mathbf{x})]I_{ij} + \frac{G}{2}\Psi^{\sigma} \sum_{k=0}^{N-1} w_k \Psi^{\bar{\sigma}}(\mathbf{x}+\mathbf{e_k}) e_{ki} e_{kj} + \frac{G}{2}\Psi^{\bar{\sigma}} \sum_{k=0}^{N-1} w_k \Psi^{\sigma}(\mathbf{x}+\mathbf{e_k}) e_{ki} e_{kj} \tag{2.9}$$

Following Eq. 2.9, the non-ideal equation of state (EOS) can be determined as:

$$p = c_s^2 \sum_{\sigma} \rho^{\sigma} + c_s^2 \sum_{\sigma\bar{\sigma}} G_{\sigma\bar{\sigma}} \Psi_{\sigma} \Psi_{\bar{\sigma}} \tag{2.10}$$

2.1.1.2 Bounce back condition

One of the most important aspects of simulating multiphase flow through a porous medium to be taken into account is the behavior of fluids near the solid surface. The fluid-solid interaction is implemented in the Shan-Chen model by a mid-grid bounce-back scheme applied at the boundaries (Succi (2001)). This scheme assigns fluid properties to the solid wall.

The particle distribution function bounce-back scheme is used at the solid boundaries to obtain no-slip velocity conditions on the solid surface. The so-called bounce-back scheme assumes that a particle distribution function streaming from a fluid node towards a solid surface is bounced back in the reversed direction (Succi (2001)). The easy implementation of the no-slip boundary condition enhances the simulation of fluid flows through complex geometries.

2.1.1.3 Physical and LBM units

Correlating physical properties to lattice units is an essential task in order to simulate physical problems. Moreover, choosing the right conversion will avoid stability problems and help us to have accurate results. As suggested in Latt (2008); Krüger et al. (2017); Thorne and Michael (2006), physical units can be related to lattice units through unit conversion or dimensionless numbers such as the Reynold, the Froude or the Bond number.

First of all, let's summarize the main parameters involved in the physical and the LB systems:

Quantity	Physical parameter	SI units	LB parameter
Distance between nodes	Δx	m	δx
Time step	Δt	s	δt
Velocity	v	m/s	v_{lb}
Density	ρ	kg/m^3	ρ_{lb}
Kinematic viscosity	ν	m^2/s	ν_{lb}
Pressure	p	$kg/(m \cdot s^2)$	p_{lb}

Table 2.1: Physical and lattice units used during numerical simulations.

Conversion factors for length, time, velocity and density are: $C_x = \dfrac{\Delta x}{\delta x}$, $C_t = \dfrac{\Delta t}{\delta t}$, $C_v = \dfrac{\Delta x}{\Delta t}\dfrac{\delta t}{\delta x}$ and $C_\rho = \dfrac{\rho}{\rho_{lb}}$. Similarly, we can find expressions for the kinematic viscosity and pressure:

• Kinematic viscosity: $C_\nu = \dfrac{C_x^2}{C_t}$. Plus, kinematic viscosity is related to the relaxation time τ as:

$$\nu = c_s^2 \left(\tau - \frac{1}{2}\right) \frac{\Delta x^2}{\Delta t} \frac{\delta t}{\delta x^2} \tag{2.11}$$

• Pressure:

$$C_p = \frac{C_x^2}{C_t^2} \tag{2.12}$$

This method presented above is consistent and can be applied to find other quantities (Krüger et al. (2017)). Nevertheless, one important constraint must be kept in mind. LBM is limited to low Mach numbers due to compressibility effects that lead to numerical instabilities (Latt (2008); Sterling and Chen (1996)). In order to conduct numerical simulations of quasi-compressible flows and reduce the numerical error, lattice Boltzmann velocities should be significantly smaller than the speed of sound ($v_{lb} << c_s$). Dimensionless numbers are extensively used to express and overcome this limitation. The first step consists of converting the physical system into a dimensionless system. After that, dimensionless units are transformed into lattice units. For the sake of clarity, let's use the Bond number to illustrate the unit conversion in terms of dimensionless number. Bond number relates capillary and gravitational forces and is defined as:

$$Bo = \frac{\rho g L_c^2}{\gamma} \tag{2.13}$$

where ρ is the fluid density, g is the gravity, L_c a characteristic length and γ the surface tension. Bo must have the same value regardless the system of units. Thus, $Bo = \frac{\rho g L_c^2}{\gamma} = \frac{\rho_{lb} g_{lb} L_{c,lb}^2}{\gamma_{lb}}$ is able to correlate the lattice Boltzmann and physical units.

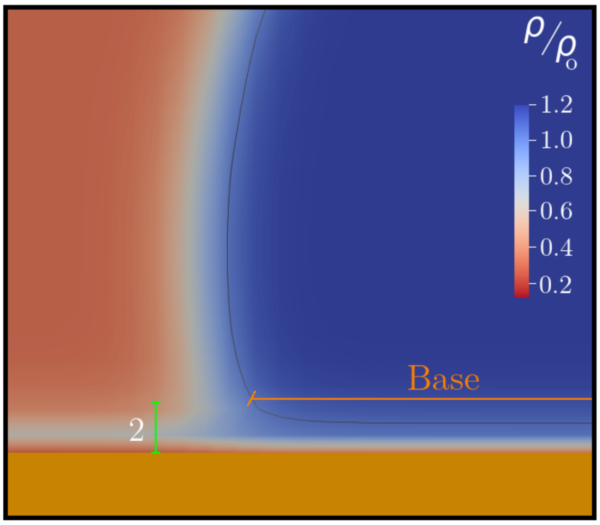

Figure 2.1: Detailed fluid-fluid-solid phase transition. The blue color corresponds to the non-wetting fluid, the red color is the wetting fluid and yellow is the solid wall. The interface forms a contact angle of approximately 102^o for a $\Psi_{wall}/\rho_o = 1.2$. A reference point situated 2 lattice units above the horizontal solid plate has been proven sufficient to represent the contact angle accurately.

2.2 Model calibration

2.2.1 Contact angle

According to the literature (Schmieschek and Harting (2009); Huang et al. (2007); Son et al. (2016)), one of the simplest way to tune the contact angle consists in adjusting the interparticle potential for the nodes of the lattice assigned at solid phase. Thus, the wettability can be controlled by Ψ_{wall} (see Eq. 2.8).

We perform simulations of static droplets on a flat solid surface, and we analyze the dependence of Ψ_{wall} on the contact angle. The simulations are performed in a 150×150×150 lattice domain. Once the simulation is stable and converged, the base length (b) and the height (h) are measured. As suggested by Yuan and Lee (2013), the geometrical characteristics of the droplet allows us to determine the contact angle $\frac{\theta}{2} = tan^{-1}(\frac{2h}{b})$ (see figure 2.2). Some error is introduced during the base measurement due to the thickness of the interface layer in the vicinity of the wall. In order to overcome the problem, the base and height of the droplet are determined from a reference point located 2 lattice units far from the interface layer (see figure 2.1 and further discussion of interface thickness in 2.3.2.3).

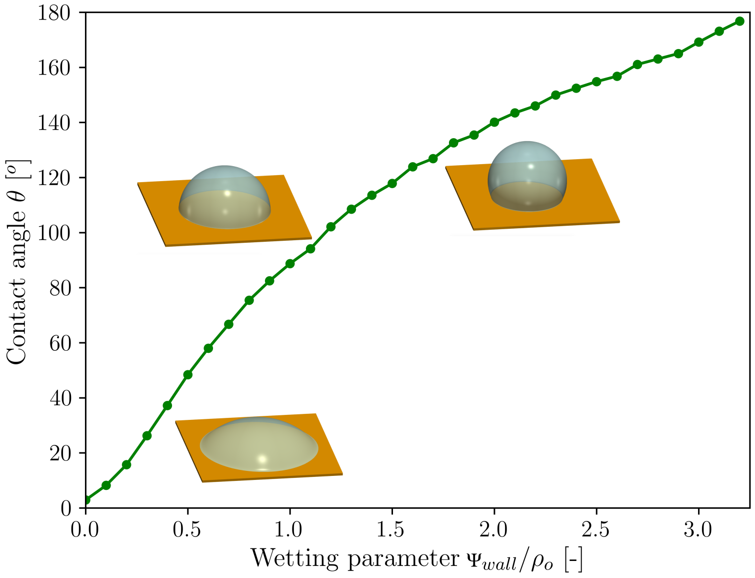

Figure 2.2: Contact angle versus the density Ψ_{wall} of the solid phase.

2.2.2 Surface tension

Likewise, surface tension can be adjusted by tuning the interaction between different fluid species. The typical numerical set-up to investigate the surface tension (γ) consist of a series of drops with different radii (R) inside a domain with periodic boundary conditions.

Physically, the droplet and the surrounding fluid are at rest and the pressure difference (p_c) inside and outside the droplet is balanced by the surface tension according to the Young-Laplace law:

$$p_c = \frac{2\gamma}{R} \tag{2.14}$$

Figure 2.3a depicts the pressure along a horizontal line that goes through the droplet. Significant pressure fluctuations in the vicinities of the fluid-fluid are found due to the sudden change of density (Chen et al. (2014)). Figure 2.3b shows the variation of p_c versus $1/R$ in dimensionless terms (R_o is the radius of the smallest droplet), where the linear relationship is evidenced. The slope of the linear fit is the dimensionless interfacial tension γ^*, which is determined as $\gamma^* = \dfrac{\gamma}{\rho_o c_s^2 R_o}$ for $G\rho_o = 1.25$. Different surface tension values are assessed for different interaction strength parameters G (see figure 2.4).

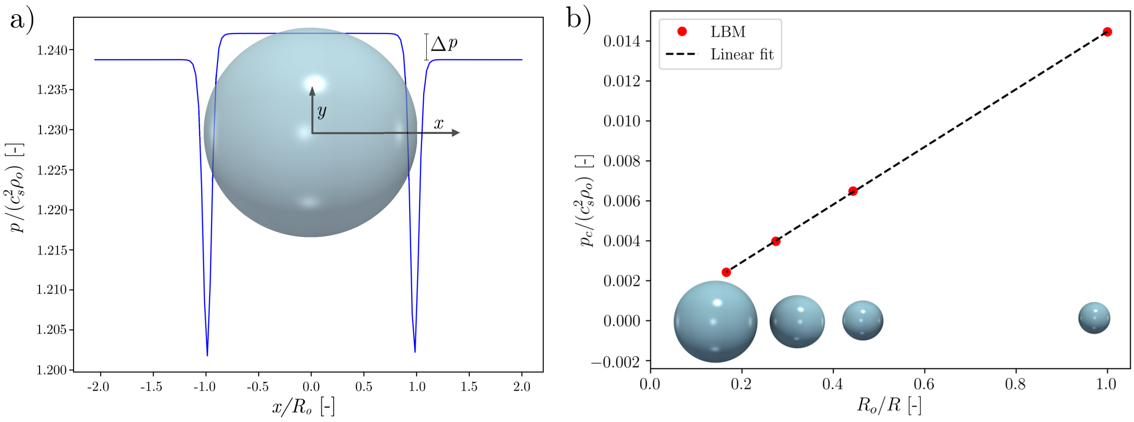

Figure 2.3: a) Pressure along a horizontal line that crosses the droplet. The pressure jump is balanced by the product of curvature and surface tension. b) Droplet test to determine surface tension.

The surface tension can also be predicted based on a two-phase system with a flat interface having a constant pressure in both phases far from the interface (Rowlinson and Widom (2013)). This technique has been adopted in many works relying on the single-component Shan-Chen model (Shan and Chen (1994); Chen et al. (2014); Benzi et al. (2006); Shan (2008)). Even though literature is scarce on the multicomponent model, some approaches have been carried out (Schmieschek and Harting (2009)). In this current study, we provide some results using the flat-interface test.

The pressure inside the bulk phases corresponds to the scalar quantity p. However, near the interface, due to the surface tension contribution, the pressure is defined as a tensor incorporating different pressure components. Moreover, in order to ensure the mechanical stability, the gradient of the pressure tensor must be zero everywhere in the fluid (Ono and Kondo (1960)). The symmetry of the surface requires that p is a diagonal tensor $p(x) = e_x e_x p_{xx}(x) + e_y e_y p_{yy}(x) + e_z e_z p_{zz}(x)$ with $p_{xx}(x) = p_{zz}(x)$, where x and z correspond to horizontal directions parallel to the flat interface, y refers to the axis orthogonal to the planar interface and e_j is a unit vector in the j-direction. Furthermore, p_{xx} and p_{zz} are function only of y, while p_{yy} is a constant:

$$p_{xx}(y) = p_{zz}(y) = p_T(y) \tag{2.15}$$

$$p_{yy}(y) = p_N(y) = p \tag{2.16}$$

where p_T and p_N are the transverse and normal components of the pressure. Both p_T and p_N can be computed using Eq. 2.9.

Consequently, surface tension can be obtained by evaluating the integral along a flat interface of the mismatch between the normal and tangential components of the pressure tensor (Rowlinson and Widom (2013)):

$$\gamma = \int_{-\infty}^{\infty} (p_N - p_T)dy = \int_{-\infty}^{\infty} (p - p_T(y))dy \tag{2.17}$$

As evidenced in figure 2.4, theoretical analysis and droplet test are in good agreement.

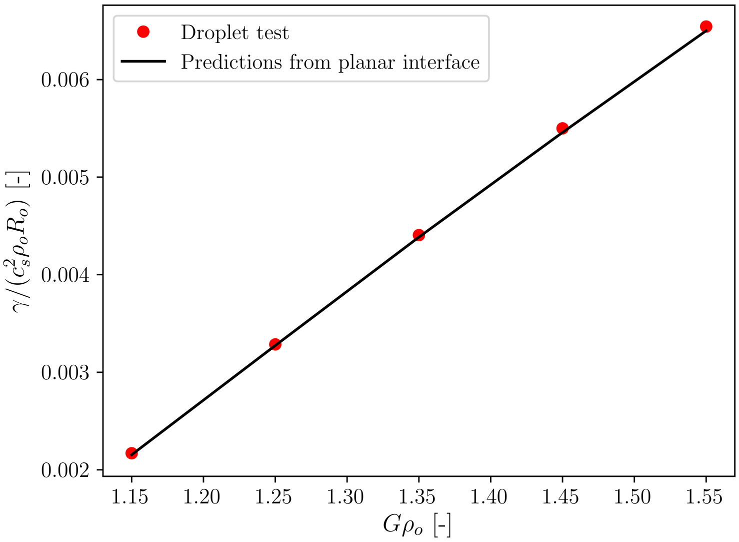

Figure 2.4: Dependence of surface tension on the interaction strength G. Black line represents the theoretical surface tensions obtained with Eq. 2.17. Red dots are the values determined using the droplet test.

2.2.3 Curvature analysis

In order to analyze the multiphase flow, attention should be paid to the shape of the fluid-fluid interface. Thus, in this section we furnish some tools to measure the interface curvature following the work of Bush (2010).

Given a fluid-fluid interfacial surface S enclosed by an arbitrary volume element V such as the one displayed in figure 2.5, we can perform a force balance on V:

Inertial force = Body force + Hydrodynamic force exerted on S + Surface tension force exerted along C

$$\int_V \rho \frac{d\mathbf{u}}{dt} dV = \int_V \mathbf{f} dV + \int_S \omega^{\mathbf{nw}}(\mathbf{n}) + \omega^{\mathbf{w}}(\hat{\mathbf{n}}) dS + \int_C \gamma \mathbf{t} dl \tag{2.18}$$

where,

- dl refers to a length increment along the closed curve C that forms its boundary (see figure 2.5),

- ρ is the fluid density,
- γ is the surface tension,
- the stress vector representing the force exerted by fluid 2 (non-wetting phase) on S (see figure 2.5) is:

$$\omega^{\mathbf{nw}}(\mathbf{n}) = \mathbf{n} \cdot \mathbf{T}^{\mathbf{nw}} \tag{2.19}$$

- the stress vector representing the force exerted by fluid 1 (wetting phase) on S is:

$$\omega^{\mathbf{w}}(\hat{\mathbf{n}}) = \hat{\mathbf{n}} \cdot \mathbf{T}^{\mathbf{w}} = -\mathbf{n} \cdot \mathbf{T}^{\mathbf{w}} \tag{2.20}$$

The stress tensors are defined by means of the local fluid pressure and velocity field as:

- $$\mathbf{T}^{\mathbf{nw}} = -p^{nw}\bar{\bar{\mathbf{I}}} + \mu^{nw}[\nabla\mathbf{u}^{\mathbf{nw}} + (\nabla\mathbf{u}^{\mathbf{nw}})^T] \tag{2.21}$$
- $$\mathbf{T}^{\mathbf{w}} = -p^{w}\bar{\bar{\mathbf{I}}} + \mu^{w}[\nabla\mathbf{u}^{\mathbf{w}} + (\nabla\mathbf{u}^{\mathbf{w}})^T] \tag{2.22}$$

where μ^{nw} and μ^{w} are the dynamic viscosities, and $\mathbf{u}^{\mathbf{nw}}$, $\mathbf{u}^{\mathbf{w}}$ the velocity vectors.

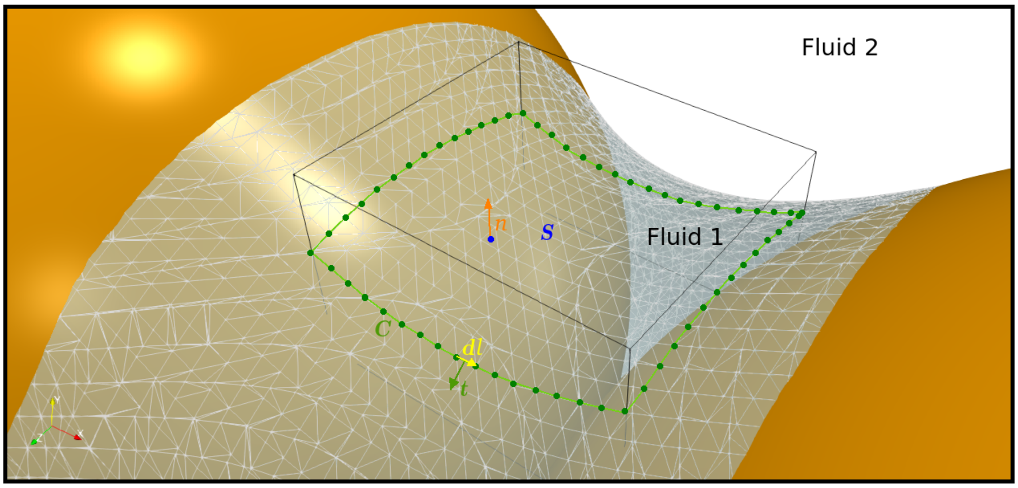

Figure 2.5: Fluid-fluid interface deformed due to surface tension. Mean curvature is determined by performing a force balance in a volume element V. Surface S and contour C result from the intersection between V and the interface. $\mathbf{n}$ represents the unit outward vector normal to S, $\mathbf{dl}$ the unit vector tangent to C and $\mathbf{t}$ the unit vector normal to C and tangent to S.

Ignoring the acceleration and body forces, the force balance reads:

$$\int_S [\omega^{\mathbf{nw}}(\mathbf{n}) + \omega^{\mathbf{w}}(\hat{\mathbf{n}})]dS + \int_C \gamma\mathbf{t}dl = 0 \tag{2.23}$$

By assuming static configurations, Eq. 2.21 and 2.22 are reduced to $\mathbf{T^{nw}} = -p^{nw}\bar{\bar{\mathbf{I}}}$ and $\mathbf{T^{w}} = -p^{w}\bar{\bar{\mathbf{I}}}$ respectively. Thus, Eq. 2.23 can be rewritten as:

$$\int_S p_c \mathbf{n} dS + \int_C \gamma \mathbf{t} dl = 0 \tag{2.24}$$

where p_c is the pressure difference between the two fluids. Eq. 2.24 states that pressure jump across a static interface is balanced by the curvature at the interface, which is an integral form of the Young-Laplace equation ($p_c = -\gamma\nabla\cdot\mathbf{n}$, where $\nabla\cdot\mathbf{n}$ is the curvature), thus:

$$\gamma \int_S (-\nabla\cdot\mathbf{n})\mathbf{n} dS + \gamma \int_C \mathbf{t} dl = 0 \tag{2.25}$$

$$(-\nabla\cdot\mathbf{n}) \int_S \mathbf{n} dS + \int_C \mathbf{t} dl = 0 \tag{2.26}$$

Finally, we can numerically evaluate the curvature of the interface given a volume element (as in figure 2.5):

$$||\nabla\cdot\mathbf{n}|| = \frac{||\int_C \mathbf{t} dl||}{||\int_S \mathbf{n} dS||} \tag{2.27}$$

2.3 Validation

Simple numerical simulations are performed and compared with analytical solutions in order to validate the model. Detailed results are presented for quasi-static displacement of interfaces inside cylindrical tubes and fluid bridges between two spherical bodies.

2.3.1 Capillary rise

In order to test the accuracy of this model we perform a capillary rise test in a cylindrical tube. If a tube with radius R is vertically introduced into a tank filled with a liquid, the liquid rises or falls due to pressure drop through the curved interface. As explained in section 2.1.1.3, Bond number can be used to link the numerical simulation to the physical system.

The following parameters have been considered to perform a capillary rise in a tube:

The Bond number corresponding to the physical system is: $Bo_{phy} = \frac{1000\cdot 9.81\cdot 0.002^2}{0.07213} = 0.544$. Since $Bo_{phy} = Bo_{lb} = 0.544 = \frac{\rho_{lb} g_{lb} R^2_{tube,lb}}{\gamma_{lb}} = \frac{1\cdot g_{lb}\cdot 20^2}{0.042}$, the value of gravity in lattice units can be easily found, $g_{lb} = 5.71\cdot 10^{-5}$. The lattice system adopted in this example leads to a velocity of $v_{lb} = 0.0076$, which is significantly smaller than $c_s \approx= 0.5774$ fulfilling the low-Mach number requirement explained in 2.1.1.3.

After performing the simulation including all the LBM input values, the fluid rises until a height of $71.20lu$ (see figure 2.6).

Quantity	Physical parameter	Value in SI units	LB parameter	Value in LB units
Density	ρ	$1000 kg/m^3$	ρ_{lb}	1
Characteristic length	R_{tube}	$0.002m$	$R_{tube,lb}$	20
Surface tension	γ	$0.07213N/m$	γ_{lb}	0.042
Contact angle	θ	0^o	θ_{lb}	0^o
Gravity	g	$9.81m/s^2$	g_{lb}	?

Table 2.2: Physical and lattice units used during the capillary rise simulation.

On the other hand, the pressure difference between the top and bottom of a liquid column of height h can be computed as:

$$\Delta P = \rho g h \tag{2.28}$$

.

Eq. 2.14 and 2.28 can be rearranged to give the capillary rise equation:

$$h = \frac{2\gamma}{\rho g R_{tube}} = \frac{2 \cdot 0.042}{1 \cdot 5.71 \cdot 10^{-5} \cdot 20} = 73.56lu \tag{2.29}$$

Consequently, the error between the analytical and the numerical simulation is: $\frac{h_{theory} - h_{simulation}}{h_{theory}} = \frac{73.56 - 71.20}{73.52} = 0.0316$. Two reasons may explain this discrepancy. On the one hand, the pressure difference and surface tension may not be exactly balanced, leading to spurious currents. On the other hand, the interface thickness is considerably large ($\approx 6lu$, which means that the thickness in the real system is $\approx 0.6mm$) and it is not trivial to establish a threshold that splits the different fluids. Therefore, we conclude that numerical result matches almost perfect with the theoretical solution despite the problems that cast doubt on the accuracy of the simulation.

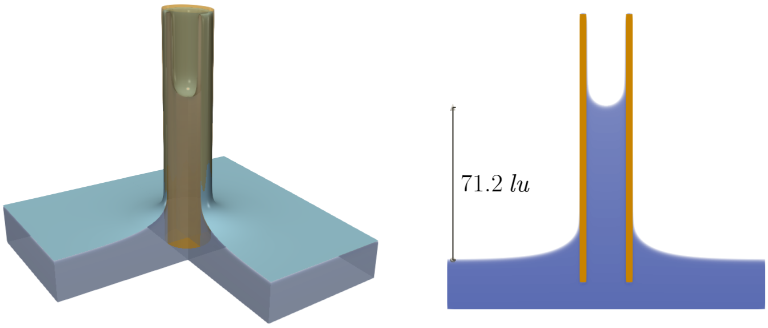

Figure 2.6: Capillary rise in a 150x200x150 lu^3 domain.

2.3.2 Flow through capillary tubes

In order to gain better understanding of multiphase flow at the pore scale, it is common to idealize the pores throats as cylindrical capillary tubes (Laroche et al.

(1999)). Immiscible flow in such capillary tubes has been simulated with various cross-sectional shapes (figure 2.7).

The fluid displacement corresponds to drainage and it is imposed by including mass sink and source terms in the time integration: wetting phase density is decreased while non-wetting phase density is increased following the technique proposed by Pan et al. (2004). In order to keep the flow quasi-static, the density is only modified when its fluctuation on one time iteration, at interface nodes, is less than a fixed tolerance ($Tol < \frac{|\rho_{it} - \rho_{it+1}|}{\rho_o}$). Otherwise, the solution is considered out-of-equilibrium and the mass sink/source is delayed.

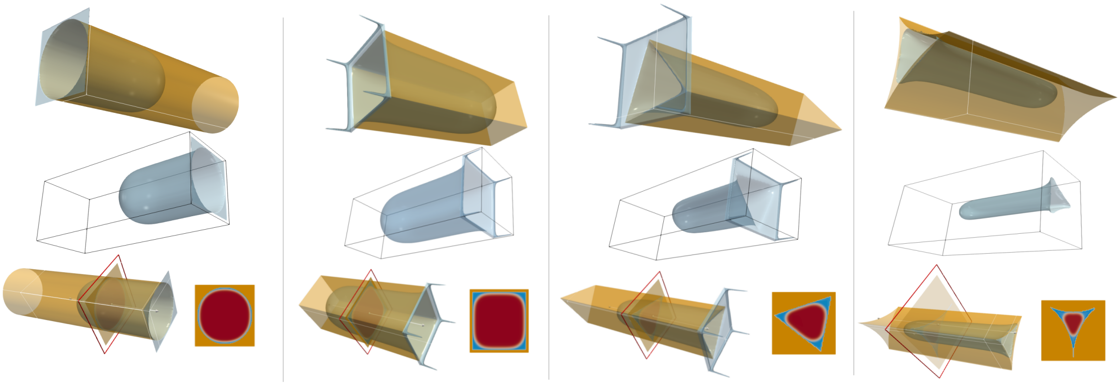

Figure 2.7: Geometry of the simulated capillary tubes. The wetting phase adopts different configurations in the corners depending on the cross-section shape. Dimensionless capillary pressure $p_c^* = \frac{2p_cL_c}{\gamma}$ is evaluated considering the following characteristics lengths: L_c= Radius, for the circular cylinder; L_c= Side length, for the square cylinder; L_c= Side length, for the triangular cylinder; L_c= Distance between two vertices, for the cylinder with curved boundaries.

2.3.2.1 MS-P method

As explained in section 1.3.5.1, the Mayer and Stowe-Princen (MS-P) model predicts the capillary pressure and the curvature of the arc meniscus of a fluid droplet of infinite length inside a cylindrical tube (Princen (1969); Mayer and Stowe (1965); Ma et al. (1996)).

The assumptions of the MS-P method are:

- uniform capillary pressure;
- no longitudinal curvature away from the main terminal meniscus.

Under these assumptions the cross-sectional curvature k^{MSP} (see figure 2.14) is given by Young-Laplace equation:

$$p_c = k^{MSP}\gamma = \frac{\gamma}{R_m} \tag{2.30}$$

where R_m is the radius of the arc meniscus.

Furthermore, capillary pressure can be obtained from a force balance between the two phases. The force due to the pressure difference on the cross-sectional area must balance the force from surface tension at the interfaces. Thus,

$$p_c A^{eff} = (L_{nw} + L_{ns} cos\theta)\gamma \tag{2.31}$$

where L_{ns} is the length of the line between the non-wetting phase and the solid, L_{nw} is the perimeter of the interface between the wetting phase and the non-wetting phase, and A^{eff} is the area filled with the non-wetting phase.

The MS-P method is used to determine the radius R_m of the arc menisci combining Eq. 2.30 and 2.31:

$$R_m = \frac{A^{eff}}{L_{nw} + L_{ns} cos\theta} \tag{2.32}$$

From now on, the MS-P is considered exact for cylindrical throats and used as a reference for comparisons. The errors in LBM solutions will be evaluated using two possible approaches:

$$Error_p = \frac{p^{MSP} - p_e^{LB}}{p^{MSP}} \tag{2.33}$$

where p_e^{LB} is the entry pressure obtained in the saturation curves (figure 2.9).

$$Error_k = \frac{k^{MSP} - k^{LB}}{k^{MSP}} \tag{2.34}$$

where k^{MSP} is compared with the curvature of the main meniscus after achieving the entry pressure. k^{LB} is found using Eq. 2.27.

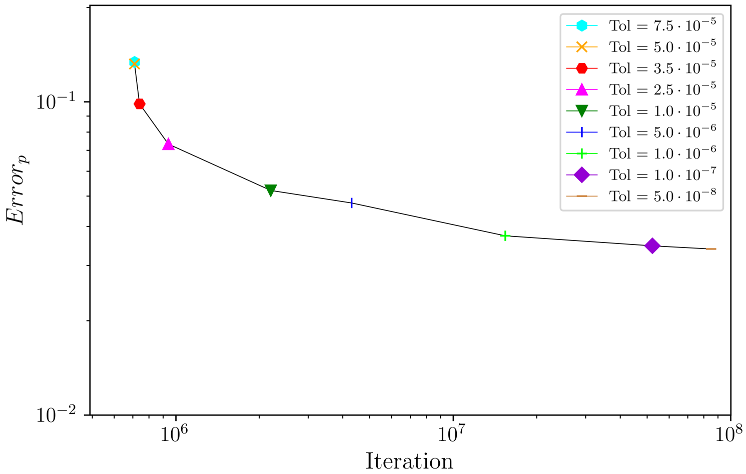

Figure 2.8: Entry capillary pressure predicted by LBM and total number of time iterations for different values of the tolerance. The error starts to increase significantly from $Tol = 10^{-5}\%$.

2.3.2.2 Results of sensitivity analysis

The invasion of a square tube has been repeated with different values of tolerance (*Tol* mentioned above) to quantify the perturbation by dynamic effects. The entry capillary pressure $p_c^{e,LB}$ in the LBM simulations is deduced from drainage curves similar to the plots in figure 2.9. The total number of iterations and the difference between $p_c^{e,LB}$ and the MS-P prediction for the different tolerance values are plotted in figure 2.8. Note that the difference is not expected to vanish even with very small tolerance since geometrical discretization errors contribute to the difference relatively independently of dynamic effects. In the sequel of this study we set the tolerance value to 10^{-5}, as it leads to marginal dynamic errors.

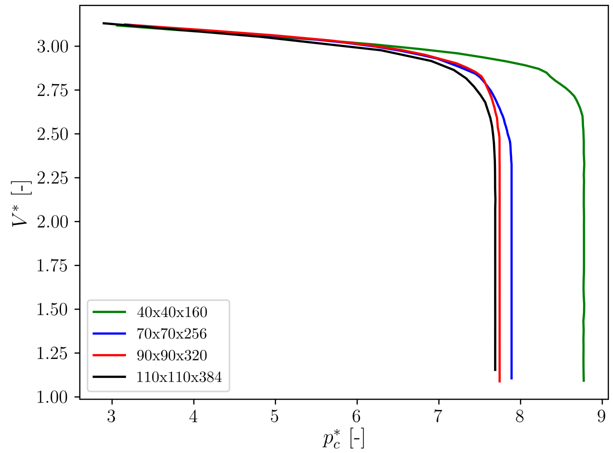

Figure 2.9: Primary drainage curves obtained by fluid displacement inside square-shaped capillary tubes of different domain size. Dimensionless capillary pressure increases until it reaches the entry pressure value (maximum capillary pressure). At this point, invasion by the non-wetting phase starts and the meniscus breaks through.

When capillary pressure p_c reaches the entry pressure value p_c^e, the wetting phase is displaced and the non-wetting phase invades the capillary tube. The progression of p_c is evidenced in figure 2.9. Hereinafter, p_c is described in dimensionless terms: $p_c^* = \dfrac{2p_cL_c}{\gamma}$, where γ is the surface tension and L_c the characteristics length. The primary drainage curves displayed in figure 2.9 correspond to numerical simulations of fluid displacements in a square-shaped capillary tube. Furthermore, several discretizations have been taken into account.

As seen in figure 2.9, mesh resolution has a non-negligible impact on the accuracy of the results. As the spatial resolution is increased (same simulation has been performed using the following domains: 40x40x160, 70x70x256, 90x90x320 and 110x110x384, from now, these domains are referred as $L_c = 40$, $L_c = 70$, $L_c = 90$, and $L_c = 110$), the error decreases considerably (figure 2.10 displays the error based on Eq. 2.33 and 2.34 respectively). From figure 2.10a we deduce that the order of convergence is 1.4 when the numerical solid wall coincides with the physical wall. In the following section we propose a technique to increase the accuracy of the results without adjustments in the mesh resolution.

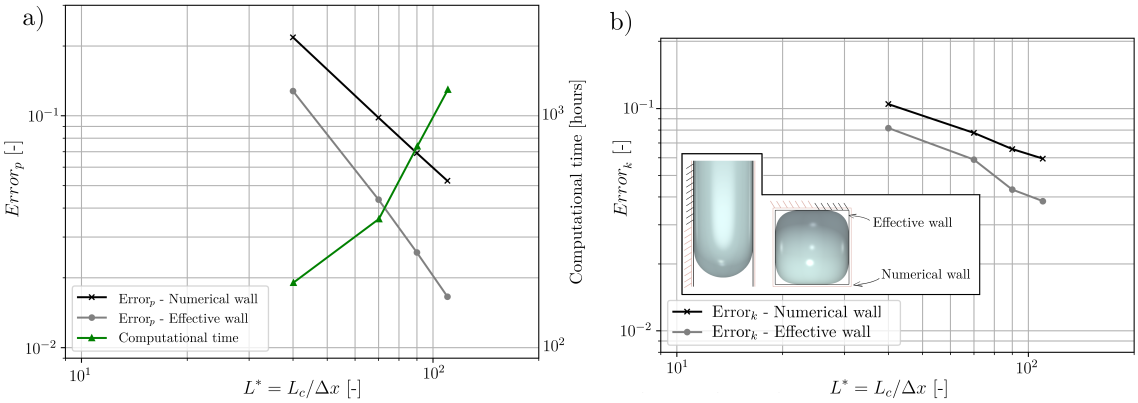

Figure 2.10: Convergence of the LBM result with mesh refinement, with regard to error defined in Eq. 2.33 on the left and error defined in Eq. 2.34 on the right. Each simulation is ran in parallel using 8 cores. L_c is the characteristic length.

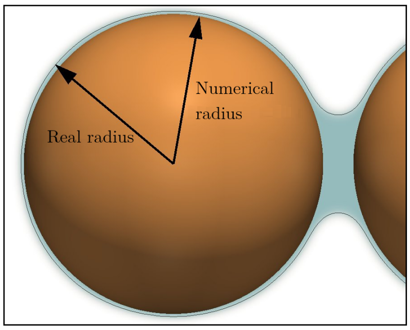

Figure 2.11: Principle of the wall retraction method. In the LBM mesh the solid boundary is retracted by $2lu$ with respect to its real position, such that the fluid-fluid contour $\rho_w/\rho_o = 0.7$ is nearly coincident with the real boundary.

2.3.2.3 Numerical thickness of interfaces

The numerical thickness of the interfaces (see section 2.2.1 and figures 2.11 and 2.14) is often considered an issue in the multicomponent Shan-Chen model. Physical intermolecular interactions lead to a fluid-fluid interface thickness, however, the thickness of the numerical film obtained with the multicomponent Shan-Chen model (see figure 2.1) does not correspond to the physical thickness. Additionally, previous works (Lee and Lin (2005); Li and Luo (2014)) have evidenced that a fluid-fluid interphase of 4-6 lu is required for numerical stability. Some works (Bao and Schaefer (2013); Otomo et al. (2016)) have attempted to increase the accuracy at fluid-solid interface by introducing new boundary models. Despite the efforts and the better results obtained near the solid region, numerical artifacts are still found underming the global accuracy. In order to overcome this issue we redefine the solid boundaries based on a wall retraction logic, to include part of the fluid-solid interface in the region normally occupied by the solid phase. As suggested in figures 2.1, 2.11 and 2.10, we now consider that fluid-solid interface is no longer aligned with the real solid wall but two lattice units above.

The optimal contour for the new solid boundaries is deduced from figure 2.12. Pressure error in figure 2.12 compares the capillary pressure obtained in Eq. 2.30

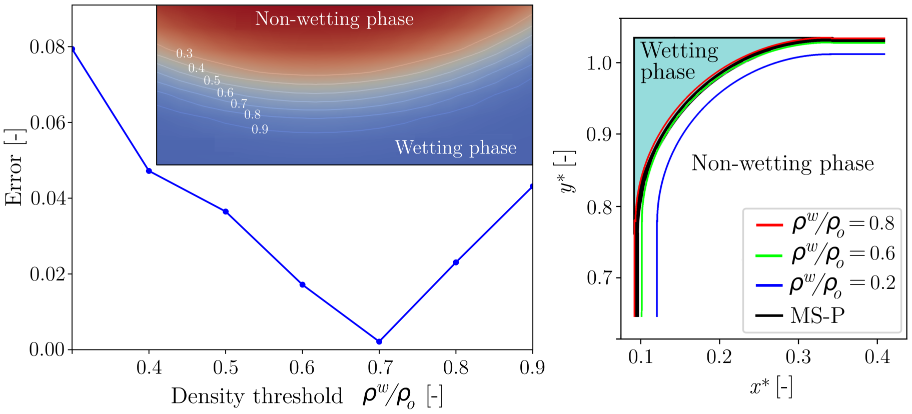

Figure 2.12: Difference in capillary pressure between LBM and the theoretical value deduced from meniscus geometry, as a function of the ρ^w contour selected to define the interface. Sub-figure on the upper-right corner shows details of the density contours. On the right, interface profiles for different ρ^w are superimposed. Both results correspond to a square cylinder.

and the pressure resulting from Eq. 2.31 using the effective area and perimeter determined in the LBM simulation:

$$p_c^{LB} = \gamma \frac{(L_{nw,LB} + L_{ns,LB} cos\theta)}{A^{eff,LB}} \tag{2.35}$$

The error between the MS-P solution and the LBM simulation reaches its minimum at around $\rho^w/\rho_o \approx 0.7$, which corresponds approximately to the average density between both phases. In our results, this specific value of density was generally reached approximately two nodes away from the solid nodes, which led to the decision to retract the walls by two lattice units.

This configuration is proven to be successful as evidenced in figure 2.10, where the error for the non-aligned interface with the real solid wall is lower than the error obtained without modifications. New boundaries are able to increase the quality of results, especially for coarse resolution simulations. This adjustment is considered for all the cases presented below. Additionally, figure 2.10 suggests that the analysis in terms of curvature is more convenient when the computational resources are limited. Indeed, the error for the coarsest grid in figure 2.10 is around two time larger in the pressure analysis. According to figure 2.10, finer meshes imply a better approximation when the error is evaluated in terms of pressure. However, there is not much difference between the methods since low error values are observed in both cases. Overall, figure 2.10 indicates the strong impact of using the retracted boundary. Such technique enhances an accurate analysis without the use of fine meshes and the subsequent high computational cost. Furthermore, when wall retraction is considered, the error is not only smaller, but also the convergence becomes quadratic as shown in figure 2.10 (without retracting wall, the convergence was superlinear with an exponent of approximately 1.4), which is a substantial improvement.

2.3.2.4 Results for different cross-sections

Numerical simulations have been performed in domain sizes of 80x80x256 lu^3 in order to reproduce the quasi-static fluid flow inside different cylindrical tubes. Capillary pressures in the tubes resulting from the numerical model are compared to the analytical solution given by the MS-P method in figure 2.13.

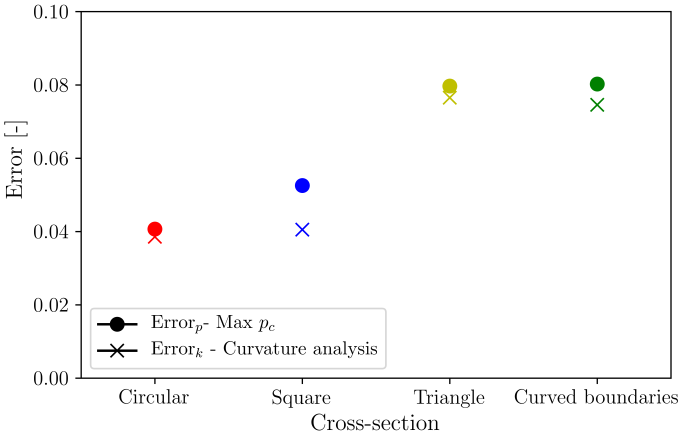

Figure 2.13: Deviation of LBM results from MS-P for different capillary tubes (see figure 2.7), in terms of capillary pressure and interface curvature, respectively.

Figure 2.13 shows good agreement between the numerical simulations and the analytical solution. It is worth noting that larger errors are observed for cylinders of triangular and curved boundaries cross-sections. This is attributed to the artificial roughness introduced by the staircased surfaces. These cross-sections are not aligned to the regular lattice grid. Furthermore, due to the bounce-back boundary condition, these cases lead to mesh-dependent results. In fact, the asymmetry is evidenced in figure 2.14, where the remaining liquid retained in the corners of the equilateral triangle is different in some parts. Nonetheless, figure 2.14 shows relatively similar numerical and analytical profiles.

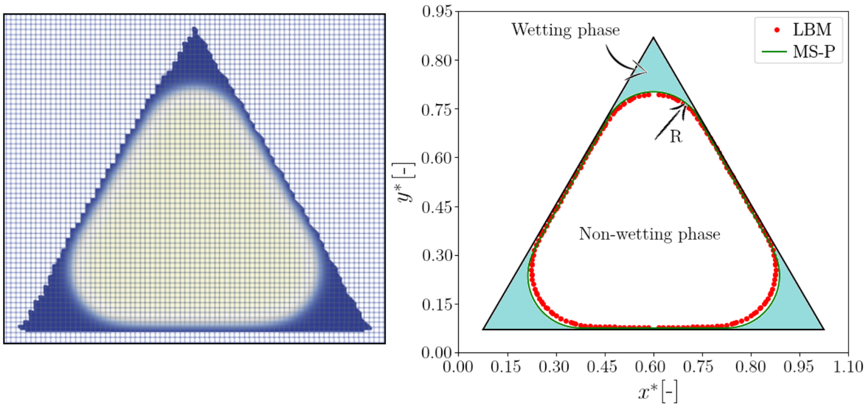

Figure 2.14: Staircased walls causing non-symmetry of the LBM solution (unequal filling of the corners).

2.3.2.5 Results for different orientations

The mesh dependency is frame dependent: it changes as function of the orientation of the throat with respect to the axis of the grid. The evolution of the errors with rotation is shown in figure 2.15, which reveals that the frame-dependent effects are actually small (of the order of 1%, dominated by other errors).

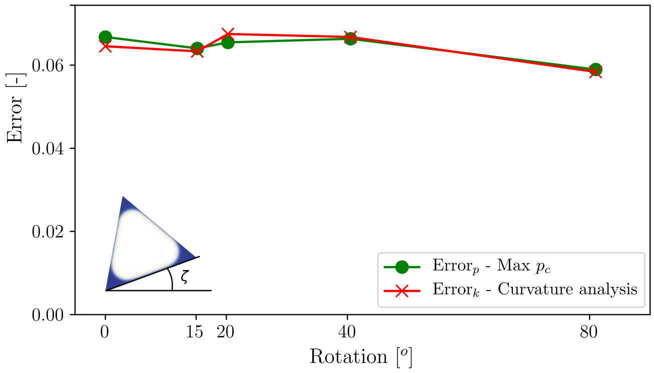

Figure 2.15: Error on pressure and curvature versus orientation of the throat (relative to LBM grid).

2.3.2.6 Accuracy as function of the analyzed height

To conclude, we review the hypothesis stating that MS-P solution is valid for cylinders of infinite extension. Due to computation limitations, short domains had to be considered, violating the assumption of droplets of infinite length. In order to test the accuracy of the numerical results under these conditions, the error on pressure has been plotted along a square cylinder. In other words, capillary pressure was computed using Eq. 2.31 for various positions of the cross-section in the final, nearly fully invaded, configuration. On the left part of figure 2.16 we observe that the remaining fluid in the corners is parallel to the cylinder walls (no longitudinal curvature). It is concluded that $H/L > 1$ is sufficient to approach the situation assumed for the MS-P method, i.e. the cross-section must be behind the main meniscus by a distance approximately equivalent to the throat aperture.

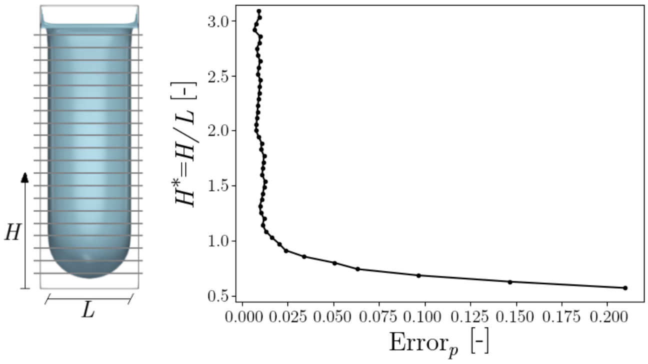

Figure 2.16: Evolution of the error on pressure by applying MS-P versus distance from the main meniscus. Drainage of a square cylinder.

2.3.3 Pendular bridge

The shape and volume of a pendular bridge between two spheres have been obtained from the LBM simulations and compared to the theoretical solution for a range of capillary pressure.

2.3.3.1 Porfile of pendular bridge

As explained in section 1.2.2.2.2, the Young-Laplace equation relates the capillary pressure difference across a fluid-fluid interface to the curvature and surface tension of the interface as:

$$p_c = \gamma\left(\frac{1}{R_1}+\frac{1}{R_2}\right) \tag{2.36}$$

where R_1 and R_2 are the principal radii of curvature.

Furthermore, the profile of a capillary bridge can be described by the Young-Laplace equation as demonstrated by De Bisschop and Rigole (1982). The mean curvature (H_m) for a pendular bridge can be written in the following form:

$$2H_m = \frac{r''}{(1+r'^2)^{3/2}} - \frac{1}{r(1+r'^2)^{1/2}} = \frac{p_c}{\gamma} \tag{2.37}$$

where $r = r(x)$ specifies the radius neck of the capillary bridge at position x. Due the impossibility of integrating Eq. 2.37 analytically, several studies have used numerical approaches to solve it (Lian et al. (1993); Willett et al. (2000); Lian and Seville (2016); Scholtès et al. (2009)).

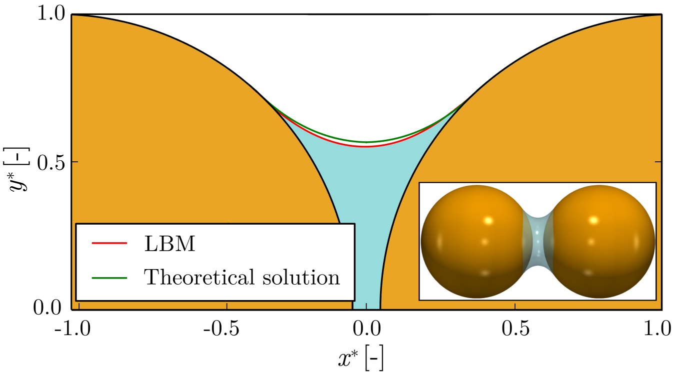

Figure 2.17: Overlapped capillary bridge profiles obtained numerically from LBM and the theoretical solution for $p_c^* = 0.6$.

2.3.3.2 Comparison between LBM and theoretical profiles

The simulation setup was as follows: a droplet of the wetting phase was inserted between two identical spheres of radius R with a gap equal to $0.14 \times R$. Once a stable state was reached, the volume of the liquid bridge was reduced slowly, by an imposed mass sink, until $p_c^* = \dfrac{2p_cR}{\gamma} = 0.6$. The shape of the pendular bridge when

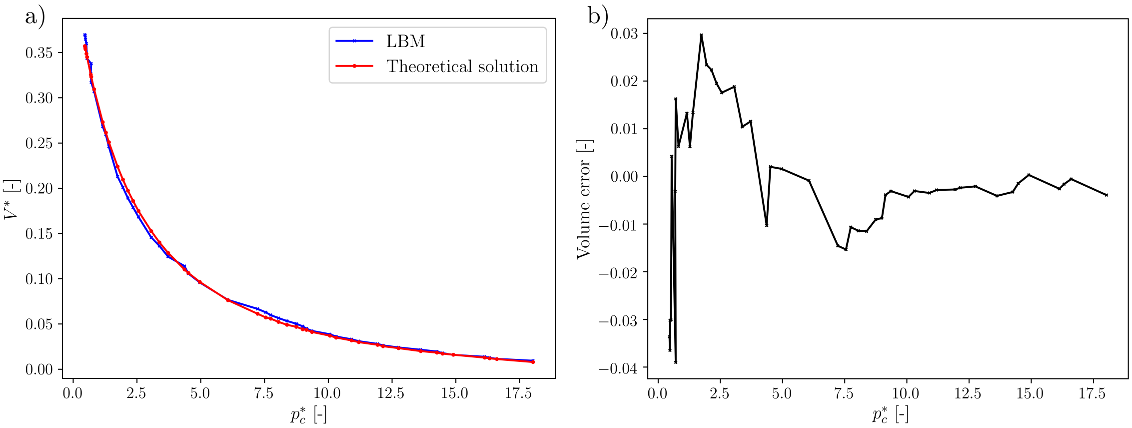

Figure 2.18: a) Volume versus capillary pressure for a pendular bridge from a LBM simylation and the numerical solution of Laplace-Young equation. b) The relative error is the difference between the simulated volume and the theoretical volume normalized as $V^* = V/R^3$.

$p_c^* = 0.6$ is compared to the direct solution of Young-Laplace equation (Lian et al. (1993)) in figure 2.17. Results show strong similarity. After reaching $p_c^* = 0.6$ the LBM simulation continued by further reducing the amount of wetting phase and recording the volume of the simulated bridge for a quantitative comparison with Young-Laplace solution. Figure 2.18 shows the volume-pressure relationship until breakage. The LBM simulation and the Laplace-Young solution follow a very similar trend, with a relative error generally lower than 10^{-2}.

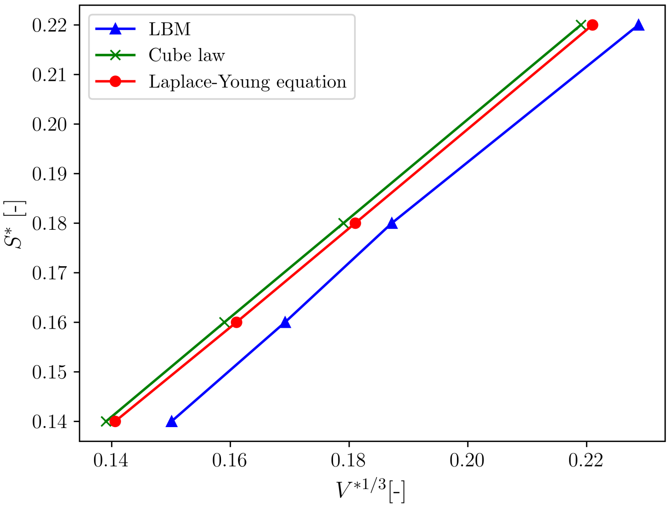

Figure 2.19: Dimensionless rupture distances ($S^* = \dfrac{S_c}{R}$) of fluid bridges between two spheres as a function of the dimensionless liquid bridge volume (V^*), calculated from Laplace-Young equation, LBM simulations and the cubic law.

2.3.3.3 Rupture distance

Likewise, the critical distance S_c (sphere separation that leads to breakage of the bridge) can be compared. S_c can be obtained on a theoretical basis: it is the distance beyond which the Laplace-Young problem degenerates into a solutionless problem (practically approached by an upper bound of the real solutions). Previous works (Lian et al. (1993)) have shown that S_c is approximately proportional to the cubic root of the volume of the bridge. This empirical relation is also compared to the results.

Figure 2.19 displays the rupture distance obtained by the different methods. The LBM follows a correct trend yet the distance is systematically underestimated, by 4% approximately. Therefore, it is less accurate than the cubic approximation. The systematic underestimation can be explained by the difficulty to approach a mechanically unstable solution numerically.

2.3.3.4 Sensitivity of mesh resolution

Unfortunately, a large computational cost is associated with LBM simulations. Therefore, we are interested in the optimal resolution capable of providing accurate results within acceptable computing times. A convergence test is carried out by performing multiple LBM simulations of liquid bridges.

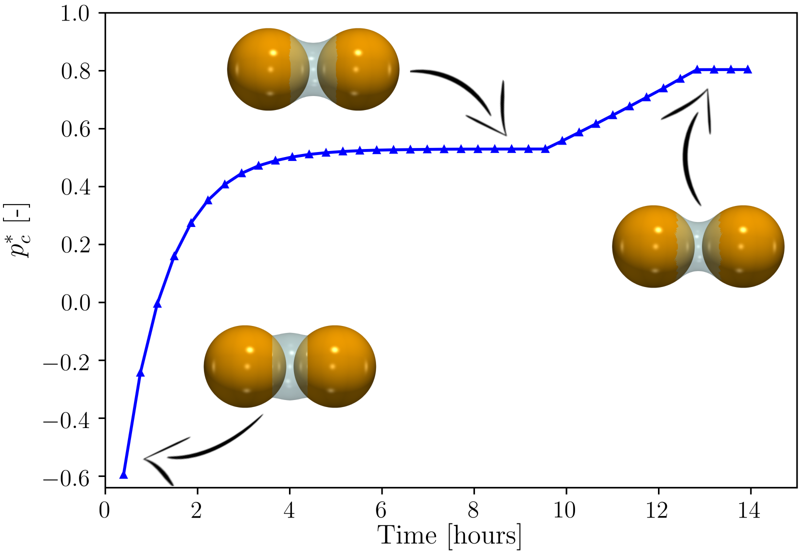

Figure 2.20: Capillary pressure evolution vs time. Capillary pressure increases after placing a liquid droplet between the spheres. Once the capillary pressure converges to a steady value, the liquid is gradually removed/added to adjust the capillary pressure to the desired value. The figure above displays the $p_c^* - Time$ plot for a $R/\Delta x = 67$, being Δx the distance between nodes equal to 1 lattice unit. After convergence, capillary pressure is increased until $p_c^* = 0.8$.

The configuration depicted in figure 2.17 is reproduced for several mesh sizes to investigate the resolution sensitivity. The initial state of each simulation is set by placing a liquid droplet between the solid spheres. No adjustment is imposed until the pressure reaches a steady-state. This configuration is achieved when

$\left|\left(\frac{p_c^{LBM^*}}{p^*_{c,t}}\right)_{it+5000} - \left(\frac{p_c^{LBM^*}}{p^*_{c,t}}\right)_{it}\right| < 5\cdot 10^{-4}$, where$p_c^{LBM^*}$ and $p^*_{c,t}$ are the LBM and the theoretical capillary pressures, respectively. Once the convergence is completed, we proceed to tune the capillary pressure by means of a mass sink/source in order to attain the desired capillary pressure. In this reference case, $p^*_c = 0.8$. Pressure is conveniently increased (see figure 2.20) or decreased until $p^*_c = 0.8$. Plus, the distance between the spherical grains is fixed to $S^* = 0.2$.

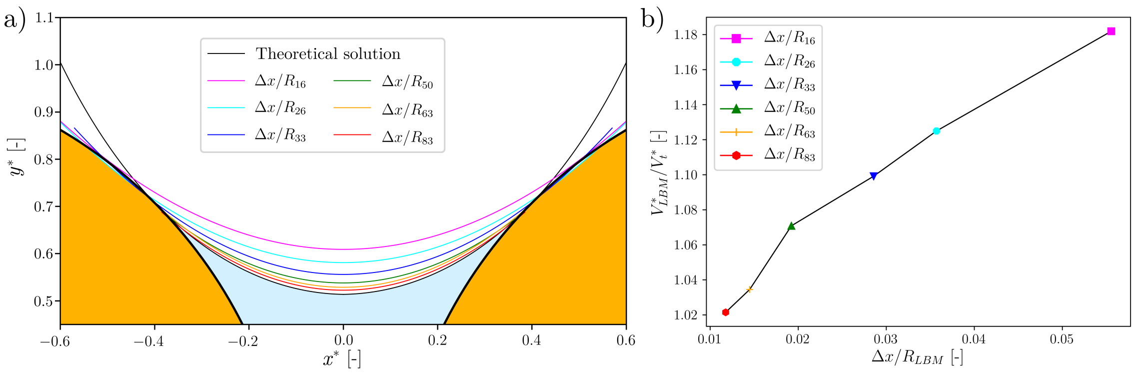

Figure 2.21: a) Overlapped profiles obtained with the LBM and Young-Laplace equation. b) Volume error vs mesh resolution. Simulations are performed in parallel using a 24 core CPU.

After adjusting the capillary pressure to obtain the desired value ($p^*_c = 0.8$) and reaching a static configuration, the bridge profile can be plotted and compared with the theoretical solution. Figure 2.21a displays the superimposed profiles, suggesting that the finer the mesh is, the more accurate results are obtained. Results range sphere radius from to $R^* = 16$ to $R^* = 83$, where R^* is the dimensionless radius defined as $R^* = \frac{R}{\Delta x}$, being Δx the distance between nodes equal to 1 lattice unit. The error associated to the resolution is graphically represented in figure 2.21b in terms of volume. Indeed, we observe that as the computational mesh resolution is increased, LBM predictions get closer to the theoretical volume of the bridge. Overall, figure 2.21 indicates that space-discretization with $R^* < 16$ are prone to give inaccurate results (an error of $\approx 20\%$ is observed between LBM and theoretical value). Whereas mesh resolution satisfying $R^* > 26$ will lead to acceptable results (errors of $< 12\%$). As expected, the finest meshes ($R^* > 63$) undoubtedly result in excellent accuracy (errors of $< 4\%$), though, this improvement incurs a non negligible additional computational cost. Details about the relation between the accuracy and computation time will be further discussed in section 3.3.1.4.

2.4 Application examples

This section presents some applications of the LBM to model typical liquid microstructures of wet granular materials. Previous section analyzed the pendular bridge between spherical bodies. In this section we extend the analysis to configurations without rotational symmetry, thus, impossible to obtain from semi-analytical treatment. Liquid topology is evaluated for different liquid clusters. More specifically, groups of 3, 4 and 7 spheres are considered.

2.4.1 Trimer

Trimers are the liquid configurations obtained after the coalescence of three pendular bridges formed between three adjacent particles. Trimers are one of the most common liquid structures during the funicular regime (Scheel et al. (2008); Semprebon et al. (2016)). In this section, the evolution of these microstructures is evaluated under drainage conditions by means of the LBM. Results are compared with numerical data provided by Wang et al. (2017) using Surface Evolver (SE). All geometrical parameters and hydrostatic properties are adjusted to reproduce the test of Wang et al. (2017). These parameters are summarized in the following list:

- Radius of the spheres: $R = 5mm$
- Surface tension: $\gamma = 0.051N/m$
- Contact angle: $\theta = 10^o$
- Three equal-sized spheres in contact.

The initial and final states are depicted in figure 2.22. The drainage is imposed by removing liquid content. This phenomenon is typically observed during the evaporation or drying processes.

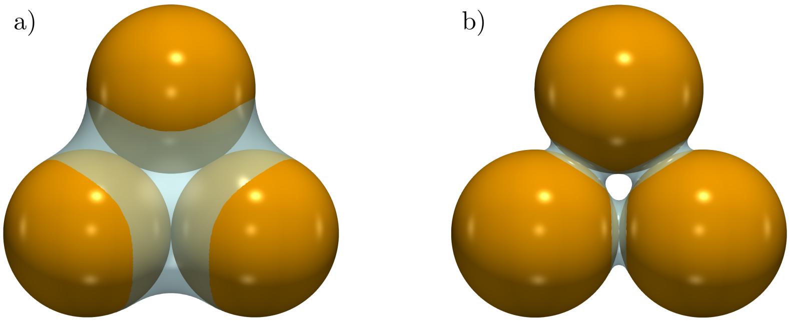

Figure 2.22: a) Initial configuration corresponding to $V^* = 0.33$. b) Final state obtained after drainage the trimer. Three isolated liquid bridges are identified.

Following the ideas of previous works (Wang et al. (2017); Melnikov et al. (2015); Gladkikh and Bryant (2005)), trimers can be decomposed into simple units. Next sections describe two approximations to determine the volume of the liquid clusters.

2.4.1.1 Pendular bridge approximation

According to Wang et al. (2017), the liquid content in a generic cluster can be divided into three isolated bridges connecting the three spherical bodies (see figure 2.23). In this scenario, the same amount of liquid is associated to each liquid bridge. Moreover, the excess of liquid due to possible liquid intersections is ignored.

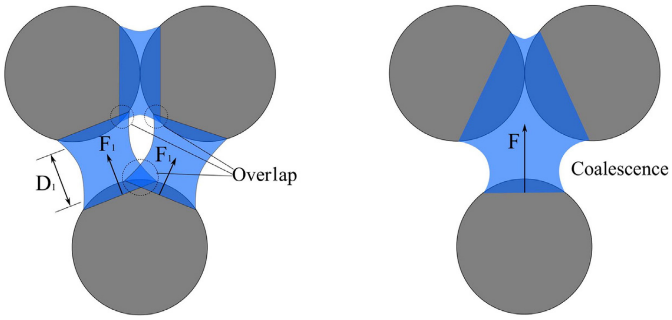

Figure 2.23: Funicular regime decomposed into three pendular bridge. Image taken from Wang et al. (2017)

2.4.1.2 Gladkikh approximation

The approximation proposed by Melnikov et al. (2015) based on Gladkikh's method (Gladkikh and Bryant (2005)) incorporates the volume of the pore throat in the previous pendular bridge approximation. Following the idea of Haines (1927) that the fluid-fluid interface between three solid grains adopts a spherical shape with constant curvature, Melnikov et al. (2015) approach considers that liquid clusters can be decomposed into three basic units: filled pore bodies, liquid bridges, and menisci. All the isolated liquid configurations beyond the pendular bridge liquid can be considered clusters. Furthermore, the smallest possible cluster is the so-called trimer. Melnikov et al. (2015) model assumes that a trimer is bounded by two menisci located in neighboring tetrahedra on both sides of the facet (pore throat) and the common liquid bridges. This technique enhances a complete analysis of more complex liquid clusters, for instance, pentamers can be constructed from two trimers sharing one liquid bridge (see figure 2.24c)

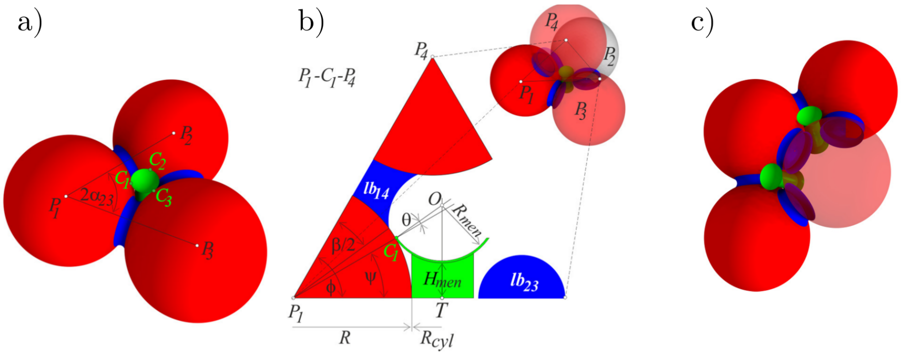

Figure 2.24: a) Trimer cluster formed by three grains with centers P_1, P_2 and P_3 . The meniscus (green region) has one contact point (C_1, C_2 and C_3) with each neighboring grain. Liquid bridges (blue regions) are illustrated as well. b) Cut section through $P_1 - C_1 - P_4$ is displayed. Point O is the center of the meniscus. lb_{14} and lb_{23} are the liquid bridges between particles $P_1 - P_4$ and $P_2 - P_3$, respectively. The green region below the meniscus shows the cut through the cylinder which approximates the meniscus volume. c) Pentamer cluster Image taken from Melnikov et al. (2015)

The volume of the pore throat is approximated as the volume of a cylinder V_{cyl} with the same axis as to normal of the pore throat, see figure 2.24b. Thus, the liquid content of the trimer is expressed as the sum of the three liquid bridges (V_{bridge}) plus the volume associated to the pore throat:

$$V_{trimer} = V_{cyl} + 3\varepsilon V_{bridge} \tag{2.38}$$

Eq. 2.38 includes a geometrical correction parameter ε that accounts for the missing volume between the main meniscus and the liquid bridges (see figure 2.24b). In this work, $\varepsilon = 1.07$ as done in Melnikov et al. (2015).

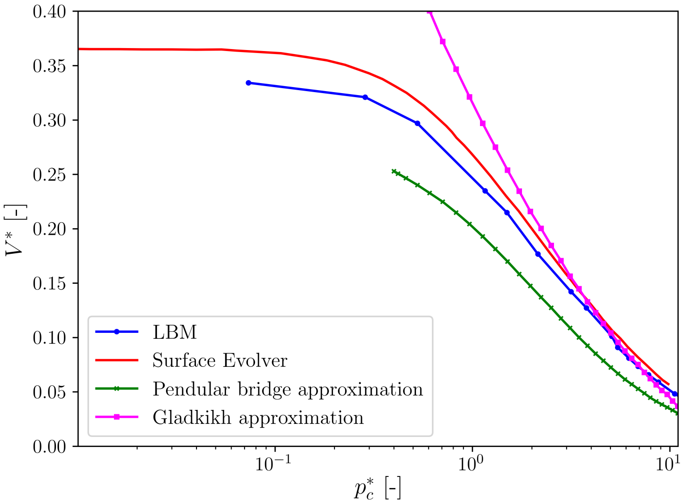

Figure 2.25: Liquid volume vs. capillary pressure for spheres in contact under drainage conditions. Comparison between semianalytical expressions, LBM and the results for SE obtained in Wang et al. (2017).

The drainage effect in terms of capillary pressure is evidenced in figure 2.25 in logarithm scale. The liquid content decrease induces a rise of capillary pressure. We emphasize the good agreement between Surface Evolver and LBM in figure 2.25. It is worth noting that results in figure 2.25 are restricted to the funicular regime, thus, further increase of capillary pressure would result in the transition towards the pendular regime (see figure 2.22). The comparison is completed with the approximations detailed in sections 2.4.1.1 and 2.4.1.2. Gladkikh approximation provides excellent results for low liquid contents ($V^* < 0.2$). However, the curve starts diverging when $V^* > 0.2$). The excess of amount of liquid observed in figure 2.25 for the Gladkikh approximation corresponds to account the same liquid volume two times (volumes of pendular bridges and pore throat are overlapped). Reasonable results are also obtained with the pendular bridge approximation. Overall, the pendular approximation achieves a better description of the $p_c^* - V^*$ hysteresis than Gladkikh approximation. This is evidenced in figure 2.25, where the pendular approximation follows an S-curve mimicking the same tendency observed in the numerical models.

2.4.2 Tetrahedron

In this section we study the evolution of a tetramer, a liquid cluster formed by 4 spherical grains, under different liquid contents (see figure 2.26). Initially, the wetting phase occupies the pore body, then, the wetting phase is progressively sucked to reproduce a drainage process. In the course of the simulation shown in figure 2.26 we evidence the transition from the capillary regime to the funicular state, and eventually, to the pendular regime. The first transition is depicted in the sequence of points "b", "c" and "d" of figure 2.26, where the non-wetting phase penetrates one of the tetrahedron facets. After the transition (figure 2.26d), the liquid cluster becomes a trimer. The second transition is illustrated between points "e" and "f" of figure 2.26, in this case, the trimer splits into three pendular bridges.

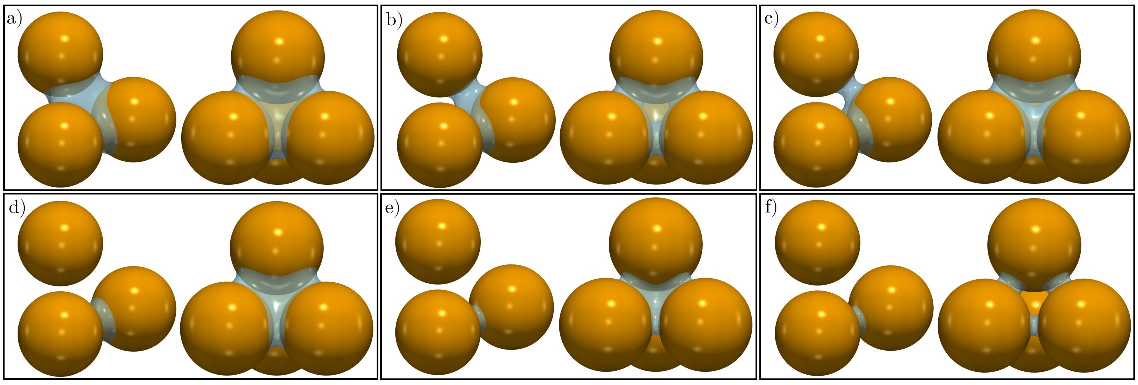

Figure 2.26: Interface evolution of a tetramer under drainage conditions. Side and bottom views are depicted for six different liquid contents.

Decreasing the amount of liquid leads to an increment of capillary pressure, and subsequently, to an interface with higher curvatures. Such changes are evidenced in figures 2.26 and 2.27. Moreover, we observe a relatively dynamic event between $V^* \approx 0.16$ and $V^* \approx 0.20$ due to the detachment of the wetting phase from one of the solid bodies. This mechanism is responsible for the pressure jump displayed in figure 2.27. The dynamic evolution results in a rapid liquid redistribution between the 3 other spherical grains forming a trimer (see figure 2.26d). A second liquid reallocation is observed for $V^* \approx 0.04$. At this moment, the trimer abruptly decays into three isolated pendular bridges (see figure 2.26f). The trimer rupture is revealed with a new dynamic episode (see the pressure drop for $V^* \approx 0.04$ in figure 2.27).

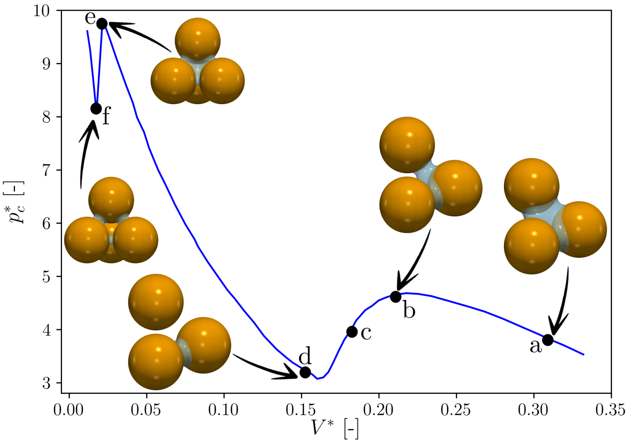

Figure 2.27: $p_c^* - V^*$ relationship of a tetramer under drainage conditions. Points indicated in the image correspond to the snapshots illustrated in figure 2.26.

2.4.3 Cluster

We extend the analysis performed in subsection 2.4.2 to a higher geometrical configuration, a liquid cluster formed by 7 equal-sized spheres.

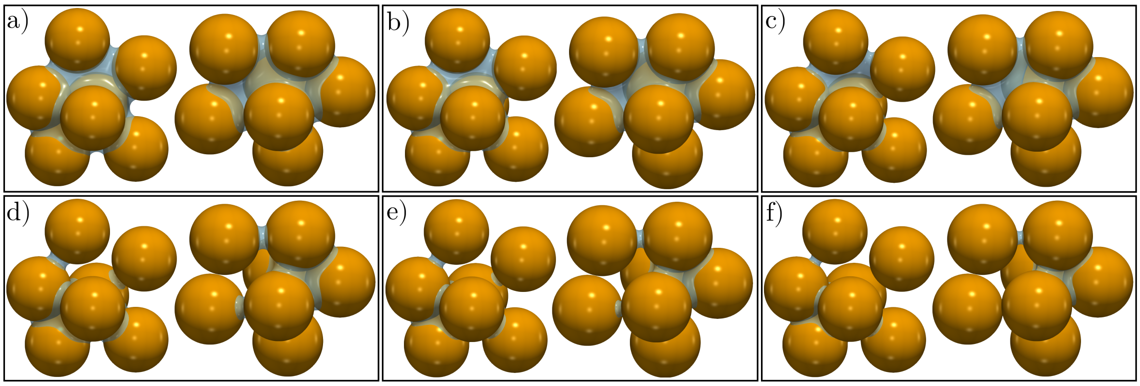

Figure 2.28: Interface evolution of a cluster under drainage conditions. Side and bottom views are depicted for six different liquid contents.

Following the same process as in subsection 2.4.2, the wetting phase is gradually removed. Consequently, the interface is displaced as shown in figure 2.28. An abrupt event is observed between figures 2.28c and 2.28d. Non-wetting phase penetrates into the cluster causing a Haines jump. This phenomenon occurs when the interface meniscus can no longer increase its curvature at the narrowest pore throat, consequently, a rapid emptying is manifested before facing the next narrow constriction. Haines jump corresponds to the transition from a quasi-static regime to a dynamic invasion. Indeed, the slow drainage of the cluster was characterized by a low $\boldsymbol{Ca}$, however, the invasion of the non-wetting phase into the pore body results into the redistribution of the liquid content within a very short time (high interfacial velocities are observed as suggested by Armstrong et al. (2015)). The evolution of the capillary pressure along the drainage process is illustrated in figure 2.29. The pressure jump is found for $V^* \approx 0.98$ in figure 2.29.

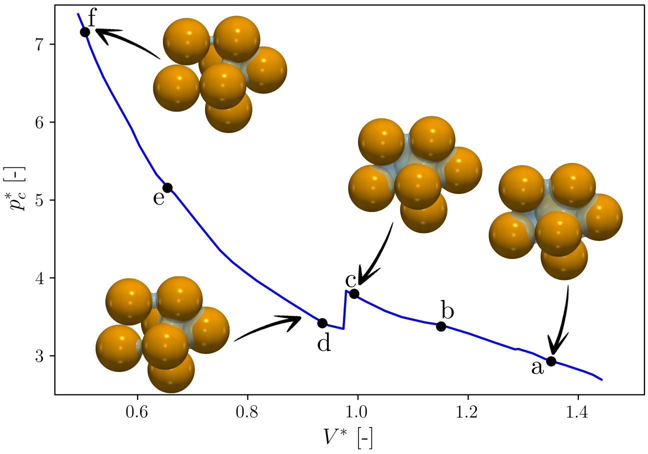

Figure 2.29: $p_c^* - V^*$ relationship of a liquid cluster under drainage conditions. Points indicated in the image correspond to the snapshots illustrated in figure 2.28.

2.5 Conclusions

Hydrostatic properties and pore-scale morphology of immiscible phases have been obtained by the multicomponent Shan-Chen LBM for systematic comparisons with other methods. This chapter analyzed the discretization errors and provided guidelines to calibrate the method and minimize errors.

Two-fluid-phase flow through capillary tubes has been analyzed and compared to the solution given by the MS-P method. Entry pressure, curvature and interface profile obtained from LBM simulations converge to the analytical solution with mesh refinement. The capillary bridges simulated between 2 spheres also converge to the solution obtained directly from Laplace-Young equation, in terms of both shape and rupture distance.

Discretization errors are introduced in part because of the solid boundaries: curved surfaces are modeled as stair-cased lines, which may not approximate the curved wall properly if the lattice resolution is not fine enough. In addition, the numerical thickness of the fluid interfaces around the solids is also a source of error. These discretization errors were found to scale nearly linearly with mesh size, and relatively independently of rotations of the grid frame. For the error due to interfacial thickness we showed (section 2.3.2.2) that a significant reduction was possible with appropriate geometrical corrections of the solid boundaries. This correction leads to shrink the size of all solid objects by a mesh-dependent length to minimize the mesh-dependency of the result. It improves the convergence of the results as discretization errors decrease quadratically with the mesh size. This technique is, therefore, systematically adopted throughout this thesis.

Finally, last section extents the research to more complex liquid structures. The evolution of trimers under drainage condition has been compared with numerical data provided by Wang et al. (2017) with satisfactory agreement. Additionally, pendular and Gladkikh approximations have been tested and considered a reliable tool to predict $p_c^* - V^*$ curves.

Chapter 3

Capillary force analysis

3.1 Introduction

Capillary forces exerted on particles of granular materials have an important impact on the macroscopic behavior. Low water contents in wet soils confer significant capillary forces that increase the cohesion of the material (Hornbaker et al. (1997)). Indeed, capillary effects are strongly influenced by the amount of water content. Accordingly, there is major interest in understanding the hydro-mechanical properties of wet granular materials. At low water content, isolated pendular bridges are formed between the solid particles.

Regarding the mechanical behavior, several studies have investigated the sensitivity of capillary cohesion at the global scale (Gröger et al. (2003); Richefeu et al. (2006)). Although considerable research has been conducted at the macro-scale, efforts should also be devoted to investigate the interactions at the pore scale due to the major effect on the macroscopic phenomena. Since the pioneering work carried out by Haines (1925); Fisher (1926), capillary forces are well studied in pendular bridges.

The dependency of the capillary forces under pendular regime has been studied as function of water content (Hotta et al. (1974)), suction (Gras et al. (2013)) and separation distance between particles (Willett et al. (2000); Lian et al. (1993)). Previous studies (Richefeu et al. (2009); Scholtès et al. (2009); Jiang et al. (2004)) enhanced the development of numerical models based on the discrete element method (DEM) to simulate unsaturated media due to the incorporation of capillary forces exerted by the pendular bridges. Nonetheless, these models are limited to low levels of water content that ensure the pendular regime. When the water content is increased, pendular bridges coalesce forming complex liquid morphologies (Scheel et al. (2008); Iveson et al. (2001)). The pendular regime vanishes and is replaced by the funicular regime. At this point, the capillary cohesion tends to reach the maximum value as suggested by Schubert (1984); Wang et al. (2017). Among the different liquid clusters observed in the funicular regime, the trimer (cluster after the coalescence of three pendular bridges formed by three adjacent particles) is found to be the most characteristic (Semprebon et al. (2016); Badetti et al. (2018)).

Previous research (Urso et al. (1999, 2002)) has shown that capillary forces from trimers can be analytically solved in 2D (and 3D in particular cases such in Gagneux and Millet (2016)). Plus, the evolution of capillary forces under funicular regime has been successfully modeled in 2D lattice Boltzmann simulations (Delenne et al. (2015)). Difficulties arise when capillary forces are evaluated in a three-dimensional space. The complexity of the liquid morphology hinders a generic analysis based on Young-Laplace equation (Wang et al. (2017)). Thus, numerical approaches have been adopted to investigate capillary forces during the funicular regime (Scheel et al. (2008); Semprebon et al. (2016); Strauch and Herminghaus (2012); Wang et al. (2017)). Recent literature (Wang et al. (2017)) analyzed the funicular regime under static conditions by means of Surface Evolver (SE).

The goal of this chapter is to develop a capillary force analysis using the multicomponent Shan-Chen lattice Boltzmann method (Shan and Chen (1993)). More specifically, two main objectives are defined: On the one hand, in this chapter we propose a method to evaluate the forces on solid objects using a multiphase LBM. So far, the force analysis was limited to 1-phase flow. Boundary forces due to the fluid flow have been investigated with LBM by means of the momentum exchange algorithm (Ladd (1994); Mei et al. (2002); Caiazzo and Junk (2008)). However, this algorithm is not suitable for multiphase flows due to a numerical film at the fluid-solid interface (considered a typical problem in the multicomponent Shan-Chen model as detailed in Chen et al. (2014)). On the other hand, the present method complements the study of capillary forces of Wang et al. (2017) and Semprebon et al. (2016). Although Surface Evolver is much faster in terms of computation time, LBM is able to reproduce all the liquid morphologies (regardless the complexity of the cluster structure) and simulations are not restricted to the quasi-static regime (Ruiz-Cabello et al. (2009); Fischer et al. (2014)). Thus, forces can be evaluated during snap-off, fast drainage or other dynamic events.

Throughout this chapter, we use the results provided by Wang et al. (2017) as a benchmark to validate and test the accuracy of the method.

3.2 Methodology

Capillary forces derived from the theoretical solution for a pendular bridge are used to validate the numerical model. Afterwards, the force evaluation method is presented.

For the purpose of this work, we use the following dimensionless variables:

- Capillary pressure: $p_c^* = \frac{2 p_c R}{\gamma}$, where γ is the surface tension, R is the radius of the spheres and p_c is the capillary pressure.
- Force: $F_c^* = \frac{F_c}{2\pi\gamma R}$
- Volume: $V^* = \frac{V(t)}{\frac{4}{3}\pi R^3}$, where $V(t)$ is the volume at time t.
- Coordinates: $x^* = \frac{x}{R}$ and $y^* = \frac{y}{R}$, where x and y are the coordinates.

- Separation between spheres: $S^* = \dfrac{d}{R}$ where d is the separation between the spherical grains.

3.2.1 Theoretical capillary forces for a pendular bridge

Let's consider an axially symmetric system of two solid spherical particles as shown in figure 3.1. When the system is at equilibrium, the attractive force at any slice orthogonal to the axis is given as a contribution of the action of the surface tension exerted by the nonwetting-wetting interface and the capillary force due to the pressure difference between phases (Fisher (1926); Woodrow et al. (1961); Lambert and Valsamis (2013)), thus:

$$F_c(x) = \pi r(x)^2 p_c + 2\pi r(x)\gamma cos\psi \tag{3.1}$$

where $p_c = p^{nw} - p^w$ is the pressure jump between the liquid bridge and the non-wetting phase, $r(x)$ is the radius of the bridge neck at any plane perpendicular to the axis, γ is the surface tension and ψ is the angle between the x-axis and the tangent line at point A. Previous parameters are depicted in figure 3.1.

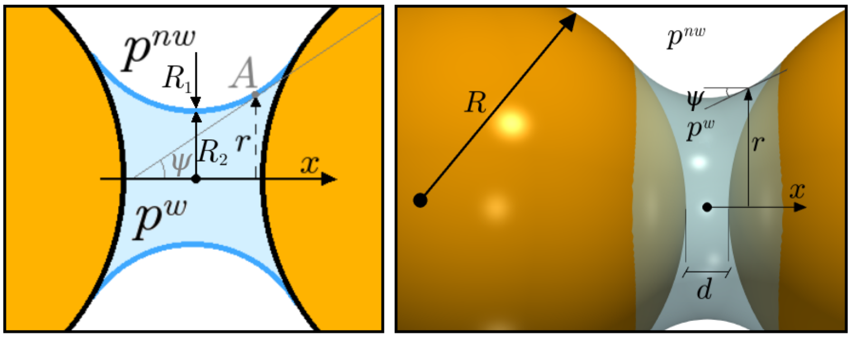

Figure 3.1: a) Liquid bridge scheme with the relevant parameters used to determine the capillary force between the solid particles. b) Parameters from a capillary bridge between two solid bodies of equal diameter separated a distance of $S^* = \dfrac{d}{R} = 0.2$ reproduced by a LBM simulation. The static capillary bridge is obtained after imposing a capillary pressure of $p_c^* = 0.4$.

The radius in Eq. 3.1 can be computed after solving Eq. 2.37 . Hereinafter, the dimensionless theoretical capillary force will be referred as $F_{c,t}^*$.

3.2.2 LBM force evaluation method for multiphase flows

The motion of unsteady, viscous, immiscible multiphase fluids is described by the Navier-Stokes momentum equation:

$$\rho^\sigma \left(\frac{\partial \mathbf{u}^\sigma}{\partial t} + \mathbf{u}^\sigma \cdot \nabla \mathbf{u}^\sigma \right) = \nabla \cdot \mathbf{T}^\sigma + \rho^\sigma \mathbf{g} \tag{3.2}$$

where ρ is the density of phase σ, $\mathbf{u}$ is the fluid velocity, $\mathbf{g}$ is the gravity vector and $\mathbf{T}$ is the stress tensor. The stress tensor can be decomposed into the hydrostatic and the deviatoric stress tensors:

$$\mathbf{T} = -p\bar{\bar{\mathbf{I}}} + 2\left(\mu^{\sigma}\bar{\bar{\mathbf{S}}}^{\sigma} + \mu^{\bar{\sigma}}\bar{\bar{\mathbf{S}}}^{\bar{\sigma}}\right) \tag{3.3}$$

The deviatoric stress $\left(S_{ij} = \frac{1}{2}\left(\frac{\delta u_j}{\delta x_i} + \frac{\delta u_i}{\delta x_j}\right)\right)$ can be reformulated in terms of LBM quantities:

$$S_{ij} = -\frac{1}{2\tau c_s^2}\Pi \tag{3.4}$$

where τ is the relaxation time, c_s the speed of sound and Π the moment of order two of the distribution function (see Eq. 2.5).

The force exerted on a solid body (see element Ω in figure 3.3) is computed by integrating the stresses over the solid boundary ($\delta\Omega$):

$$\mathbf{F_c} = \int_{\delta\Omega} \mathbf{T}\cdot\mathbf{n}dA \tag{3.5}$$

where $\delta\Omega$ is the surface of the grain, $\mathbf{n}$ is the normal vector to the solid surface and dA is the differential area.

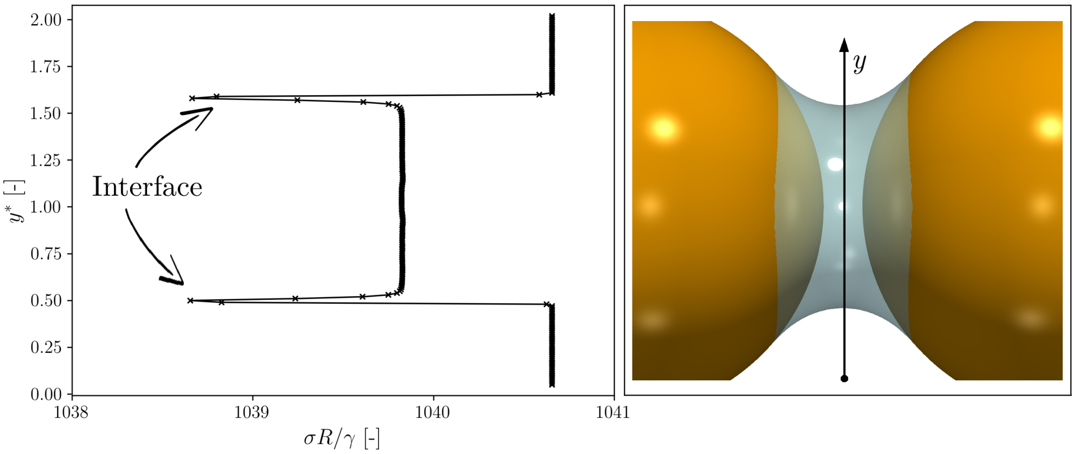

Figure 3.2: Horizontal stress along the vertical axis.

As evidenced in figure 3.2 and discussed in previous works (Chevalier et al. (2018); Kistler and Schweizer (1997)), surface tension leads to perturbations in the normal stress at the interface between two immiscible fluid. The deviatoric part represents what is left over from the total stress when the spherical contribution is subtracted from the pressure. Thus, the deviatoric part becomes significant at the interface.

In the Shan-Chen model, interactions properties similar to those of an additional fluid are assigned to the solid nodes (Huang et al. (2007)). This configuration results in a non-physical layer between the fluid and the solid (Chen et al. (2014)). Therefore, heterogeneous and non real stresses are found in the solid vicinities. To overcome the complexities presented near the solid objects, we propose to analyze the stresses inside a volume element far from the solid-fluid interface (see element Ω' in figure 3.3). Most of our research is conducted with sphere packings, hence, spherical volume elements are taken into account. However, other elements, such as cubes, tetrahedra, planes, ellipsoids may be considered.

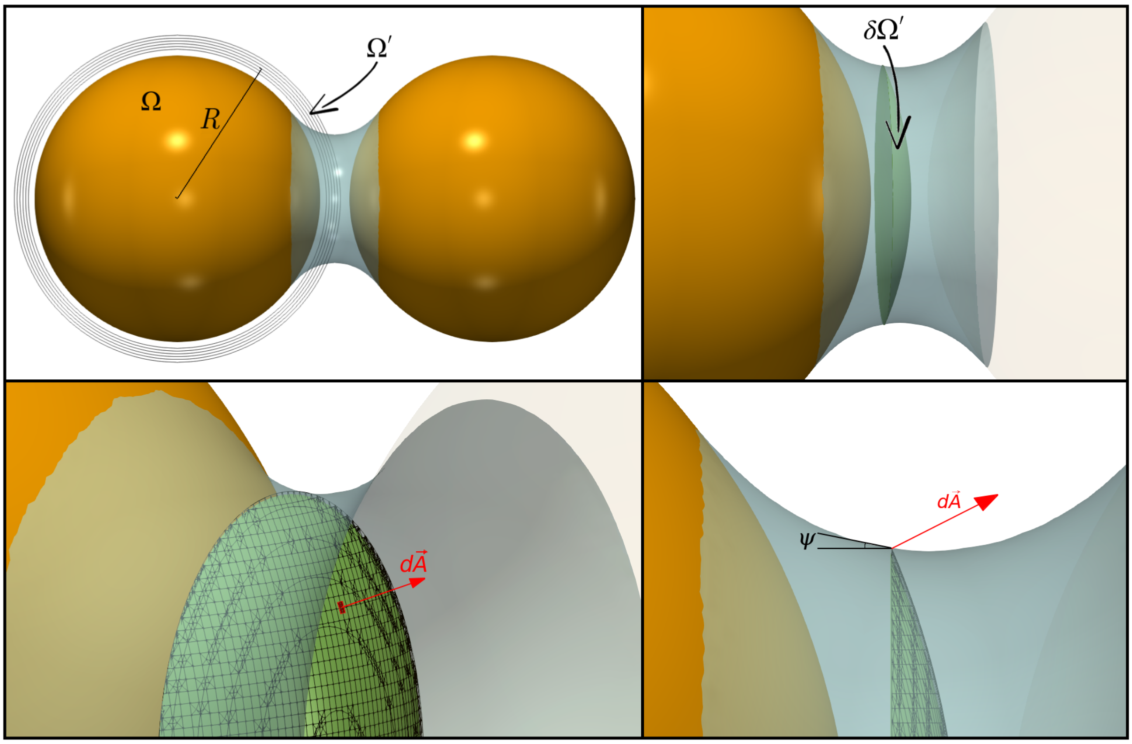

Figure 3.3: At the top left corner, several spherical volume elements (Ω's) enclose the spherical grain indicated as Ω. The other images illustrate the surface obtained as a result of the intersection ($\delta\Omega'$) between the capillary liquid bridge and the spherical volume element. Stresses are integrated over all the points of $\delta\Omega'$.

Thus, the force acting on the spherical grains is evaluated by the following integral:

$$\mathbf{F_c} = \int_{\delta\Omega'} -[p\delta_{ij} - c_s^2(2\tau - 1)S_{ij}]\mathbf{dA} \tag{3.6}$$

where $\delta\Omega'$ is the surface resulting from the intersection between the spherical volume element and the liquid bridge (see schemes in figure 3.3) and **dA** is the normal area vector as displayed at the bottom of figure 3.3.

3.3 Results

3.3.1 Pendular bridge

The purpose of this section is to validate the numerical approach through theoretical solutions. In particular, the LBM results are contrasted with the solution presented in section 3.2.1.

3.3.1.1 Sensitivity of the bundling sphere size

First of all, capillary force has been evaluated for different spherical volumes (see the different Ω' elements in figure 3.3) using Eq. 3.6. Results presented in figure 3.4

are in good agreement with the theoretical solution provided that the radius of the wrapping sphere is at least 5 lattice units larger than the radius of the solid sphere. The error drops to a constant low value for volume elements that: $\dfrac{R_{env} - R}{\Delta x} > 5$. Indeed, large errors are observed when the bundling sphere is too close to the solid-fluid interface as evidenced in figure 3.4. Henceforward a spherical volume element of 6 lattice units larger than the solid grain will be used during the force analysis. Additionally, the force obtained with Eq. 3.6 will be referenced as $F^*_{LBM,s}$ from now on if we use a spherical element to evaluate the force acting on the object.

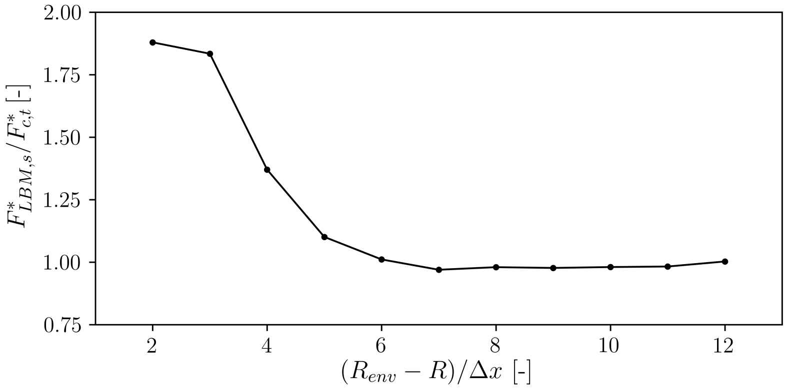

Figure 3.4: Force evaluated for different spherical volume elements with radius R_{env} that enclose a spherical grain of radius R. Results are obtained for a pendular bridge between two grains separated a distance $S^* = 0.1$ under a capillary pressure of $p^*_c = 1.7$. Mesh resolution: $\dfrac{R_{LBM}}{\Delta x} = 83$.

3.3.1.2 Force analysis during drainage process

In this section capillary forces are examined during drainage. The comparison between the LBM and the theoretical solution confirms the validity of the force evaluation method. We evidence similar paths followed by LBM simulation and Laplace-Young solution in figure 3.5 when the liquid from the bridge is progressively removed. Figure 3.5a illustrates almost coincident curves for relatively large volumes. However, error increases rapidly when capillary pressure is high, and we approach the breakage point. The high discrepancies observed at $p^*_c \approx 15$ in figure 3.5 are attributed to the spurious currents (Shan (2006); Pooley and Furtado (2008)). These currents are non-physical velocities that appear near the curved interfaces due to the discretization of the space. Near the bridge rupture, interface is approaching an unstable event. At this moment, the interface curvature is considerably high and the contribution of the deviatoric stress in Eq. 3.6 becomes the most significant part. During the previous stages, spurious velocities were still present, however, their action did not have a strong influence in the force analysis, and the hydrostatic action in Eq. 3.6 (which involves more accurate results) was predominant. Despite the error introduced by the spurious velocities, the present method is able to track the force during the drainage process with good accuracy.

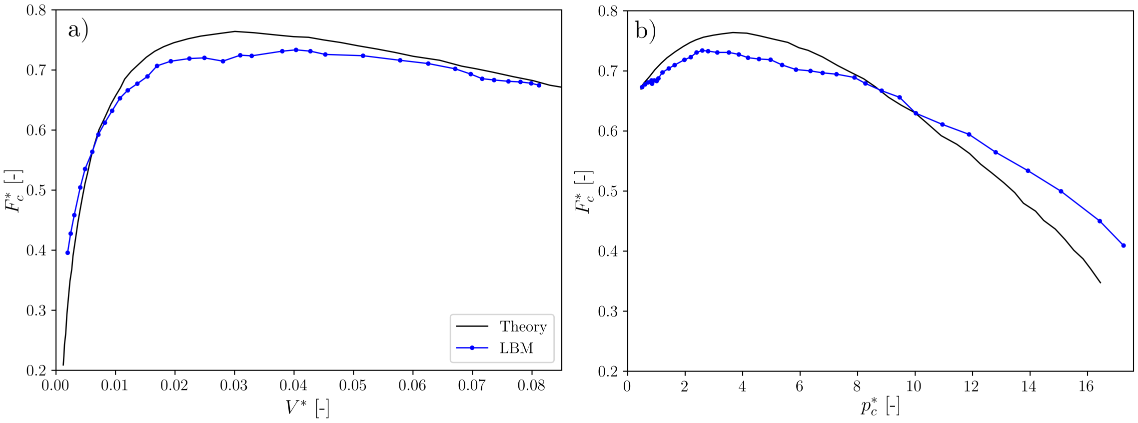

Figure 3.5: Evolution of capillary force vs volume (a) and capillary force vs capillary pressure (b) during the drainage of a liquid bridge. Results are obtained for a pendular bridge between two grains separated a distance $S^* = 0.1$. Mesh resolution: $\dfrac{R_{LBM}}{\Delta x} = 83$.

3.3.1.3 Force analysis for different orientations

In order to illustrate that the applicability of the method is not mesh-dependent, capillary force was evaluated for different angles between the z-axis and the bridge axis. Figure 3.6 shows that similar results are obtained for the same liquid bridge when it is not aligned to the mesh. Thus, the force evaluation method can be employed regardless the position of the spheres.

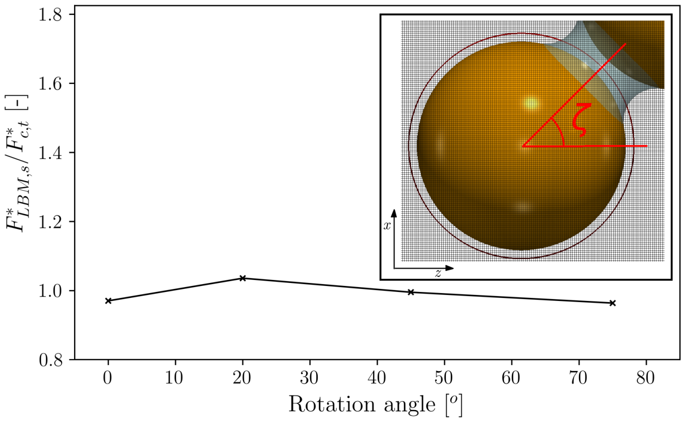

Figure 3.6: Error force evaluated for different rotation angles between the axis that passes through the two sphere centers and the z-axis. Simulations correspond to a capillary pressure of $p_c^* = 0.4$ and a separation distance of $S^* = 0.2$ between the spheres. Mesh resolution: $\dfrac{R_{LBM}}{\Delta x} = 50$.

3.3.1.4 Sensitivity of mesh resolution

Due to the large computational cost associated with LBM simulations, it is crucial to find the optimal resolution capable of providing accurate results within acceptable computing times. The convergence test is carried out following the steps explained in section 2.3.3.4.

The theoretical capillary force is determined in terms of bridge geometry (Eq. 2.37 and 3.1). By assuming a dimensionless capillary pressure of $p_c^* = 0.4$, the radius neck is $r^* = \dfrac{r}{R} = 0.52$. The radius r of Eq. 3.1 (see figure 3.1) is evaluated at the plane that passes through the origin where the neck radius is minimum. Replacing $r^* = \dfrac{r}{R}$ and $p_c^* = \dfrac{2p_cR}{\gamma}$ in Eq. 3.1 results in the following theoretical force expression:

$$F_{c,t} = \pi(r^*R)^2\frac{p_c^*\gamma}{2R} + 2\pi r^*R\gamma \tag{3.7}$$

In terms of dimensionless variables, Eq. 3.7 becomes: $F_{c,t}^* = 0.54$

According to Eq. 3.1, capillary force remains constant regardless the value of $r(x)$. After adjusting the capillary pressure in the LBM simulations to obtain the desired value ($p_c^* = 0.4$) and reaching a static configuration as shown in figure 3.1b, capillary forces are evaluated for the range of resolutions. In this particular test, capillary forces are not evaluated using a spherical volume element as displayed in figure 3.3. Instead, stresses are analyzed with Eq. 3.1. Thus, measuring the radius of the neck ($r_{LBM}(x)$) for different values of x we can compute the capillary force using Eq. 3.1 reformulated as:

$$F_{LBM,p}^* = \frac{\pi r_{LBM}^2 p_{c,LBM} + 2\pi r_{LBM}\gamma cos\theta_{LBM}}{2\pi r_{LBM}R} \tag{3.8}$$

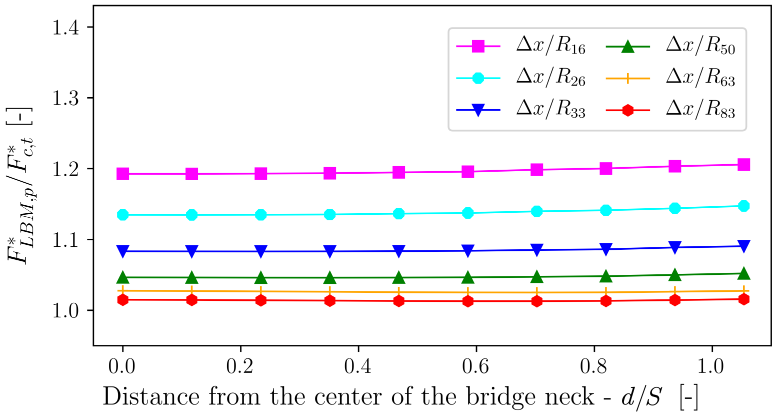

Figure 3.7: Capillary forces error as function of mesh size and distance (d) from the center of the bridge neck. All the simulations correspond to a capillary pressure of $p_c^* = 0.4$ and a separation distance of $S^* = 0.2$ between the spheres. Force is evaluated with Eq. 3.1 after computing the radius neck for each LBM simulation.

Figure 3.7 evidences almost identical forces are obtained along the bridge axis. Even the coarsest mesh leads to a constant capillary force regardless the position of the analyzed point. These results suggest that in spite of the larger error of coarse meshes, no discrepancies are found between different local curvatures. Additionally, figure 3.7 shows the results for different mesh resolutions. Notwithstanding the overestimation of capillary forces for low resolutions, good agreement is found between the theoretical force and the LBM simulations. It should be noted that the force analysis provided in figure 3.7 based on Eq. 3.1 is restricted to capillary bridges. As we will see in the next section, more complex morphologies are present in partially saturated media. The method explained in section 3.2.2 overcomes such limitations.

Figure 3.8 displays the comparison for different resolutions between the theoretical force and the LBM force evaluated using Eq. 3.6 (with a spherical volume element). As expected, capillary force error decreases with the mesh refinement. Figure 3.8 implies that error does not significantly reduce for $\frac{R_{LBM}}{\Delta x} > 50$. Moreover, error associated with $\frac{R_{LBM}}{\Delta x} > 33$ is found to be acceptable. Thus, we strongly recommend using spherical grains satisfying the following condition $40 > \frac{R_{LBM}}{\Delta x} > 25$. LBM simulations conducted with smaller grains may cause the detriment of the accuracy while finer meshes lead to long computation times without substantial error reduction.

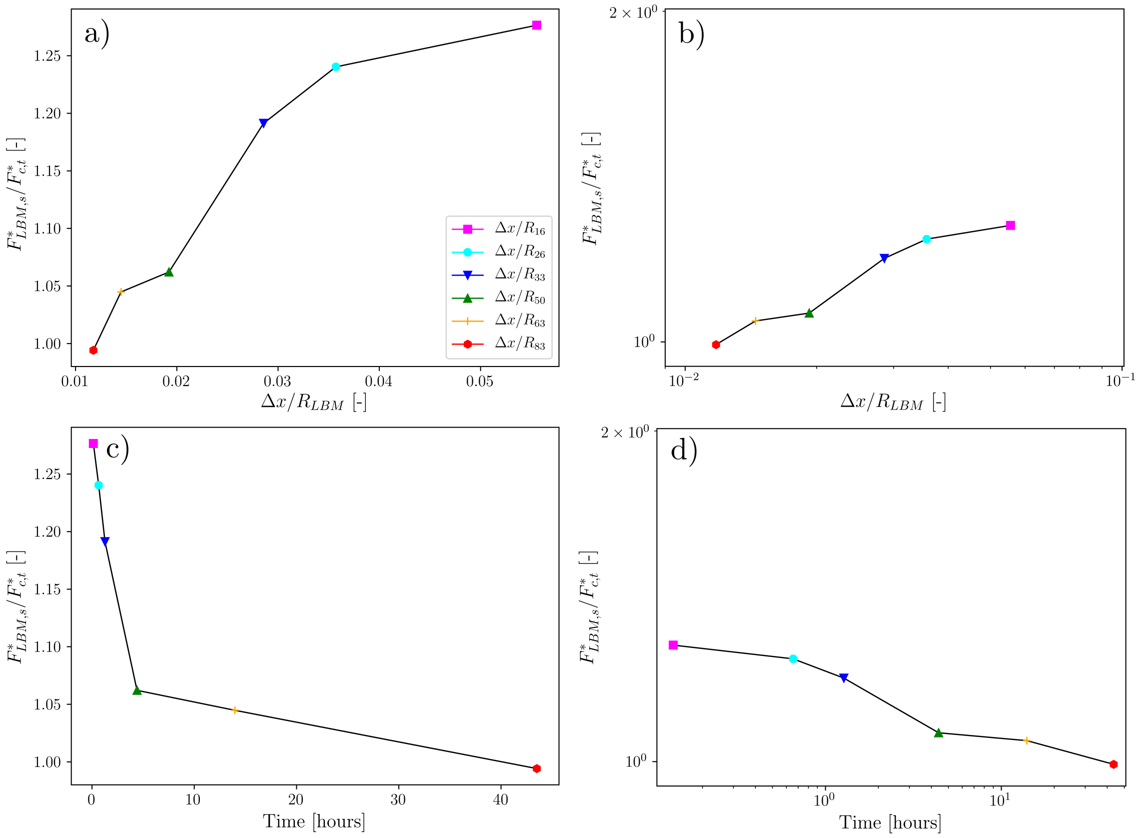

Figure 3.8: Converging mesh test for a pendular bridge. Capillary force errors are obtained for different mesh resolutions. Results are shown with linear (a) and logarithmic scale (b). Capillary force error vs computing time to reach convergence is displayed in linear (c) and logarithmic scale (d). Simulations correspond to a capillary pressure of $p_c^* = 0.4$ and a separation distance of $S^* = 0.2$ between the spheres.

3.3.1.5 Further considerations on the characteristic length

Even though adopting a reference spherical radius of $R \in [25-40]lu$ is encouraged, the accuracy of the LBM is strongly related to the curvature of the fluid-fluid interface. Thus, we might have better performances adapting the geometric LBM parameters arguing in terms of curvature rather than the mean grain radius. Unfortunately, choosing a reference interface curvature is an intricate task due to the complex liquid morphology observed inside porous media. Yet, results from pendular bridge test (sections 2.3.3.4 and 3.3.1.4) and capillary tubes (section 2.3.2.2) may shed some light on the subject. The reference curvature should not be confused with the local radii of curvatures or the mean curvature. The reference curvature is the one that will be reproduced several times in the simulation having a strong impact on the phenomenon. Therefore, in porous media simulations, very small pores should be excluded in the curvature criterion, even if they have a coarse representation. Otherwise, the computation time would rapidly increase. Let's illustrate the different concepts of curvature with the pendular bridge example. As shown in figure 3.1a, the liquid bridge has two radii of curvature. Radii can be either positive or negative depending on the geometry of the bridge. In figure 3.1a $R_1 > 0$ and $R_2 < 0$. According to Young-Laplace equation (see Eq. 2.36), capillary pressure is proportional to the sum of principal curvatures. In a cartesian framework, the mean curvature for a pendular bridge can be written as in Eq. 2.37. Additionally, as detailed in section 2.3.3.3, it is possible to determine the maximum separation between the spheres, given a certain liquid volume, before the liquid bridge vanishes. This separation is termed rupture distance. Finally, it is crucial to adopt a space discretization that balance optimally the computation time and the quality of the results. In this case, an adequate solution consists in setting the reference curvature equal to the rupture curvature. Such technique ensures interface curvatures over the reference. Consequentely interfaces are accurately represented until the breaking point.

Discretization	**Pendular bridge**			**Square tube**
Curvature $[lu^{-1}]$	Volume error	Force error	Time [*hours*]	Curvature error
1/9	0.134	0.241	0.6	0.083
1/12	0.110	0.189	1.1	0.061
1/17	0.071	0.062	3.8	0.044
1/20	0.037	0.041	13.9	0.036

Table 3.1: Summarized errors and computation times for different mesh resolutions. Discretization errors are described as function of curvature for two tests: pendular bridge (see figures 2.21b and 3.8) and fluid displacement through a capillary tube with a square cross-section (see figure 2.10).

Sensitivity analysis of the mesh resolution have been conducted as function of volume and force for the pendular bridge test (see figures 2.21 and 3.8), and curvature for the capillary tube (see figure 2.10). The conversion from these results to a comprehensive framework in terms of curvature has been carried out as follows: First, we evaluated the transversal curvature (in lu^{-1}) of the wetting phase remaining in the corner (see figure 2.12) for the different spacial-resolution displayed in figure 2.10. We point out that such analysis is performed for the fluid displacement test through a capillary tube with a square cross-section. The curvature values are listed in the first column in table 3.1. In addition, the errors found in the previous chapter (figure 2.10) are also included in the last column (**"Square tube"**) of table 3.1. Concerning the pendular bridge simulations, suction has been adjusted (following the procedure explained in 2.3.3.2) to match the mean curvature to the transversal curvature found for the capillary tubes. We emphasize that, regardless of the mesh resolution, all pendular bridge simulations are evaluated under the same p_c^*. Volume and force error are summarized in table 3.1 (column indicated as "**Pendular bridge**") as well as the computation time to reach a stable state.

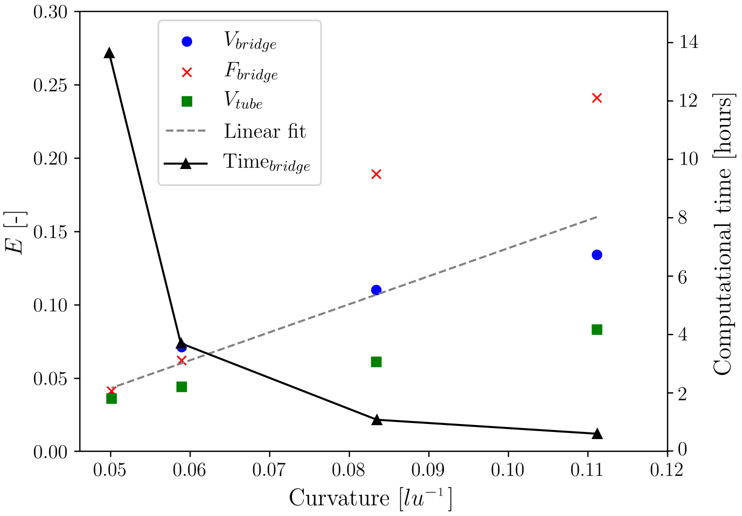

Figure 3.9: Summarized errors and computation times for different mesh resolutions. The errors are plotted in terms of curvature for two tests: pendular bridge (see figures 2.21b and 3.8) and fluid displacement through a capillary tube with a square cross-section (see figure 2.10). A linear regression line of the error upon the curvature is included.

The results compiled in table 3.1 are also available graphically in figure 3.9. From this analysis, we evidence that low curvatures (as a result of fine meshes), $k < 0.055 lu^{-1}$, lead to huge computational costs without a significant gain in accuracy. Thus, we recommend adjusting the geometric LBM parameters to enhance critical reference curvatures that $k \in [0.06 - 0.09] lu^{-1}$. Although the curvature criterion is difficult to implement due to the complex geometry of granular media, we believe that it provides orientative information that can be taken into account when it comes to decide the dimensions of the computational domain. Furthermore, this method could be extremely useful for multiphase flow through porous media with regular sphere-packings (Genty and Pot (2014)) or regular arrays of circular cylinders (Daneyko et al. (2011)). In such cases, knowing the geometry in advance may help predict the critical curvature (for instance, the one associated to the entry capillary pressure). It is worth noting that, beyond porous media, this criterion offers advantages to other research fields where the typical curvature in multiphase flow is easy to estimate. Consequently, the applicability of the curvature criterion is highly constrained by the possibility to determine a reference curvature.

Another interesting feature reflected in figure 3.9 is the disparate error values resulting from the force, curvature and volume analysis. All the approaches follow, approximately, linear trends. However, we observe that both curvature (for the capillary tube) and volume (pendular bridge) errors are considerably smaller than the error associated to the capillary force. In particular, a scaling factor of two is found for coarse meshes between V_{bridge} and F_{bridge} errors. Results in figure 3.9 suggest a strong sensitivity of force evaluation to the resolution of the mesh. The dependency on the spacial discretization has a lower effect on the analysis of volume and curvature. This conclusion should be taken into account when choosing the lattice spacing. Therefore, depending on the phenomenon and mechanisms we are investigating, grid resolutions will have different impact on the results.

3.3.2 Liquid clusters

In this section we extend the force study to complex liquid configurations impossible to be studied through analytical solutions.

By increasing the liquid content in a granular assembly in the pendular regime, the liquid bridges coalesce resulting into more complex liquid phase morphologies such as the dimer, trimer, pentamer, etc. Recent studies (Badetti et al. (2018)) suggest that trimers and large clusters compose the majority of the liquid configurations during the funicular regime. The complex liquid morphologies encountered during the funicular regime hinder a detailed analysis on the cohesive strength. However, some studies (Richefeu et al. (2016); Mitarai and Nori (2006)) have attempted to describe the relationship between cohesion and saturation degree.

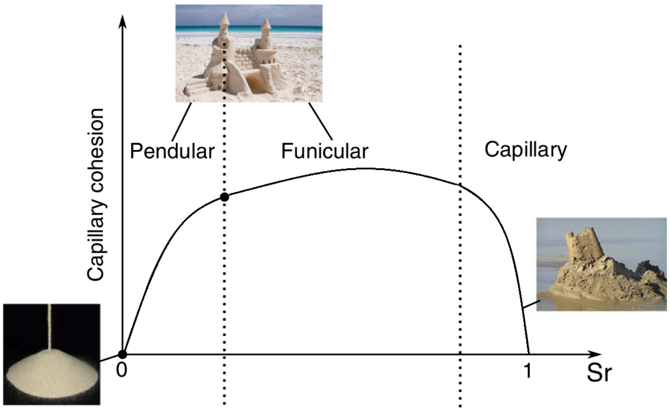

Figure 3.10: Qualitative diagram of cohesive stress - liquid content relationship. We have modified the image taken from Wang et al. (2017).

Capillary cohesion rapidly increases during the pendular regime as the liquid content is incremented. Adding more liquid triggers the transition from the pendular regime to the funicular state. During the funicular regime, the increment of the amount of liquid within the granular media leads to a smooth increase of cohesive strength (Cohesive stress - saturation degree relationship is schematically displayed in figure 3.10). Even though the capillary forces dependency on the saturation degree is not fully understood during the funicular regime, previous research (Wang et al. (2017); Mitarai and Nori (2006)) show that during this state, capillary cohesion reaches the maximum value.

Hereafter, forces are investigated for clusters of three and four spherical grains with filled pore throats under drainage conditions.

3.3.2.1 Three-sphere case

Forces are evaluated in the funicular regime for three spherical bodies of equal diameter and compared with experimental data and other numerical results. Experimental measurements were taken by Wang et al. (2017) following the test designed by Lambert (2007). Furthermore, the experimental data were contrasted with numerical results obtained with Surface Evolver in Wang et al. (2017). All geometrical parameters and hydrostatic properties are adjusted to reproduce the test of Wang et al. (2017). These parameters are summarized in the following list:

- Radius of the spheres: $R = 0.93 mm$
- Surface tension: $\gamma = 0.073 N/m$
- Two different liquid volumes are considered: $V^* = 0.178$ and $V^* = 0.2$

3.3.2.1.1 Force evaluated during the displacement of one sphere

The effect of the separation of one particle from the others is studied in this section. Initially, the three spheres are in contact and the liquid volume is fixed. Then, one of the spheres is displaced and the separation is progressively increased while the volume is kept constant.

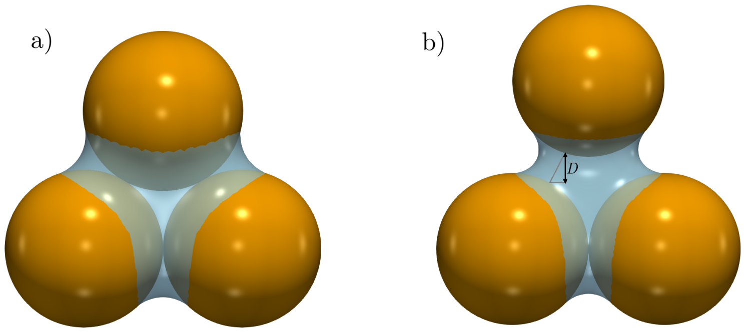

Figure 3.11: Evolution of the funicular regime for different displacements. Images are obtained after LBM simulations under volume controlled conditions. On the left, the top sphere has a vertical displacement of $D^* = 0$. Right figure displays the fluid configuration corresponding to a vertical displacement of $D^* = 0.39$.

Figure 3.11 shows the configuration of the 3 spheres at the initial state on the left. The configuration after increasing the inter-particle distance is depicted on the right of figure 3.11. The displacement of the top sphere is defined as $D^* = \dfrac{D}{R}$, where D is the distance shown in figure 3.11. Capillary forces are determined throughout the simulation. It is pertinent to mention that contact angle was not constant during the experimental tests (Wang et al. (2017)). The equilibrium contact angle adopts values between the so-called advancing contact angle and receding contact angle due to chemical heterogeneities and physical imperfections of the solid surface as explained by Tadmor (2004). Wang et al. (2017) used polynomial fitting equations to mimic the experimental contact angles in the Surface Evolver (SE) simulations. Concerning the LBM simulations performed in this chapter, the equilibrium contact angle is set to $\theta \approx 0^o$. Although the previous literature (Wang et al. (2013); Zhang and Kwok (2004)) has studied the contact angle hysteresis using multiphase LBM, it is still unclear how to determine the macroscopic quantities of advancing and receding contact angles. Therefore, we warn the reader that, in our simulations, the variations of the contact angle are not imposed to match the advancing and receding angles. In the LBM , the contact angle remains very small ($\theta \approx 0^o$) throughout all the simulations.

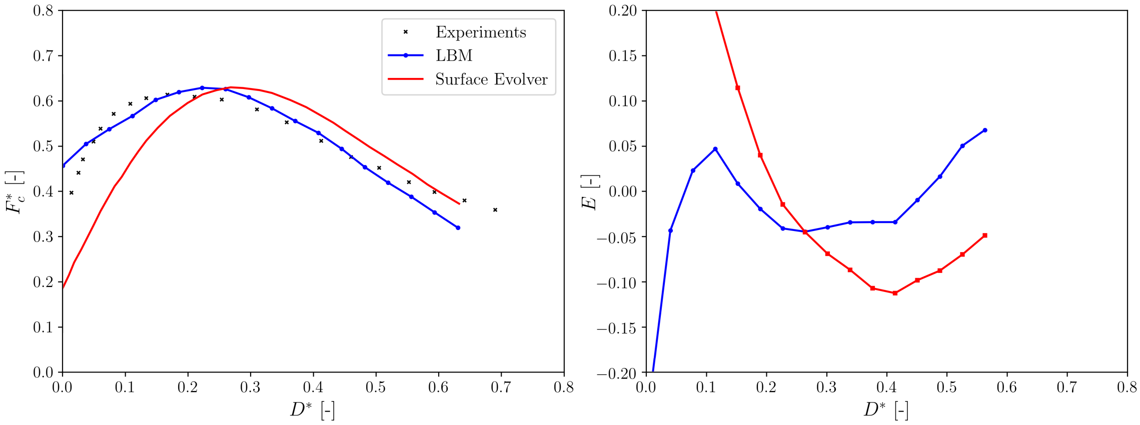

Figure 3.12: Comparison between the experimental results and the numerical approaches for $V^* = 0.178$. The experimental results and Surface Evolver data have been obtained from Wang et al. (2017). Three spheres of equal diameter in contact are set as initial configuration. One of the spherical grains is progressively displaced from the rest. a) Capillary force acting on the separating sphere is evaluated during the process. b) Force error between the experimental results and the numerical approaches.

Figure 3.12 shows the comparison of LBM, SE and experiments. Capillary force increases at the beginning of the test due to the pinning effect. As summarized by Willett et al. (2003), the so-called pinning effect is manifested when a force acts on the liquid and the three-phase contact line remains stationary between intermediate values of the contact angle limits. When one of these limits is reached, the three-phase contact line slips. According to Wang et al. (2017); Willett et al. (2003); Joanny and De Gennes (1984), pinning mechanism leads to an increment in the force with increasing the inter-particle distance. After reaching the peak, the test proceeds under slip condition resulting to a decrease in capillary force with increasing the separation distance. Figure 3.12 shows similar paths for all the approaches. We highlight the good accuracy of the maximum capillary force (similar peak values are observed in figure 3.12a). On the other hand, SE curve is shifted respect the experimental results and LBM curve is not capable to mimic accurately the same pinning effect (an expected result, considering that contact angle is fixed to $\theta \approx 0^o$). Indeed, SE and experimental curves are steeper than the LBM curve for $D^* < 0.2$. Even though the effects of advancing/receding contact angles are not incorporated, we find that LBM solutions offer an accurate prediction of the capillary forces.

The differences between the numerical approaches and the experiments are illustrated in figure 3.12b. High errors are observed when the three spheres are in contact. The errors rapidly drop and stabilize as the particle is detached from the others. Both SE and LBM can give acceptable results in this test.

In order to enhance a better comparison between the SE and LBM, we remove the dependency of the contact angle by setting the SE contact angle equal to $\theta = 0^o$ (SE data is taken from Wang et al. (2017)). Figure 3.13a shows the evolution of the capillary force for different inter-particle distances. Good agreement is found between the two numerical approaches, especially, after $D^* > 0.1$

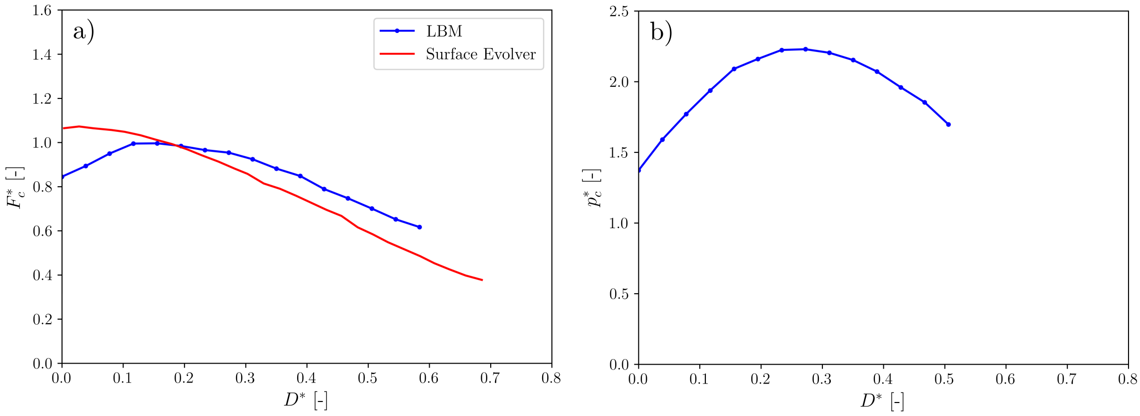

Figure 3.13: Comparison between the experimental results and the numerical approaches for $V^* = 0.2$. The Surface Evolver results have been obtained from Wang et al. (2017). Three spheres of equal diameter in contact are set as initial configuration. One of the spherical grains is progressively displaced from the rest. a) Capillary force acting on the separating sphere is evaluated during the process. b) $p_c^* - D^*$ curve is determined during a LBM simulation.

Finally, figure 3.13b illustrates the variation of capillary pressure with the inter-particle distance.

3.3.2.1.2 Force evaluated under drainage conditions

The present section investigates the effect of decreasing the liquid content of the trimer. Three spheres in contact have been considered to reproduce the test of Wang et al. (2017). Contact angle is set to $\theta = 0^o$ and the initial amount of liquid is $V^* = 0.33$. The initial and final states can be found in figure 2.22.

When $V^* < 0.04$ the trimer is replaced by three un-coalesced pendular bridges as shown in figure 2.22. This configuration is not reached in figure 3.14. Hydrostatic properties were evaluated and tracked until the last stable configuration of the trimer, thus no result is depicted for the three isolated bridges resulting from the trimer decay. Figure 3.14 shows that the liquid content decrease induces a rise of capillary pressure. Besides, the reduction of liquid content results in an increment of the capillary forces.

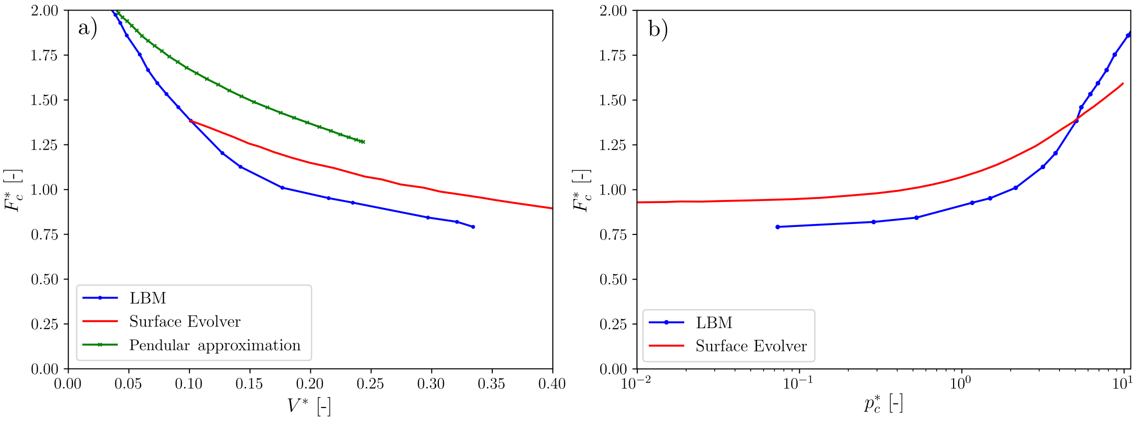

Figure 3.14: a) Liquid volume vs. capillary force for spheres in contact under drainage conditions. Comparison between pendular approximation, LBM and the results for SE obtained in Wang et al. (2017). b) Evolution of capillary force with the suction. Comparison between LBM and the results for SE obtained in Wang et al. (2017) in logarithmic scale

Overall, figure 3.14 displays similar paths for the Surface Evolver and LBM approaches. Yet, the accuracy is lower than the volume-suction curves (see section 2.4.1). The comparison is completed with the pendular approximation based on sections 2.4.1.1 and 3.2.1. According to Wang et al. (2017), the liquid content in a trimer can be divided into three isolated bridges connecting the three spherical bodies (see figure 2.23). Thus, the capillary force acting on each spherical grain is given by the contribution of two capillary bridges. The force of each pendular bridge is based on the equations detailed in 3.2.1. The pendular approximation provides higher capillary forces than LBM and SE for large liquid contents. On the contrary, the pendular approximation converges to the LBM for very small liquid contents ($V^* \approx 0.04$). At this saturation degree, the trimer is reaching an unstable state, such that further liquid volume decrease will cause the trimer decay. Then, the liquid cluster is going to be replaced by 3 isolated pendular bridges (see figure 2.22). Consequently, we suggest that due to the difficulties of distinguishing the clusters that are about to convert from the funicular to the pendular regime, we should rely on numerical methods as long as it is possible.

3.3.2.2 Tetramer case

This section explores the transition from the funicular regime to the pendular state for a group of four spherical grains in terms of capillary forces. The capillary pressure - saturation curves and liquid morphologies studied in section 2.4.2 under drainage conditions are complemented with the present force analysis. To the best of our knowledge, this study is the first to report capillary forces on tetramers (clusters made up of 4 spheres), however, it is worth mentioning that a similar analysis was performed by Grof et al. (2008) to investigate the strength of liquid clusters of 4 circular disks (2D) as function of the liquid saturation.

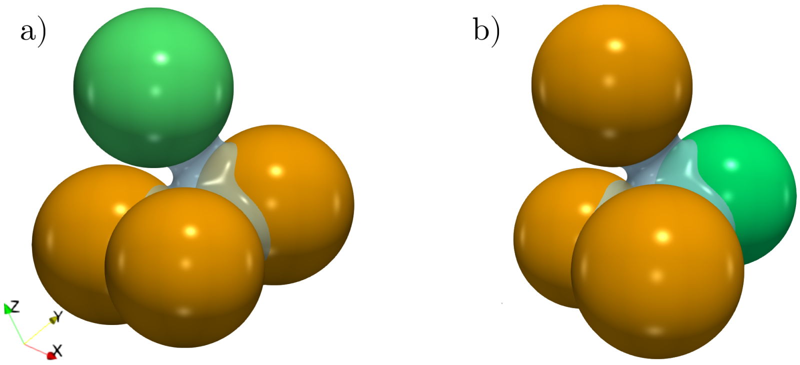

Figure 3.15: Capillary forces are evaluated under drainage conditions on the spherical bodies depicted in green.

The liquid structure is displayed in figure 3.15. In particular, capillary forces are computed exclusively on the spheres depicted in green. The initial state of the simulation corresponds to the capillary state. Therefore, the void space between the spheres is filled with the wetting phase. The image sequence displayed in figure 2.26 shows the transition from capillary regime to the pendular state passing through the funicular regime as the liquid volume is gradually removed.

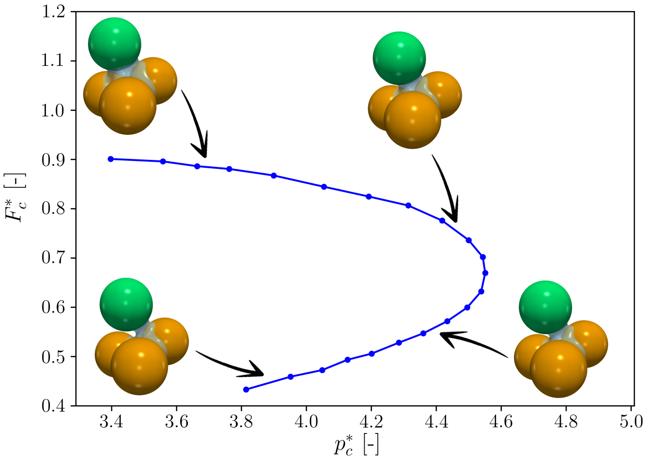

Figure 3.16: Evolution of capillary force with the liquid content under drainage conditions on the green spherical grain of figure 3.15a.

The change of the capillary force induced by the liquid removal is illustrated in figures 3.17a and 3.18b. First, we will focus on the spherical grain depicted in green in figure 3.15a. The capillary force on the solid grain decreases monotonously as the drainage goes on (see figure 3.17a) and gets completely detached from the rest of the cluster when $V^* \approx 0.18$. Capillary forces are decomposed into y- and z-axis in figure 3.17 (coordinates are found in figure 3.15). Additionally, the pressure peak is achieved before entering into the funicular regime ($p_c^* \approx 4.55$) as evidenced in figures 3.16 and 3.17b.

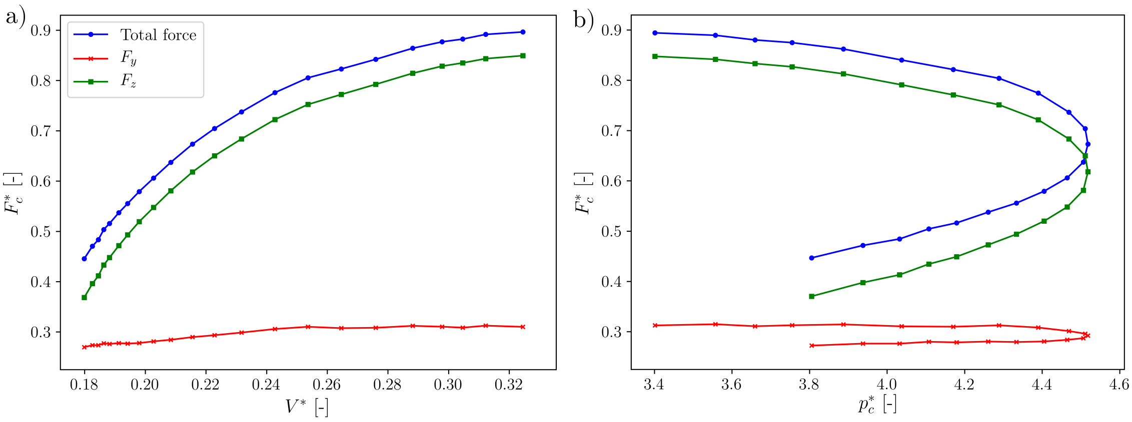

Figure 3.17: Force analysis on the green spherical grain of figure 3.15a. a) Evolution of capillary force with the liquid content under drainage conditions. b) Capillary force vs suction. In both cases, forces have been decomposed into the vertical and horizontal contributions

Now, let's discuss about the capillary force exerted on the green sphere displayed in figure 3.15b. Six states are found in figure 3.18 through the drainage process:

A - Initial state, the cluster is completely filled.

B - Capillary forces build up during the drainage. Capillary force reaches a peak before the detachment between the interface and the solid grain begins.

C - The interface is rapidly displaced during the transition from the tretramer to the trimer. The event results in a capillary force drop. According to the research carried out by Grof et al. (2008), the position and size of the force drop strongly depends on the contact angle. Several configurations adopted by the interface during the transition are reflected in the non-monotonic capillary pressure path of figure 3.18a.

D - The fluid-fluid interface is fully detached from the fourth sphere, the new configuration is a trimer.

E - As drainage continues, the capillary force slowly increases. The interface adopts higher curvature as a consequence of the capillary pressure increment.

F - Another drop in terms of capillary force (much smaller than the previous one though) indicates the transition from the funicular regime to the pendular state. The force has a flat maximum during the pendular regime (similar to the situation observed in figure 3.5 for a single bridge).

One of the most remarkable things that can be inferred from figure 3.18 is that the maximum capillary force is found at the very beginning of the funicular regime. This is when the structure is filled with liquid but the non-wetting phase is about to invade the pore body and modify the liquid morphology to replace the tretramer by a trimer. This is consistent with the findings of Grof et al. (2008) in which a clear maximum located at the capillary/funicular transition was found for a group

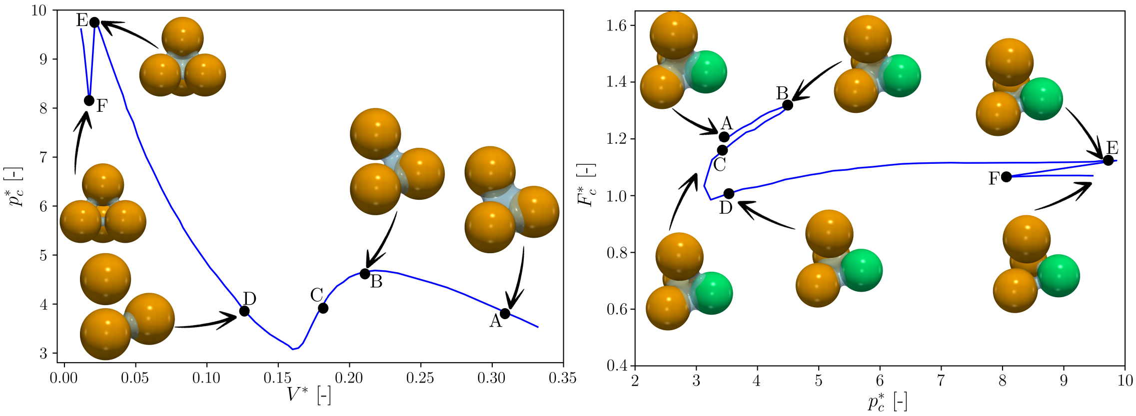

Figure 3.18: Force analysis on the green spherical grain in figure 3.15b. a) Evolution of capillary force with the liquid content under drainage conditions. b) Capillary force vs suction.

of 4 disk particles. Overall, the results show significant similarities with the work performed by Grof et al. (2008). In particular, Grof et al. (2008) results for a 4-disk-packing are not only in good qualitative agreement with figure 3.18 in terms of peak position, but also with the capillary force - liquid content curves.

The fact that the maximum capillary force exerted on the green sphere displayed in figure 3.15b is located between the pendular and the capillary regimes supports the idea introduced by Mitarai and Nori (2006); Richefeu et al. (2016). Both studies observed that in wet granular materials, cohesion increases beyond the coalescence of pendular bridges reaching a maximum during the funicular regime, and decreasing again in the capillary regime. Such hysteresis is qualitatively illustrated in figure 3.10 and 3.19. Indeed, Richefeu et al. (2016) suggests that funicular regime should be split into: primary funicular state, where the capillary bridges merge one another, and secondary funicular state, where the liquid volume percolates and groups of particles become fully immersed. The two states are separated by the cohesion peak (see figure 3.10). The cohesion strength - liquid content curve obtained by Richefeu et al. (2016) for a 2D granular packing evidenced a maximum cohesion at $S_r \approx 0.4$ (slightly after the pendular/funicular transition). It is worth highlighting that Richefeu et al. (2016) simulations were performed by increasing the amount of liquid from an initial pendular state. Conversely, Mitarai and Nori (2006) suggested that cohesive stress - saturation relationship varies significantly in the funicular state, thus, it is impossible to determine the location of the peak without experiments or numerical simulations. Nonetheless, the results of the present work and the conclusion drawn by Grof et al. (2008) show that, under drainage conditions, the maximum capillary strength take place right after the capillary/funicular transition. Such observations reinforce the conclusions asserted by Baltodano-Goulding (2006). In their work, cohesion strength of unsaturated sands was studied as function of the liquid content. Baltodano-Goulding (2006) argued that cohesion has two peak values in the entire range of degree of saturation. The first peak occurring at saturations ranging from $[15\% - 35\%]$. A second peak takes place at about $[50\% - 65\%]$ for the loose sand samples, and $[80\% - 90\%]$ for dense specimens. A conceptual illustration regarding the double-peak behavior is illustrated in figure 3.19.

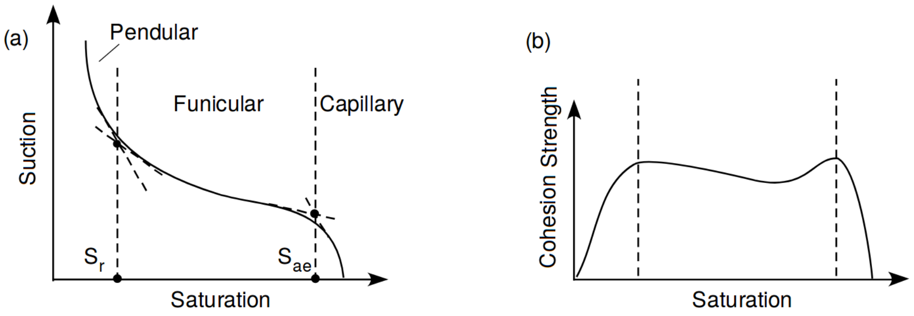

Figure 3.19: Conceptual illustration of soil-liquid retention regimes (a) and cohesive strength - liquid content relationship (b). We have modified the image taken from Baltodano-Goulding (2006).

The analysis of previous works (Wang et al. (2017); Baltodano-Goulding (2006); Richefeu et al. (2016); Mitarai and Nori (2006)) and the results of this thesis suggest that cohesion is maximized during the transition between regimes: pendular/funicular when we increase the liquid content to initially dry grains, and capillary/funicular transition when the saturation is decreased from a fully saturated granular assembly (see figure 3.19). Many factors (i.e. soil properties, boundary conditions, etc) influence the position and magnitude of the two peaks. Therefore, different hydro-mechanical behaviors are expected and found in previous literature (double-peak behavior in Baltodano-Goulding (2006); Lu et al. (2007) or single peak in Richefeu et al. (2016); Grof et al. (2008)).

In this context, it is worth mentioning the work of Yuan et al. (2018). They examined the link between the effective stress and the contact stress in partial saturated soils. Contact stress were obtained averaging micromechanical quantities and found extremely close to the effective stress. In recent years, it is common to assume $\chi_B = S_w$, thus, capillary action is due to the term $S_w p_c$ of Bishop's expression (see Eq. 1.14). According to Yuan et al. (2018), the unique relationship between χ_B and S_w may describe the macroscopic behavior in terms of the $p_c - S_w$ curve (thus, on the system geometry) and the saturation changes in porous media (drainage and/or imbibition).

3.4 Conclusion

In this study, capillary forces were investigated during the pendular and funicular regime. Lattice Boltzmann simulations were performed using the Shan-Chen multiphase model. We developed a method to evaluate the forces acting on solid objects in contact with two or more fluids. Our approach is based on the integration of stresses around the solid bodies. The volume element used for the integration is slightly larger than the solid object, thereby, we overcome the difficulties associated with the non-physical numerical film around the solid boundary.

This method is validated by the theoretical solution given by Young-Laplace equation for a pendular bridge. Plus, the sensitivity of the mesh resolution and the orientation of the mesh have been tested. LBM simulations are also contrasted with the theoretical solution during the drainage of the liquid bridge. Fairly good agreement is found between LBM and the theoretical solution. Nevertheless, capillary forces become inaccurate for significant low liquid volumes. Such scenario corresponds to liquid configurations with narrow liquid bridges close to the rupture point. At this stage, spurious velocities present in the fluid-fluid interface have a non negligible influence in the capillary force leading to inaccurate results.

The method presented in this chapter complements the mesh sensitivity analysis performed in sections 2.3.2.2 and 2.3.3.4. The global analysis depicted in figure 3.9 implies that reasoning in terms of curvature is a key point to choose the mesh resolution. Unfortunately, the complex and heterogeneous geometry inherent in porous media hinders the implementation of a curvature criterion. The analysis illustrated in figure 3.9 also shows that accuracy of capillary forces is strongly influenced by the mesh resolution (at least, more than other parameters such as the liquid content and curvature).

The work extends the research carried out by Wang et al. (2017). The good agreement between the LBM results, the theoretical solutions and the experiments leads to the conclusion that our simulations are able to evaluate the capillary forces with similar accuracy as the models based on energy minimization. We believe LBM simulations are better suited for complex liquid morphologies and dynamic states than Surface Evolver, however the high computational cost associated with LBM may restrict its applicability. Thus, further studies in this direction are needed to distinguish the field of application for each numerical approach. The discrepancies become significant when the liquid volume is low and trimers approach the breaking point. Unfortunately, experimental data are lacking to contrast the numerical results on drainage tests. Furthermore, the pendular approximation is also presented in this chapter. Such approximation can be used when the computational resources are limited.

The results obtained for the tretramer case in terms of capillary force support the idea of previous research that the highest cohesion values take place during the regime transitions. The evolution of capillary forces exerted on the particles at the pore scale might explain the global response of wet granular materials since similar behavior at the macro-scale has been reported in literature. Notwithstanding the previous findings, the dependence of the cohesive force is strongly influenced by the separation distance between the solid particles. Therefore, we recommend further analysis on a wide a range of liquid saturations and separation distances for similar microstructures (groups of 4 solid spheres). The position and magnitude of the cohesion peak should also be studied in granular assemblies with different geometric characteristics (dependence on particle size distribution, void ratio, etc). Additionally, cohesion - saturation curves should be performed under different conditions in order to have better insight on the qualitative analysis summarized in figure 3.19.

Chapter 4

A 2D Throat-Network model for three-phase flow in porous media

4.1 Introduction

The Throat-Network (TN) approach of the present chapter offers an accurate description of the geometry of the pore space and the evolution of the menisci in 2D. In this work, fluid flow is governed by capillary and viscous forces. Diffusion effects and gravity are neglected. Numerous articles have already studied multiphase flow controlled by capillarity (Bakke et al. (1997); Hilpert and Miller (2001)). Nonetheless, the geometrical simplifications of the complex nature may hinder the description of the phenomena. Plus, some works with 3D pore networks (Gao et al. (2012)) opted to remove the isolated liquid structures (trimer, pentamer and other clusters) as they are prone to numerical error. In order to overcome the difficulties related to geometrical idealization, we propose a numerical model in 2D based on analytical solutions and a network extracted from the pore geometry as detailed in Gladkikh and Bryant (2005); Yuan et al. (2016). Additionally, the present approach emphasizes the importance of simulating at the meniscus/throat scale (rather than the pore body scale) to avoid the limitations associated to imbibition in porous media (Vogel et al. (2005); Patzek et al. (2000)).

Overall, this work aims to set a preliminary study for the attainment of a numerical model with a better prediction of multiphase displacement through porous media. Thus, this chapter acts as a proof of concept for upcoming hybrid models based on pore-network approaches and semi-analytical expressions (Chareyre et al. (2017)). The accuracy of the model is tested with the results provided by a multicomponent Shan-Chen lattice Boltzmann method (Shan and Chen (1993)).

4.2 Throat-Network model based on analytical solutions

Following the idea of Blunt et al. (2002); Sinha and Wang (2007), the present model evaluates the position of the fluid-fluid interface by means of Young-Laplace equation and the pressure field in the network. Two immiscible phases are considered

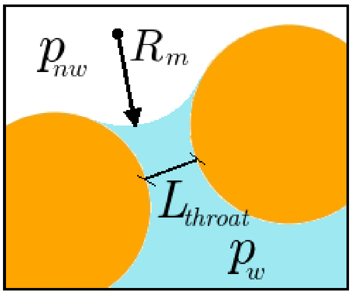

Figure 4.1: According to the Young-Laplace equation (Eq. 4.2), the pressure jump $(p^{nw} - p^w)$ across a fluid-fluid interface is proportional to the product of the surface tension and the curvature of the interface $\left(k = \frac{1}{R_m}\right)$.

(typically air and water). Plus, conservation of mass is assumed within each pore body.

4.2.1 Pore-scale decomposition

Pore bodies and throats are studied after a decomposition of the pore space (as presented in Chareyre et al. (2012)). A regular triangulation is considered to represent the topology of the pore space (Helba et al. (1992); Thompson and Fogler (1997); Bryant and Johnson (2003)). In this particular case, the three vertices of the triangle correspond to the three particle centers. This scheme is adopted because the domain is divided into nearest-neighbor groups of three disks. In a dense particle packing, each group defines a pore body. Moreover, two adjacent cells result in a connecting pore throat (see figure 4.2). Hence, this decomposition leads to a throat network model where geometric features are well represented.

4.2.2 Governing equations

According to the Young-Laplace equation (Blunt et al. (2002); Young et al. (1805)), the pressure jump across a fluid-fluid interface is proportional to product of the surface tension and the curvature of the interface (see figure 4.1):

$$p_c = p^{nw} - p^w = \gamma \left(\frac{1}{R_1} + \frac{1}{R_2} \right) \tag{4.1}$$

where p_c is the capillary pressure, p^{nw} and p^w are the non-wetting phase and wetting phase pressures respectively, γ is the surface tension, and R_1 and R_2 are the principal radii of curvature. Since our research is limited to 2D, we adopt the following Young-Laplace expression:

$$p_c = p^{nw} - p^w = \gamma \frac{1}{R_m} cos\theta \tag{4.2}$$

where θ is the contact angle and R_m is the radius of the meniscus. From now on, we assume a contact angle of $\theta \approx 0$, yet the model can be trivially extended to $\theta \neq 0$.

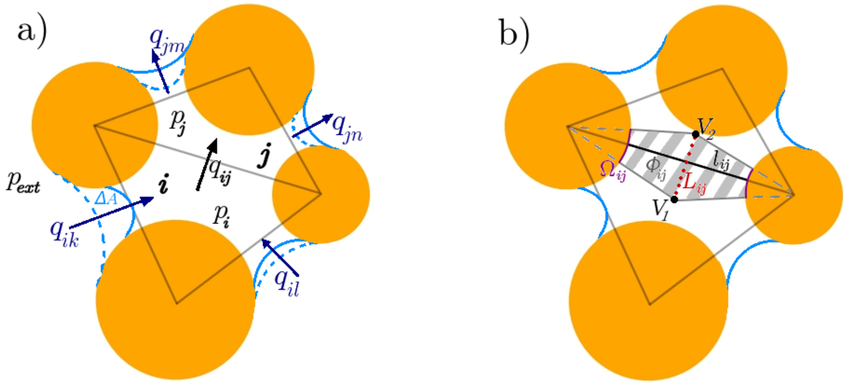

Figure 4.2: a) Triangular elements after the decomposition. q_{ij} is the flux between pore bodies i and j. Fluid interface at time t is displayed with a dashed line. At time $t+\Delta t$ the flow towards element j leads to a new configuration depicted with a continuous line. b) Geometrical quantities of a pore throat following the steps of Chareyre et al. (2012).

During the interface displacement due to suction, p_c is increased and the radii of menisci are reduced according to Eq. 4.2. The non-wetting phase starts invading the pore body when the diameter of the meniscus is equal to the length of the pore throat (the minimum distance between two solid bodies), i.e. $2 \cdot R_m = L_{throat}$, see figure 4.1 for a graphical explanation. At this moment, the corresponding capillary pressure is called entry capillary pressure:

$$p_c^e = \frac{2\gamma}{L_{throat}} \tag{4.3}$$

In reality (a three-dimensional space), fluid displacement is rather complex to be simulated due to the difficulties to determine the entry pressure p_c^e. Indeed, p_c^e is usually found after some simplifications. Haines (1927) proposed that entry pressure is inversely proportional to the radius of a sphere that is in contact with the particles that define the pore. Recent research (Yuan et al. (2016)) based on the MS-P method Mayer and Stowe (1965); Princen (1969) assumes that entry pressure p_c^e corresponds to a cylindrical throat of infinite length tangent to the solid particles at the narrowest cross section. Regarding the 2D simulations, the complexity of the problem is conveniently reduced. Three-dimensional problems can be simplified into 2D in particular cases such as the study of flow perpendicular to random cylindrical rods (Saito and De Lemos (2005)) or the evaluation of permeability in fibrous porous media (Spaid and Phelan Jr (1997)).

For the sake of simplicity, we consider samples with incompressible fluids and static particles. Thus, Eq. 1.19 presented in section 1.3.4.3.1 becomes:

$$\sum_{j=1}^{3} q_{ij} = 0 \tag{4.4}$$

where q_{ij} is the flux between pore bodies i and j (see figure 4.2a).

Moreover, as introduced in section 1.3.4.3.1, the flux q_{ij} can be expressed, at low Reynolds numbers, in terms of an inter-pore gradient:

$$q_{ij} = g_{ij}\frac{p_i - p_j}{L_{ij}} \tag{4.5}$$

where $p_i - p_j$ is the pressure difference between two adjacent cells, L_{ij} is the length of the pore throat defined as the distance between the Voronoi vertices (the Voronoi diagram is dual to the Delaunay triangulation), and g_{ij} is the local conductance that can be evaluated as:

$$g_{ij} = \chi\frac{l_{ij}{R^h_{ij}}^2}{\mu} \tag{4.6}$$

where l_{ij} is the length of the aperture of the throat, μ is the fluid dynamic viscosity, R^h_{ij} is the hydraulic radius of the pore defined as $R^h_{ij} = \dfrac{\phi_{ij}}{\Omega_{ij}}$ (ϕ_{ij} is the shaded area occupied by the fluid in figure 4.2b and Ω_{ij} the perimeter of solid-fluid interface displayed in figure 4.2b), and χ is the non-dimensional conductance factor, which will be assumed equal to 0.5 as in Chareyre et al. (2012). See figure 4.2b to have a better idea of the geometrical quantities. Essentially, Eq. 4.6 has been adjusted from Eq. 1.21 to handle the parameters in a 2D framework.

4.2.3 Boundary conditions

Eq. 4.5 is modified for those throats connecting a filled and an empty pore body, in other words, the pore throats that include a fluid-fluid interface (from now on, they will be called ”open” throats). In this particular case, expression Eq. 4.5 is replaced by:

$$q_{i,ext} = g_{i,ext}\frac{p_{ext} - p_i + p_c}{L_{i,ext}} \tag{4.7}$$

In order to mimic the displacement of the interface, a source or a sink is introduced in Eq. 4.4:

$$\sum_{j=1}^{3} q_{ij} = \Theta \tag{4.8}$$

where Θ adopts positive values for imbibition or condensation processes and negative values for drainage and evaporation. If $\Theta = 0$, no source is taken into account.

To conclude the set of boundary conditions, a fixed external pressure (p_{ext}) is imposed in the non-wetting reservoir.

4.2.4 Multiphase algorithm

Following the steps of Bakke et al. (1997) and Sinha and Wang (2007), we can determine the pressure field of our network after solving the following set of linear equations:

$$\mathbf{QP} = \mathbf{f} \tag{4.9}$$

where **Q** is a sparse matrix including the information of the conductivities, **P** is the matrix containing the pressure values of the triangular cells (**P** is unknown) and **f** represents the sources and/or sinks. The internal values of **f** are only non-zero for the interface throats in which a source or a sink is fixed.

Independently of having a ”source” or a ”sink”, the following procedure is carried out for each time step:

1. The pressure field is determined after solving Eq. 4.9. Each cell has a certain pressure.
2. Capillary pressure, p_c, is computed for all the interfaces (thus, the ”open” throats). If p_c achieves the entry pressure ($p_c = p_c^e$) the fluid penetrates the throat and begins invading the cell.
3. Fluxes are evaluated with Eq. 4.5 and 4.7 for each throat.
4. The position of the interface is found as function of the capillary pressure. The radius of the meniscus is found following Eq. 4.2, hence, $R_m = \dfrac{\gamma}{p_c}$. The interface corresponds to the arc of circle tangent to the two disks that form the throat.
5. The mechanism is repeated for each time step.

4.2.4.1 Local rules

During the drainage or imbibition process, the radii of the menisci increase or decrease as a consequence of the fluid redistribution. Several local rules have been taken into account to reproduce the motion of multiphase flow:

- Once the non-wetting phase breaks through a throat ($p_c = p_c^e$), the radius of the meniscus quickly build up to keep the flow that invades the cell. This phenomenon is called Haines jump (Haines (1930)) and it’s rather unstable. Even though quasi-static approaches are frequently adopted in this chapter, the geometric configuration of the porous media leads to several dynamic events. Indeed, as the capillary pressure increases, fluid-fluid interfaces are displaced towards the narrow throats. After achieving the entry capillary pressure, the non-wetting phase rapidly invades the wide pore space. Such invasion results into a pressure drop associated to the quick change of meniscus curvature. This phenomenon is illustrated in the image sequence of figure 4.4.
- Isolated liquid bridges or clusters can form during drainage, this phenomenon is well described in the model as shown in figure 4.4d. Liquid bridges are treated as disconnected structures that can also increase or decrease their volume if they are under condensation/evaporation. The interface of the bridges is updated according to the mean value of capillary pressure and Eq. 4.2. This feature can be optionally turned off if we consider that clusters are isolated and liquid mass is unaltered.

- During the invasion of a cell, a meniscus splits into two menisci when the interface gets in contact with a solid object (see sequence between figures 4.4a and 4.4b). Mass is conserved during the whole process.

- Likewise, two menisci can merge into a single meniscus if there is a contact point between the two interfaces (see figure 4.7).

4.2.5 Hydro-mechanical Throat-Network coupled model for partially saturated porous media (TN-DEM)

In this section, we propose a hydro-mechanical coupling between the Throat-Network model and the Discrete Element Method, termed as "TN-DEM". After solving the fluid forces on the solid phase as shown in Eq. 1.24, the DEM can be employed to reproduce the mechanical response of the solid grains. DEM was proposed originally by Cundall and Strack (1979) and has become a popular tool in the study of granular media.

In this chapter, the solid particles are idealized as disks interacting with each other. Each particle k is identified by its radius R_k, mass m_k and rotational inertia I_k. Particle motion is described by Newton's second law. Thus:

$$m_k \frac{\mathbf{du_k}}{dt} = \mathbf{F_k^c} + \mathbf{F_k^g} + \mathbf{F_k^f} \tag{4.10}$$

where $\mathbf{u_k}$ is the translational velocity of particle k, $\mathbf{F_k^c}$ is the contribution of the contact forces, $\mathbf{F_k^g}$ is the gravitational force and $\mathbf{F_k^f}$ is the fluid force acting on the solid grain (computed using Eq. 1.24).

This work is based on a linear contact model, in which the force-displacement relationship between two solid bodies is represented by linear springs. The relationship is defined by the normal and shear stiffness, k_n and k_t, respectively, and an inter-particle friction angle ϕ_c.

The normal forces $\mathbf{F_n}$ are directly computed from the relative normal displacement δ_c between each pair of particles (see figure 4.3a):

$$\mathbf{F_n} = F_n\mathbf{n} = k_n \delta_c \mathbf{n} \tag{4.11}$$

As illustrated in figure 4.3a, particles in contact are allowed to overlap among each other. Such overlap reflects the deformation near the contact.

Concerning the tangential component, $\mathbf{F_s}$ is computed at each time step as function of the increment of tangential relative displacement Δu_s:

$$\Delta\mathbf{F_s} = F_s\mathbf{t} = k_t \Delta u_s \mathbf{t} \quad \rightarrow \quad \mathbf{F_s}^{(t)} = \mathbf{F_s}^{(t-\Delta t)} + \Delta\mathbf{F_s}^{(t)} \tag{4.12}$$

The normal stiffness can be expressed in terms of the bulk modulus of the numerical assembly and the radius of the interacting particles:

$$k_n = 2E \cdot \frac{R_A \cdot R_B}{R_A + R_B} \tag{4.13}$$

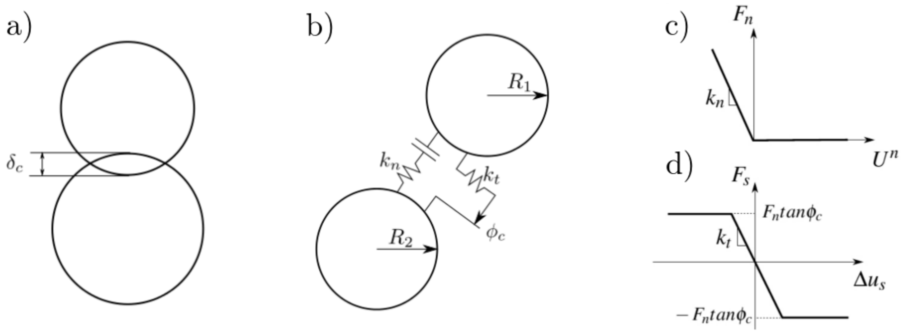

Figure 4.3: (a) Definition of normal particle displacement. (b) Normal and shear stiffnesses at contacts. Schemes of elastic-plastic contact model: Normal (c) and tangential (d) interaction law. Images taken from (Catalano, 2012; Yuan, 2016).

The shear stiffness is defined as function of k_n and a dimensionless parameter a related to the Poisson's ratio:

$$k_t = a k_n \tag{4.14}$$

The shear strength follows the Coulomb friction law. We denote $\mathbf{F_s}$ as the upper limit of the tangential force, then, tangent sliding occurs when:

$$\| \mathbf{F}_s \| > \mathbf{F}_n tan\phi_c \tag{4.15}$$

The implementation of the TN-DEM model is based on the open-source code "Yet Another Dynamical Engine" (YADE) platform (Šmilauer and Chareyre (2010)). YADE has been employed for particle-fluid coupling (Chareyre et al. (2012); Lominé et al. (2013)), analysis of soil-structure interaction (Effeindzourou et al. (2016)), FEM-DEM coupling (Guo and Zhao (2014)), etc.

4.3 Results

Several examples are illustrated in this section in order to validate the accuracy of the model and the ability to track the motion of fluid-fluid interfaces.

Hereinafter, results will be presented in terms of the following dimensionless variables:

- Volume: $V^* = \dfrac{V(t)}{V_o}$, where $V(t)$ is the volume at time t and V_o is the initial volume.
- Capillary pressure: $p_c^* = \dfrac{p_c R}{\gamma}$, where γ is the surface tension and R is the average disk radius. p_c is the average capillary pressure, hence, $p_c = p_{ext} - \dfrac{1}{N}\sum_{j=1}^{N} p_j$, where N is the number of cells.
- Coordinates: $x^* = \dfrac{x}{R}$ and $y^* = \dfrac{y}{R}$, where x and y are the coordinates and R is the average disk radius.

4.3.1 Slow drainage

This scenario considers a quasi-static drainage of an isolated cluster (see figure 4.4) with very low capillary number ($Ca = 5 \cdot 10^{-6}$). The wetting phase is gradually removed from the meniscus located in the throat formed by particles B and C. We have divided the dying process into 4 points to highlight the main characteristics throughout the drainage process:

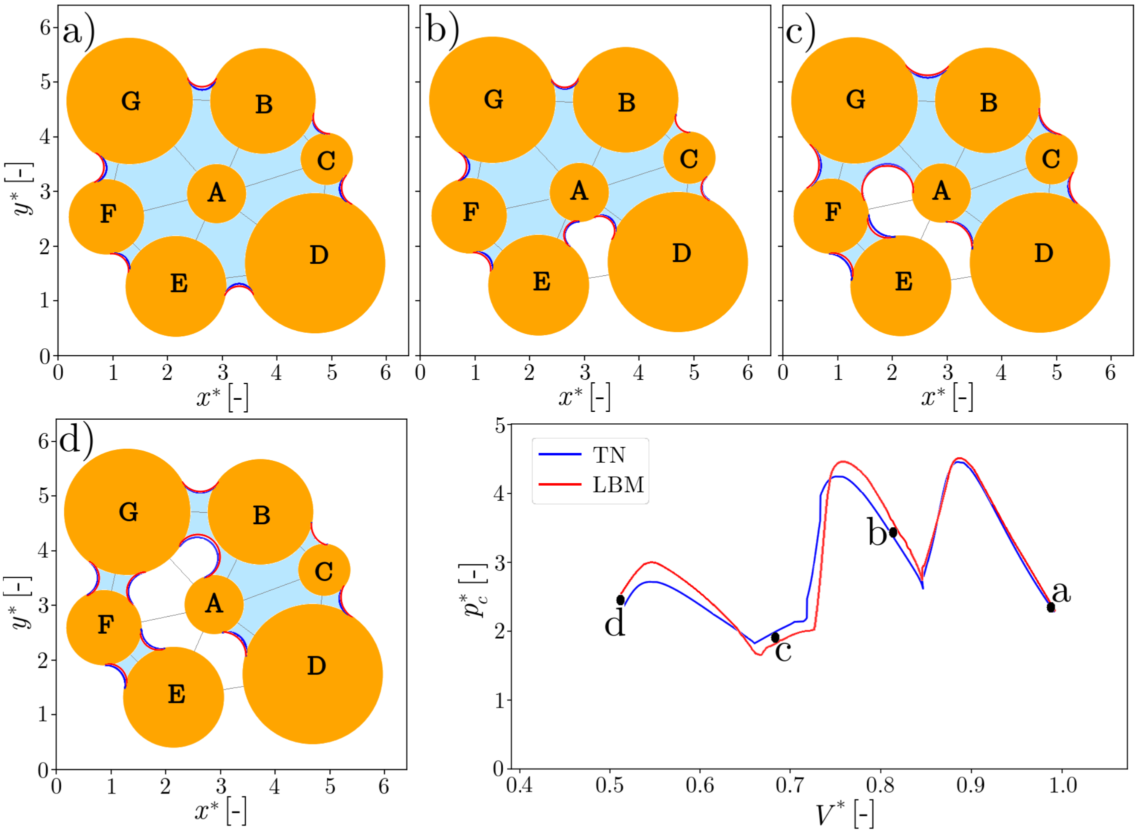

Figure 4.4: Comparison of interface position and saturation curve between LBM and TN models. Quasi-static drainage is assumed. Various liquid contents are displayed: a) $V^* = 0.98$, b) $V^* = 0.81$, c) $V^* = 0.69$ and d) $V^* = 0.51$.

- a) An isolated liquid cluster made up of 6 disks of different diameter is the starting point. The system is in equilibrium and fully saturated. The initial geometric configuration and the starting point of the saturation curve are displayed in figure 4.4a.

- b) Capillary pressure is slowly increased to guarantee quasi-static conditions, hence, according to Eq. 4.2, the meniscus radii are reduced. Once the entry pressure is achieved $\left(p_c = \dfrac{\gamma}{R_m} = \dfrac{2\gamma}{L_{throat}} = p_c^e\right)$, the non-wetting phase penetrates the pore body (see figure 4.4b). The throat between particles E and D is the widest one, thus, the one with lower entry pressure and the first to be invaded. The instant before the invasion of pore throat D-E corresponds to the peak displayed on the saturation curve of figure 4.4b. Then, a sudden dynamic jump is observed, this phenomenon was mention before, referred as Haines jump. At this stage, fluid motion is considered dynamic and the quasi-static conditions imposed during drainage are no longer fulfilled. The fast invasion of the pore (see transition between points "a" and "b" in figure 4.4) results into a pressure drop (see the saturation curve of figure 4.4), consequently, the rest of the "open" pore throats are refilled to keep the volume constant. Finally, the meniscus touches a solid surface (disk A) splitting into two menisci that have the same curvature. At this moment, throat D-E is considered "empty". Besides, throats A-E and A-D become "open" throats. Once the dynamic event is over, capillary pressure starts building up again in order to continue the drainage process under quasi-static conditions (see the increasing path after point "b" in the $p_c^* - V^*$ curve of figure 4.4).

- c) The non-wetting phase keeps invading the cluster (see figure 4.4c). After the invasion of throat D-E, the widest "open" throat is the one between particles A and E (even though it might not be visible to the plain eye). Therefore, throat A-E is the next to be invaded. During the process we observe almost a perfect match between the interface obtained with the TN and LBM models. Regarding the saturation curve, very similar paths are found using the two different models.

- d) By the end of the drainage process (see figure 4.4d), two pendular bridges (E - F and F - G) and a small cluster remain present and disconnected. Results obtained with the Throat-Network model are in good agreement with the lattice Boltzmann simulations.

4.3.2 Fast drainage

In this example, the same configuration as in subsection 4.3.1 is assumed, however, in this scenario the suction rate is increased. Therefore, we proceed to quickly drain the liquid content ($Ca = 5 \cdot 10^{-3}$). The liquid phase is removed from the meniscus of the throat formed by particles B and C with a higher suction rate than subsection 4.3.1.

As evidenced in figure 4.5a, the non-wetting phase penetrates through throat D-E as in the previous subsection 4.3.1. In contrast, after the first invasion, non-wetting phase does not follow the same path (see figure 4.5b). Due to the viscous effects, a significant pressure gradient is found between the adjacent triangle of throat A-D. Despite the fact that throat A-E has a lower entry pressure than A-D, the capillary pressure achieves higher values in throat A-D than throat A-E. Consequently, the non-wetting phase flows through throat A-D.

Regarding the accuracy of the TN model, we observe that results are consistent with the LBM simulations even though saturation curves are not as close as they were in the quasi-static regime.

A relevant feature observed in figure 4.5b is the non-constant curvature of the meniscus of throat A-D obtained with LBM. The strong pressure gradient is the driving force that leads to a dynamic displacement of the interface. On the contrary, all the menisci provided by the Throat-Network model correspond to circular arcs. In

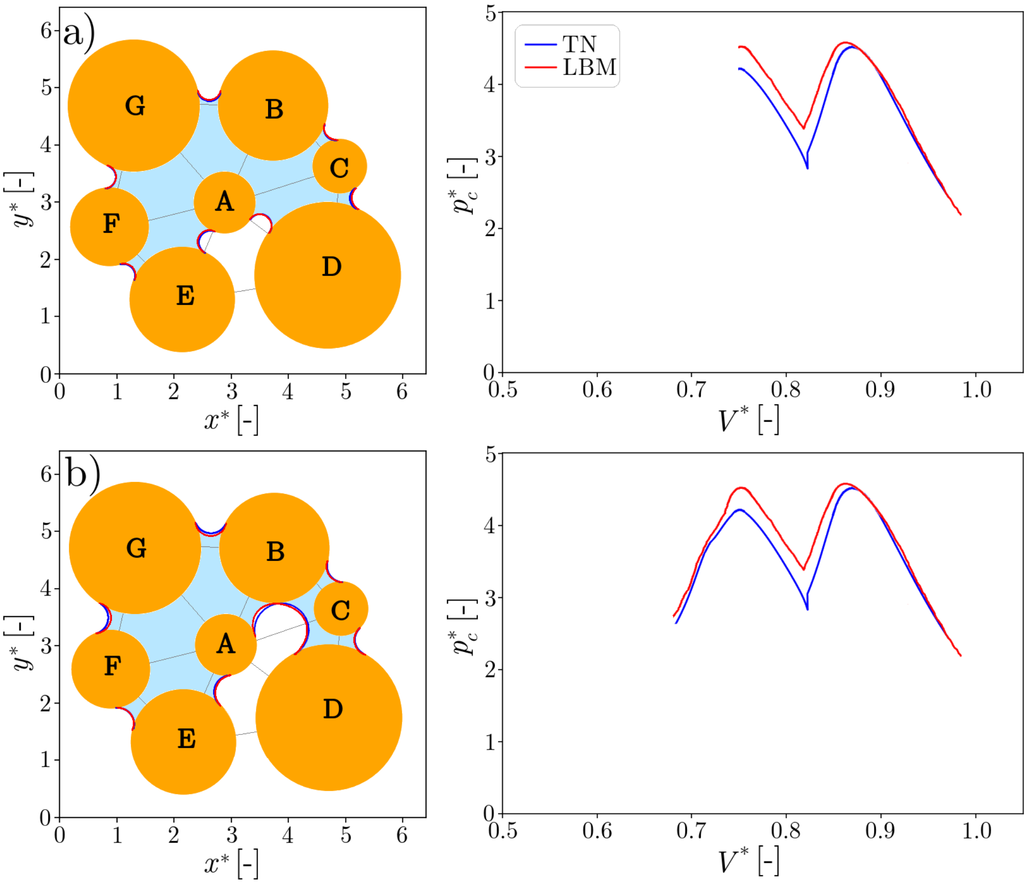

Figure 4.5: Comparison of interface position and saturation curve between LBM and TN models. Fast drainage is considered. Various liquid contents are displayed: a) $V^* = 0.75$ and b) $V^* = 0.68$.

spite of the non-circular menisci obtained with LBM, the TN interfaces follow almost the same path and very few differences are observed. In contrast of subsection 4.3.1, the viscous forces play an important role in the fast drainage situation. Thus, menisci adopt a wider range of radius. Even though there is a slight mismatch between some interfaces, we consider that the TN model is able to mimic the menisci interfaces realistically under more dynamic conditions.

The peaks observed in the saturation curve correspond to the non-wetting phase invasions of throats E-D and A-D. It is worth noting that the first peak is almost coincident with the one obtained under quasi-static conditions. A non-negligible difference is observed between LBM and TN model saturation curves in the lowest point between the peaks. The approximation in Eq. 4.6 is the main reason of the mismatching and it hinders the evaluation of the fluid motion. Notwithstanding these difficulties, the TN model is still able to reproduce the dynamic behavior.

Figure 4.6 illustrates the pressure gradient inside the cluster. The column on the left displays the evolution of the pressure field according to the TN model. On the right, the discrepancies between the pressure field obtained with the LBM and the TN are depicted as $\dfrac{p^*_{c,LB} - p^*_{c,TN}}{p^*_{LB,max} - p^*_{LB,min}} \cdot 100$, where $p^*_{LB,max}$ and $p^*_{LB,min}$ are,

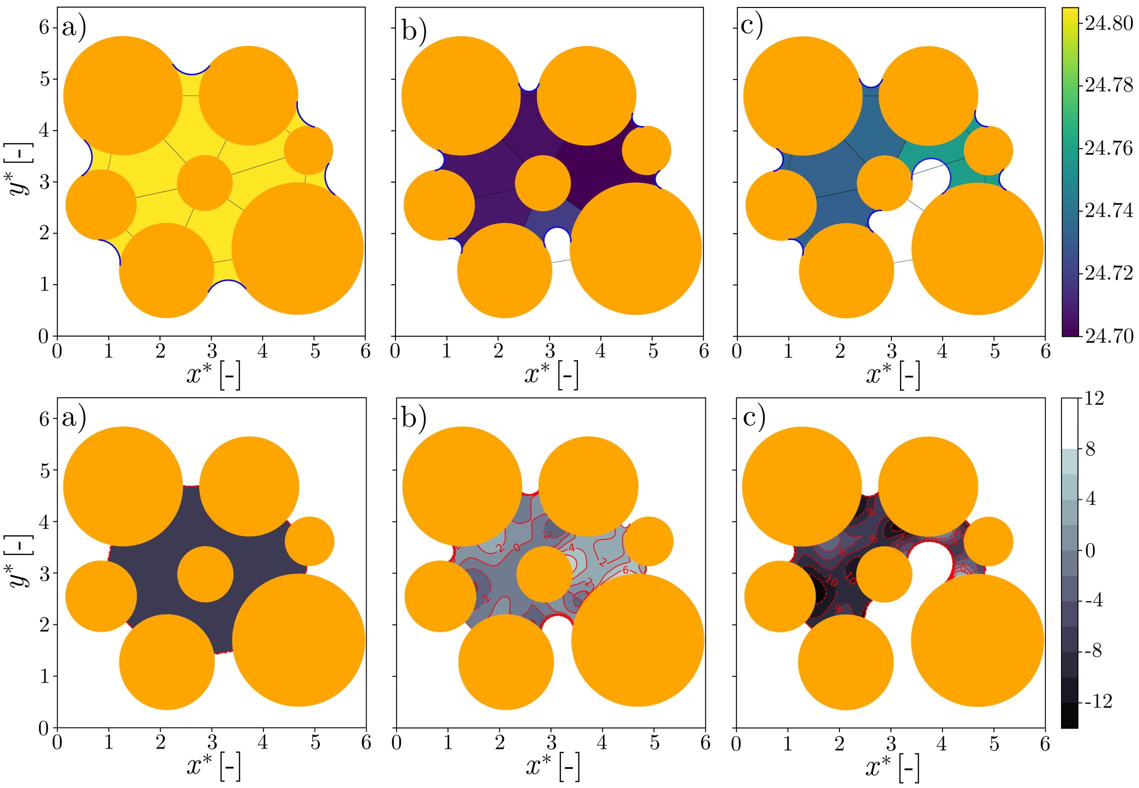

Figure 4.6: Evolution of pressure field during a fast drainage. On the top row, the pressure in each cell obtained with the TN model. At the bottom row, the difference in terms of pressure between LBM and TN models. Various liquid contents are displayed: a) $V^* = 1.00$, b) $V^* = 0.86$, and c) $V^* = 0.72$.

respectively, the maximum and minimum capillary pressure obtained with LBM. At the beginning of the simulation, no significant pressure differences are observed as shown in figure 4.6a. Figure 4.6b displays the fluid configuration and pressure field at the beginning of the invasion of the first pore throat (throat D-E). We point out the low pressure values (dark colors are observed on the left of figure 4.6b) as a consequence of the high capillary pressure (see the first peak of the saturation curve in figure 4.5). Moreover, the bottom row of figure 4.6b evidences a nearly negligible error between the LBM and the TN pressure fields. Finally, the pressure gradient becomes more visible in figure 4.6c after the invasion of the second throat (throat A-D). The negative values observed at the bottom of figure 4.6c suggest that TN model tends to overestimate the pressure field. Nonetheless, figure 4.6 shows the error is considerably low during the drainage process, therefore, the TN model is suitable to study the pressure field.

4.3.3 Imbibition of a macropore

This section illustrates a typical phenomenon observed in porous media: coalescence. Isolated or trapped clusters usually merge/coalesce during imbibition. More particularly, we simulate a macropore under imbibition conditions. The flux is imposed on the interfaces so that capillary pressure decreases. Therefore, menisci get larger and merge once they touch other menisci (see figure 4.7). The number of menisci is reduced (as the radii increase) until the macropore is almost fully saturated (see figure 4.7c).

Except for very few cases, menisci curvature decrease (interfaces move towards wider pore spaces). Thus, quasi-static conditions are assured throughout the simulation. The lack of dynamic events leads to an almost perfect match between LBM and TN profiles (see figure 4.7). It should be underlined that capillary pressure - saturation curves (see figure 4.7) are also in good agreement, however, slight discrepancies are noticed at the small pressure drops. Those jumps correspond to minor Haines' events that occur when the wetting phase passes through the throat and starts occupying a wider space. Only a few of Haines jumps take place during the imbibition macropore, thus, dynamic effects are insignificant compared to the ones observed in previous sections 4.3.1 and 4.3.2. Additionally, figure 4.7 underscores the fact that $p_c - V^*$ relationship gets smoother (due to the lower menisci curvatures) as the wetting phase fills the macropore. Overall, LBM and TN results are coincident, suggesting that TN is capable to reproduce the coalescence mechanism.

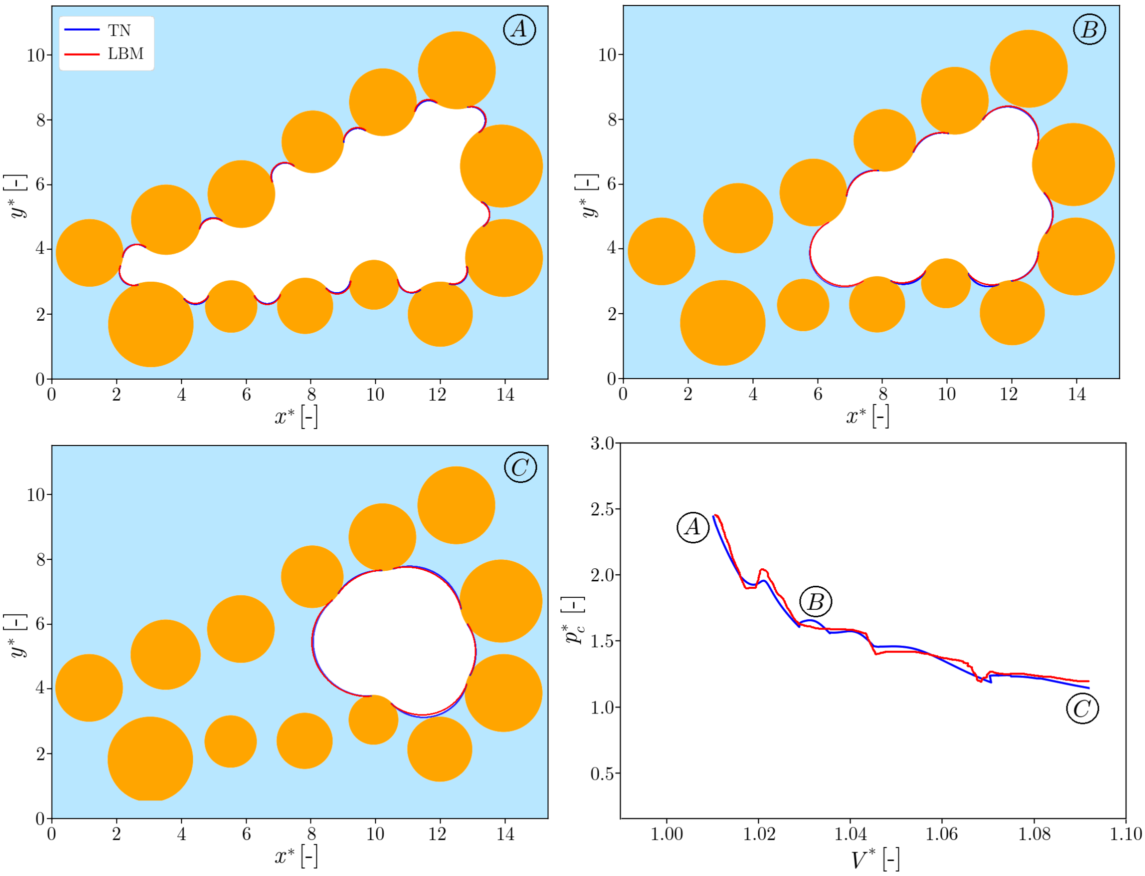

Figure 4.7: Comparison of interface position between LBM and TN models. The capillary pressure is deliberately reduced to force the imbibition of the macropore. The menisci begin merging with other menisci as they increase the radii. Gradually, the system is getting more saturated. Various liquid contents are displayed: Ⓐ $V^* = 1.01$, Ⓑ $V^* = 1.03$ and Ⓒ $V^* = 1.09$.

4.3.4 Pore refillig

The present section aims to reproduce the "pore refilling" mechanism. As we mention in the previous examples, the motion of the fluid-fluid interface from a narrow throat to a wide pore body results into a Haines jump, and subsequently, to a quick fluid redistribution. Technically, a strong dynamic event could lead to the refilling of a pore throat that was already empty. In order to mimic this phenomenon, we have adopted the disk configuration displayed in figure 4.8. Quasi-static conditions have been assumed to ensure drainage kinetics. The most remarkable events during the drainage processa are listed below:

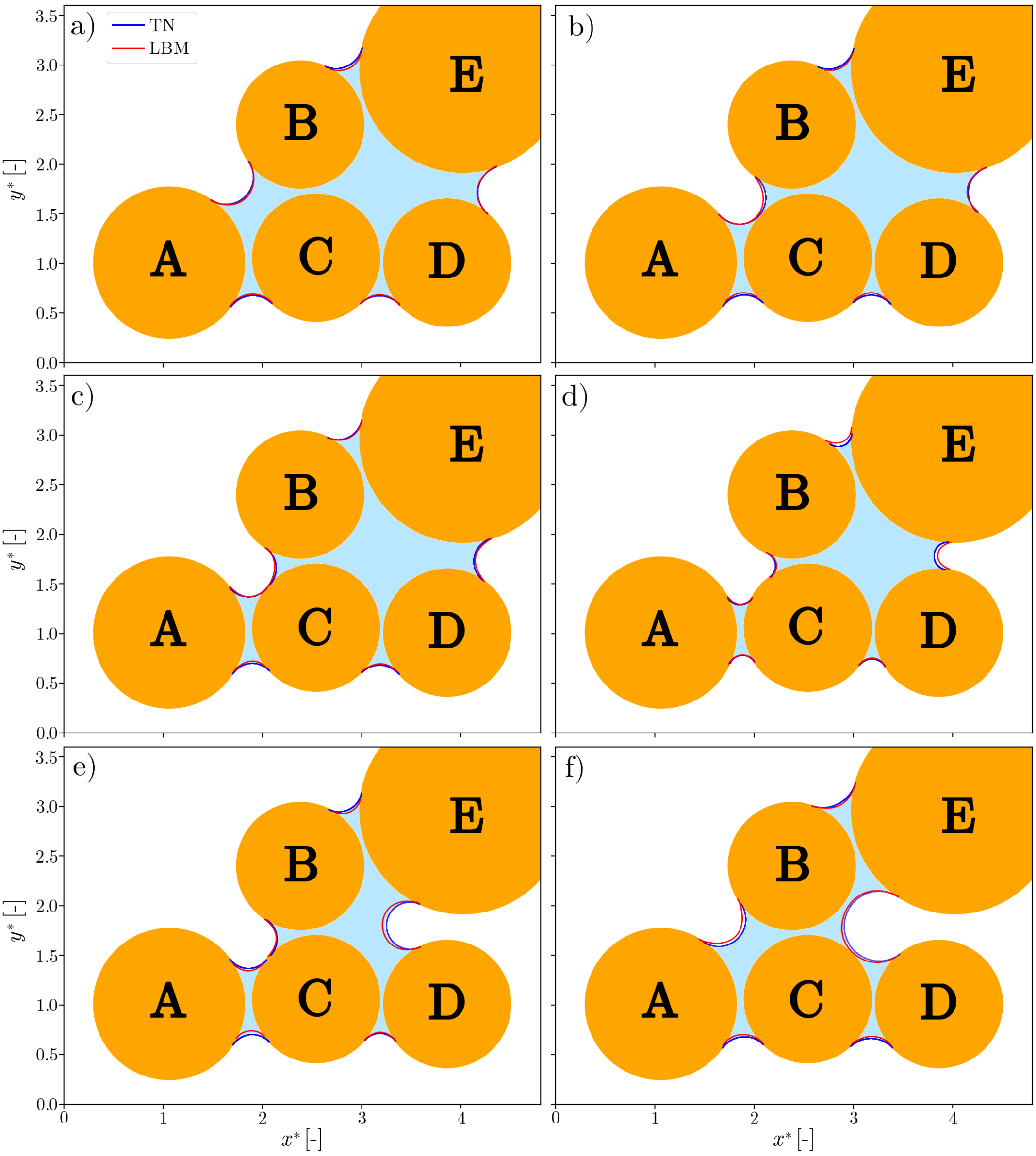

Figure 4.8: Comparison of interface position between LBM and TN models. Various liquid contents are displayed: a) $V^* = 0.97$, b) $V^* = 0.82$, c) $V^* = 0.80$, d) $V^* = 0.69$, e) $V^* = 0.58$ and f) $V^* = 0.54$.

- a) The 5-disk assembly is initially fully saturated as shown in figure 4.8a.
- b) The non-wetting phase penetrates through throat A-B. The A-B meniscus slightly grows until it encounters disk C. Figure 4.8b evidences that cell ABC is not much wider than throat A-B. Consequently, capillary pressure is marginally reduced (no relevant pressure drop is observed) after reaching the entry capillary pressure of throat A-B (see figure 4.9).
- c) A-B meniscus splits into two menisci when reaches disk C. The new configuration is a cluster formed of 4 disks (B-C-D-E) and an isolated bridge (A-C). The advance of the interface continues while capillary pressure is increased (see figure 4.9).
- d) The D-E meniscus interface keeps increasing its curvature until invading the pore throat. At this stage, capillary pressure (entry capillary pressure for throat D-E) reaches the peak in figure 4.9.
- e) The arc meniscus D-E displaces the wetting phase filling the pore body contained by particles B-C-D-E. The rapid invasion causes a pore refilling. All the menisci reduce their curvature. The most remarkable fluid displacement is found at throat B-C. The dynamic action induced by the Haines jump starts filling the ABC pore body. Besides the refilling mechanism illustrated in 4.8e, we observe the significant pressure drop that triggers the refilling phenomenon in figure 4.9.
- f) ABC pore body is completely refilled with the wetting phase. From the last three images of the sequence (figures 4.8d, 4.8e and 4.8f), we evidence that non-wetting phase penetrates the cluster through throat D-E and pushes the liquid cluster towards the left side, eventually refilling the cell made up of particles A-B-C. The simulation was stopped when the arc meniscus D-E touched disk C.

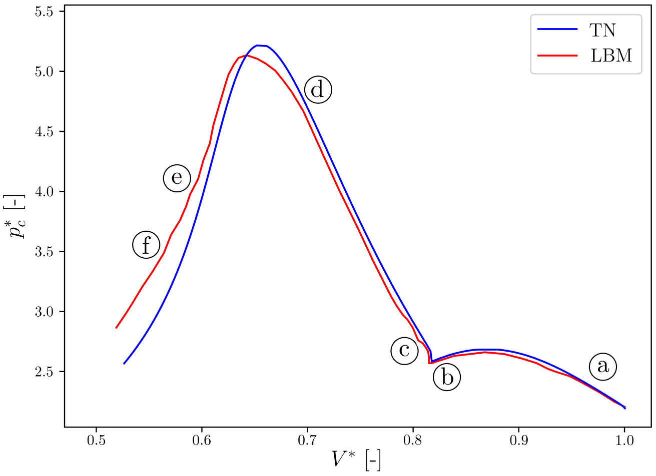

Figure 4.9: Comparison of capillary pressure - liquid content curve between LBM and TN models. The liquid contents of figure 4.8 are included in this image.

Excellent agreement is found between the numerical models (TN and LBM). Slight differences are only revealed during the Haines jump (see figure 4.8e). Regarding the capillary pressures - saturation curves, the predicted capillary pressure curve obtained with the TN model is in good agreement with LBM. Once again, some discrepancies become evident during the dynamic event (see points ”e” and ”d” in figure 4.9).

4.3.5 Drainage within porous media

After validating the TN model for the local mechanisms described in previous examples, we now consider a drainage-imbibition cycle in a small 2D granular assembly consisting of equal-sized disks.

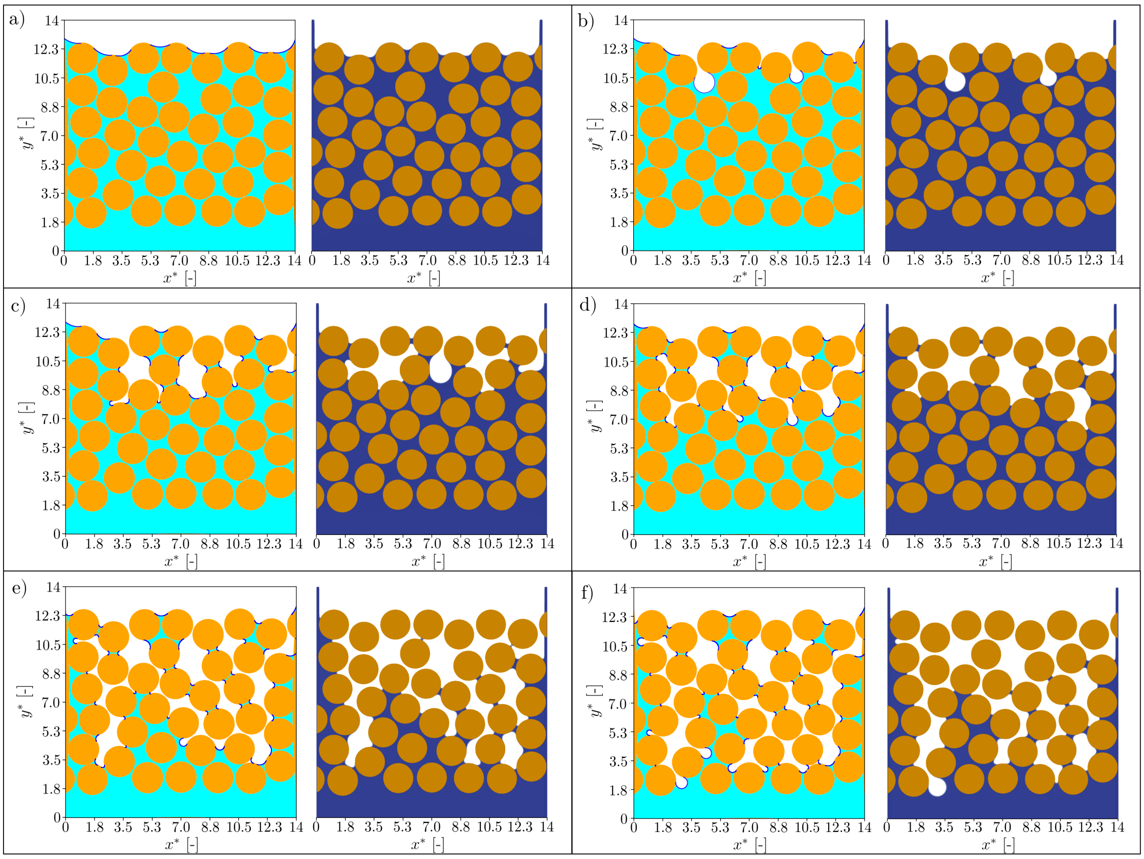

Figure 4.10: Comparison between fluid distributions of TN (left images for each column where wetting phase is depicted in light blue) and LBM (right images for each column where wetting phase is depicted in dark blue) models during the drinage. Various liquid contents are displayed: a) $V^* = 1.00$, b) $V^* = 0.92$, c) $V^* = 0.81$, d) $V^* = 0.66$, e) $V^* = 0.44$ and f) $V^* = 0.38$.

Initially, the sample is fully saturated with the wetting phase (see figure 4.10a). Impermeable walls are considered along the vertical sides. A pressure gradient between the two phases is imposed to trigger the motion of the interface. As a consequence, the non-wetting phase advances through the porous medium passing through the widest throats. Figure 4.10 shows the complete sequence of drainage for the TN and LBM models. In particular, the fluid distributions displayed in figure 4.10 correspond to different liquid contents during drainage. The saturations for each model were matched as closely as possible. It should be noted that numerical simulations were not controlled for liquid content, instead, flux was adjusted to drain the granular assembly.

Figures 4.10b, 4.10c and 4.10d show that non-wetting phase advances according to a stable displacement, as a matter of fact, three pore throats are invaded almost at the same moment. In this example, $Ca \approx 7 \cdot 10^{-2}$, such capillary number infers quasi-stationary regime is not fully satisfied. These flow properties accompanied by a similar width among the three invaded pore throats, lead to a stable non-wetting front. Conversely, the final part of the drainage (figures 4.10e and 4.10f), is driven by a process that shares some similarities to those of fingering mechanism. It should be reminded that in Chapter 1 (section 1.2.2.1.1), we indicate, as suggested by Lenormand (1990), that capillary number and dynamic viscosity ratio are the two main parameters that affect the fluid displacement behavior.

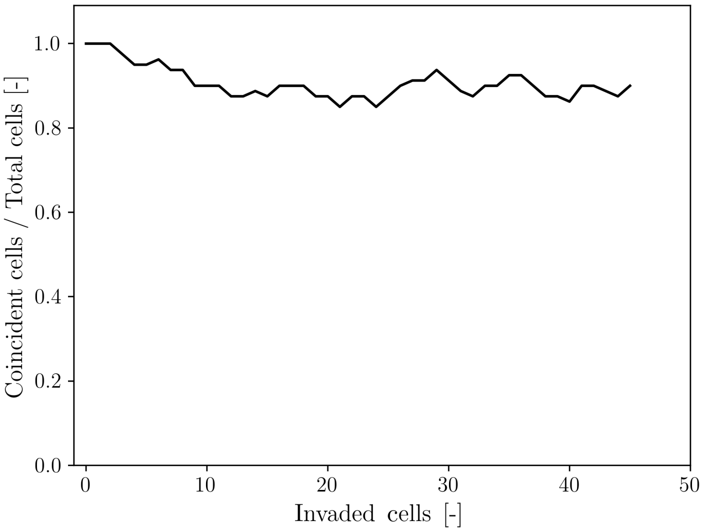

Figure 4.11: Number of invaded cells VS coincident cells.

Qualitative good agreement is observed for the fluid distributions. We emphasize that both LBM and TN follow almost the same pattern throughout the drainage. The main discrepancy is found in the isolated liquid clusters. Both models are able to capture the wetting phase trapped in the porous media during drainage. However, figure 4.10f shows that TN model includes several pendular bridge and a couple of trimers, whereas the LBM model ends with very few bridges. The sequence illustrated in figure 4.10 evidences that liquid bridges obtained with LBM decrease their volume much faster than the TN model. The reason is associated to the mass transfer between liquid clusters through a solid surface. Physically this corresponds to the film flow over particle surfaces. This phenomenon is well represented by the mulicomponent SC-LBM. On the other hand, laminar flow over solid surface is not an available feature in the current TN model.

The good accuracy revealed in figure 4.10 is quantitatively summarized in figure 4.11. Essentially, figure 4.11 accounts for the invasion sequence. The coincident cells (pore bodies) between LBM and TN models are evaluated during the drainage as the cells are progressively invaded. As suggested in figure 4.11, TN and LBM models not only end up with very similar fluid distribution, but also follow the same preferential path. In average, 91 % of the cells are coincident between LBM and TN model during drainage.

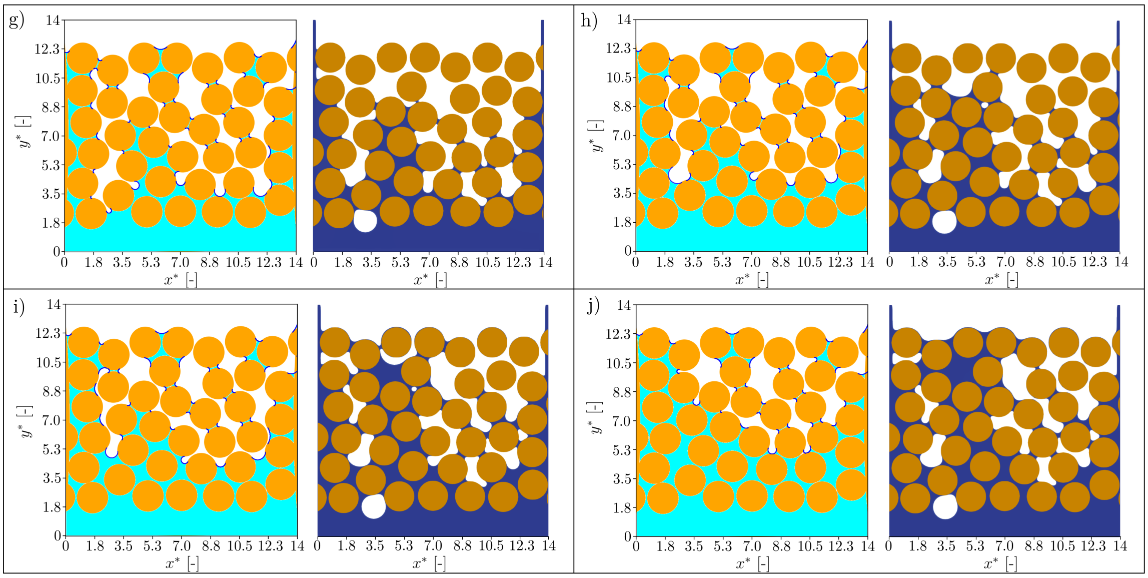

Figure 4.12: Comparison between fluid distributions of TN (left images for each column where wetting phase is depicted in light blue) and LBM (right images for each column where wetting phase is depicted in dark blue) models during the imbibition. Various liquid contents are displayed: g) $V^* = 0.40$, h) $V^* = 0.48$, i) $V^* = 0.51$ and j) $V^* = 0.60$.

Imbibition starts from the end-point of the drainage simulation (see figure 4.10f). Figure 4.12 indicates that LBM and TN follow significantly different fluid patterns. The main reason is, once again, related to the diffusive interface typically associated to the multicomponent Shan-Chen LBM. Fluid flowing over solid surfaces is evidenced in the LBM sequence of figure 4.12. Mass transfer becomes relevant when two solid objects are close. Due to the diffusive layer between the fluid and the solid (Chen et al. (2014), the wetting phase rises up through the solid-fluid interface. During the imbibition procedure, liquid bridges are spontaneously formed as a consequence of the vapor diffusion. This phenomenon is physically explained by Forcada (1993): first, liquid films spread over the solid surfaces. Then, if the solid surfaces are close enough, a fluctuation might change the thickness of the film. When the films get in contact, surface tension forces pull the liquid towards the junction and a bridge is formed. The formation of pendular bridges eases the presence of trapped non-wetting fluid. The size of the residual non-wetting phase during the imbibition varies depending on the pore topology.

On the other hand, no trapping is possible in the TN model. A frontal displacement of the wetting phase is observed in all the TN imbibition sequence (see figure

4.12). In order to improve the TN model, it would be desirable to incorporate the absorption of the wetting phase into a laminar liquid film over the solid surfaces. Such feature could be a potential improvement to enhance the mass transfer process between solid bodies.

Despite the general disagreement depicted in figure 4.12, we observe that differences are significantly reduced if we neglect the trapped non-wetting phase and focus on the main front displacement. In fact, figure 4.12j shows that wetting phase distributions occupy the left side of the granular assembly while no significant changes (non-wetting phase is present during the imbibition) are observed on the right region. Thus, TN gives an acceptable agreement with LBM when the non-wetting phase in residual areas are not taken into account.

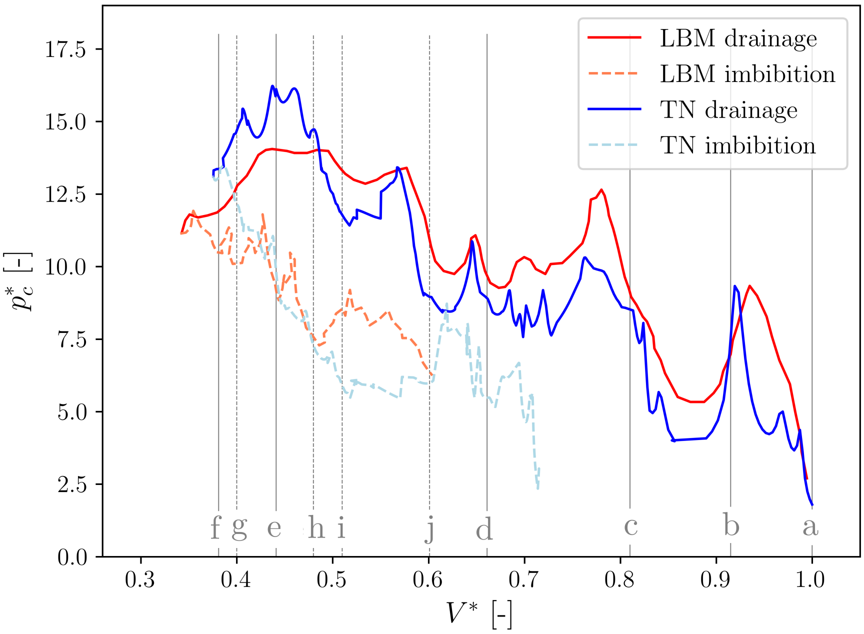

Figure 4.13: Comparison of $p_c^* - V^*$ curves obtained from the TN and LBM simulations. The liquid contents of figures 4.10 and 4.12 are included in this image.

Drainage and imbibition $p_c^* - V^*$ curves are presented in figure 4.13. The liquid contents associated to the fluid distributions of figures 4.10 and 4.12 are incorporated in figure 4.13 with vertical lines. Relatively good agreement is observed between the TN and LBM drainage curves. Results are not as encouraging as the fluid distribution patterns in figure 4.10 or the examples of local phenomena presented in previous subsections. Notwithstanding local differences, the same behavior and trend are observed in both drainage curves. The three most prominent p_c^* peaks ($V^* \approx 0.44$, $V^* \approx 0.76$ and $V^* \approx 0.91$) are found for very similar liquid contents. Such peaks appear when the non-wetting phase faces significant narrow pore throats. Important Haines jumps are observed for the first two peaks ($V^* \approx 0.76$ and $V^* \approx 0.91$). It is particularly interesting to relate the three dynamic events to the fluid distribution depicted in figure 4.10:

- *First peak* - Capillary pressure builds up as the non-wetting phase advances following a stable displacement (figure 4.10a) until reaching the entry capillary pressure that leads to the invasion of the wide pore bodies below the top granular layer (see figure 4.10b).

- *Second peak* - The non-wetting phase occupies the widest pore bodies after the first invasions. Then, capillary pressure is increased as the drainage proceeds (see figure 4.10c). The non-wetting phase penetrates through the pore throats (figure 4.10d) when the meniscus curvature attains the critical curvature associated to the entry pressure. The second important invasion is accompanied by another pressure drop.
- *Third peak* - The non-wetting phase flows through three preferred paths as displayed in figure 4.10e. Such invasion occurs with a gentle slope in the $p_c^* - V^*$ curve, specially in the LBM simulation. Finally, the non-wetting phase breaks through the bottom disk layer and the drainage simulation is stopped (figure 4.10f).

In general, TN and LBM simulations follow the same $p_c^* - V^*$ drainage curve. The main difference is associated to the smoothness of the lines. LBM simulation follows a smooth drainage curve. Whereas TN has a saw-like curve. Both following the same trend and able to reproduce the main dynamic effects. The reason of these differences is related to viscosity. Even though we have imposed the same viscosity ratio ($M = 1$), TN fluctuations observed in figure 4.13 suggest that LBM drainage occurs under a more dissipating process than the TN simulation.

During imbibition, it is evident that there is less agreement between LBM and TN simulations. Different slopes are found in figure 4.13. Moreover, local events, such as the wetting phase invasion through narrow pore throats, are not coincident in the imbibition curves. The main source of inaccuracy is the important role played by the film flow in the LBM simulation. Due to the formation of pendular bridges during the imbibition, the fluid distribution is strongly modified (see figure 4.12) hindering the comparison of the $p_c^* - V^*$ imbibition curves.

4.3.6 TN-DEM results

This section presents the results obtained with the TN-DEM approach for the simulation of a biaxial test in drained conditions. Vertical (y-axis) compression at constant strain rate and constant lateral (x-axis) stress were applied. The simulation was performed on a 2D mono-disperse granular assembly. We reproduce two different scenarios: a dry specimen and a partially saturated sample (see figure 4.14).

The following parameters were employed in the TN-DEM model to generate and evaluate the hydro-mechanical response of the two granular assemblies:

- Number of particles: $N_b = 500$
- Inertial number: $\Lambda = \dfrac{\dot{\gamma} \cdot R}{\sqrt{\sigma_{iso}/\rho}} = 6.9 \cdot 10^{-7}$
- Dimensionless normal stiffness: $\varsigma = \dfrac{k_n}{R \cdot \sigma_{iso}} = 13.33$

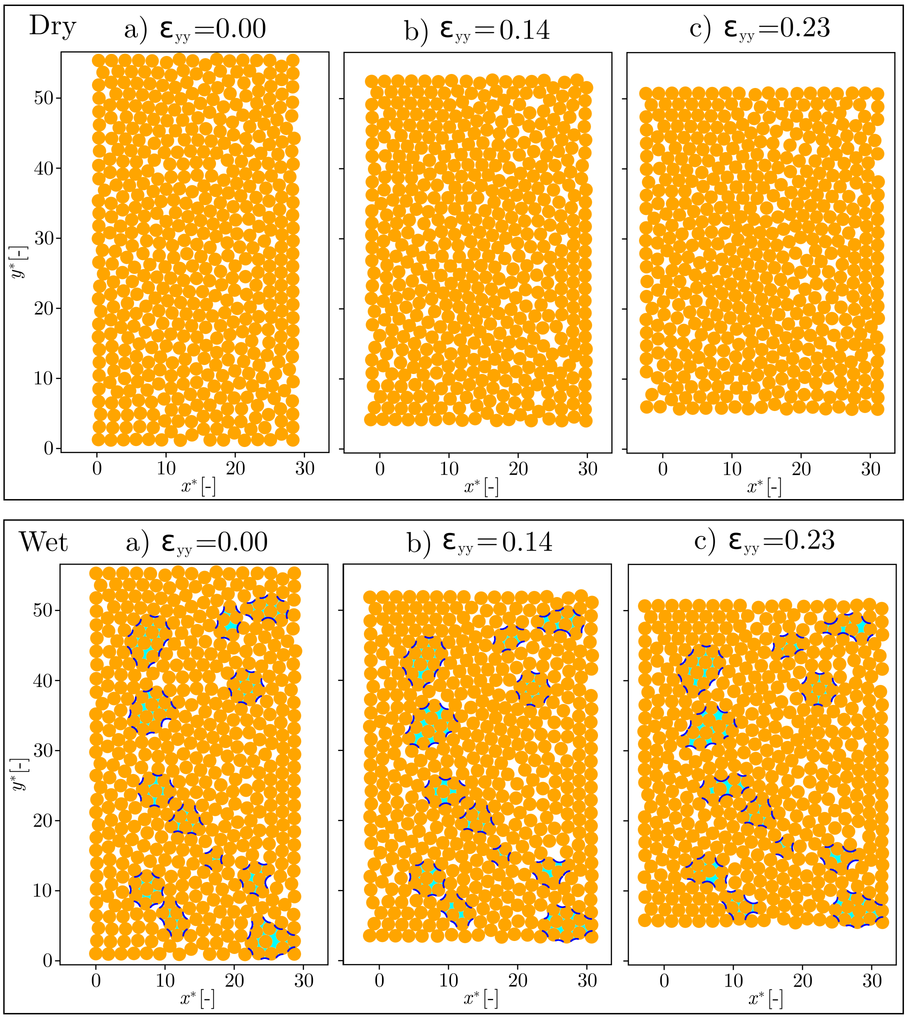

Figure 4.14: Evolution of the phases of a dry and a wet granular assembly during a biaxial test. The saturation degree of the partially saturated sample is: $S_w = 0.12$. The configurations of the granular assembly are illustrated for different vertical strains: a) $\varepsilon_{yy} = 0$, b) $\varepsilon_{yy} = 0.14$ and c) $\varepsilon_{yy} = 0.23$

- Stiffness ratio: $\dfrac{k_s}{k_n} = 0.25$
- Inter-particle friction coefficient: 45^o
- Wall-particle friction: 0^o

where $\dot{\gamma}$ is the shear rate, R is the radius of the grains, ρ is the density of the grains, σ_{iso} is the isotropic pressure, k_n is the normal stifness and k_s is the shear stiffness.

After the generation of the specimen, the granular assembly was isotropically consolidated under a constant pressure of σ_{iso}. Then, the sample was vertically compressed with the top wall moving downward and the bottom wall moving upward at a constant velocity. Meanwhile, horizontal pressure on the granular assembly remained constant.

The macroscopic mechanical responses of the two granular assemblies are described in terms of the following dimensionless variables:

- Deviatoric stress: $q^* = \dfrac{\sigma_{yy} - \sigma xx}{\sigma_{iso}}$
- Volumetric strain: ε_v

where the deviatoric stress (q^*) is obtained by subtracting the main stresses ($\sigma_{yy} - \sigma xx$), thus, it is responsible for the distortion of the soil, and the volumetric strain (ε_v) refers to the unit change in volume.

Figure 4.15 illustrates the typical macroscopic behavior of a dense sand. We observe that both dry and unsaturated sample have similar deviatoric stress - vertical strain and volumetric strain - vertical strain curves. Figure 4.15a shows the deviatoric stress increases with a nonlinear behavior until reaching the peak ($q^* \approx 1.0$). The increment of ε_{yy} after the peak leads to a constant residual q^*. Concerning the $\varepsilon_{yy} - \varepsilon_v$ relationship displayed in figure 4.15b, the volumetric strain reveals a weak compression first, then ε_v increases (expansion of the sample) with the vertical strain. This mechanical behavior is in good agreement with the experimental observation on dense sands.

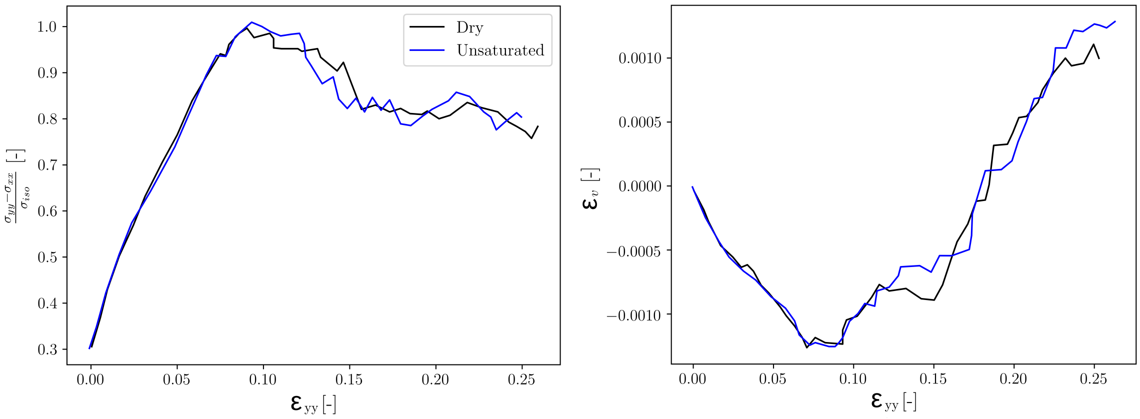

Figure 4.15: Stress-strain relationship of a dry and a wet granular assemblies during a biaxial test. a) Deviatoric stress - vertical strain and b) Volumetric strain-vertical strain curves.

4.4 Conclusion

The present work presents a pore-throat network model capable to model three-phase flow in 2D porous media made of packed circular particles. This model overcomes the difficulties related to the geometric simplification of most of pore-network models. The position of the interface is well described and proven to be almost identical to the LBM fluid-fluid interface in most of the basic examples (simulations from section 4.3.1 to 4.3.4). Saturation curves and pressure field are also in good agreement. Throughout the elementary simulations, it becomes evident that TN model can handle several local events such as: Haines jump (figure 4.4), meniscus rupture into independent menisci (figure 4.4b), coalescence of two menisci (figure 4.7) and pore refilling due to dynamic effects (figure 4.8). Moreover, the algorithm of the current Throat-Network model strongly reduces the computation time respect to the lattice Boltzmann simulations. In particular, TN model speeds up the computation time with a factor of 20-40 depending on the simulation.

We remark that TN applies to both quasi-static and dynamic flow. Even though accounting for different kinds of flows overcomes the difficulties of previous models to deal with dynamic fluid displacement, the TN model is restricted to simulations in a 2D granular medium consisting of disks.

The accuracy of the TN model is slightly reduced in the drainage-imbibiton cycle of a 2D granular assembly. The front of the advancing phase is not able to perfectly mimic the interface displacement obtained with LBM. However, the fluid pattern observed during the drainage is almost coincident and the $p_c^* - V^*$ curves are reasonably similar. Overall, TN captures correctly the dynamic events and the non-wetting preferred paths. Unfortunately, several mismatches are found during the imbibition procedure. Such discrepancies are attributed to the mass transfer mechanisms associated to the LBM simulations. The diffusion process allows the reconnection of the wetting phase trapping the non-wetting phase in the porous medium, whereas in the TN model, no trapping (of the non-wetting phase) is possible. Film flow mechanism should be considered for future developments in the TN model. However, we argue that imbibition simulation performed with LBM matches the reality since the film of the wetting phase around the solid surface is much thicker than the one observed in a physical framework. Therefore, the diffusive films easily interact forming bridges between particles. The lack of diffusion mechanism in the TN model contrasts with the excess of mass transport observed in the LBM. Consequently, very few similarities are manifested during imbibition.

In the future, TN model could be employed to study the three typical displacement patterns in terms of the capillary number and viscosity ratio: capillary fingering, viscous fingering, and stable displacement (see section 1.2.2.1.1). Huang et al. (2014) studied the flow pattern through 2D porous media as function of M and Ca. The present model (TN) is a potential tool to validate and complement their work. In particular, TN could provide new insight into the transitions from stable displacement to capillary fingering.

In this chapter we have also introduced the Throat-Network - Discrete Element Method coupling scheme, referred as TN-DEM. The coupling has been implemented by means of the open-source code YADE-DEM. This model is devoted to simulate the two-phase fluid flow in deformable poly-disperse 2D granular materials. The capillary forces induced by the motion of the wetting phase are evaluated for each solid disk. Then, the fluid forces are incorporated in the DEM to solve the contact forces and displacements of the solid grains. The macroscopic mechanical response has been analyzed for a mono-disperse granular assembly containing 500 disks during a biaxial compression test. The simulation has been performed using a completely dry sample (DEM) and a partially saturated assembly (TN-DEM). No significant differences between the dry and unsaturated samples are evidenced during the biaxial test. Such results suggest that, in this scenario, liquid clusters have a low effect on the macroscopic mechanical behavior. Consequently, TN is suitable for applications involving hydro-mechanical analysis, such as the volumetric and shear strength behaviors under different loading-unloading.

The analytical solutions used in the present 2D model are no longer valid in 3D, however, new efforts (Chareyre et al. (2017)) are geared towards the simulation of multiphase flow in 3D systems to complement previous works in the same field (Blunt et al. (2002); Sinha and Wang (2007); Yuan et al. (2016)). In this direction, this work can be a starting point to set the basis for a new model based on semianalytical expression able to mimic three-phase flow through porous media. In fact, next chapter is devoted to develop a hybrid model that combines the efficiency of the Pore-Network approach and the accuracy of the LBM to evaluate the local rules at the pore scale.

Chapter 5

Study of an isolated pore throat

5.1 Introduction

In previous chapters we evidenced that capillary pressure plays a crucial role in determining the motion of fluids within the porous media. Overall, capillary pressure increases gradually during drainage. However, abrupt pressure drops appear when the non-wetting phase passes through a narrow pore throat to penetrate into a wider pore body (Haines (1930)). Such instability is caused when locally, the capillary pressure exceeds the entry capillary pressure ($p_c^e < p_c$). p_c^e can be approximated by the Incircle method (Sweijen et al. (2016)), the Mayer-Stowe-Princen (MS-P) method (Joekar-Niasar et al. (2010b); Yuan et al. (2016)), or direct fluid simulations.

Direct fluid dynamics simulations based on computational fluid dynamics (CFD) are suitable to reproduce the motion of multiphase flows with excellent accuracy at the pore-scale. However, such models present computational limitations at the macro-scale. Several studies based on the lattice Boltzmann method (LBM) (Pan et al. (2004); Van Kats and Egberts (1999); Ahrenholz et al. (2008)) and Smoothed Particle Hydrodynamics (SPH) (Tartakovsky and Meakin (2006)) simulations have successfully described the interface displacement in complex geometries. Even though both methods are easily parallelized, simulations are restricted to relatively small domains due to the high computation cost. Additionally, recent works (Raeini et al. (2012)) have analyzed the evolution of the fluid-fluid interface by means of the volume-of-fluid (VOF) method.

In contrast, more computationally efficient methods have been developed to avoid the tedious and expensive computation demand of CFD methods. Such methods rely on estimations and approximations that predict the behavior of multiphase flow within an acceptable computation time in detriment of the accuracy. Pore-network (PN) models have been largely used to predict the motion of fluids through porous media (Fatt et al. (1956); Fenwick et al. (1998); Blunt (2001)). PN models manage to reduce the computation time by simplifying the pore geometry.

This chapter establishes preliminary steps for a Hybrid model in which small subsets of a granular system are extracted from a granular assembly. Each subdomain is solved using direct simulations, in particular, LBM simulations. The fluid displacement through porous media of an initially saturated assembly is strongly influenced by the distribution of the entry capillary pressure. It is, thus, crucial to determine p_c^e for every LBM elementary problem. In addition to the accuracy given by the LBM to find p_c^e for each pore throat, useful hydrostatic properties are accessible from direct simulations (pendular rings formed between particles, capillary force, pressure and velocity fields, $p_c - S_w$ curves, etc). The results are provided for different geometric configurations. Moreover, the local properties obtained for individual pore throats by means of the LBM are compared to approximation methods (MS-P and Incircle methods), which are an interesting choice when the computational resources are limited.

5.2 Pore-scale Volume Decomposition

The pore-scale network is based on the 2PFV-DEM scheme developed by Yuan and Chareyre (2017), which combines a three-dimensional triangulation method and DEM for simulating the hydro-mechanical couplings in deformable granular materials.

The same triangulation method is employed in this study to create the network implementing some new extensions to adapt the computational domain for the LBM simulations. Herein we briefly recall the essential part of the method in order to introduce the new features. More details about 2PFV-DEM scheme can be found in Yuan et al. (2016); Yuan and Chareyre (2017).

In a multiphase system (a water-air-soil aggregation in soil mechanics, for instance), the solid is idealized to be a random packing of poly-disperse spheres, which is created by Yade-DEM (Šmilauer et al. (2015)). The pore space is decomposed into large pore bodies and narrow pore throats by using the Regular Triangulation (RT) method. RT may be seen as a weighted form of the classical Delaunay triangulation, where the weight accounts for the size of each sphere. Its dual Voronoi graph is entirely contained in the pore space, thus, the graph can be used to describe the path available to the fluids (see figure 5.1).

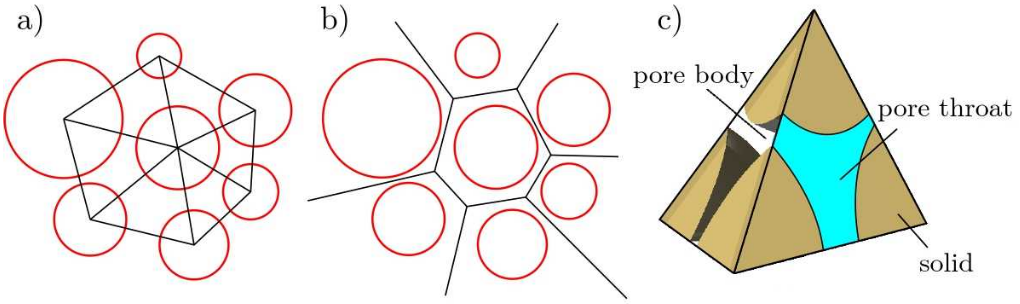

Figure 5.1: (a) Decomposition of void space by Regular Triangulation method and (b) corresponding Voronoi graph in 2D based on the 2PFV-DEM scheme of Yuan and Chareyre (2017). (c) a pore unit in 3D.

In the triangulated geometry of 2PFV-DEM, a pore body is defined as the irregular cavity within a tetrahedron, and bounded by four solid spheres (whose centers are the vertices of the corresponding tetrahedron). A pore throat is defined by the cross-sectional area extending within a tetrahedral facet (2D object). Pair interactions (including solid-solid contacts) act along the edges (1D object) of the triangulation. Finally, the 0D points are attached to the solid objects.

5.3 Pore-scale approximations

Following the triangulation scheme described in 5.2, a sphere packing can be decomposed as shown in figure 5.2. The topology of the pore throats is described by each elementary subset. In particular, the shape of a pore throat is defined by the cross-sectional area extending within a tetrahedral facet (see figure 5.3).

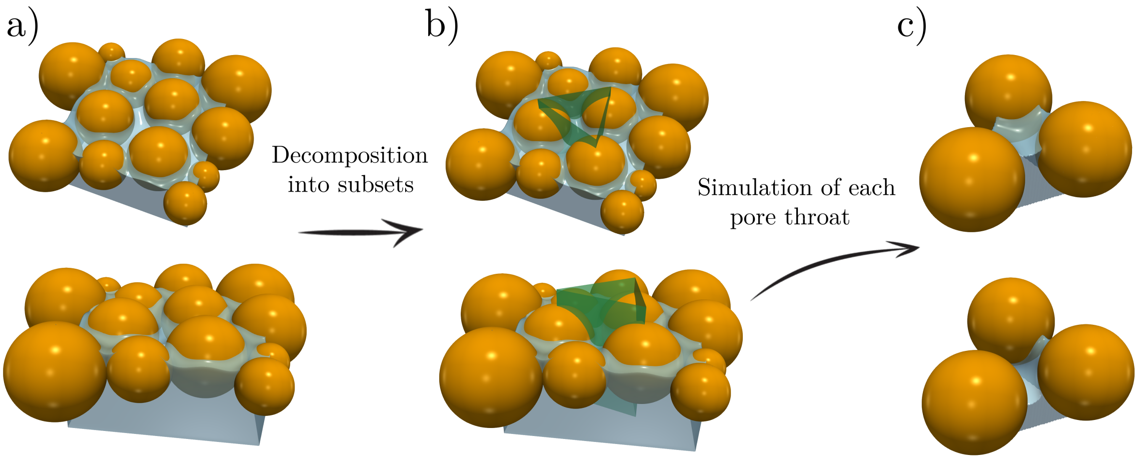

Figure 5.2: Decomposition of the granular assembly (a) into small subsets (b). Each subset is made up of 3 spheres (c).

As detailed in section 1.3.5.1, entry capillary pressure is one of the main factors controlling drainage. The following criterion is considered to reproduce the non-wetting phase invasion: if the capillary pressure (p_c) is larger than the entry pressure ($p_c^e < p_c$), the non-wetting phase invades the pore body. Thus, the displacement of the non-wetting phase is directly linked to the capillary pressure.

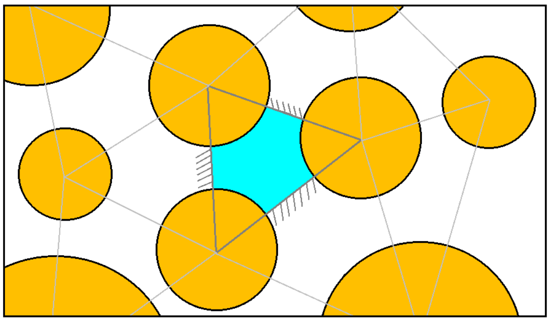

Figure 5.3: Top view of the computing domain after the decomposition.

During the fluid displacement, the interface adopts very complex shapes. In fact, the interface menisci observed in a typical subset as depicted in figure 5.2c show no translational or rotational symmetry. According to Laplace-Young equation, the analysis of the meniscus shape requires solving a nonlinear, second-order, partial differential equation, which involves a high computational cost. Due to this limitation, it seems reasonable to consider other approaches that can predict the entry capillary pressure and the meniscus shape. In this chapter, we employ direct fluid simulations based on the LBM to determine the main hydro-mechanical properties. Nonetheless, for practical purposes, when the computational resources are limited, semianalytical expression can be used to predict the entry capillary pressure. The most common approximations are the Haines Incircle method (Sweijen et al. (2016)) and the Mayer-Stowe-Princen (MS-P) method (Joekar-Niasar et al. (2010b); Yuan et al. (2016)).

5.3.1 MS-P

Mayer-Stowe-Princen (MS-P) model predicts the capillary pressure of the arc meniscus of a fluid droplet of infinite length inside a cylindrical tube (Princen (1969); Mayer and Stowe (1965); Ma et al. (1996)).

In the 2PFV-DEM scheme, the entry capillary pressure p_c^e of the pore throat is computed by following the MS-P method, which employs the balance of forces on the non-wetting - wetting interface in the transient state. The balance on a specific throat is written as:

$$\sum \mathbf{F}(p_c) = \mathbf{F^p}(p_c) + \mathbf{F^t}(p_c) = 0 \tag{5.1}$$

where, $\mathbf{F^p}$ is the capillary force acting on pore throat section domain and $\mathbf{F^t}$ is the total tension force along multi-phase contact lines (see figure 1.7b). p_c^e is the value of p_c such that $\sum \mathbf{F}(p_c) = 0$.

5.3.2 Haines Incircle approximation

Haines Incircle approximation (Haines (1930)), "Incircle method" hereinafter, proposes that the curvature of the interface passing through the pore throat is that of a sphere in contact with the spherical grains defining the pore throat. Therefore, the entry capillary pressure is $p_c^e = 2\gamma/r_{ins}$, where γ is the surface tension and r_{ins} is the radius of the circle inscribed in the pore throat.

5.3.3 LBM simulation of a single throat

This section provides an alternative method to determine the entry capillary pressure (p_c^e) for each pore throat. Instead of using the MS-P or Incircle approximations, hydrostatic properties are obtained from direct fluid dynamics simulations. As explained in section 5.2, the pore space is decomposed into a series of throat-domains defined by a regular triangulation (see figure 5.2). The decomposition leads to a list of pore throats that are solved independently. A multicomponent multiphase Shan-Chen LBM is employed to simulate the motion of the fluids and estimate the primary drainage curve and the entry capillary pressure for each pore throat. The computation domain is a triangular-shaped prism defined by three solid walls orthogonal to the pore throat (plane defined by the three spheres as evidenced in figure 5.2b). Each of these solid boundaries passes through two of the spheres centers (two vertex of the triangle defined by the 3 spheres centers). The reader is directed to figures 5.2 and 5.3 for a more comprehensive view. A contact angle of 90 degrees is imposed on the boundaries to mimic symmetrical conditions for each solid wall. Moreover, the domain is enclosed by two triangles at the top and bottom of the prism representing the inlet and outlet sections of the LBM simulations.

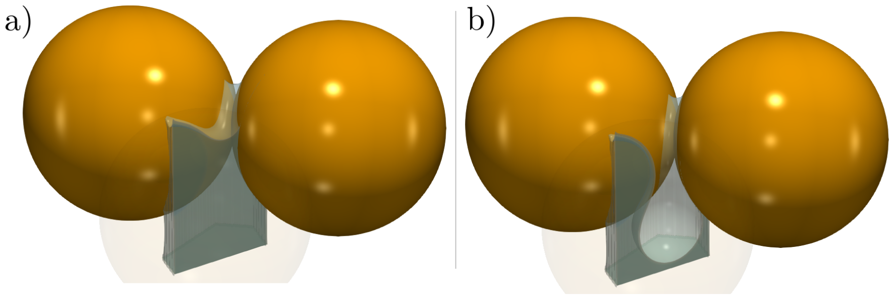

Figure 5.4: Invasion by a non-wetting phase of a pore throat formed by three spheres. Notice the translucent third sphere in front of the other spheres.

Initially, both wetting and non-wetting phases are in equilibrium for each elementary problem. Figure 5.4 shows the evolution of a typical subset configuration. In this case, the pore throat is formed by three equal-sized spheres in contact. The mass source and sink at the nodes located in the inlet and outlet sections are imposed to gradually increase the capillary pressure. Such increment triggers the displacement of the fluid-fluid interface (see figures 5.2c and figure 5.4). The curvature of the interface increases as the capillary pressure builds up.

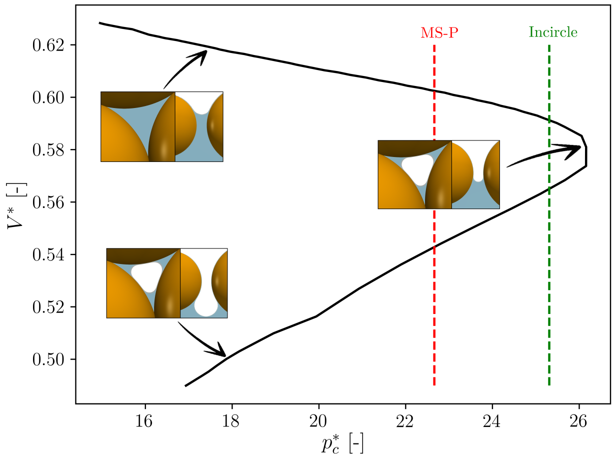

Figure 5.5: Volume change and capillary pressure upon invasion of the throat, superimposed with entry capillary pressure predicted by the MS-P and the Incircle methods. Three snapshots displaying vertical and horizontal slices of the simulation evidence the liquid morphology before, during and after the pore invasion.

The evolution of normalized capillary pressure ($p_c^* = \dfrac{2p_cR}{\gamma}$, where γ is the surface tension, R is the radius of the spheres and p_c is the capillary pressure) during the invasion is related to the change of volume of the wetting phase in figure 5.5. p_c is defined as the difference between the averaged non-wetting ($\overline{p^{nw}}$) and wetting phase ($\overline{p^{w}}$) pressures for the nodes far from the diffusive interface:

$$p_c = \overline{p^{nw}} - \overline{p^{w}} \tag{5.2}$$

The dimensionless volume is defined as:
$V^* = \dfrac{V(t)}{\dfrac{4}{3}\pi R^3}$, where $V(t)$ is the volume at time t .

The entry capillary pressure p_c^e is defined as the maximum value reached by p_c^* during the invasion process. When p_c reaches the entry capillary pressure ($p_c = p_c^e$), the non-wetting phase penetrates into the pore body (see figures 5.4 and 5.5). Immediately after the invasion, the interface meniscus expands leading to a reduction of the capillary pressure. This procedure is repeated for all the pore throats of the sample. Thus, p_c^e is determined for all the subsets and incorporated into the global problem handled by the pore-network.

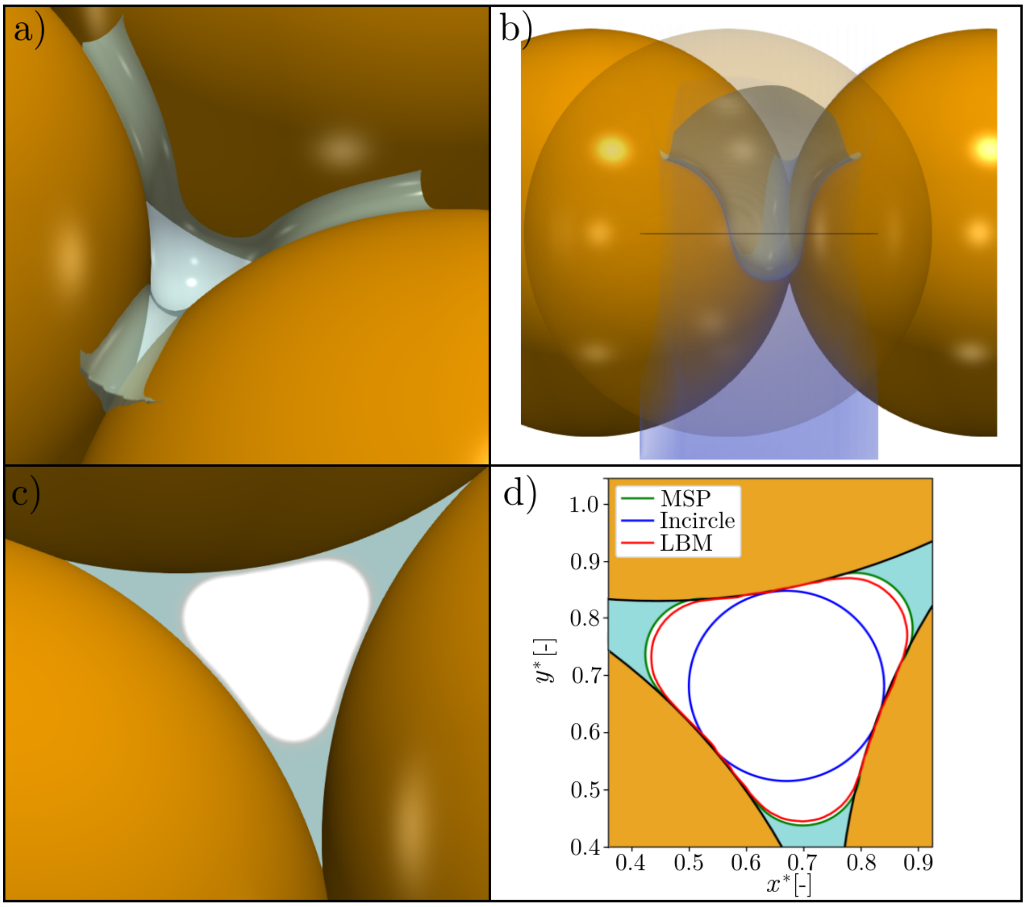

Figure 5.6: Non-wetting phase invasion of a pore throat formed by three equal-sized spheres in contact. a) Fluid-fluid interface deforming due to increments of capillary pressure. b) Vertical slice providing a detailed view of the incipient pore throat. c) Horizontal slice cutting the spheres in half. Wetting phase is accumulated in the corners while in the center non-wetting phase fills the pore throat. d) Overlapped MS-P, Incircle and simulated profiles.

LBM results are compared to the entry pressure given by the MS-P method in figure 5.6 for a particular case: Three equal-sized spherical particles in contact. The MS-P is applied considering a cylindrical throat with solid walls defining the same cross-sectional shape as the three spheres (see figure 5.6c and 5.6d). It is clear that after this crude simplification the MS-P is not expected to yield an exact value of the entry capillary pressure, yet evaluating the corresponding error is of interest since the same simplification has been used by previous authors (see e.g. Yuan et al. (2016)). Another classical approximation of the entry pressure also considered is the Incircle method (Haines (1930); Sweijen et al. (2017a)).

For this particular throat geometry, the MS-P prediction underestimates the maximum pressure from LBM with a relative error of -0.114 (see figure 5.5). The error is of the same sign but significantly smaller with the Incircle method (-0.049). It confirms the trend that was suggested previously on the basis of macroscopic water retention data (Sweijen et al. (2017a)).

Finally, figure 5.6 displays the state when $p_c^* = p_c^{*,e}$ and the non-wetting phase starts invading the pore body. The liquid morphology is depicted in figures 5.6a and 5.6b. Figure 5.6c shows a slice going through sphere centers to visualize the arc menisci between the beads, in the corners of the pore throat. Figure 5.6d offers a comparison with the interface geometry which is assumed for determining p_c^e analytically in the MS-P and the Incircle method, respectively. Interestingly, the MS-P profile is approximating details of the solution in a more realistic way - including in-plane curvature, although the best prediction of p_c^e is obtained using Haines Incircle method (figure 5.5). The mathematical reason of this inversion is due to the mean curvature value $k = \frac{1}{R_1} + \frac{1}{R_2}$ being calculated differently in the two methods. Haines Incircle method takes the meniscus as a spherical cap, hence the principal radii of curvature R_1 and R_2 are taken both equal to the radius of the inscribed sphere. The MS-P method, on the other hand, is based on the assumption of no longitudinal curvature, hence if R_1 is taken as the in-plane curvature, it leaves $R_2 = \infty$. For the same in-plane curvature, the pressure difference $\Delta p = k\gamma$ from MS-P would thus be half the value from Incircle method. Underestimating the in-plane curvature by the Incircle turns out to be more than balanced by this factor two on the mean curvature, and it finally gives the best approximation. Additionally, 5.6b evidences that the longitudinal meniscus curvature is a non-zero value, which technically breaks the MS-P assumption of a droplet of infinite length. Even so, MS-P is capable to reproduce accurately the arc menisci (see figure 5.6d) after the invasion and predict reasonable entry capillary pressures.

5.4 Validation of the decomposition scheme

As a validation step for the upcoming Hybrid model based on a decomposition of a granular assembly into multiple pore throats, we analyze and compare the results for a horizontal granular layer made up of spheres (see figure 5.7) and the widest pore throat (the first to be invaded). The differences between the two simulations are therefore crucial to decide whether the Hybrid model provides a reliable prediction.

The granular bed is illustrated on the top of each row in figure 5.7 in different projections (a) perspective view, b) top view and c) front view). Likewise, the single pore throat based on the decomposition scheme is depicted at the bottom of each row in figure 5.7. A low capillary number ($Ca \approx 0.0001$) is imposed in both simulations to ensure a quasi-static drainage. Capillary pressure is increased for both computational domains in order to reproduce drainage mechanism. As a result, the non-wetting phase breaks through the granular layer passing through the widest pore throat. The same phenomenon is observed for the elementary subset. Overall, figure 5.7 evidences almost coincident liquid morphologies throughout the drainage. It is worth noting the similar evolution of the meniscus shape after the invasion (see figure 5.7c). Additionally, the final liquid configuration of the subset analysis suggests that only one liquid bridge out of three is possible after the invasion (see figure 5.7b). The remaining wetting phase is well reproduced in the decomposed scenario, with shape and volume very similar to the result with the full layer.

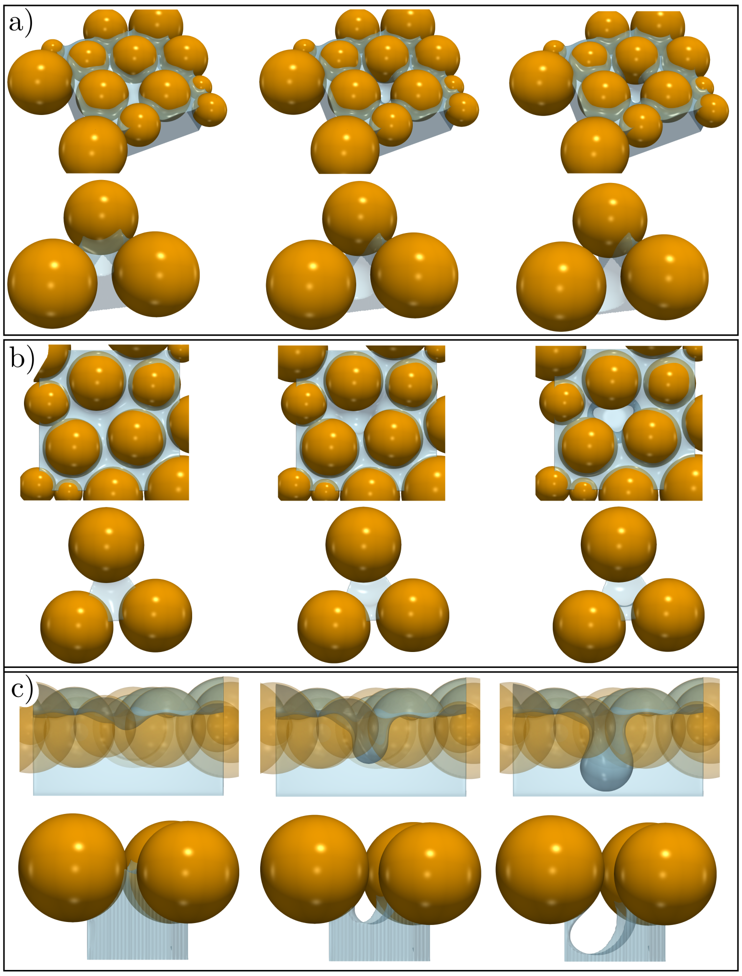

Figure 5.7: Evolution of the interface during a drainage simulation. A granular layer is depicted on the top of each row. The assembly is initially saturated and drained until the non-wetting phase penetrates the layer. The invasion of the throat is reproduced a second time following the decomposition scheme at the bottom of each row. The interface displacement is displayed in a) perspective view, b) top view and c) front view.

Analogous results are found in quantitative terms. The primary drainage curve is plotted in figure 5.8 for both LBM simulations. Suction is evaluated for different interface heights ($L^* = \dfrac{L(t)}{L_o}$, where L_o is the initial height of the lower point of the main meniscus). Good agreement is observed between the two curves. We emphasize the similarity of the entry capillary pressure values and the lack of discrepancies during the drainage.

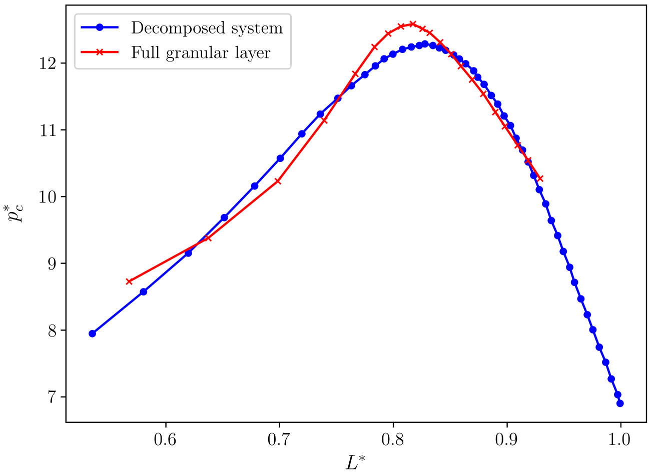

Figure 5.8: Capillary pressure evolution during the drainage simulations depiected in figure 5.7.

It is worth to point out the Haines jump observed in figures 5.7 and 5.8. This phenomenon was observed in previous chapters (see figures 2.28 and 4.4). During the Haines jumps, the velocity field increases locally near the interface and reduces back to a quasi-static regime after the liquid redistribution. As detailed by Berg et al. (2013), capillary forces accelerate the meniscus interface whereas the inertial and viscous forces resist to the fluid redistribution. In our test, inertial forces are larger than the viscous forces ($Re/Ca = \dfrac{\gamma \rho^w r_{throat}}{\mu^2} \approx 15$), which is associated to a capillary-interial flow. Up to now, Haines jumps were basically observed for individual pore throats, however, typical saturated granular materials are drained in cascade-like events. This is an important feature to take into account in an environment with multiple throats as shown in the next chapter.

5.5 Parametric study of an isolated pore throat

Pore-space filling during the fluid displacement is strongly influenced by the pore geometry and the fluid distribution in the adjacent pores (Berg et al. (2013)). In this section we investigate the effect of the geometrical configuration on the saturation curves. More specifically, the influence of the inter-particle distances or radius ratio is studied in four scenarios: 1) the three spherical beads are equally separated from each other, thus, a pore throat formed by three particles symmetrically placed that gets wider as the inter-particle distance increases. 2) One of the solid spheres is shifted away from the rest, meaning that two particles are always in contact. 3) Similar to case 2) but the two immobilized spheres are not touching. 4) The radius ratio of the third sphere is modified. Besides the sensitivity of these geometrical parameters on the $p_c^* - V^*$ relationship, the accuracy of the MS-P and Incircle methods to evaluate the interface profiles is tested.

Before going into details, it should be mentioned that hereinafter, we will usually distinguish narrow and wide pore throat. The size of a pore throat is frequently assumed to the radius of the circle fitting within its narrowest point, thus, the Incircle radius (r_{ins}). Therefore, wide and narrow por throats cover a range of r_{ins} that varies from nanometer to hundreds of micrometers. In this part of the thesis, we will refer to narrow throats those that satisfy the following condition: $r_{ins} < 0.4 \cdot R$. In contrast, wide thorats correspond to r_{ins} of same (or larger) order of magnitude as the radius of the spheres ($r_{ins} \geq R$).

5.5.1 Three spheres equally separated

We perform LBM simulations for subsets defined by 3 equal-sized spheres arranged to form equilateral triangles (see figure 5.9). Thus, the length of each triangle side is: $L = 2 \cdot R + d$, where R is the radius of the particles and d is the separation between two spheres. From now on, the dimensionless separation distance is expressed as $S^* = \frac{d}{R}$. The main hydrostatic properties are investigated for pore throats with separation distances ranging from $S^* = 0$ (three spheres in contact) to $S^* = 0.8$.

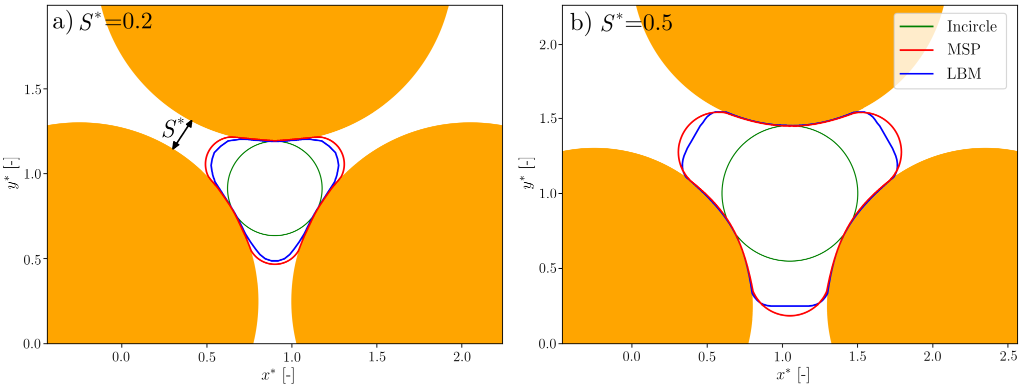

Figure 5.9: Overlapped MS-P, Incircle and LBM profiles when the 3 spherical bodies are moved away from each other. a) $S^* = 0.2$ and $p^{e,*}_{c,LB} = 15.0$. b) $S^* = 0.5$ and $p^{*,e}_{c,LB} = 8.4$.

Figure 5.9 displays slices going through sphere centers to visualize the arc menisci between the spheres. In particular, figure 5.9 illustrates two pore throats of different size. In figure 5.9a, we observe a narrow pore throat. This configuration enhances the existence of arc menisci between each particle pair. Such liquid morphology was already found in figure 5.6. The wetting phase gradually retreats as p_c increases and the fluid interface becomes more curved. According to Young-Laplace equation, the interface shape at the moment of the invasion is given by the mean curvature (critical curvature) associated to the entry pressure. Consequently, at the narrowest part of the pore throats (open edges of the triangle displayed in figure 5.9a), the meniscus cannot exceed the critical curvature, which entails the presence of the wetting phase in the pore throat corners. As illustrated in figure 5.9a, the amount of liquid in the narrowest areas given by the MS-P and LBM are relatively similar, however, less agreement is found with the Incircle method.

On the other hand, a wider pore throat is evidenced in figure 5.9b. In this case, the pore geometry enhances the invasion of the non-wetting phase through the pore throat. Due to the wide aperture observed in figure 5.9b, the critical curvature is significantly lower than in the previous example. Therefore, the non-wetting phase passes through the pore throat as a stable advancing front rather than adopting sharped curved shapes. Furthermore, in this scenario, the non-wetting phase reaches all the corners and manage to invade the whole pore space. Consequently, the wetting phase is entirely displaced leaving no trace in the particle-pair edges (see figure 5.9b). This phenomenon is well described by the MS-P approximation, which considers that wetting phase trapping does not occur. Whereas the Incircle method fails to reproduce the shape of the interface during the invasion.

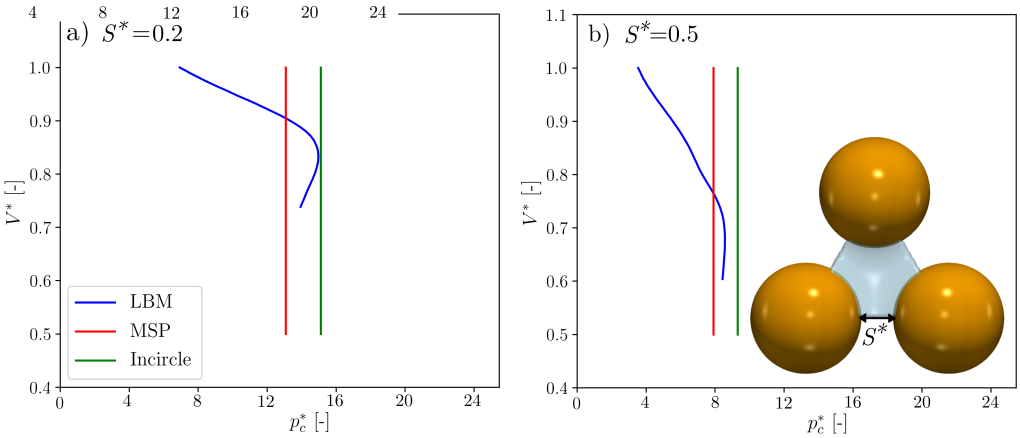

Figure 5.10: Capillary pressure - saturation relationships for a primary drainage of pore throats formed by three spheres equally separated. a) $S^* = 0.2$. b) $S^* = 0.5$.

Figure 5.10 shows the results of the test in terms of capillary pressure and saturation. Regarding the narrow aperture, figure 5.10a evidences a very abrupt event at $p_c^* = p_c^{*,e} \approx 15.0$. At this moment, a Haines jump takes place since the non-wetting phase passes from a narrow throat into a wider pore body. The drop in capillary pressure results into a rapid interface displacement. On the contrary, 5.10b shows a less prominent peak for $p_c^* = p_c^{*,e} \approx 8.4$. After reaching the entry capillary pressure, p_c^* barely decreases. In contrast to the narrow aperture, the non-wetting phase invasion occurs under fully quasi-static conditions (no Haines jump is observed). Indeed, the interface shape is not strongly modified after the invasion of the pore throat. In this case, the pore throat - body ratio is closer to 1 than in the previous scenario, which turns to have a weaker impact on the entry pressure and the prominence of the $p_c^* - V^*$ curve.

We remark that the drainage of the pore throat displayed in figure 5.9a eventually leads to the formation of pendular rings around the sphere-pairs. A graphical evidence of the pendular bridges after the drainage is found in figure 5.11a. The presence of disconnected and trapped wetting phase in the pore throats as pendular bridges is only reported for $S^* \leq 0.2$. Larger distances, as evidenced in figure 5.9b and 5.11b, lead to a convex meniscus that advances through the wide pore throat without leaving wetting phase behind, thus, the non-wetting phase invades all the region that was previously occupied by the wetting phase.

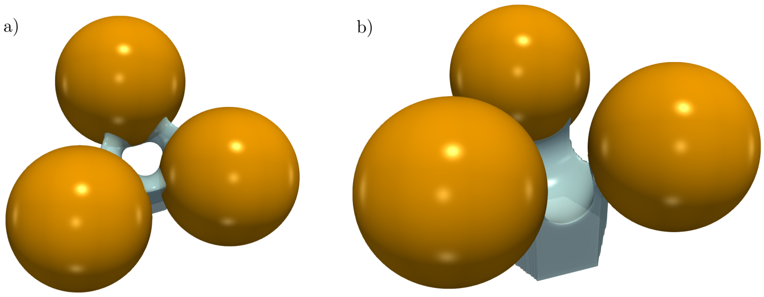

Figure 5.11: a) Pendular regime observed after the drainage of a pore throat with $S^* = 0.2$. b) Fluid interface passes through the pore throat without wetting phase trapping for $S^* = 0.5$.

5.5.2 One distant sphere

Following the previous subsection, we now investigate the hydrostatic response of a system formed by three spheres, in which one of them is moved away from the other two. The gap between the moving sphere and the two other spheres is illustrated in figures 5.12, 5.13a, 5.14 and 5.15b. Plus, the distance is expressed in dimensionless terms as: $D^* = \dfrac{D}{R}$. Liquid morphology and $p_c^* - V^*$ curves are studied for distances ranging from $D^* = 0.0$ to $D^* = 0.8$. We first investigate the sensitivity of the results when the two remaining spheres are in contact, afterwards, we will evaluate the results when the rest of the spheres are kept separated within a constant distance while the third sphere is moved away.

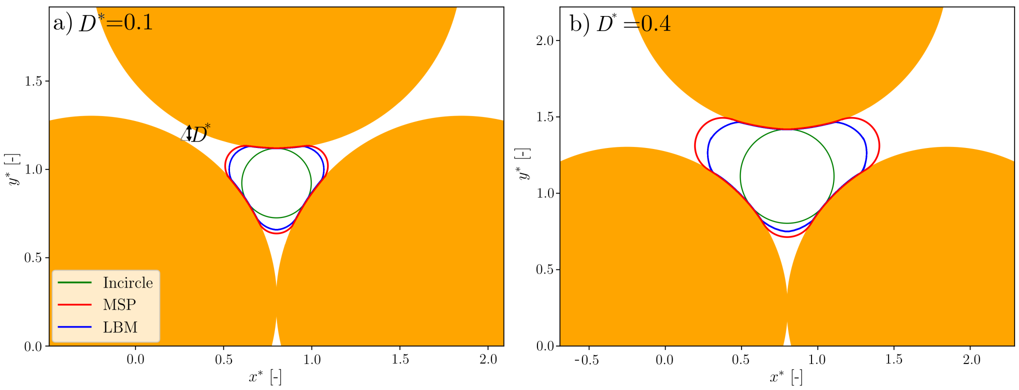

Figure 5.12: Overlapped MS-P, Incircle and LBM profiles when one of the grains is moved away from the other two while the rest remain in contact. a) $D^* = 0.1$ and $p^{*,e}_{c,LB} = 24.4$. b) $D^* = 0.4$ and $p^{*,e}_{c,LB} = 13.2$.

Similarly to section 5.5.1, we observe that narrow throats (figure 5.12a) require high interface curvatures to penetrate the pore neck and occupy the pore body. The narrow and complex pore geometry is not only responsible for the sharp interfaces, but also a determinant factor in the amount of wetting phase present in the corners. On the contrary, in situations including pore bodies slightly larger than the throats (figure 5.12b), the pore space filling occurs with an advance of relatively flat front (low interface curvature). The most noticeable aspect observed in figure 5.12 is the amount of wetting phase located in the particle pairs. The liquid content changes much less for the edge linking the two spheres in contact. The meniscus recedes much more on the other edges with larger gaps. When $D^* > 0.4$, due to topological reasons, the wetting phase is only found in the corner of the two touching spheres.

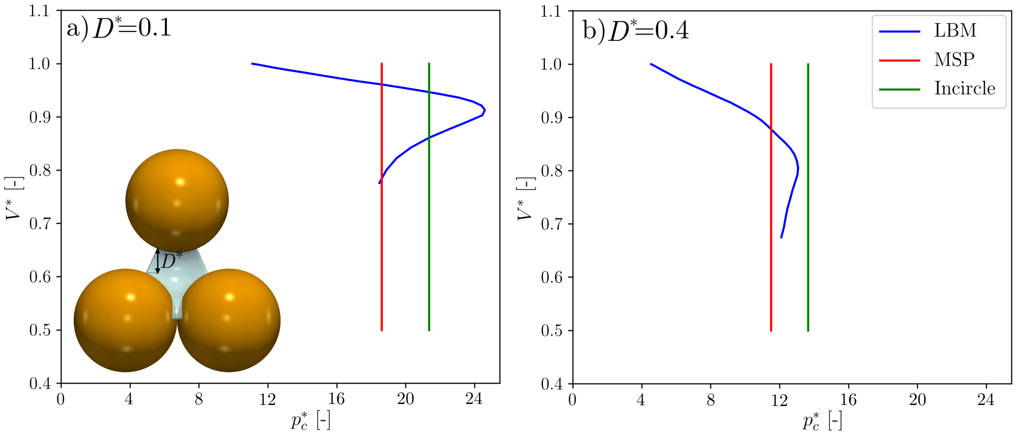

Figure 5.13: Capillary pressure - saturation relationships for a primary drainage of pore throats formed by three spheres in which one of them is moved away from the others that remain in contact. a) $D^* = 0.1$. b) $D^* = 0.4$.

The morphological discrepancies observed in figure 5.12 are also revealed in terms of capillary pressure - saturation curves. Figure 5.13a shows a clear peak ($p_c^* = p_c^{*,e} \approx 24.4$) followed by a sudden pressure drop. Whereas the wider throat (figure 5.13b) achieves a smoother peak at $p_c^* = p_c^{*,e} \approx 13.2$, then, the non-wetting phase slowly invades the pore body. The lack of a dynamic event (no Haines jump observed) in the latter case is manifested in figure 5.13b with a gentle reduction of capillary pressure.

The next example illustrates a typical configuration found in very loose granular materials. It is common in such systems to deal with three solid objects that do not share a single contact point. In particular, we consider two spheres that remain immobilized throughout the simulation with a constant separation (see bottom particles in figure 5.14). The third sphere is initially in contact with the other two. Then, it is gradually moved away from the rest as shown in figure 5.14.

Two important results are evident from figure 5.14. First, the profiles predicted by the approximations are far from the LBM meniscus interface. MS-P offers a better description of the meniscus than the Incircle method, however, differences are much more relevant in this case than previous examples (see figures 5.9 and 5.12). Secondly, the significant distance that separates the two grains at the bottom of figure 5.14 prevents the formation of a bridge between this particles-pair, nonethe-

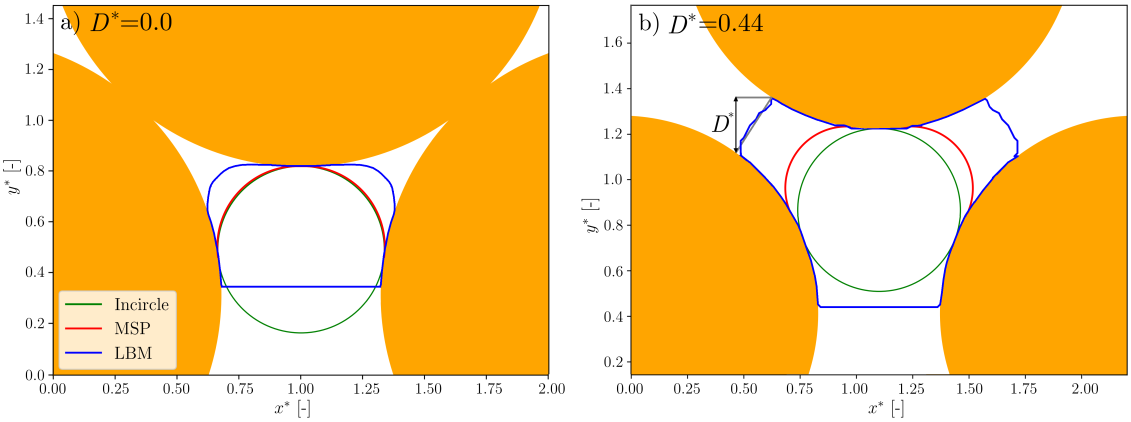

Figure 5.14: Overlapped MS-P, Incircle and LBM profiles when one of the grains is moved away from the other two. The rest of the spheres are not in contact. a) $D^* = 0.0$ and $p^{*,e}_{c,LB} = 14.8$. b) $D^* = 0.44$ and $p^{*,e}_{c,LB} = 8.4$.

less, Incircle method fails to account for this feature and a meniscus is displayed in figure 5.14b. Instead, the lack of a bridge between the bottom spheres is properly estimated with the MS-P method.

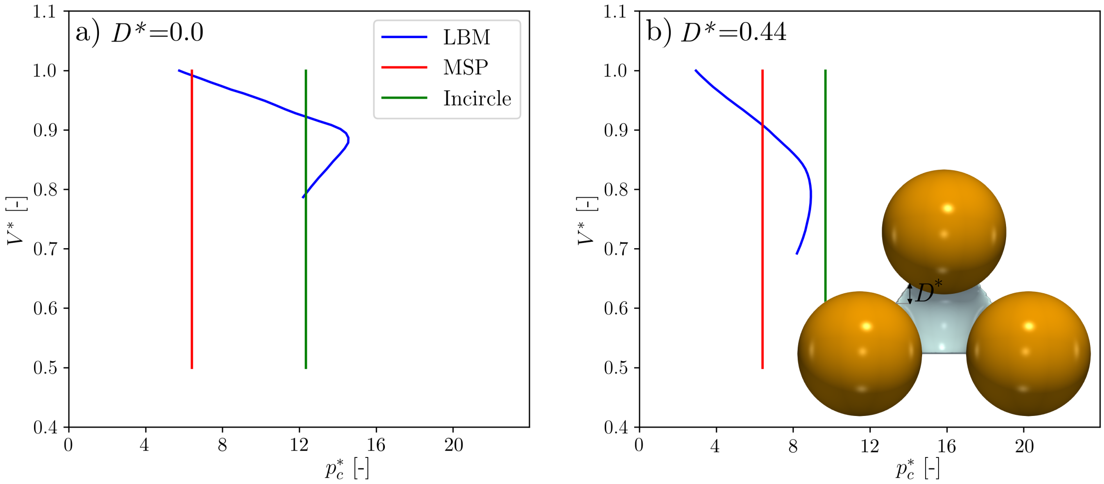

Figure 5.15: Capillary pressure - saturation relationships for a primary drainage of pore throats formed by three spheres in which one of them is moved away from the others while the rest are not in contact. a) $D^* = 0.0$. b) $D^* = 0.44$.

All the examples presented so far indicate that MS-P method provides reliable results in terms of interface profile as long as the particles are close to each other. Discrepancies arise when the particles are moved away from the others. On the contrary, figure 5.15 shows $p_c^* - V^*$ behavior is analogous to the one observed in previous sphere configurations. Thus, entry capillary pressure predictions are less influenced by the geometrical configuration than the interface profile. Moreover, figure 5.15 evidences wider pore throats lead to better MS-P predictions in detriment of the Incircle results that overestimate the entry capillary pressure.

5.5.3 Influence of the radius ratio

Several studies have evaluated the effect of the particle shape on the mechanical behavior of a granular assembly (Cavarretta et al. (2010); Yang and Luo (2015)). Along that same line, we now investigate the influence of different radius ratios on $p_c^* - V^*$ curves and meniscus profiles. The two spheres located at the bottom (see figure 5.16) remain unchanged (R_2), whereas the radius of the third sphere (R_1) is modified according to the radius ratio $a^* = \dfrac{R_1}{R_2}$ ranging from $a^* = 0.4$ to $a^* = 2.0$.

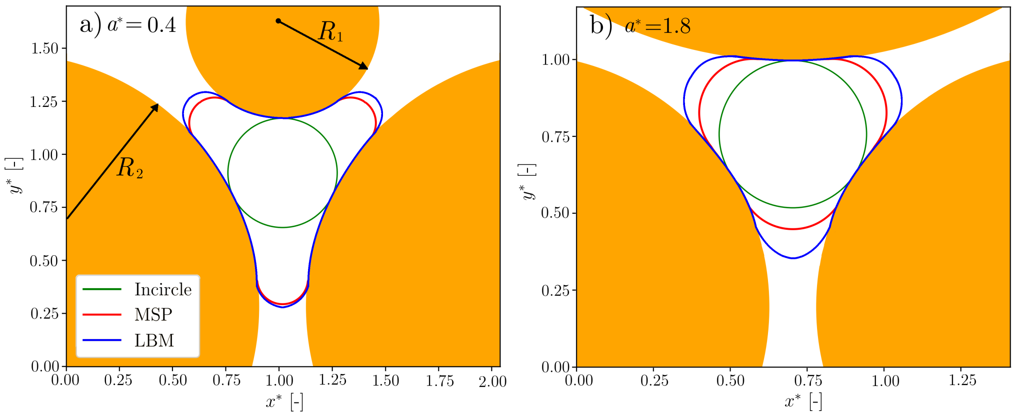

Figure 5.16: Overlapped MS-P, Incircle and LBM profiles for different radius ratios. a) $a^* = 0.4$ and $p^{*,e}_{c,LB} = 12.0$. b) $a^* = 1.8$ and $p^{*,e}_{c,LB} = 16.4$.

Both figures 5.16 and 5.17 reinforce the content covered in the previous examples, which basically emphasize the idea that narrow pore throats (see the increasing $p_c^{*,e}$ Incircle predictions with the radius ratio in figure 5.17, hence, r^*_{ins}, is reduced as a^* increases) are well described in terms of interface profile by the MS-P and entry capillary pressure by the Incircle method. Predictions become less credible when the particles are separated (in terms of dimensionless distances). Figure 5.17a (wider pore throat) shows a reversed situation in which MS-P method estimate $p_c^{*,e}$ with better accuracy than the Incircle method.

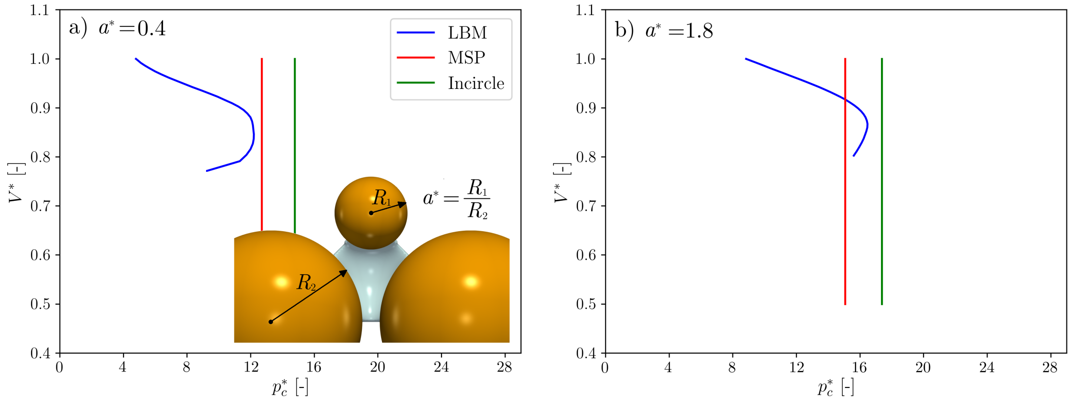

Figure 5.17: Capillary pressure - saturation relationships for a primary drainage of pore throats of different radius ratios. a) $a^* = 0.4$. b) $a^* = 1.8$.

An interesting feature depicted in figure 5.17 is the prominence of the p_c^* peaks. Due to the monodisperse spheres considered in previous examples, prominent peaks were detected in narrow pore throats (see figures 5.10a, 5.13a and 5.15a) and gentle peaks were manifested for wide pore throats (see figures 5.10b, 5.13b and 5.15b). The reverse situation is revealed in figure 5.17, in which the narrow pore throat caused by the radius enlargement also leads to a smoother throat-body transition, and the subsequent gentle peak.

The parametric analysis of the present section is completed with an error comparison between the LBM results and the approximations obtained in previous configurations. From figures 5.9, 5.12, 5.14 and 5.16 it is clear that the MS-P method is capable to reproduce the meniscus profile in a more realistic way than the Incircle method. Figures 5.10, 5.13, 5.15 and 5.17, however, show the Incircle method is slightly better in predicting the entry capillary pressure, specially when narrow pore throats are considered (high a^* values and low D^* and S^* distances).

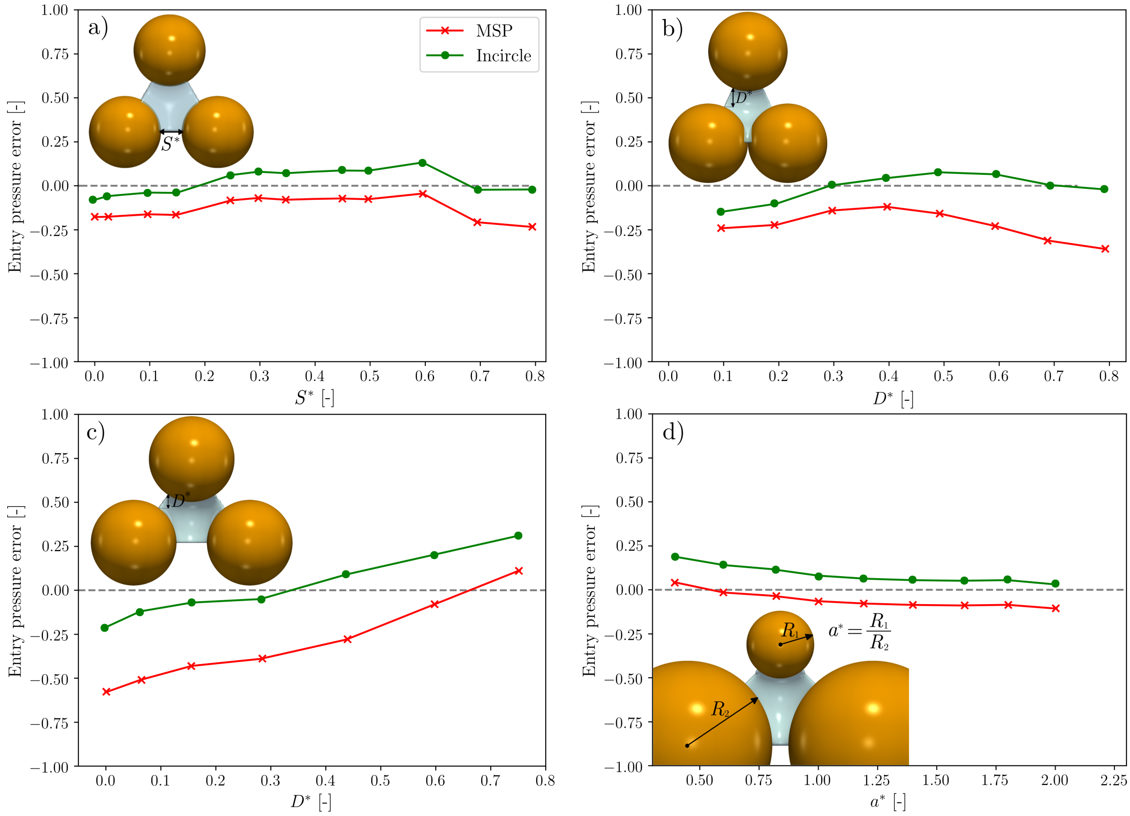

Figure 5.18: Error obtained for the MS-P method and the Incircle approximation. Error is evaluated for different bead configurations: a) When the separation between the solid grains is the same for all the pairs. b) When one of the particles is moved away from the rest while the other two remain in contact. c) When one of the particles is moved away with the rest separated a constant distance. d) When the radius ratio is modified for one of the spheres.

A quantitative analysis is displayed in figure 5.18 where the entry pressure obtained with the approximations has been compared to the LBM results. First, we observe that, regardless the throat size, MS-P nearly always underestimates the entry pressure. Plus, the Incircle approximations offers better results than the MS-P method for narrow throats (low D^* and S^*, and high a^*). The results reported throughout the sensitivity analysis indicate MS-P is preferred to determine the interface profile for all the sphere configurations. However, the best method to predict the entry capillary pressure may not be a trivial choice. As explained before, relatively narrow apertures are accurately described with the Incircle method. Unfortunately, more ambiguous results are found for wide throats (high D^* and S^*, and low a^*), figures 5.18a and 5.18b show that Incircle method is the best choice to determine $p_c^{*,e}$, whereas MS-P method approximates the entry capillary pressure better for the cases depicted in figures 5.18c and 5.18d. In order to clarify the remaining uncertainties and reach clear conclusions, we strongly recommend further parametric studies (accuracy of the methods as function of the distances and the radius ratio). Regardless of the approach we choose, it is worth emphasizing that error is, in general, lower than 25%, hence, acceptable for simulations that must be carried out with a very limited computation time.

5.5.4 Drainage-Imbibition cycle of a throat formed between 3 equal-sized spheres

In this section we simulate two-fluid-phase flow through a porous throat during a drainage - imbibition cycle. In this example, the pore throat is composed by three equally sized spheres forming an irregular triangle. As we know, capillary pressure controls the distribution of fluids in the porous media, thus, we are particularly interested to investigate the $p_c^* - V^*$ hysteresis during drainage and imbibition. The sequence of the drainage and imbibition mechanism is depicted in figures 5.19 and 5.20, respectively. Additionally, the stages observed during the simulation are indicated in the $p_c^* - V^*$ curve of figure 5.21.

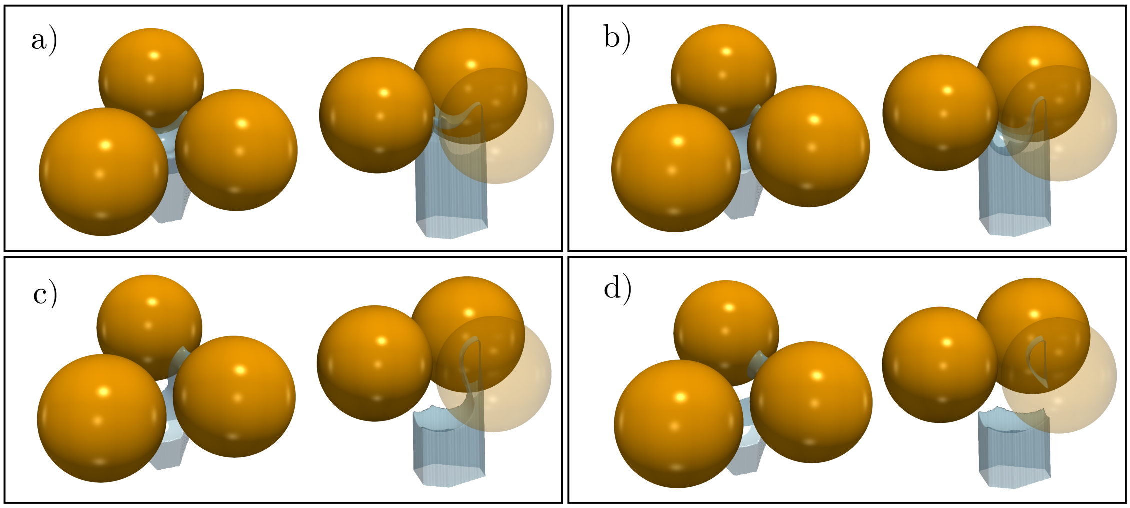

Figure 5.19: Interface evolution through a pore throat during drainage. The non-wetting phase penetrates the throat once the entry pressure is reached.

Capillary pressure was increased until reaching the peak, $p_c^* = p_c^{*,e} \approx 16.2$ (figures 5.19b and 5.21b). In this case, the throat is sufficiently narrow to trigger a dynamic movement of the fluid interface. Such phenomenon is accompanied by a pressure drop (figures 5.19c and 5.21c). It is interesting to point out the slope change at point "c" in the $p_c^* - V^*$ curve of figure 5.21. The reason for this local event is the contact of the meniscus with the artificial solid walls that enclose the computational domain defined by the three particle centers. The presence of the solid walls restricts the size of the pore body and modify the meniscus shape. The non-wetting phase keeps invading the pore space until a small amount of the wetting fluid is disconnected and trapped in a corner as a pendular bridge (figures 5.19d and 5.21d). At this moment, the non-wetting phase advances as a stable front without changing its curvature, hence, capillary pressure remains constant.

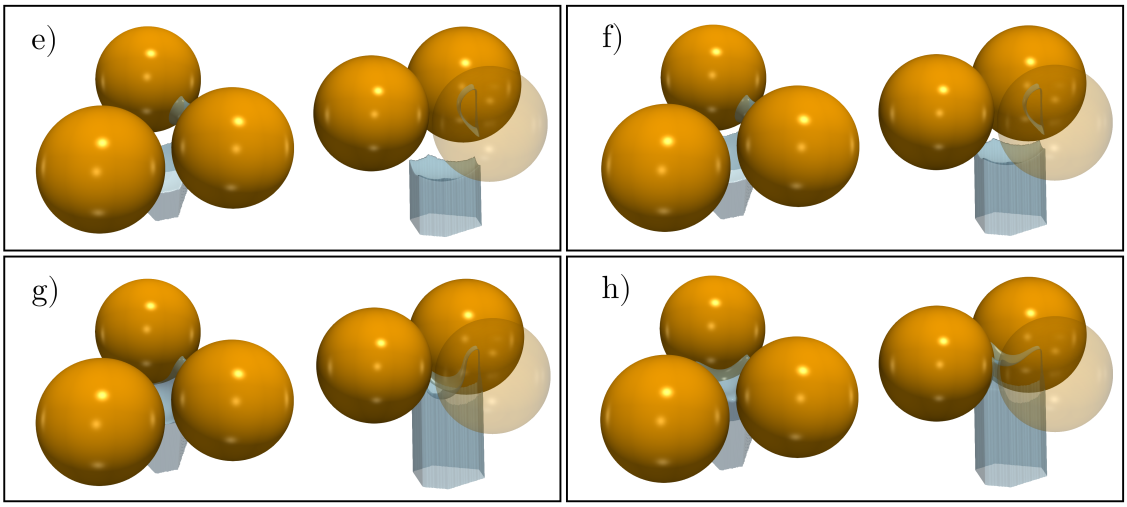

Figure 5.20: Interface evolution through a pore throat during imbibition. The wetting phase is displaced towards the top refilling the pore throat.

The microscopic behavior of imbibition in porous media is much more complicated than drainage (Oren et al. (1997); Patzek et al. (2000)). In the simulation, the starting point for the imbibition is the final configuration after drainage (figures 5.20e and 5.21e). The flow is imposed so that wetting phase is filling the throat. From figures 5.20f and 5.21f we observe that the fluid is displaced by piston-type imbibition with no changes in curvature. At point "f" (figures 5.20f and 5.21f), the meniscus gets in contact with the spherical objects inducing a change of curvature. Indeed, capillary pressure increases to accommodate higher curvatures that ease the motion of the interface towards the pore throat. The main terminal meniscus merges with liquid bridge at point "g" (figures 5.20g and 5.21g), this local event results into a small perturbation in the $p_c^* - V^*$ curve. Right after the coalescence, the interface keeps increasing its curvature until the wetting phase is able to pass through the throat (peak point in figure 5.21). Finally, the capillary pressure decreases as the fluid interface adopts smoother shapes (figures 5.20h and 5.21h).

It is worth mentioning that throughout this thesis we have assumed quasi-static conditions for most of the simulations. Dynamic events, such as the Haines jump, are only revealed when the non-wetting phase passes from a narrow throat to a wide body. Furthermore, as detailed in section 1.3.5.2, two mechanisms govern the interface displacement: snap-off and piston-type displacement. Previous studies

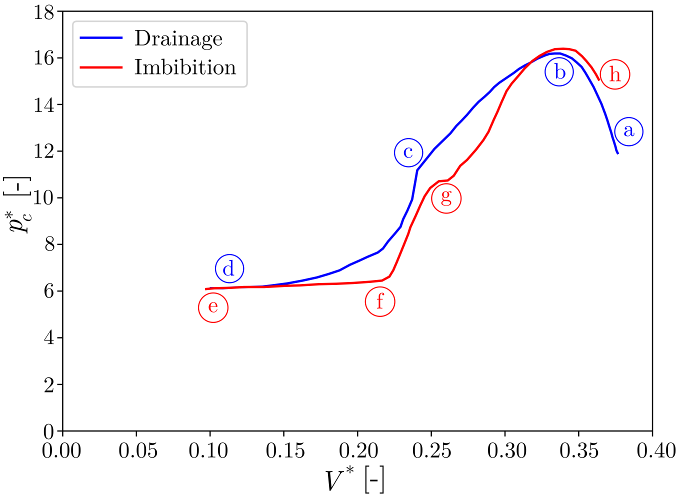

Figure 5.21: $p_c^* - V^*$ relationship at a pore throat under a drainage-imbibition cycle.

(Lenormand (1986)) have evidenced that pore geometry and fluid flow determines which mechanisms occur. Nonetheless, it is remarkable to convey that no snap-off episode has been obtained in any LBM simulations. This situation might be explained by the specific features of sphere packings, which produce a limited contrast between pore and throat size.

5.6 Conclusions

The study of a single pore throat provides preliminary evidence of the accuracy of direct LBM simulations at the throat scale for the upcomming Hybrid model. The relevant hydrostatic properties can be extracted from each throat. In contrast to approximation methods in which the entry capillary pressure is the only significant parameter used to predict the invasion of the pore throat, direct LBM simulations provide a full and detailed description of the volume - pressure relationship for the throat. Beyond the $p_c - V$ curves, LBM simulations capture the liquid morphology during the drainage. Consequently, capillary forces can be evaluated by means of the analysis explained in Chapter 3 during the pore throat invasion.

The encouraging results from the granular layer - pore throat comparison show that local properties are barely altered after the decomposition of the granular layer into subsets. The good agreement in terms of $p_c - V$ curve and interface shape validates the applicability of the Hybrid method.

The last part of this chapter was devoted to systematically explore the influence of the radius ratio and pore throat/body size ratio on the $p_c - V$ curves and interface profiles. In most cases, there is a pressure reduction after invading the pore throat (after reaching the entry capillary pressure). The magnitude of the pressure jump is directly linked to the pore throat/body size ratio: the narrower the pore throat, the larger the pressure difference. Assuming that LBM simulations reproduce a realistic description of the fluid motion through the porous media, the accuracy of the approximation methods was tested. From the comparison with geometrical approximation methods, we conclude that Incircle method is generally more accurate than

MS-P (though not always). Conversely, the interface profile was better predicted by the MS-P than by the Incircle method.

Chapter 6

Hybrid multiscale model for partially saturated media based on a pore network approach and LBM

6.1 Introduction

We present a Hybrid model based on a pore-network approach that enables a decomposition of the granular assembly into small subsets. Lattice Boltzmann simulations are performed for each pore throat to determine the hydrodynamic properties (entry capillary pressure, primary drainage curve, liquid morphology, etc) at the micro-scale. The local properties obtained with LBM are incorporated at the network to carry out the simulation at a larger scale. This strategy leads to a significant decrease of the computation time at the sample-scale compared to a fully resolved method. Therefore, the Hybrid method combines the efficiency of the pore-network approach and the accuracy of the LBM as suggested by Chareyre et al. (2017).

As an application case, we perform a fully resolved LBM drainage of a 40-sphere packing. A low capillary number ($Ca \approx 0.0001$) is considered to ensure quasi-static conditions. Such simulation provide reference data for the Hybrid model and other approximations. This includes capillary pressure - saturation relations, the residual wetting phase entrapment and fluid invasion paths. As reported in Berg et al. (2014); Edery et al. (2018), slow drainage are usually characterized by large pressure fluctuations (Haines jumps) that can produce significant burst events. This is consistent with our results that evidence sudden rapid advances of the non-wetting phase through a series of pores.

6.2 Flow through a 40-sphere packing

This section presents the results of a drainage process in an assembly of 40 spheres. A full LBM simulation has been performed and is taken as the reference solution. The results are compared with the Hybrid model alongside the MS-P and Incircle methods.

6.2.1 Numerical setup

A random sphere pack is created by the open-source code YADE. A cubic box of 10 mm × 10 mm × 10 mm is defined in which 40 polydisperse spheres are packed. The mean sphere radius is 1.26 mm. The generation of the pore network by regular triangulation is inherited from the 2PFV-DEM scheme, which is implemented in C++ (Chareyre et al. (2012)) using the CGAL library (Boissonnat et al. (2000)). The following assumptions are made during the numerical simulations:

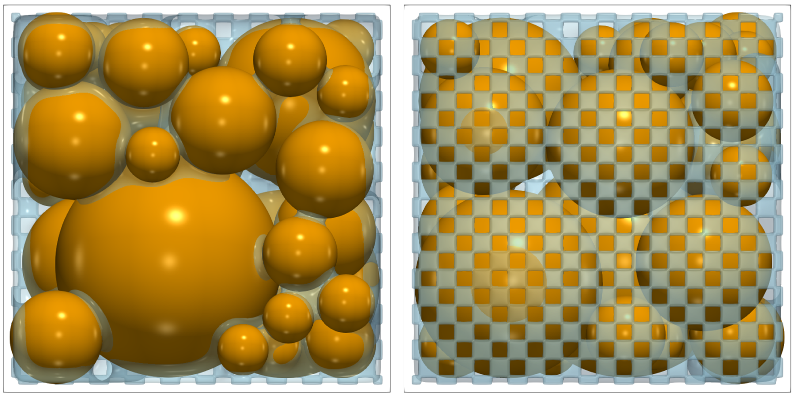

Figure 6.1: Top and bottom views of the 40-sphere packing. The blue isosurface indicates the interface between the two fluids. On the right, the porous membrane located at the bottom of the assembly is displayed.

- Drainage is evaluated under quasi-static flow.
- We assume perfect wetting of the solid by the wetting phase.

6.2.2 Full LBM simulation

This fully resolved LBM simulation is intended to give a data set to benchmark future numerical simulations. Data is submitted to Open Science Framework repository (Montellà (2019)). The dataset includes VTK Image Data files with all the essential information to visualize and evaluate the phase distribution, pressure and velocity field.

The following parameters have been considered to perform the LBM simulation:

- Each lattice unit (lu) spacing represents 0.00005 m. This spatial discretization leads to a computational domain of 220x250x220 lu^3 and a mean radius of 25.3 lu.
- A quasi-static flux is imposed by a mass sink/source located at the inlet and outlet. Flow is only modified when the density fluctuation on one time iteration, at interface nodes, is less than a fixed tolerance $\left(Tol = 10^{-5} < \dfrac{|\rho_{it} - \rho_{it+1}|}{\rho_o}\right)$. Such tolerance leads to a macroscopic capillary number of $Ca \approx 0.0001$.
- Contact angle: $\theta \approx 0^o$.

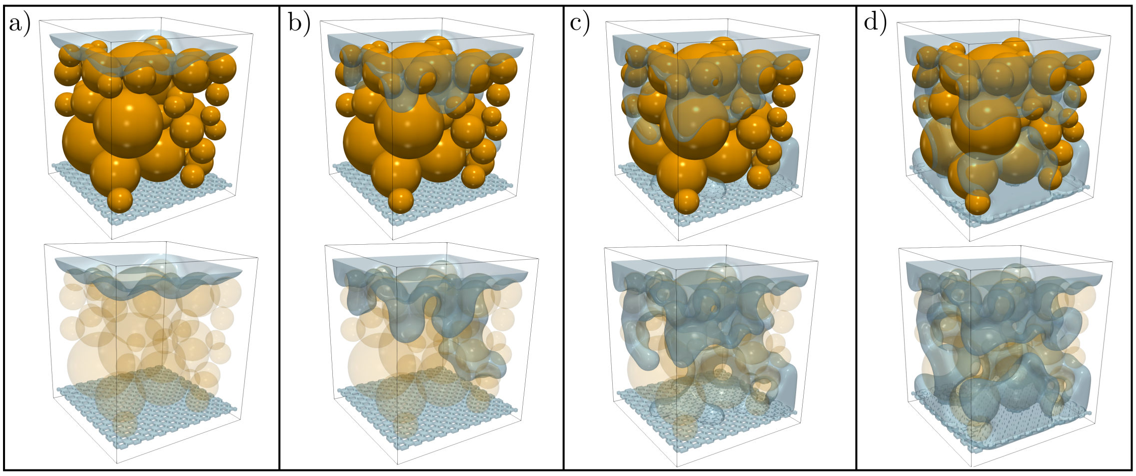

Figure 6.2: Evolution of the interface between the two fluids during a drainage simulation of a 40-sphere packing. For the sake of clarity, the bottom row of the figure includes translucent spheres. a) $V^* = 60$, b) $V^* = 35$, c) $V^* = 20$ and d) $V^* = 11$.

Initially, the granular assembly is completely saturated (see figure 6.2a). A porous membrane is located at the bottom of the sample in order to prevent the non-wetting phase to reach the outlet and ensure a complete drainage (see right image in figure 6.1).

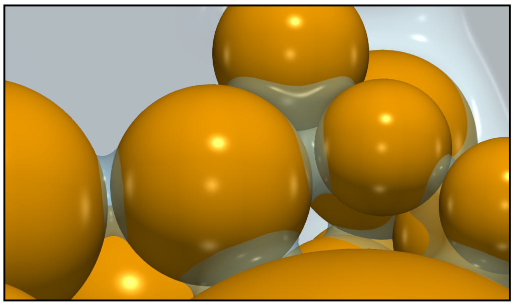

Figure 6.3: Distribution of the wetting phase after the drainage simulation of a 40 sphere packing. The wetting phase is trapped in some areas of the sample as pendular bridges, trimers or more complex clusters.

The displacement of the interface is controlled by an imposed flux between the non-wetting reservoir (top of the sample) and the wetting reservoir (bottom of the granular assembly). As illustrated in figure 6.2, the non-wetting phase advances through the porous media occupying the pore space of the sample. The steady regime is evidenced in figure 6.4, where the pressure field for the wetting phase is mapped for a vertical slice. No significant pressure differences are observed in the wetting phase. The interface flows towards the bottom driven by the flux invading the largest pores first. Capillary pressure is increased and recorded until all the nodes above the porous plate are filled with the non-wetting phase (see figure 6.2d). At this moment, the remaining wetting phase is trapped in the granular assembly in form of liquid clusters.

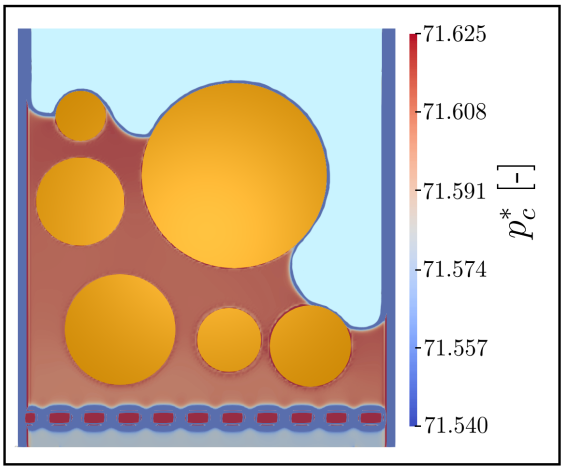

Figure 6.4: Pressure field for the wetting phase. Quasi-static drainage ensures homogeneous pressure values. In addition to that, we observe a pressure drop due to the porous membrane located at the bottom. Notice the non-physical pressure values at the interface caused by the spurious currents as suggested in Connington and Lee (2012).

6.2.3 Comparison of the methods

In this section the results obtained with the fully resolved LBM (section 6.2.2) are confronted with the predictions given by the Hybrid, the MS-P and the Incircle models. The accuracy and computation time to determine the main hydrostatic properties are evaluated for all the methods.

The generation and triangulation of the granular assembly follows the same procedure described in the numerical setup (subsection 6.2.1). The following conditions are set in the Hybrid, MS-P and Incircle models after the decomposition reported in subsection 5.2:

- The 40-sphere packing yields a network of 212 pores cells and 382 pore throats after the decomposition.
- Simulations start with 29 cells connected to the non-wetting phase reservoir at the top of the sample.
- The Hybrid method considers the same spatial discretization $\left(\frac{1lu}{0.00005m}\right)$ and a quasi-static flux to enhance a fair comparison with the fully resolved LBM simulation. More particularly, both scenarios consider the same tolerance $\left(Tol = 10^{-5} < \frac{|\rho_{it} - \rho_{it+1}|}{\rho_o}\right)$ that ensures an imposed flux under low capillary numbers.

After the generation and triangulation, either the Hybrid model or a approximation method is implemented. Figure 6.5 shows the flow chart for both possibilities. From the fixed pore space topology, the entry capillary pressure of each throat can be computed separately after direct LBM simulations or by means of the approximation methods (MS-P or Incircle). Other local hydrostatic properties are obtained (or predicted in case of using an approximation method) during this step (i.e. $p_c - S_w$ relationships and liquid morphology). Such properties are assembled and incorporated into the network to solve the global problem. The next step consists in defining the initial boundary conditions. At this point, the drainage simulation starts. For each invasion step, the boundary conditions are updated (fluid pressures of the phase reservoirs are modified) whereas the drainage and entrapment mechanisms are implemented in the ”Two-phase flow calculation” step.

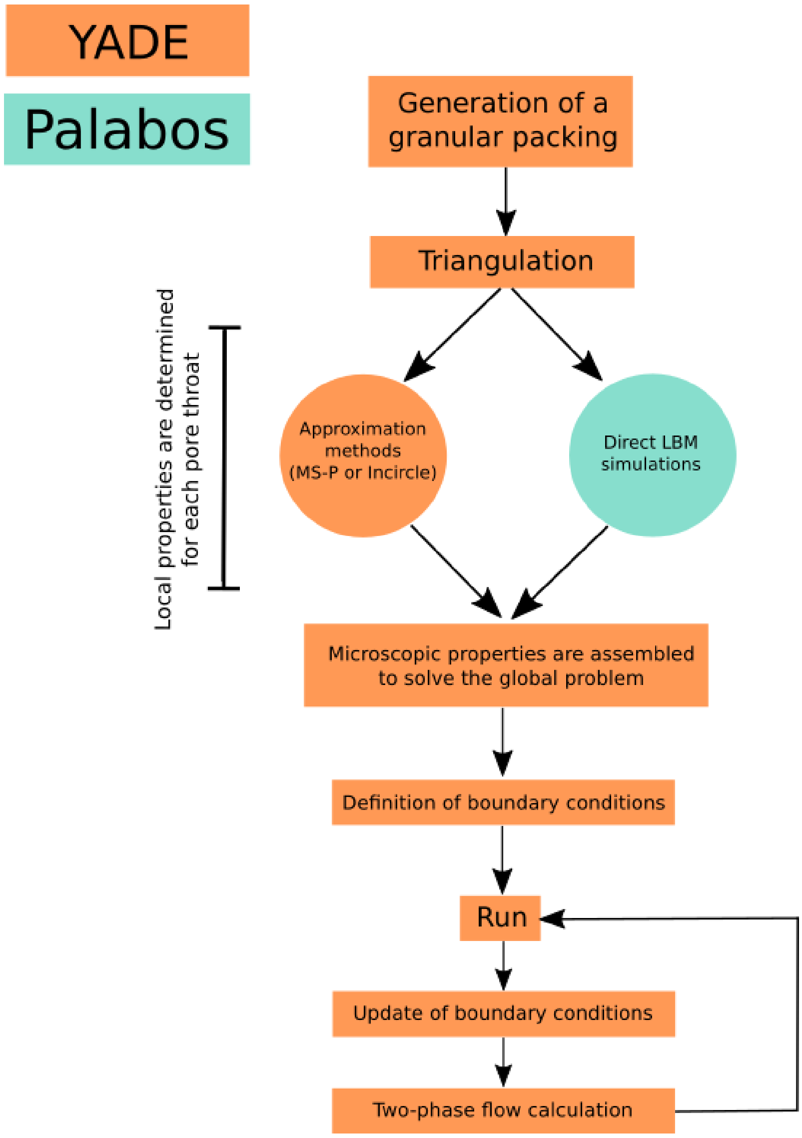

Figure 6.5: Coupled DEM-flow algorithm. Local properties can be computed after direct LBM simulations (Hybrid model) or approximation methods (MS-P or Incircle).

The implementation of the Hybrid model is based on the open-source code “Yet Another Dynamical Engine” (YADE) platform (Šmilauer and Chareyre (2010)). YADE is an extensible open-source C++ framework that allows the development of three dimensional discrete numerical models. Likewise, the fluid flow solution for each pore throat by means of direct LBM simulations is based on the open-source library Palabos written in C++ (Latt (2009)). LBM simulations are generated and solved using a C++ code. Conversely, Python language is used for construction, simulation control and postprocessing for the remainig tasks, that includes generation of the sphere packing, triangulation, definition of boundary conditions, drainage control, etc. Additionally, Boost.Python C++ library is incorporated to export classes and objects between C++ and Python programming languages.

6.2.3.1 Capillary pressure – saturation relationship

Capillary pressure - liquid content curves for primary drainage are studied in this subsection. The comparison between predicted saturation curves and numerical data is presented in figure 6.6a. Both Incircle (green) and Hybrid (blue) curves reproduce the full LBM capillary curve (black) with excellent accuracy. MS-P follows the same trend and good agreement is found, however, the curve is slightly undervalued in terms of capillary pressure. The underestimation of the capillary pressure values was already manifested in figure 5.5. Despite the better results in terms of interface profile shown in figure 5.6, Incircle approximation offers a more accurate description of the saturation curve.

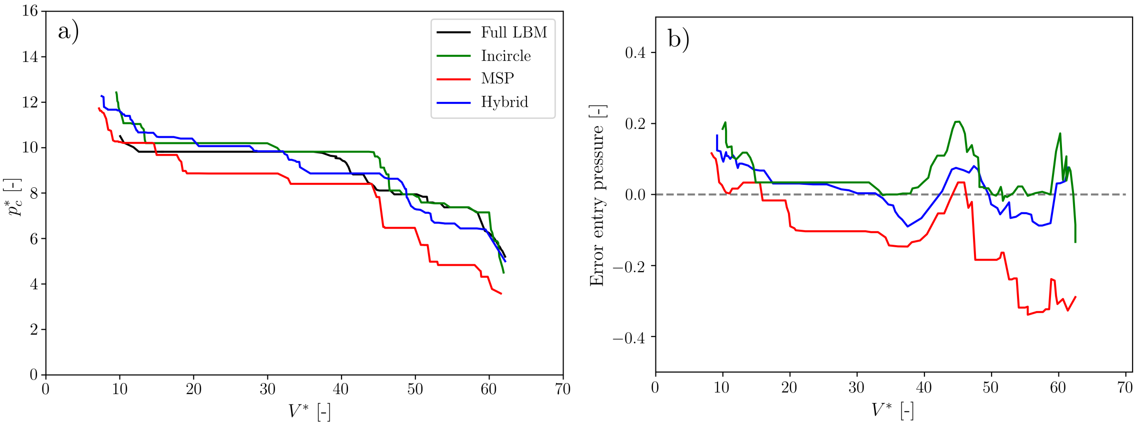

Figure 6.6: a) Primary drainage curves obtained with different methods. b) Error associated to the Hybrid, Incircle and MS-P when predicting the primary drainage curve.

The full LBM model has a smooth transition at the beginning of the drainage until reaching a steady capillary pressure ($p_c^* = 9.8$) that leads to the first intrusion of the non-wetting phase in the sample. Such intrusion is revealed in the finger-like fluid distribution observed in figure 6.2b, where it is clear that the non-wetting phase penetrates through a preferred path to almost reach the porous membrane at the bottom. Conversely, the rest of the models show a steeper transition before starting the main invasion.

It is worth to point out the similar wetting phase content ($V^* \in [8 - 10.5]$) obtained at the end of the simulation. At this stage, liquid still remains in form of continuous phase in trapped regions of the granular assembly. Entrapped wetting phase is found as pendular bridges and trimers (see figure 6.3). Such configurations are possible in the funicular regime. According to Flemmer (1991), the upper limit that distinguishes the pendular and funicular regimes corresponds to a wetting phase saturation degree of $S_w = 34.1\%$, which woud lead to a volume of $V^* \approx 20$. This limit was obtained for equal-sized spherical particles and a porosity of 0.4. Thus, the limit may be different for our case due to the different size of the spheres. Indeed, we observe that, even though many pendular bridges are found at the end of the simulation, some trimers or more complex liquid structures are manifested in figure 6.3 below the S_w bound fixed by Flemmer (1991), which suggests that the pendular/funicular transition threshold might be different for polydisperse spheres.

The divergence between the full LBM simulation and the predictive models is displayed in figure 6.6b. Despite the evident discrepancy between MS-P and the full LBM simulation at the beginning of the drainage, all the approaches give a decent representation of the saturation curve.

Figure 6.6a accounts exclusively for the liquid of the filled pore bodies whereas the liquid bridges or menisci volumes are not included (except for the fully resolved LBM curve in which the real liquid volume is considered). Thus, only the volume of the filled tetrahedra is considered. We have followed different approaches to incorporate the missing volume:

- Regarding the Hybrid method, we include the liquid content from every elementary LBM simulation. For instance, adding the volume on the upper part of the slice that passes through the three grain centers (see figure 5.4a). By means of the $p_c - V$ relationship for each pore throat (see figure 5.5 as an example), we can recover the volume of the wetting phase between the meniscus and the tetrahedron facet for a certain p_c. Indeed, this is a substancial improvement that enables a continuous tracking of the liquid content during the drainage without simplifications.

- MS-P and Incircle approximation must rely on the decompositions explained in section 2.4.1, in which we stated that a liquid cluster is formed by three basic units: filled pore body, liquid bridges, and meniscus. Following Wang et al. (2017), the liquid content in a trimer is divided into three isolated bridges connecting the three spherical bodies (see figure 2.23). Hence:

  $$V = \sum_{i=0}^{N_p} V_{pore,i} + \alpha \sum_{i=0}^{N_{men}} \sum_{k=0}^{m} V_{bridge,i,k} \tag{6.1}$$

  where the volume of the wetting phase V is obtained from the sum of all the filled pore bodies and menisci in the interface. $V_{pore,i}$ stands for the volume of the pore body contained within the tetrahedral cell i, N_p the number of filled pore bodies, N_{men} denotes the number of menisci (facets of the tetrahedral elements that separate two phases), m is the parameter that indicates the number of bridges that can formed between each particle pair (m ranging from 0 to 3), and α accounts for the portion of liquid bridge included in the tetrahedron. Note that for every meniscus, only a portion of the liquid bridge volume is considered (α). The whole liquid volume associated to a certain particle pair is accounted as the sum of bridge portions of the same edge for different tetrahedral cells.

Another approach to compute the liquid content above the tetrahedral facets that separate two phases is based on the Gladkikh approximation detailed in section 2.4.1.2. Unlike the Pendular approximation, in this case, we include the volume between the meniscus and the tetrahedral facet as a cylindrical body V_{cyl}. Consequently, Eq. 6.1 is written as:

$$V = \sum_{i=0}^{N_p} V_{pore,i} + \sum_{i=0}^{N_{men}} ((\alpha + \varepsilon) \sum_{k=0}^{m} V_{bridge,i,k} + V_{cyl}) \tag{6.2}$$

where ε is a parameter that accounts for the missing volume between the main meniscus and the liquid bridges (see figure 2.24b). In this work, $\varepsilon = 0.07$ as done in Melnikov et al. (2015).

Previous approaches account for all the liquid content within the granular assembly enhancing a more realistic view. The new drainage curves are illustrated in figure 6.7. The new formulation is included in the $p_c^* - V^*$ curves with dashed lines. The Hybrid method is indicated as "Hybrid - Modified" when it includes all the liquid volumes. MS-P and Incircle method are designated with the words "Pendular" or "Gladkikh" depending on the approximation they are based on. The comparison between the previous analysis and the volumes added in figure 6.7 shows no significant differences. A modest improvement is observed in the Hybrid and MS-P models. Incircle method, instead, shifted to the higher-error side. Despite using a more realistic description of the interface shape and obtaining slightly better $p_c^* - V^*$ relationships in the Hybrid and MS-P models, we observe a weak influence of the extra liquid volume in form of meniscus above the tetrahedral facets.

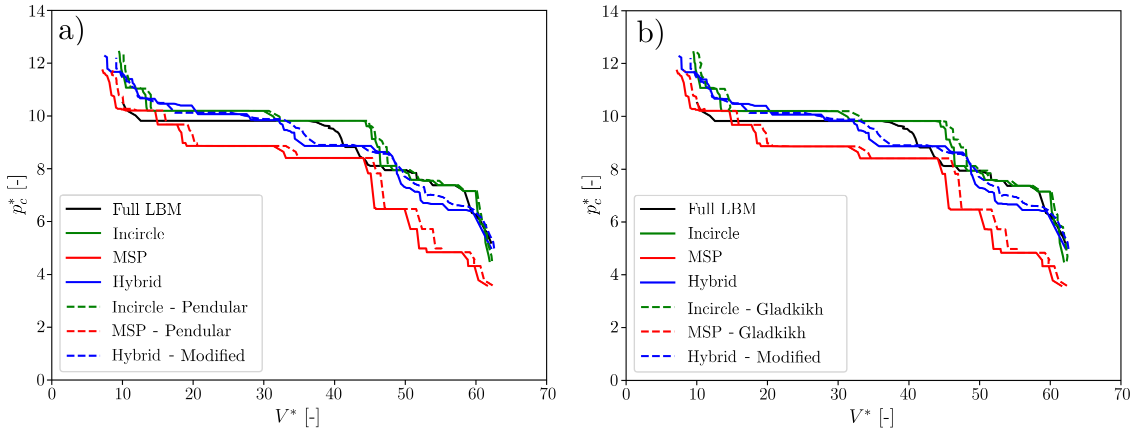

Figure 6.7: Primary drainage curves obtained with different methods including meniscus. MS-P and Incircle account for the extra volume by means of the Pendular (a) and Gladkikh approximation (b).

The average error is quantified for each method in table 6.1. The error is also evaluated incorporating the volume contained beneath the menisci and above the facets separating two phases. We emphasize that the lowest error is achieved for the "Hybrid - Modified" method.

Incircle	Incircle - P	Incircle - G	MS-P	MS-P - P	MS-P - G	Hybrid	Hybrid - M
4.9 %	5.9 %	6.8 %	13.5%	11.7 %	12.3 %	5.9 %	4.4 %

Table 6.1: Average error associated to the Hybrid, Incircle and MS-P methods when predicting the primary drainage curve. The letter P stands for the volume added using the pendular approximation. The letter G stands for the volume added using the Gladkikh approximation. The letter M stands for the volume added when the liquid in the outer part of the facet is included for the Hybrid method.

6.2.4 Computation time

The main purpose of this chapter is to optimize the computational effort by replacing fully resolved methods (full LBM drainage in this work) with alternative models that are computationally more efficient. In this section, MS-P and Incircle approximations are excluded from the comparison due to the low computation cost associated with these two models.

The simple formulation of LBM makes it highly suitable for parallel computing (Kandhai et al. (1998)). For this reason, the results shown for the full LBM model could be executed on 24 cores in parallel. In contrast, one single core per throat has been employed to run the Hybrid model. Computation times are summarized in table 6.2. In order to enhance the comparison between the full LBM and the Hybrid model, the elapsed real time is converted into CPU time, hence, the amount of time of the Hybrid model as if we had 24 available cores. As detailed in table 6.2, the CPU time for the full LBM corresponds to 29.6 days. On the other hand, by using the Hybrid model, the computational cost is reduced down to 11.2 days. This means that the full LBM model takes about 264 % more CPU time than the Hybrid model.

Method	CPU time [days]
Full LBM	29.6
Hybrid	11.2
Hybrid modified 2	6.9

Table 6.2: Execution times to complete the drainage simulation of a 40-sphere packing using 24 parallel computing cores (Full LBM). 1 single CPU core was used for each pore throat for the Hybrid model. We also present the computation time for the Hybrid model when the pore throats that take more than 48 hours are removed and replaced by the Incircle approximation (Hybrid modified 2).

As shown in figure 6.8, pore throat LBM simulations can adopt a wide range of computation time. Some geometric configurations, such as pore throats with large cross-sectional area or high elongation (the relationship between the maximum and minumin length of the pore throat indicate the elongation) usually require a larger computational domain that leads to more demanding tasks. Peaks in figure 6.8 are relatively rare and most of the LBM Hybrid simulations are carried out in a few hours. Pore throats with complex and large geometric domains correspond to

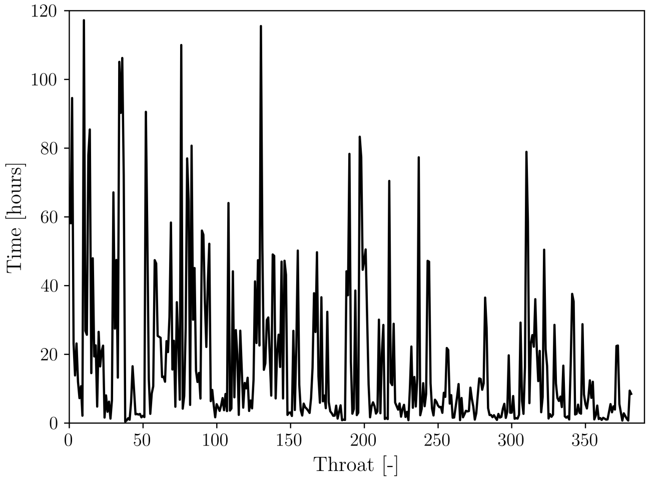

Figure 6.8: Computation time for each pore throat.

isolated cases as illustrated in figure 6.9. The vast majority of pore throats are evaluated within 1 day. Plus, a significant amount of pore throats need less than 5 hours to provide all the hydrostatic properties to the pore-network model.

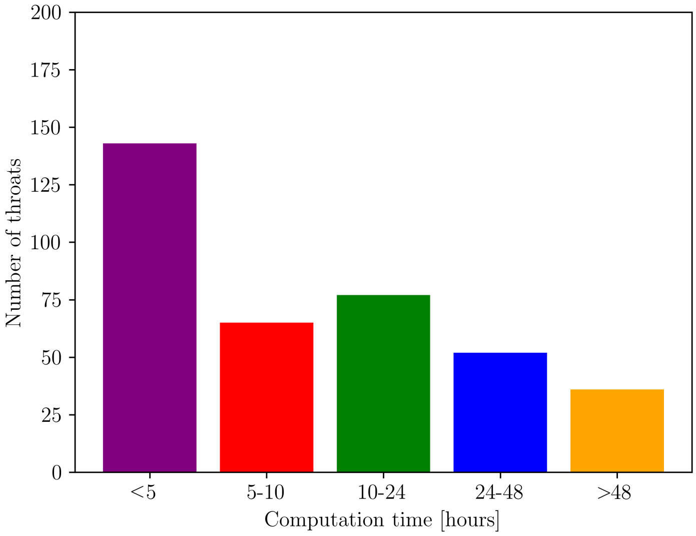

Figure 6.9: Number of throats divided into 5 different computation time groups. The majority of the throats are analyzed in less than 10 hours per throat.

The wide range of computation time reduces considerably the efficiency of the Hybrid model. Towards the optimization of the method, we propose some arrangements to decrease the computation time without sacrificing important data. Thus, we replace the LBM simulations of the pore throats that take more than 2 days by the approximation provided by the Incircle method. This modification leads to a poor description of the fluid-fluid interface and the incapacity to reproduce the $p_c - S_w$ relationship of the pore throat. However, this technique implies a significant benefit in favor of the total computation time. Replacing only the 7.8 % of the pore throats (those that require more than 48 hours to obtain the hydrostatic properties) yields a total computation time of 6.9 days (see "Hybrid - modified 2" in table 6.2 using series simulations in 24 cores), which represents the 23 % of the total time for the full LBM simulation. New entry capillary pressure values for the treated pore throats are found and incorporated into the pore-network. Such modification results into a slight change in the capillary pressure - liquid content relationship of the granular assembly (see figure 6.10). Overall, the trade-off for the Hybrid model remains unaltered at the beginning and the end of the drainage simulation. In contrast, the capillary pressure that leads to the main invasion of the sample is attained earlier ($V^* = 42$) than in the original Hybrid model. This new strategy gives a better description of the $p_c - S_w$ curve than the original Hybrid model. Nonetheless, the information is scarce and more numerical simulations should be performed with different granular assemblies before reaching a general conclusion.

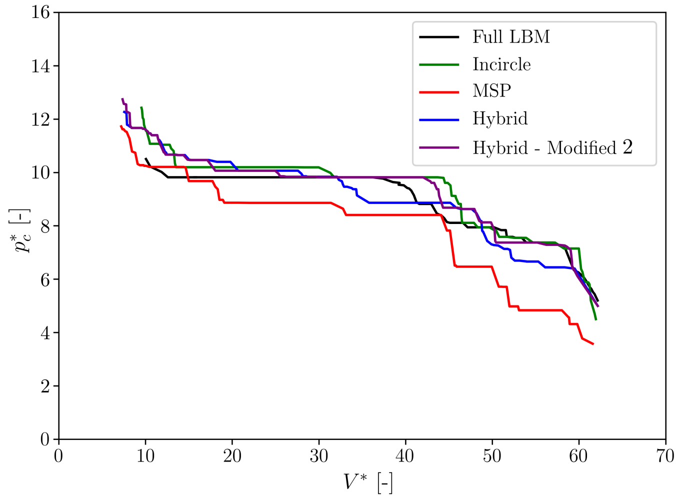

Figure 6.10: Primary drainage curves obtained with different methods. This figure includes the saturation curve obtained with the Hybrid model ("Hybrid - Modified 2") when the pore throats that take more than 48 hours are replaced by the results of the Incircle approximation.

It is not trivial do determine in advance which pore throats are highly demanding in terms of CPU time. Therefore, we suggest different approaches to decide which pore throats should be replaced by the Incircle method:

- Fixing a maximum length (L) for a computational domain. Then, pore j is approximated with the Incircle method instead of a direct LBM simulation when: $nx_j > L$ or $ny_j > L$ or $nz_j > L$. Example: $L = 100lu$.
- Imposing a maximum angle (ς_L) between the solid walls that form the prism. If the angle between two particle pairs is larger than ς_L, then the throat is considerably elongated. Example: $\varsigma_L = 170^o$.
- Setting a maximum and a minimum inscribed circle radius (r_{ins}^{min} and r_{ins}^{max}). When r_{ins} is out of the fixed bounds, the direct LBM simulation is either very

time-consuming (when $r_{ins} > r_{ins}^{max}$) or significantly inaccurate (if $r_{ins} < r_{ins}^{min}$). Example: $r_{ins}^{max} = 40lu$ and $r_{ins}^{min} = 3lu$.

6.2.4.1 Towards the optimization of computation time

There are several ways to speed up the simulations, however, they usually come in detriment of other parameters. Indeed, one of the main advantages to use the Hybrid model is to obtain valuable information beyond the entry capillary pressure predicted by approximation. Direct LBM simulations provide an accurate description of the $p_c - V$ relationship and liquid morphology during the invasion of the pore throat. As a result, capillary forces can be easily evaluated for each solid particle and menisci volumes over the filled tetrahedra can be considered. These are two important features that make a difference compared to the approximation methods. Nonetheless, we might not be interested in all the parameters provided by the Hybrid model. Therefore, it is worth to redefine the computation domain or some of the boundary conditions in order to optimize the computation resources.

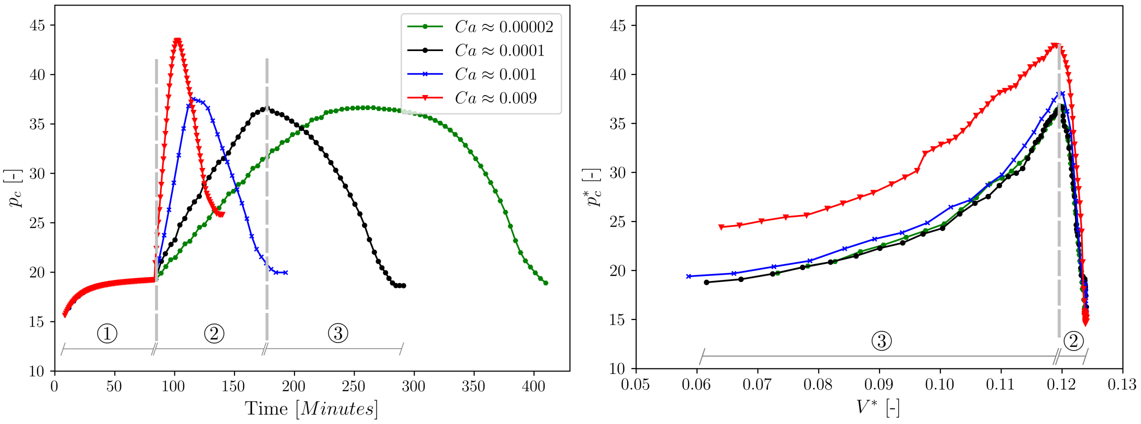

Figure 6.11: Typical a) capillary pressure - time evolution and b) $p_c^* - V^*$ relationship for two different capillary numbers. ① Reaching the equilibrium, ② Increasing p_c and ③ Invasion of the pore throat.

Figure 6.11 illustrates the evolution of p_c in time and liquid content. Three steps are distinguished (the categories are depicted in figure 6.11 for $Ca \approx 0.0001$ - Black curve):

① *Reaching the equilibrium:* Initially, the pore throat is fully saturated. Several iterations are required for the interface to reach a steady-state in which capillary and pressure forces are balanced.

② *Increasing p_c:* A flux is imposed to displace the interface. p_c increases until it reaches the entry capillary pressure (peak values in figure 6.11).

③ *Invasion of the pore throat:* After the peak ($p_c = p_c^e$), the non-wetting phase penetrates the pore throat. Flux is no longer imposed, however, p_c decreases considerably as the interface is redistributed in the pore body.

Figure 6.11 illustrates the influence of viscous forces on time and the $p_c - V$ relationships. It is worth noting that Ca is a result and not a controlled parameter. As mentioned in subsection 6.2.3, the flux is imposed and it depends on a fixed tolerance between the density on one time iteration at the interface nodes. Large tolerances ($Tol = 10^{-4} \rightarrow Ca \approx 0.009$) trigger a fast drainage where dynamic effects are evidenced during the invasion of the pore body. Whereas restrictive tolereances ($Tol = 5 \cdot 10^{-6} \rightarrow Ca \approx 0.00002$) lead to slow drainage close to a complete quasi-static flow.

From figure 6.11 we deduce three potential ways to reduce the computation time:

- Increasing the capillary number as long as $Ca << 1$. Such scenario introduces some dynamic effects as the viscous forces become relevant with increasing Ca. Figure 6.11 shows a weak impact on the value of p_c^e is manifested as long as $Ca < 0.001$. Indeed, the pressure peaks of the curves of figure 6.11 for $Ca < 0.001$ are almost coincident. The dynamic effects are also unnoticeable during the invasion of the pore body, in which we observe a parallel decay of p_c in terms of volume with a small gap between the curves in figure 6.11b. Conversely, the $Ca \approx 0.009$ curves plotted in figure 6.11 show the viscous contribution is not negligible. It is particularly interesting to observe the viscous dissipation of $Ca \approx 0.009$ illustrated as a p_c^* gap in figure 6.11b.

- Another time-saving technique consists in skipping or reducing the *Reaching the equilibrium* step (see ① in figure 6.11). The decrease of computation time, however, would introduce some error at the beginning of the $p_c - V$ relationship. We remind the reader that the global volume occupied by the wetting phase is the sum of filled tetrahedra plus the volume between the interface and the tetrahedra facets. The latter volume is obtained for each pore throat using the corresponding $p_c - V$ (see figure 6.11b). Consequently, the strategy adopted when skipping the ① *Reaching the equilibrium* step might introduce inaccuracies in the menisci volumes, specially for low p_c values.

- If we are mainly interested in the primary drainage curve and the invasion path, the most relevant parameter is the entry capillary pressure. It is, thus, reasonable to stop the simulation after reaching $p_c = p_c^e$. The information furnished by ③ *Invasion of the pore throat* is exclusively devoted to the final liquid morphology, which might not be important if we are not interested in the study of capillary forces.

Besides acting on the flow conditions or the steps of figure 6.11, the spatial discretization can be adjusted to optimize the computational resources. In section 3.3.1.5 we discussed the possibility to adapt the mesh resolution to optimally balance the computation time and the quality of the results. This could be done by setting the reference curvature equal to the curvature at the moment of invasion (we could approximate this value using the Incircle method). In contrast to the previous approaches in which pore throats with large domains were simulated using an important amount of CPU time and small pore throats were inaccurately represented due to the presence of sharp interfaces in coarse meshes, the implementation of this technique results into different mesh resolutions (one for each pore throat), that provide accurate hydro-mechanical information to the global the Pore-Network approach as long as the fixed reference curvature has an acceptable spatial discretization.

6.2.5 Invasion paths

The aim of the present section is to characterize and quantify the invasion path of the non-wetting phase through the porous media. As the capillary pressure is increased, the interface moves through the larger pore throats with the lowest entry capillary pressure. During the drainage process, the receding wetting-phase can be entrapped in the granular assembly in the form of disconnected clusters. The evolution of the interface was tracked (see figure 6.2) throughout the full LBM and compared with the invasion pathways obtained with the Hybrid, MS-P and Incircle methods.

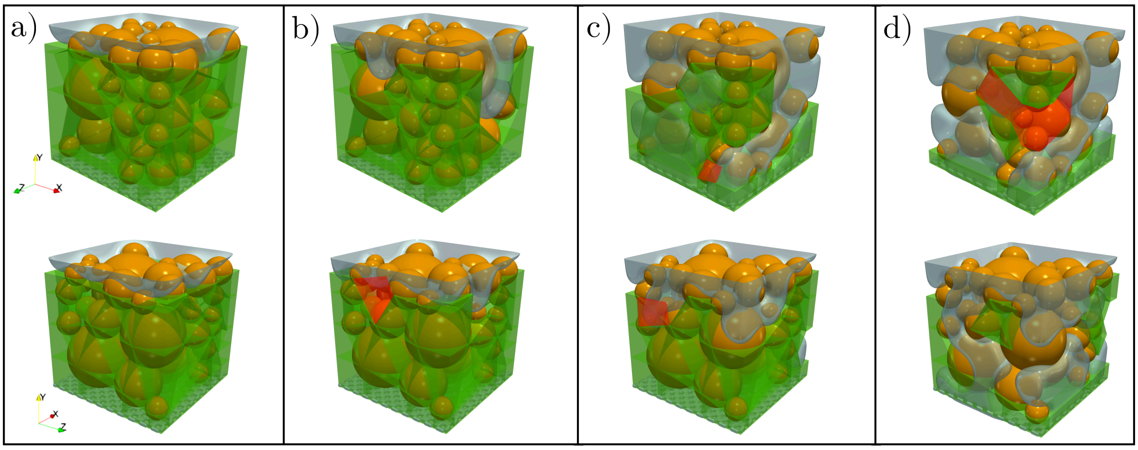

Figure 6.12: Comparison of the invasion path between the full LBM simulation (blue isosurface) and the prediction obtained with the Incircle method (wetting phase displayed in green). Mismatch between the two models is depicted in red. Two different views are displayed. a) $p_c^* = 4.8$, b) $p_c^* = 6.6$, c) $p_c^* = 8.4$ and d) $p_c^* = 10.6$.

Figure 6.12 captures the invasion path for different time steps. This sequence superposes the full LBM interface (translucid blue isosurface) and the cells filled with wetting phase after running the Incircle model (translucid green). Figure 6.12b and figure 6.12c show almost identical pathways. Thus, Incircle method is able to accurately reproduce the first intrusion. Only the regions depicted in red correspond to cells with different phases for the two models. As the drainage proceeds, the non-wetting phase keeps occupying the sample leaving behind some disconnected liquid clusters (see figure 6.12d). Even though wetting phase trapped in the assembly is well represented with the Incircle method, figure 6.12d suggests that there is a phase mismatch between the two models at some points of the sample.

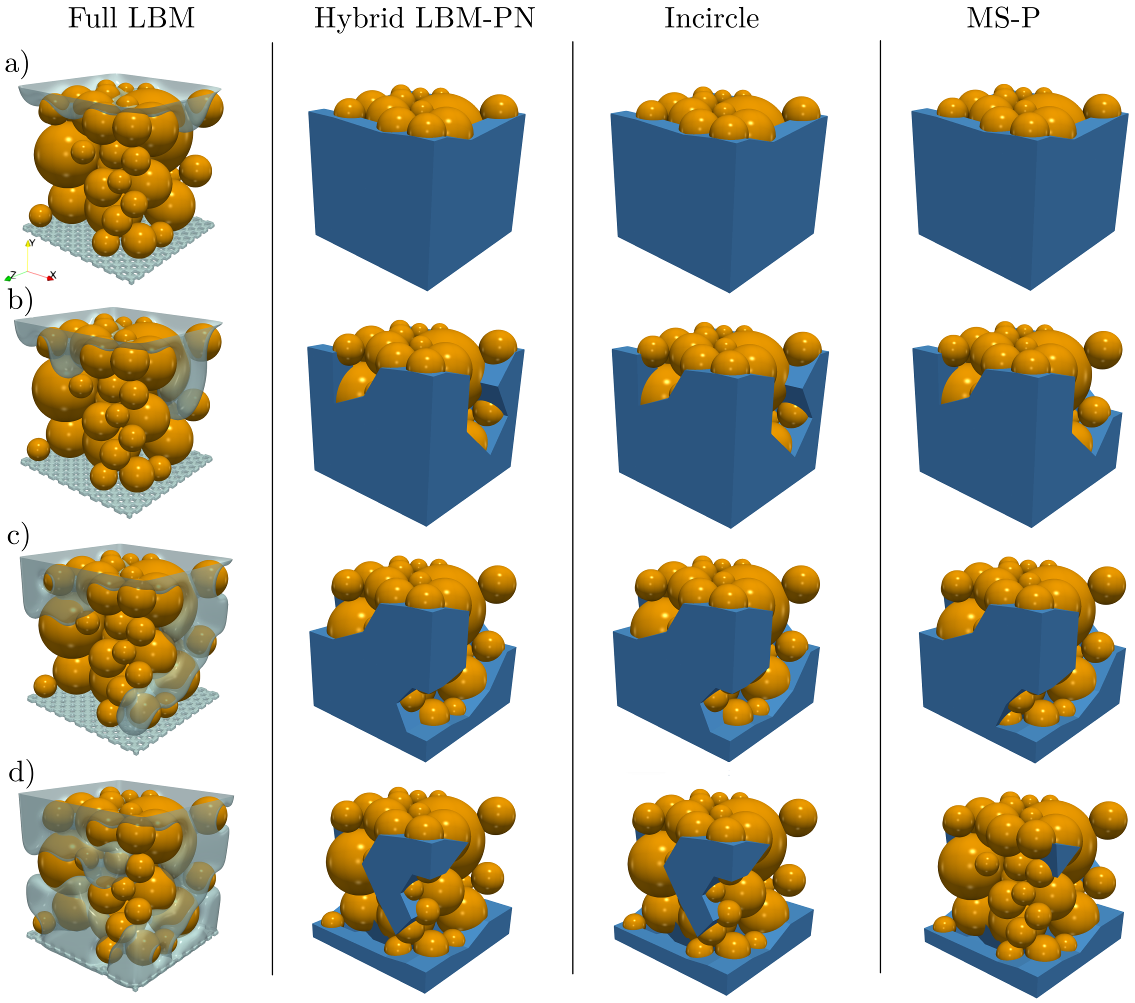

Figure 6.13: Comparison of the invasion path between the full LBM simulation, Hybrid, MS-P and Incircle methods. Back view. a) $p_c^* = 4.8$, b) $p_c^* = 6.6$, c) $p_c^* = 8.4$ and d) $p_c^* = 10.6$.

The comparison illustrated in figure 6.12 is similarly reproduced for the rest of the models in figures 6.13 and 6.14, where the wetting phase is illustrated in blue. We remark the ability of all the methods to predict the first preferential path (the same intrusion is observed in figures 6.13b and 6.13c). All the methods show good agreement except for figures 6.13d and 6.14d, this stage corresponds to the end of the simulation when the liquid is mainly found in disconnected clusters. The wetting phase adopts different configurations at this moment. Hybrid and Incircle models produce almost coincident liquid structures at the end. On the other hand, MS-P presents higher discrepancies with respect to the full LBM. The liquid cluster identified in figure 6.13d for the Hybrid and the Incircle model has some similarities with the wetting phase region observed in the full LBM, in which, the liquid is still connected with the bottom, therefore, it is not an isolated cluster. The same characteristics are found in figure 6.14d. In this case, the cluster obtained in MS-P, Incircle and Hybrid models resembles the meniscus shape adopted by the full LBM. All the liquid structures would match better if the wetting phase in the full LBM was getting disconnected to form isolated clusters.

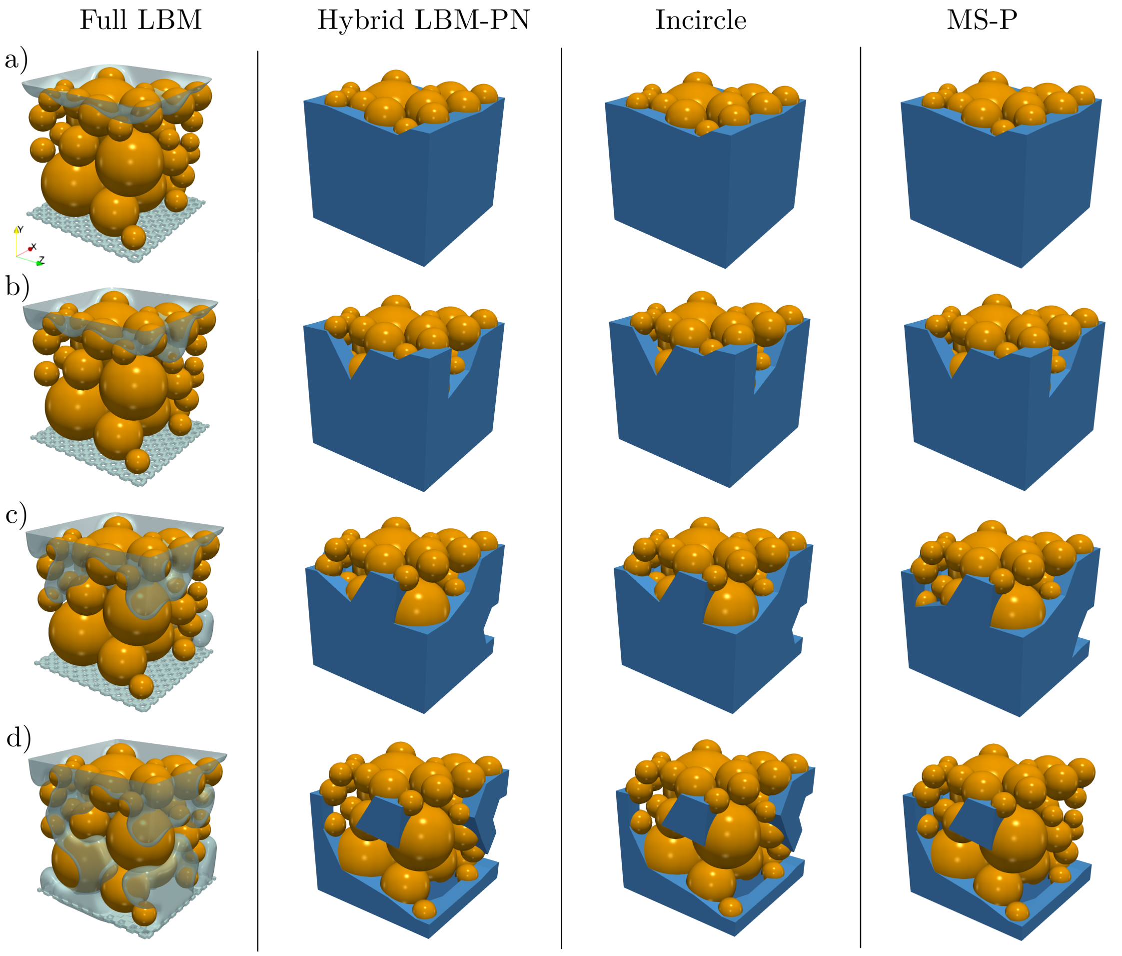

Figure 6.14: Comparison of the invasion path between the full LBM simulation, Hybrid, MS-P and Incircle methods. Front view. a) $p_c^* = 4.8$, b) $p_c^* = 6.6$, c) $p_c^* = 8.4$ and d) $p_c^* = 10.6$.

In order to have a better visualization of the granular skeleton, the distribution of phases is graphically represented in three vertical slices (see figure 6.15). It is worth mentioning that figures 6.16, 6.17 and 6.18 are based on a triangulation, thus, the fluid distribution depicted in the planes is strongly dependent on the position of the vertical slice. Consequently, we recommend to study the preferred path and fluid patterns from 3D visualizations as shown in figures 6.13 and 6.14.

The first intrusions are well interpreted in all the methods as shown in figure 6.16 and figure 6.18. Less satisfactory results are obtained at the latest stage of the drainage. The models are unable to predict the entrapped liquid phase with the same accuracy as the first intrusions. Good agreement between the full LBM and the Hybrid model is observed in figures 6.16d and 6.18d. MS-P and Incircle methods reveal reasonably acceptable results in figures 6.16d and 6.18d. Finally, all the models are less successful to estimate the wetting phase clusters in figure 6.17d. It should be noted that film flow becomes relevant at low saturation degrees for the fully resolved LBM simulation. This situation is not manifested in the rest of the models in which the wetting phase in isolated clusters or bridges remains completely disconnected.

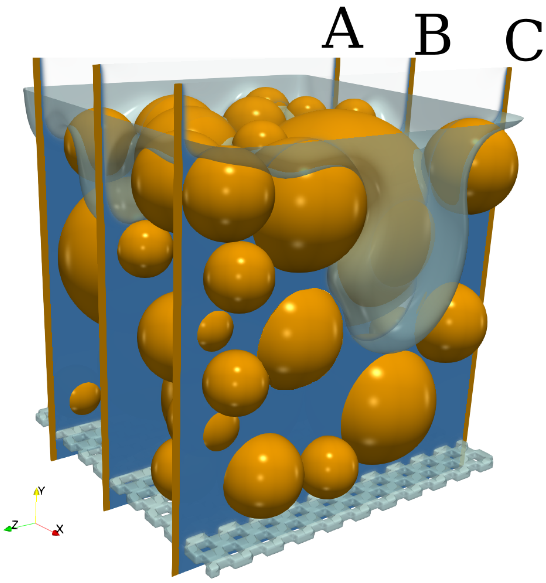

Figure 6.15: Vertical slices of the granular assembly.

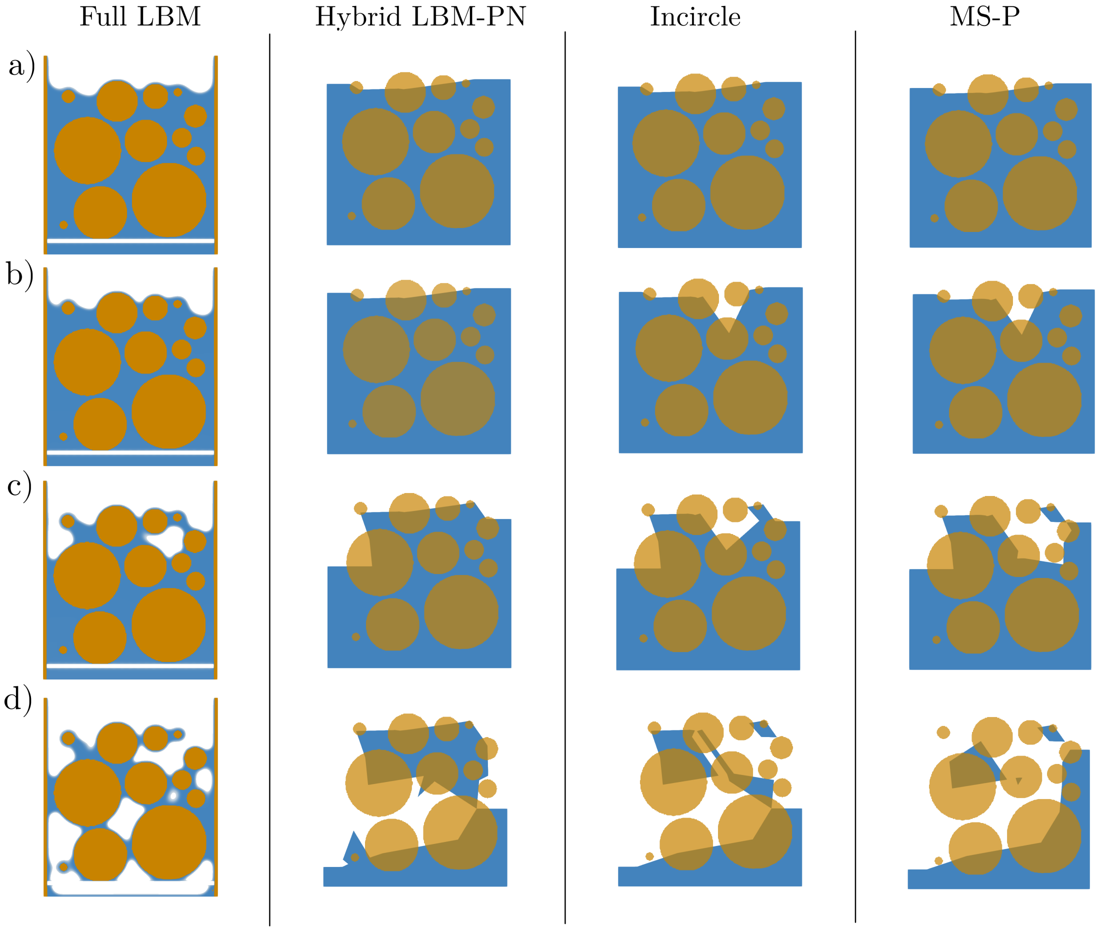

Figure 6.16: Comparison of the invasion path for plane A (see figure 6.15). a) $p_c^* = 4.8$, b) $p_c^* = 6.6$, c) $p_c^* = 8.4$ and d) $p_c^* = 10.6$.

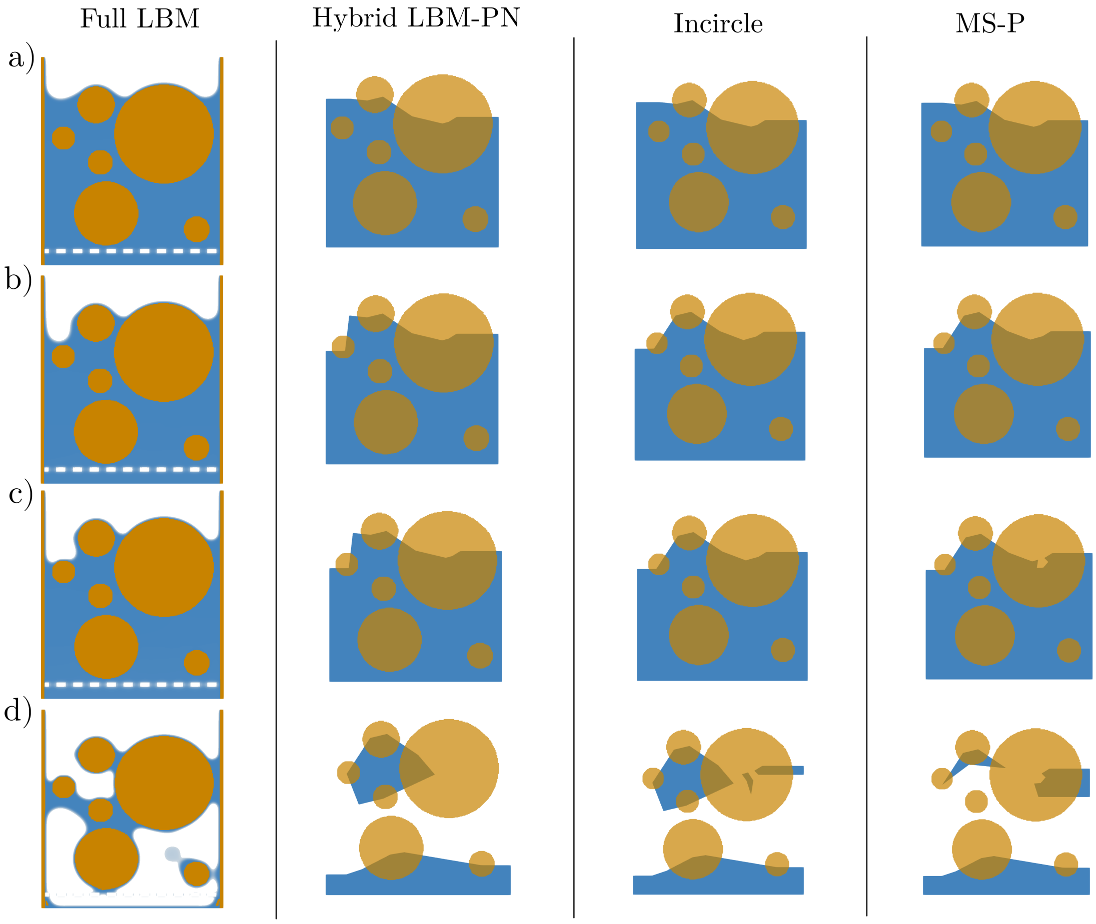

Figure 6.17: Comparison of the invasion path for plane B (see figure 6.15). a) $p_c^* = 4.8$, b) $p_c^* = 6.6$, c) $p_c^* = 8.4$ and d) $p_c^* = 10.6$.

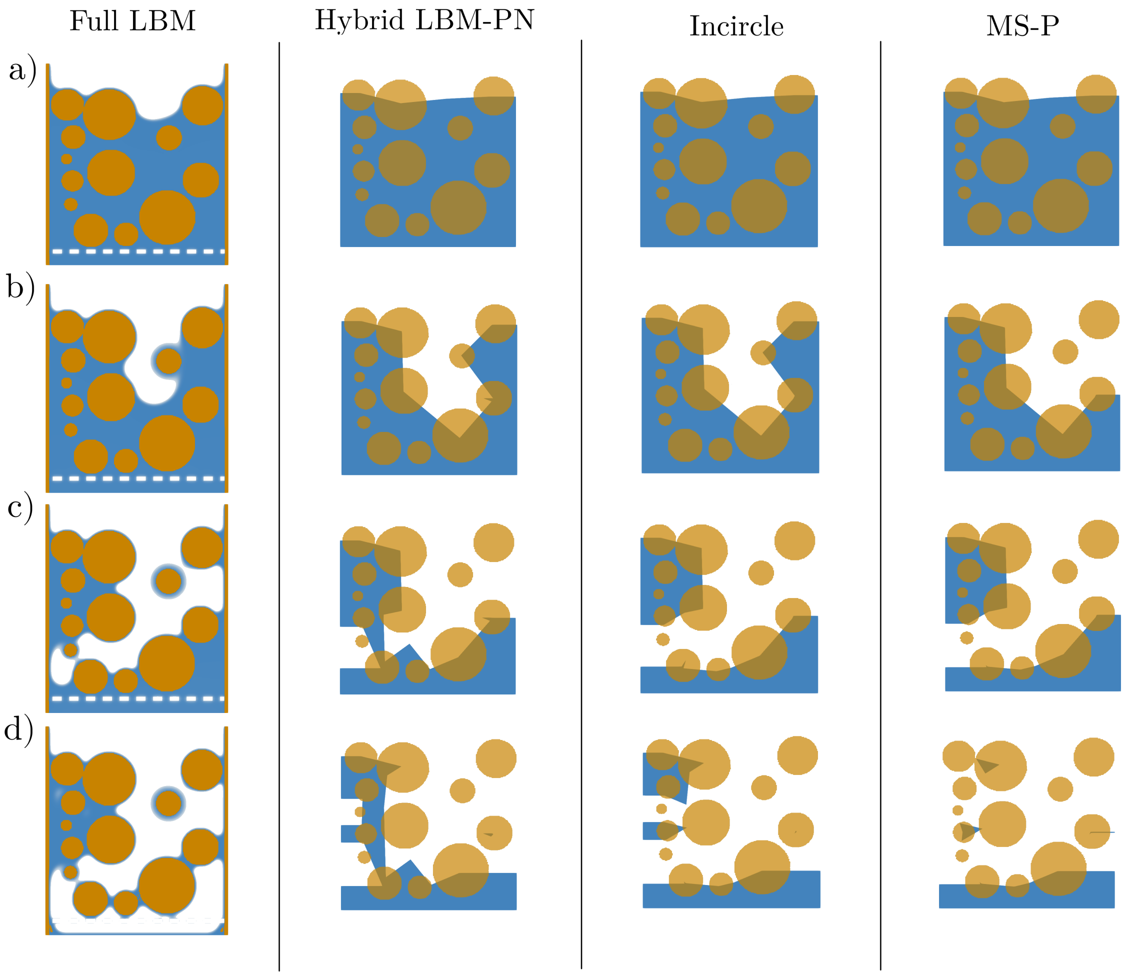

Figure 6.18: Comparison of the invasion path for plane C (see figure 6.15). a) $p_c^* = 4.8$, b) $p_c^* = 6.6$, c) $p_c^* = 8.4$ and d) $p_c^* = 10.6$.

Although the series of figures presented before offer an easy and straightforward way to interpret the invasion paths, we propose another approach to account for the invasion sequence. Figure 6.19 shows the coincident volume and coincident throats between the full LBM and the rest of the methods in the y-axis. The intersected volumes and throats are evaluated during the drainage as the cells and throats are progressively invaded. Figure 6.19 evidences that the sequence of invasion is accurately reproduced for all the methods. As a matter of fact, around the 80 % of the volume and throats of the wetting phase coincide with the ones obtained in the full LBM at the end of the simulation.

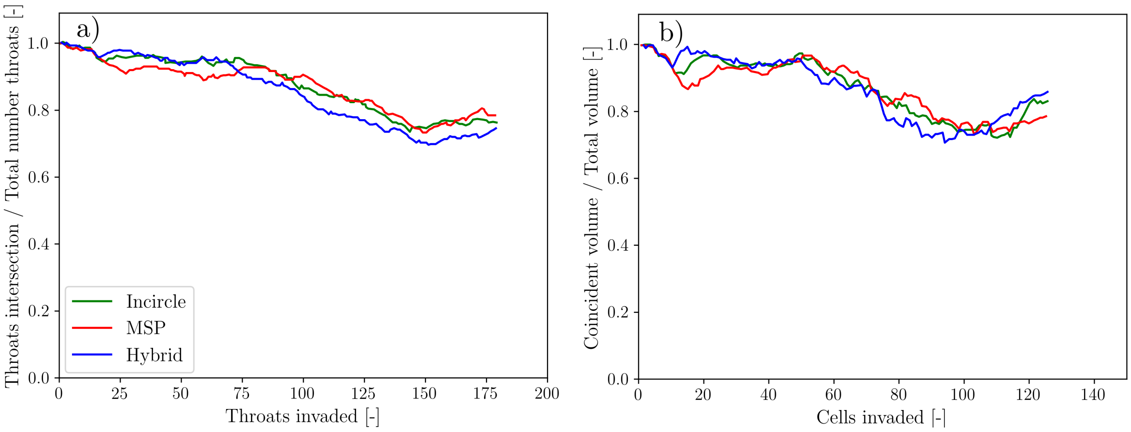

Figure 6.19: a) Number of invaded throats VS intersected throats. b) Number of invaded cells VS intersected volume

6.2.6 Liquid morphology comparison

Understanding the liquid morphology is crucial to have better predictions on the capillary forces for mechanical couplings. In this section, a comparison in terms of liquid morphology is carried out between the Hybrid and the full LBM model.

When the non-wetting phase penetrates the pore throat, a meniscus known as the main terminal meniscus (MTM) is created. Likewise, the interface meniscus between the wall and a sphere-sphere connection forms what we call arc menisci (AM). The evolution of these menisci is observed in figures 6.20 and 6.21, and in the graphical material provided in the Appendix. Over the course of the invasion process, the Hybrid model is mostly in reasonable agreement with the full LBM. The Hybrid model overestimates the volume the MTM wetting phase, whereas the menisci between the spherical particles are underestimated.

Furthermore, the series of figures 6.20 and 6.21 reveal that the Hybrid model is able to identify which sphere pair is likely to be connected with a pendular bridge. The last picture of figure 6.20 shows that only one pendular bridge is formed. As expected, the pendular bridge obtained in the full LBM model is axisymmetric around the axis connecting the centres of the two particles (see figures 6.20 and 6.21). Unfortunately, the pendular bridge obtained in the Hybrid model is clearly not symmetrical. The upper part of the bridge mimics the full LBM bridge with decent accuracy, however, the lower part is misrepresented by the Hybrid model. The solid walls bounding the pore throat (see figure 5.2 and figure 5.3) distort the real geometry and hinders a good representation of interface meniscus.

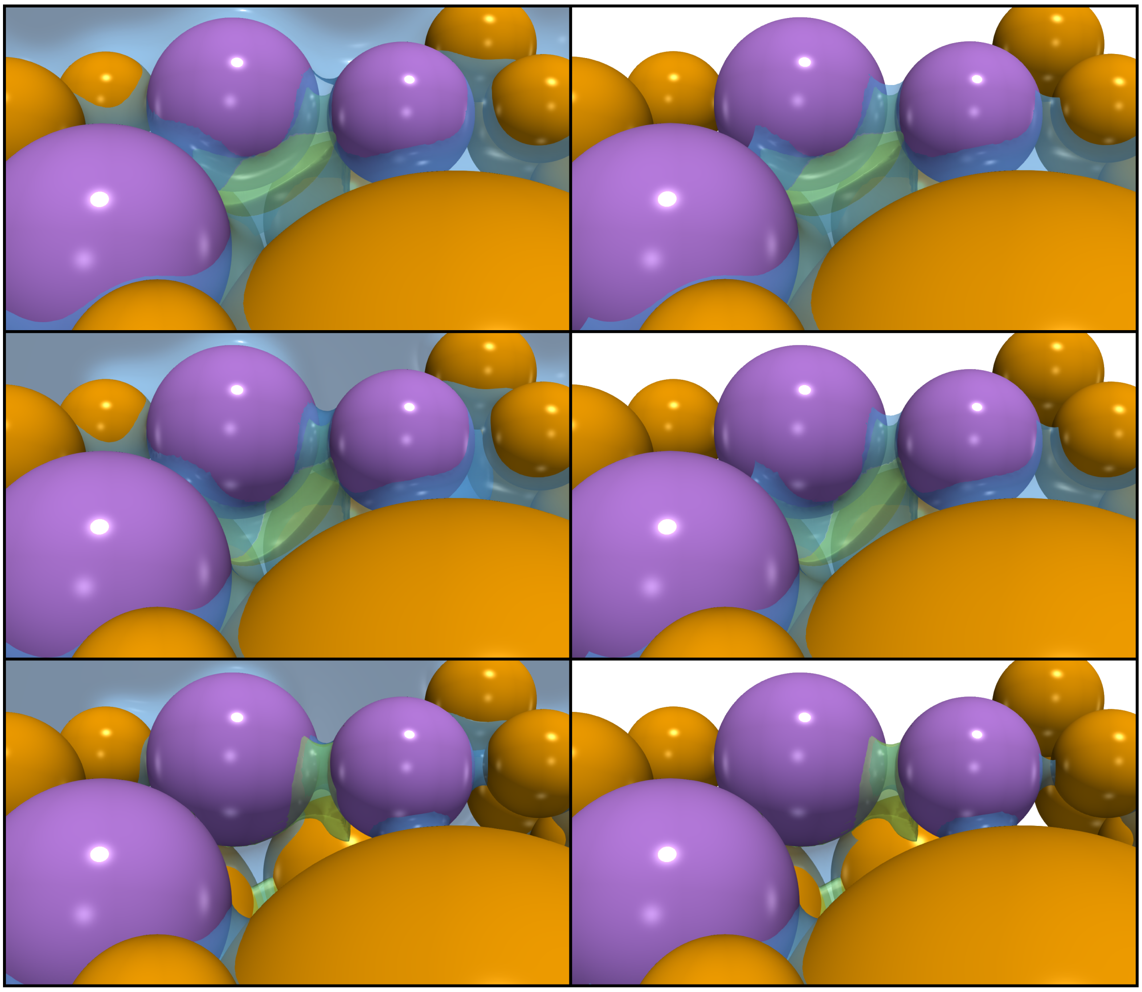

Figure 6.20: Superposition of the interfaces obtained with the full LBM analysis and the Hybrid method.

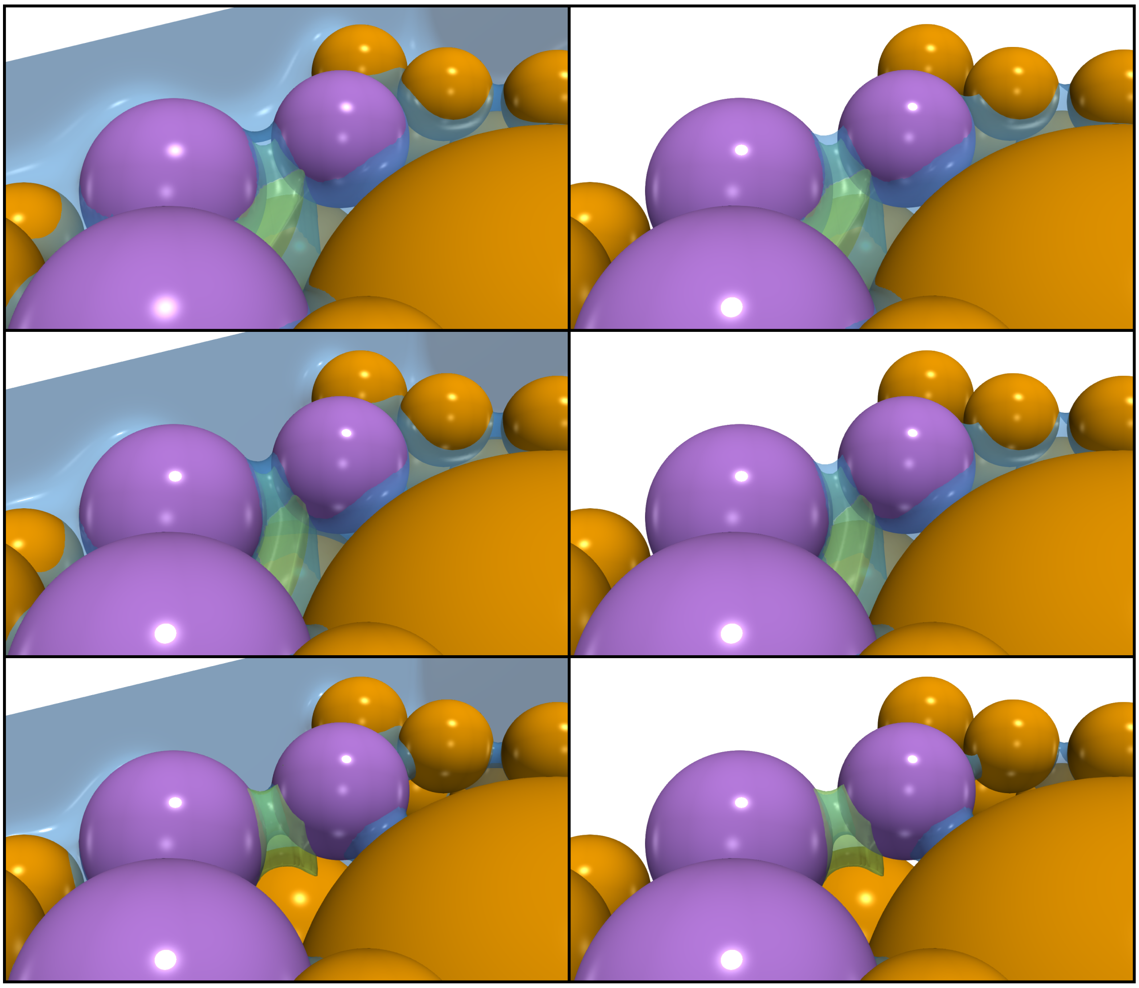

Figure 6.21: Superposition of the interfaces obtained with the full LBM analysis and the Hybrid method.

6.3 Conclusions

We developed a Hybrid method base on the LBM and a pore network model. In comparison with a fully resolved method (in this work: the LBM), the decomposition into small subsets leads to more efficiency in terms of computation time. The Hybrid method is able to reproduce accurately the movements of the interface during the drainage of the pore space. Liquid bridges are easily identified and well described after the invasion of every pore throat. The computational cost can be reduced by replacing the largest and most elongated pore throats. Such throats with specific geometric configurations are particularly demanding in terms of computation time, thus, simple approximation are used instead. Besides, we introduce potential improvements that can be implemented to further reduce the computational time (reducing or skipping the initialization process until equilibrium, increasing the capillary number, stopping the simulation after reaching the entry capillary pressure, etc).

Both the Hybrid model and simple approximations (Incircle and MS-P methods) provide fairly good agreement with the full LBM simulation concerning the primary drainage curves. Likewise, the invasion sequence of the non-wetting phase during the drainage is predicted with good accuracy with all the pore-scale methods. The slight improvement in accuracy by the Hybrid model might seem less compelling respect to the approximations considering that Incircle and MS-P methods predict the main hydrostatic properties without important computational resources. However, the Hybrid model is able to determine the capillary pressure – wetting-phase content relationship for each pore throat and the liquid morphology after the invasion of the non-wetting phase. Such feature makes a significant difference in comparison with the rest of the pore-scale approximations for two reasons: On the one hand, tracking the $p_c - V$ relationship for each pore throat is crucial to reconstruct the primary drainage curve. The total liquid content for a certain capillary pressure is recovered as the sum of filled tetrahedra plus the menisci volumes. The later volumes are frequently neglected or approximated. In the Hybrid model, however, the volume over each tetrahedron facet is easily accessible by means of the $p_c - V$ relationship for the corresponding pore throat. Additionally, the strategy of the Hybrid method could shed some light on the analysis of complex phenomena such as the ”pore refilling” studied in section 4.3.4 in 2D. Determining the $p_c - V$ relationships for each pore during drainage and imbibiton (see section 5.5.4) is a first step towards a more detailed description of the local mechanisms. On the other hand, knowledge of geometry of interfaces is necessary to study the hydro-mechanical couplings involving accurate determinations of forces on the solid particles. Those forces can be deduced from the interface shape as explained in Chapter 3, and they could be integrated in a hydro-mechanical model similarly to Chapter 4, where the Throat-Network model was coupled with the DEM.

Despite following very similar paths during the drainage, some discrepancies are found at the end of the simulation. The Hybrid model reproduces slightly better than the MS-P and the Incircle methods the clusters trapped in the granular assembly. The results not only show evidence of the promising capabilities of the novel Hybrid model, but they also validate the use of the Incircle and MS-P as reliable methods to approximate the primary drainage curve and the invasion sequence when the computational resources are limited.

Chapter 7

Conclusions and Perspectives

The main objective of this thesis was to evaluate the hydrostatic properties of liquid microstructures beyond the pendular regime by means of lattice Boltzmann (LBM) simulations. We focused on different approaches to describe the liquid morphology and the capillary forces at the pore scale. Additionally, we have developed new techniques to study multiphase flow through porous media. This final chapter summarizes the main conclusions of the research carried out in the thesis and introduces a brief discussion of the perspectives for future work.

Conclusions

The first part of this thesis (Chapters 2 and 3) was devoted to examine the accuracy of the lattice Boltzmann method based on the multicomponent Shan-Chen model (SC-LBM) and the ability to reproduce multiphase flow at the micro-scale:

- The LBM was calibrated and validated by comparison with theoretical and numerical solutions. The numerical simulations presented almost coincident results in terms of liquid morphology and $p_c - V$ relationship.
- Even though the multicomponent Shan-Chen lattice Boltzmann method (SC-LBM) can accurately reproduce the fluid displacement through porous media, the thickness of the film over the solid objects does not correspond to a physical thickness. In order to maintain reasonable computational costs and ensure the accuracy of the results without substantially increasing the discretization of the mesh, we proposed a geometrical correction of the solid boundaries. This correction led to shrink the size of all solid objects by a fixed length to minimize the mesh-dependency of the results. Furthermore, this method led to quadratic convergence in contrast to the superlinear convergence (with an exponent of approximately 1.4) without the retracting wall.
- The study has been extended to more complex liquid structures, such as the trimers or higher-order liquid clusters. The evolution of trimers under drying condition was compared with numerical data provided by Wang et al. (2017)

with satisfactory agreement. Additionally, Pendular and Gladkikh approximations were included and considered as possible alternatives to predict $p_c - V$ curves.

- In Chapter 3, we developed a method to evaluate the forces acting on solid objects in contact with two or more fluids. Our approach was based on the integration of stresses around the solid bodies. The volume element used for the integration was slightly larger than the solid object, thereby, we overcame the difficulties associated with the non-physical numerical film around the solid boundary. Fairly good agreement was found between SC-LBM and the theoretical solution given by Young-Laplace equation for a pendular bridge. SC-LBM results were also compared to experimental data for trimer structures with reasonable agreement.

- The study on capillary forces during the funicular regime suggested that the shape of the interface has a stronger impact on the forces than the capillary pressure far from the regime/shape transitions. Indeed, no significant discrepancies were revealed for certain configurations (trimers, tetramers, bridges) whereas sudden capillary force jumps were manifested from one liquid structure to another. The mechanism is obviously related to the abrupt change of curvature adopted in the new liquid configuration, when the fluid interface is displaced to accommodate the same liquid volume.

- The results obtained for the tretramers in terms of capillary force confirmed a phenomenon previously reported but not fully understood, the fact that the highest cohesion values take place during the regime transitions (capillary regime to funicular and funicular regime towards pendular state). The evolution of capillary forces exerted on the particles at the pore scale may explain the global response of wet granular materials.

- Results obtained in Chapters 2 and 3 evidenced that low interface curvatures ($k < 0.055 lu^{-1}$), related to fine mesh resolutions, lead to huge computational costs without a significant gain in accuracy. Thus, we recommend adjusting the geometric LBM parameters to enhance critical reference curvatures that $k \in [0.06 - 0.09] lu^{-1}$. In order to accomplish this, the spatial resolution is adapted to accommodate numerical curvatures equal or lower than the critical reference curvature. Although the curvature criterion is difficult to implement due to the complex geometry of granular media, we believe that it provides orientative information that can be taken into account when it comes to decide the dimensions of the computational domain. Furthermore, this method could be extremely useful for multiphase flow through porous media with regular sphere-packings or regular arrays of circular cylinders. In such cases, knowing the geometry in advance may help predict the critical curvature (for instance, the one associated with the entry capillary pressure). It is, therefore, much more efficient to redefine the mesh resolution for a certain capillary pressure than adjusting the spatial discretization as function of the particle size.

Due to the high computational cost associated to LBM simulations, Chapters 4 and 5 explored the possibility of hybrid models based on the decomposition of the granular assembly to evaluate the hydro-mechanical properties with an acceptable computation time.

- Chapter 4 presented a 2D Throat-Network model (TN) inspired by previous pore-network models but not relying on the concept of pore-bodies with partial saturation. TN is based on analytical solutions and capable to reproduce three-phase flow in 2D porous media made of packed circular particles. The position of the fluid-fluid interface was well described and proven to be almost identical to the LBM solution in elementary examples. Throughout the simulations it became evident that the TN model can handle several local events such as: Haines jump, meniscus rupture into independent menisci, coalescence of two menisci and pore refilling through dynamic events. Because of its versatility and accuracy, TN is an attractive alternative to simulate multiphase problems in 2D. For instance, the flow through cylindrical rods or the evaluation of permeability in fibrous porous media. The extension of the concept to 3D models is challenging, though, and was only partially addressed in the sequel of the thesis.

- The Throat-Network was coupled with the Discrete Element Method (TN-DEM). This model was devoted to simulate the multiphase fluid flow in deformable polysdisperse 2D granular materials.

- In Chapters 5 and 6 we proposed a Hybrid model that takes advantage of both the efficiency of the pore-network models and the accuracy of direct fluid dynamics solutions obtained with LBM. The Hybrid method was able to reproduce accurately the movements of the interface during the drainage process. Pendular bridges were easily identified and well described after the invasion of every pore throat. The procedure was further optimized by replacing the throats with complex geometric configurations by simple approximations. Relying exclusively on approximation methods (MS-P and Incircle methods) is another alternative to predict the main hydrostatic properties without important computational cost. As a matter of fact, the Hybrid model did not offer a much better solution than the Incircle approximation when studying the invasion path or the primary drainage curve. In contrast, Hybrid model is the only one able to determine the pressure - volume relationship for each pore throat and the liquid morphology after the invasion of the non-wetting phase. Identifying the remaining interfaces is an important feature if we want to evaluate the inter-particle capillary forces. Additionally, the pressure - volume relationship is a key ingredient for non-trivial evolution such as pore refilling. The Hybrid model is, indeed, a promising tool to investigate complex phenomena at the pore scale. Besides the valuable information obtained after the $p_c - V$ relationships, the liquid morphology is fully described during the regime transitions.

- We believe that the Hybrid model would probably have a stronger impact on a lager problem with thousands of pore throats. In parallel simulations with relatively small computational domains, the execution speed is multiplied by a factor two doubling the number of cores. Large-scale problems that require the exploitation of massively parallel systems are frequently accompanied by a drop in efficiency. In the Hybrid method, however, the scalability is optimal. Due to the fact that each pore throat (small domains) are assignated to a single core, efficiency does not depend on the size of the granular assembly. Besides, some regions of the sample can be excluded from the simulation (empty pores and isolated cluster with no flux). Finally, the $p_c - V$ relationships obtained during the drainage allow a prediction of the imbibition procedure without further simulations. Conversely, a fully resolved LBM performance requires the imbibition simulation to complete the drainage-imbibition cycle.

- When the computational resources are limited and we are obliged to use simple approximations, the results suggested that the Incircle method is the best choice to study the $p_c - V$ relationship. Conversely, MS-P provides more reliable results in terms of interface profile. Throughout the thesis, several MS-P cross-sectional throat profiles were found similar to the LBM solutions. Moreover, at the pore scale, Gladkikh approximation was found to be a good approach to compute the liquid content of isolated clusters.

Perspectives

The multicomponent SC-LBM introduced in this thesis is able to accurately reproduce multiphase flow within porous media. However, the high computational cost leads to a growing interest to investigate the phenomena by means of alternative methods.

First of all, it would be interesting to evaluate the advantages and limitations of other multiphase LBM models. Previous researches have reported direct comparison between the single-component Shan-Chen model, the color gradient model and the free energy model in terms of density and viscosity ratio, diffusion properties, level of parallelism, ability to describe capillary fingering, etc. Yet, we recommend to investigate the accuracy and efficiency of the Hybrid model replacing the multicomponent Shan-Chen model with other multiphase LBM models.

Further analysis on the capillary forces during the regime transitions is also required. Research in this direction could shed some light and find compelling reasons supporting the idea of maximized cohesion during the capillary-funicular and funicular-pendular transitions. The study should consider a wide a range of liquid saturations and separation distances for similar microstructures (groups of 4 or 5 solid spheres). Additionally, the position and magnitude of the cohesion peak should also be studied in granular assemblies with different geometric characteristics (dependence on particle size distribution, void ratio, etc).

Our Hybrid model is a first step towards a more efficient technique to study the flow in granular materials. It is worth noting that the LBM simulations of each subset took into account the same geometry provided in the full LBM. Some of the considered throats had extremely large or small cross-sectional area or high elongation, which has a non-negligible impact on the computation time. The small pore throats lead not only to high capillary pressure and curvatures, but also to high spurious velocity which significantly slows down the simulation and affects the numerical stability. Regarding the large or elongated throats, large computation domain (compared to the average computation domain of the total number of pore throats) are required to obtain the hydrostatic properties. For this reason, we replaced those pore throats with simple approximations (MS-P or Incircle). Instead, we could apply the curvature criterion described in Chapter 3. As mentioned before, knowing the geometry in advance may help predict the critical curvature. In order to overcome the problem related to very narrow throats, we could adapt the computation domain to use a more refined mesh (acting as a sort of adaptive mesh refinement). In contrast, large or elongated throats could be simulated with lower resolution to decrease the computation time.

Additionally, there are potential ways to optimize the computational resources in the Hybrid model that should be tested: 1) Increasing the capillary number, 2) Skipping or shortenning the time before reaching the equilibrium and, thus, move forward the drainage of the pore throat, 3) Stop the simulation after reaching the entry capillary pressure.

In terms of implementation and extension, in Chapter 4 we proposed to include film flow and mass transfer mechanism in future developments of the TN model. These new feature would be a great asset to mimic the coalescence and trapped phases in a more realistic way.

The analysis of the multiphase flow through 40 spheres could be complemented with the study on capillary forces for all the solid objects. Results should be compared with the forces evaluated in the Hybrid method and the solutions given by the Pendular and Gladkikh approximations.

Viscosity ratio and the flow rate have a strong influence on the fluid-fluid interface displacements. Such parameters may lead to complex phenomena: secondary pore imbibition, various patterns of fingering, etc. Some of these mechanisms could be treated accounting for the viscous coupling effects (as similarly done in the Throat-Network model presented in Chapter 4). Additionally, accurate predictions of the microscopic properties are essential to reproduce local mechanisms. The $p_c - V$ relationships obtained with the Hybrid model for each throat are a promising starting point towards the description of such complex events.

Finally, the capability of the Hybrid model is not restricted to the drainage process. Indeed, valuable information during the imbibition could be extracted from the Hybrid model following the case detailed in section 5.5.4. Imbibition can proceed by a piston-type displacement or a progressive coalescence of pendular bridges. In contrast to approximation methods, which provide scarce information on the imbibition events, the interface movements and $p_c - V$ relationships at the pore scale can be accurately obtained from direct LBM simulations. Local properties furnished by LBM could be used to further reconstruct, macroscopically, more detailed imbibition curves.

Chapter 8

Appendix

Liquid morphology comparison

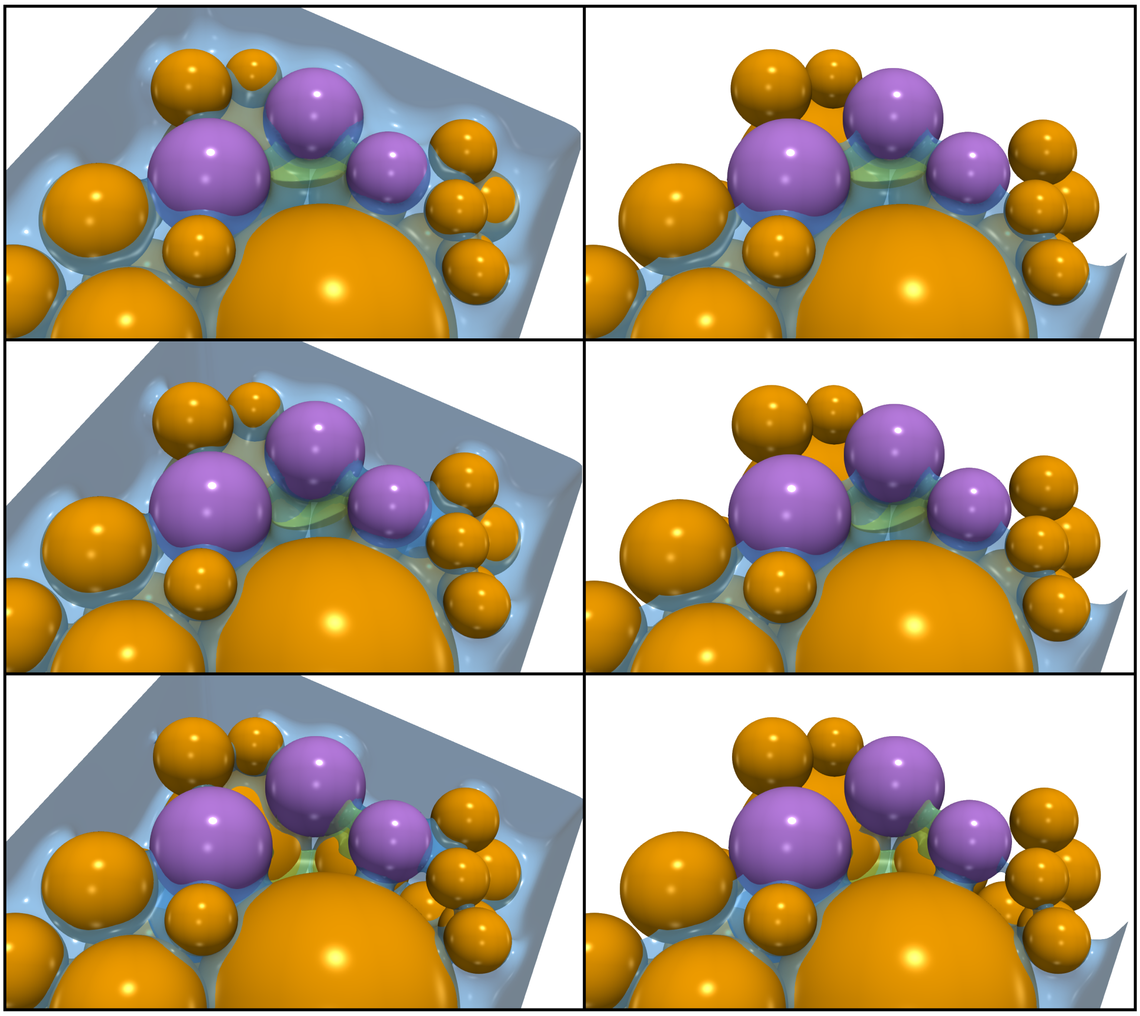

Figure 8.1: Superposition of the interfaces obtained with the full LBM analysis and the hybrid method. Similar liquid morphologies are observed.

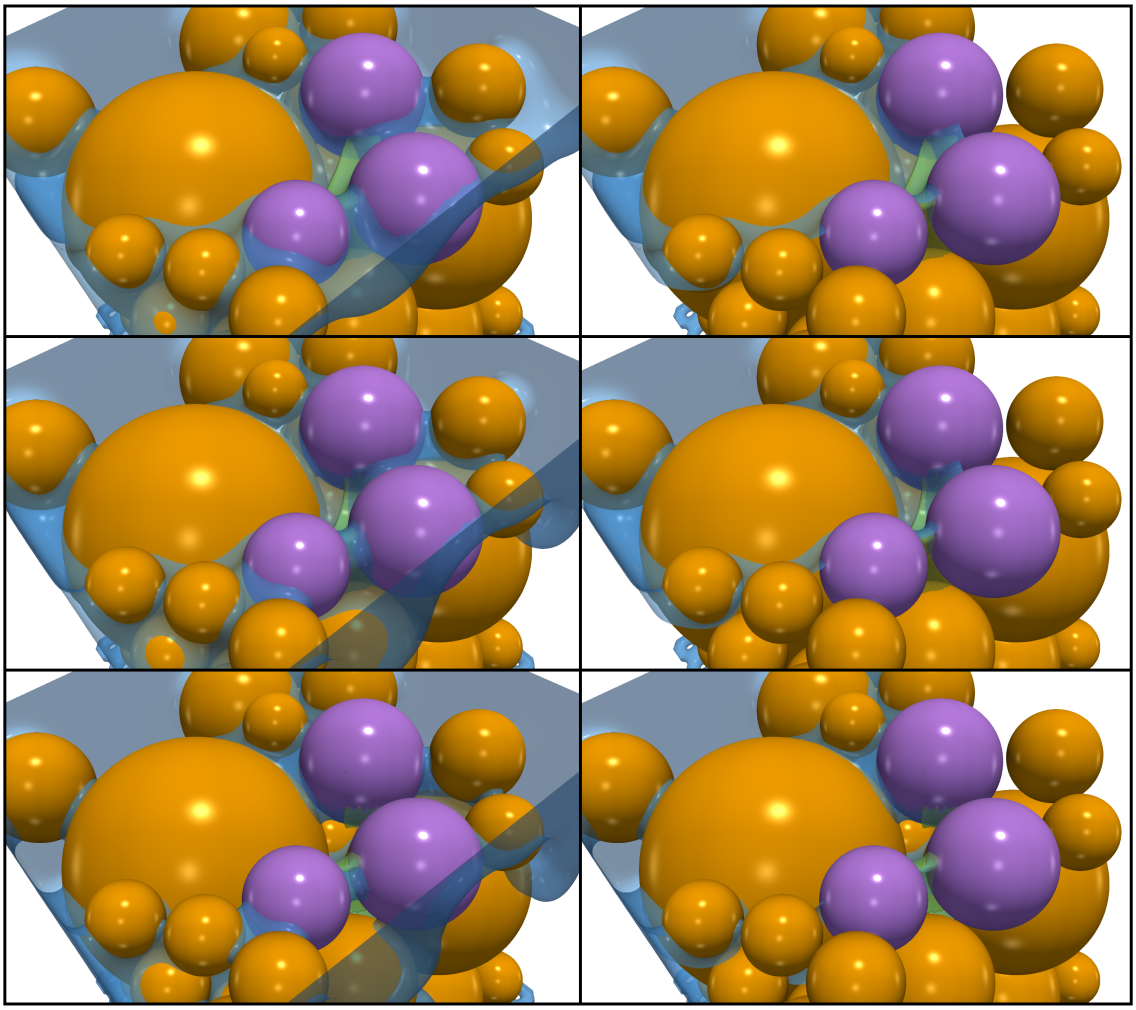

Figure 8.2: Superposition of the interfaces obtained with the full LBM analysis and the hybrid method. Similar liquid morphologies are observed.

Bibliography

Abriola, L. (1988). Multiphase flow and transport models for organic chemicals: A review and assessment. Technical report, Electric Power Research Inst., Palo Alto, CA (USA); Michigan Univ., Ann Arbor (USA). Dept. of Civil Engineering.

Adrover, A. and Giona, M. (1996). A predictive model for permeability of correlated porous media. *The Chemical Engineering Journal and The Biochemical Engineering Journal*, 64(1):7–19.

Ahrenholz, B., Tölke, J., Lehmann, P., Peters, A., Kaestner, A., Krafczyk, M., and Durner, W. (2008). Prediction of capillary hysteresis in a porous material using lattice-boltzmann methods and comparison to experimental data and a morphological pore network model. *Advances in Water Resources*, 31(9):1151–1173.

Al-Gharbi, M. S. and Blunt, M. J. (2005). Dynamic network modeling of two-phase drainage in porous media. *Phys. Rev. E*, 71:016308.

Al-Gharbi, M. S. H. (2004). *Dynamic pore-scale modelling of two-phase flow.* PhD thesis, University of London.

Al-Kharusi, A. S. and Blunt, M. J. (2007). Network extraction from sandstone and carbonate pore space images. *Journal of Petroleum Science and Engineering*, 56(4):219–231.

Al-Raoush, R. and Willson, C. (2005). Extraction of physically realistic pore network properties from three-dimensional synchrotron x-ray microtomography images of unconsolidated porous media systems. *Journal of hydrology*, 300(1-4):44–64.

Alonso, E. E., Gens, A., and Josa, A. (1990). A constitutive model for partially saturated soils. *Géotechnique*, 40(3):405–430.

Anderson, T. B. and Jackson, R. (1967). Fluid mechanical description of fluidized beds. equations of motion. *Industrial & Engineering Chemistry Fundamentals*, 6(4):527–539.

Armstrong, R. T., Evseev, N., Koroteev, D., and Berg, S. (2015). Modeling the velocity field during haines jumps in porous media. *Advances in Water Resources*, 77:57–68.

Badetti, M., Fall, A., Hautemayou, D., Chevoir, F., Aimedieu, P., Rodts, S., and Roux, J.-N. (2018). Rheology and microstructure of unsaturated wet granular materials: Experiments and simulations. *Journal of Rheology*, 62(5):1175–1186.

Bakke, S., Øren, P.-E., et al. (1997). 3-d pore-scale modelling of sandstones and flow simulations in the pore networks. *Spe Journal*, 2(02):136–149.

Balcázar, N., Lehmkuhl, O., Jofre, L., Rigola, J., and Oliva, A. (2016). A coupled volume-of-fluid/level-set method for simulation of two-phase flows on unstructured meshes. *Computers & Fluids*, 124:12–29.

Baltodano-Goulding, R. (2006). *Tensile strength, shear strength, and effective stress for unsaturated sand*. PhD thesis, University of Missouri–Columbia.

Bao, J. and Schaefer, L. (2013). Lattice boltzmann equation model for multi-component multi-phase flow with high density ratios. *Applied Mathematical Modelling*, 37(4):1860–1871.

Bear, J. (1972). *Dynamics of fluids in porous media*. Courier Corporation.

Benzi, R., Biferale, L., Sbragaglia, M., Succi, S., and Toschi, F. (2006). Mesoscopic modeling of a two-phase flow in the presence of boundaries: the contact angle. *Physical Review E*, 74(2):021509.

Berg, S., Armstrong, R., Ott, H., Georgiadis, A., Klapp, S., Schwing, A., Neiteler, R., Brussee, N., Makurat, A., Leu, L., et al. (2014). Multiphase flow in porous rock imaged under dynamic flow conditions with fast x-ray computed microtomography. *Petrophysics*, 55(04):304–312.

Berg, S., Ott, H., Klapp, S. A., Schwing, A., Neiteler, R., Brussee, N., Makurat, A., Leu, L., Enzmann, F., Schwarz, J.-O., et al. (2013). Real-time 3d imaging of haines jumps in porous media flow. *Proceedings of the National Academy of Sciences*, 110(10):3755–3759.

Bhatnagar, P. L., Gross, E. P., and Krook, M. (1954). A model for collision processes in gases. i. small amplitude processes in charged and neutral one-component systems. *Physical review*, 94(3):511.

Bishop, A. W. and Blight, G. (1963). Some aspects of effective stress in saturated and partly saturated soils. *Géotechnique*, 13(3):177–197.

Blunt, M., King, M. J., and Scher, H. (1992). Simulation and theory of two-phase flow in porous media. *Physical Review A*, 46(12):7680.

Blunt, M. and King, P. (1991). Relative permeabilities from two-and three-dimensional pore-scale network modelling. *Transport in porous media*, 6(4):407–433.

Blunt, M. J. (2001). Flow in porous media—pore-network models and multiphase flow. *Current opinion in colloid & interface science*, 6(3):197–207.

Blunt, M. J., Jackson, M. D., Piri, M., and Valvatne, P. H. (2002). Detailed physics, predictive capabilities and macroscopic consequences for pore-network models of multiphase flow. *Advances in Water Resources*, 25(8-12):1069–1089.

Boek, E. S. and Venturoli, M. (2010). Lattice-boltzmann studies of fluid flow in porous media with realistic rock geometries. *Computers & Mathematics with Applications*, 59(7):2305–2314.

Boissonnat, J.-D., Devillers, O., Teillaud, M., and Yvinec, M. (2000). Triangulations in cgal (extended abstract). In *Proceedings of the Sixteenth Annual Symposium on Computational Geometry*, SCG '00, pages 11–18, New York, NY, USA. ACM.

Bryant, S. and Blunt, M. (1992). Prediction of relative permeability in simple porous media. *Phys. Rev. A*, 46:2004–2011.

Bryant, S. and Johnson, A. (2003). Wetting phase connectivity and irreducible saturation in simple granular media. *Journal of colloid and interface science*, 263(2):572–579.

Bush, J. (2010). Interfacial phenomena. 18.357.

Caiazzo, A. and Junk, M. (2008). Boundary forces in lattice boltzmann: Analysis of momentum exchange algorithm. *Computers & Mathematics with Applications*, 55(7):1415–1423.

Catalano, E. (2012). *A pore–scale coupled hydromechanical model for biphasic granular media. Application to granular sediment hydrodynamics.* PhD thesis, PhD thesis, Université de Grenoble.

Catalano, E., Chareyre, B., and Barthélemy, E. (2014). Pore-scale modeling of fluid-particles interaction and emerging poromechanical effects. *International Journal for Numerical and Analytical Methods in Geomechanics*, 38(1):51–71.

Cavarretta, I., Coop, M., and O'SULLIVAN, C. (2010). The influence of particle characteristics on the behaviour of coarse grained soils. *Géotechnique*, 60(6):413–423.

Chandler, R., Koplik, J., Lerman, K., and Willemsen, J. F. (1982). Capillary displacement and percolation in porous media. *Journal of Fluid Mechanics*, 119:249–267.

Chareyre, B., Cortis, A., Catalano, E., and Barthélemy, E. (2012). Pore-scale modeling of viscous flow and induced forces in dense sphere packings. *Transport in Porous Media*, 92(2):473–493.

Chareyre, B., Yuan, C., Montella, E. P., and Salager, S. (2017). Toward multiscale modelings of grain-fluid systems. In *EPJ Web of Conferences*, volume 140, page 09027. EDP Sciences.

Chen, L., Kang, Q., Mu, Y., He, Y.-L., and Tao, W.-Q. (2014). A critical review of the pseudopotential multiphase lattice boltzmann model: Methods and applications. *International Journal of Heat and Mass Transfer*, 76:210–236.

Chen, S. and Doolen, G. D. (1998). Lattice boltzmann method for fluid flows. *Annual review of fluid mechanics*, 30(1):329–364.

Chevalier, L., Bruchon, J., Moulin, N., Liotier, P.-J., and Drapier, S. (2018). Accounting for local capillary effects in two-phase flows with relaxed surface tension formulation in enriched finite elements. *Comptes Rendus Mécanique*.

Cho, S., Takahashi, F., and L DRYER, F. (1989). Some theoretical considerations on the combustion and disruption of free slurry droplets. *Combustion science and technology*, 67(1-3):37–57.

Connington, K. and Lee, T. (2012). A review of spurious currents in the lattice boltzmann method for multiphase flows. *Journal of mechanical science and technology*, 26(12):3857–3863.

Crespo, A. (2008). *Application of the Smoothed Particle Hydrodynamics model SPHysics to free-surface hydrodynamics. 158p.* PhD thesis, Dissertação de doutoramento, Universidade de Vigo, Vigo, Espanha.

Cui, X., Li, J., Chan, A., and Chapman, D. (2012). A 2d dem–lbm study on soil behaviour due to locally injected fluid. *Particuology*, 10(2):242–252.

Cui, X., Li, J., Chan, A., and Chapman, D. (2014). Coupled dem–lbm simulation of internal fluidisation induced by a leaking pipe. *Powder Technology*, 254:299–306.

Cui, Y., Delage, P., et al. (1996). Yeilding and plastic behaviour of an unsaturated compacted silt. *Géotechnique*, 46(2):291–311.

Cundall, P. A. and Strack, O. D. (1979). A discrete numerical model for granular assemblies. *geotechnique*, 29(1):47–65.

Daneyko, A., Khirevich, S., Höltzel, A., Seidel-Morgenstern, A., and Tallarek, U. (2011). From random sphere packings to regular pillar arrays: effect of the macroscopic confinement on hydrodynamic dispersion. *Journal of Chromatography A*, 1218(45):8231–8248.

De Bisschop, F. R. and Rigole, W. J. (1982). A physical model for liquid capillary bridges between adsorptive solid spheres: The nodoid of plateau. *Journal of Colloid and Interface Science*, 88(1):117–128.

De la Cruz, V. and Spanos, T. (1983). Mobilization of oil ganglia. *AIChE Journal*, 29(5):854–858.

Delenne, J.-Y., Mansouri, M., Radja , F., El Youssoufi, M. S., and Seridi, A. (2011). Onset of immersed granular avalanches by dem-lbm approach. In *Advances in Bifurcation and Degradation in Geomaterials*, pages 109–115. Springer.

Delenne, J.-Y., Richefeu, V., and Radjai, F. (2015). Liquid clustering and capillary pressure in granular media. *Journal of Fluid Mechanics*, 762.

Dias, M. M. and Payatakes, A. C. (1986). Network models for two-phase flow in porous media part 1. immiscible microdisplacement of non-wetting fluids. *Journal of Fluid Mechanics*, 164:305–336.

Dong, H. and Blunt, M. J. (2009). Pore-network extraction from micro-computerized-tomography images. *Physical review E*, 80(3):036307.

Edery, Y., Berg, S., and Weitz, D. (2018). Surfactant variations in porous media localize capillary instabilities during haines jumps. *Physical review letters*, 120(2):028005.

Effeindzourou, A., Chareyre, B., Thoeni, K., Giacomini, A., and Kneib, F. (2016). Modelling of deformable structures in the general framework of the discrete element method. *Geotextiles and Geomembranes*, 44(2):143–156.

Fatt, I. et al. (1956). The network model of porous media.

Fenwick, D. H., Blunt, M. J., et al. (1998). Network modeling of three-phase flow in porous media. *SPE Journal*, 3(01):86–96.

Fischer, G., Bigerelle, M., Kubiak, K., Mathia, T., Khatir, Z., and Anselme, K. (2014). Wetting of anisotropic sinusoidal surfaces—experimental and numerical study of directional spreading. *Surface Topography: Metrology and Properties*, 2(4):044003.

Fisher, R. (1926). On the capillary forces in an ideal soil; correction of formulae given by wb haines. *The Journal of Agricultural Science*, 16(3):492–505.

Flemmer, C. (1991). On the regime boundaries of moisture in granular materials. *Powder technology*, 66(2):191–194.

Forcada, M. L. (1993). Instability in a system of two interacting liquid films: formation of liquid bridges between solid surfaces. *The Journal of chemical physics*, 98(1):638–643.

Fredlund, D., Morgenstern, N. R., and Widger, R. (1978). The shear strength of unsaturated soils. *Canadian geotechnical journal*, 15(3):313–321.

Frisch, U., Hasslacher, B., and Pomeau, Y. (1986). Lattice-gas automata for the navier-stokes equation. *Physical review letters*, 56(14):1505.

Gagneux, G. and Millet, O. (2016). An analytical framework for evaluating the cohesion effects of coalescence between capillary bridges. *Granular Matter*, 18(2):16.

Gallipoli, D., Gens, A., Sharma, R., and Vaunat, J. (2003). An elasto-plastic model for unsaturated soil incorporating the effects of suction and degree of saturation on mechanical behaviour. *Géotechnique.*, 53(1):123–136.

Gao, S., Meegoda, J. N., and Hu, L. (2012). Two methods for pore network of porous media. *International Journal for Numerical and Analytical Methods in Geomechanics*, 36(18):1954–1970.

Gens, A. and Alonso, E. (1992). A framework for the behaviour of unsaturated expansive clays. *Canadian Geotechnical Journal*, 29(6):1013–1032.

Gens, A., Sánchez, M., and Sheng, D. (2006). On constitutive modelling of unsaturated soils. *Acta Geotechnica*, 1(3):137.

Genty, A. and Pot, V. (2014). Numerical calculation of effective diffusion in unsaturated porous media by the trt lattice boltzmann method. *Transport in porous media*, 105(2):391–410.

Gibou, F., Chen, L., Nguyen, D., and Banerjee, S. (2007). A level set based sharp interface method for the multiphase incompressible navier–stokes equations with phase change. *Journal of Computational Physics*, 222(2):536–555.

Gladkikh, M. and Bryant, S. (2005). Prediction of imbibition in unconsolidated granular materials. *Journal of colloid and interface science*, 288(2):526–539.

Gras, J.-P., Delenne, J.-Y., and El Youssoufi, M. S. (2013). Study of capillary interaction between two grains: a new experimental device with suction control. *Granular Matter*, 15(1):49–56.

Grof, Z., Lawrence, C. J., and Štěpánek, F. (2008). The strength of liquid bridges in random granular materials. *Journal of colloid and interface science*, 319(1):182–192.

Gröger, T., Tüzün, U., and Heyes, D. M. (2003). Modelling and measuring of cohesion in wet granular materials. *Powder Technology*, 133(1-3):203–215.

Gunstensen, A. K., Rothman, D. H., Zaleski, S., and Zanetti, G. (1991). Lattice boltzmann model of immiscible fluids. *Physical Review A*, 43(8):4320.

Guo, N. and Zhao, J. (2014). A coupled fem/dem approach for hierarchical multiscale modelling of granular media. *International Journal for Numerical Methods in Engineering*, 99(11):789–818.

Guo, Z. and Zhao, T. (2002). Lattice boltzmann model for incompressible flows through porous media. *Physical Review E*, 66(3):036304.

Gupta, A. and Kumar, R. (2008). Lattice boltzmann simulation to study multiple bubble dynamics. *International Journal of Heat and Mass Transfer*, 51(21-22):5192–5203.

Haines, W. B. (1925). Studies in the physical properties of soils: Ii. a note on the cohesion developed by capillary forces in an ideal soil1. *The Journal of Agricultural Science*, 15(4):529–535.

Haines, W. B. (1927). Studies in the physical properties of soils: Iv. a further contribution to the theory of capillary phenomena in soil. *The Journal of Agricultural Science*, 17(2):264–290.

Haines, W. B. (1930). Studies in the physical properties of soil. v. the hysteresis effect in capillary properties, and the modes of moisture distribution associated therewith. *The Journal of Agricultural Science*, 20(1):97–116.

Halsey, T. C. and Levine, A. J. (1998). How sandcastles fall. *Physical Review Letters*, 80(14):3141.

Han, Y. and Cundall, P. A. (2013). Lbm–dem modeling of fluid–solid interaction in porous media. *International Journal for Numerical and Analytical Methods in Geomechanics*, 37(10):1391–1407.

Hassanizadeh, S. M. and Gray, W. G. (1993). Thermodynamic basis of capillary pressure in porous media. *Water resources research*, 29(10):3389–3405.

Helba, A., Sahimi, M., Scriven, L., Davis, H., et al. (1992). Percolation theory of two-phase relative permeability. *SPE Reservoir Engineering*, 7(01):123–132.

Hilpert, M., McBride, J. F., and Miller, C. T. (2000). Investigation of the residual–funicular nonwetting-phase-saturation relation. *Advances in Water Resources*, 24(2):157–177.

Hilpert, M. and Miller, C. T. (2001). Pore-morphology-based simulation of drainage in totally wetting porous media. *Advances in Water Resources*, 24(3-4):243–255.

Hirt, C. W. and Nichols, B. D. (1981). Volume of fluid (vof) method for the dynamics of free boundaries. *Journal of computational physics*, 39(1):201–225.

Holdych, D., Rovas, D., Georgiadis, J., and Buckius, R. (1998). An improved hydrodynamics formulation for multiphase flow lattice-boltzmann models. *International Journal of Modern Physics C*, 9(08):1393–1404.

Hornbaker, D., Albert, R., Albert, I., Barabási, A.-L., and Schiffer, P. (1997). What keeps sandcastles standing? *Nature*, 387(6635):765.

Hotta, K., Takeda, K., and Iinoya, K. (1974). The capillary binding force of a liquid bridge. *Powder Technology*, 10(4-5):231–242.

Hou, S., Shan, X., Zou, Q., Doolen, G. D., and Soll, W. E. (1997). Evaluation of two lattice boltzmann models for multiphase flows. *Journal of Computational Physics*, 138(2):695–713.

Huang, H., Huang, J.-J., and Lu, X.-Y. (2014). Study of immiscible displacements in porous media using a color-gradient-based multiphase lattice boltzmann method. *Computers & Fluids*, 93:164–172.

Huang, H., Krafczyk, M., and Lu, X. (2011). Forcing term in single-phase and shan-chen-type multiphase lattice boltzmann models. *Physical Review E*, 84(4):046710.

Huang, H., Sukop, M., and Lu, X. (2015). *Multiphase lattice Boltzmann methods: Theory and application*. John Wiley & Sons.

Huang, H., Thorne Jr, D. T., Schaap, M. G., and Sukop, M. C. (2007). Proposed approximation for contact angles in shan-and-chen-type multicomponent multiphase lattice boltzmann models. *Physical Review E*, 76(6):066701.

Inamuro, T., Tajima, S., and Ogino, F. (2004). Lattice boltzmann simulation of droplet collision dynamics. *International journal of heat and mass transfer*, 47(21):4649–4657.

Ioannidis, M. A. and Chatzis, I. (1993). Network modelling of pore structure and transport properties of porous media. *Chemical Engineering Science*, 48(5):951–972.

Iveson, S. M., Litster, J. D., Hapgood, K., and Ennis, B. J. (2001). Nucleation, growth and breakage phenomena in agitated wet granulation processes: a review. *Powder technology*, 117(1):3–39.

Jiang, F., Oliveira, M. S., and Sousa, A. C. (2007a). Mesoscale sph modeling of fluid flow in isotropic porous media. *Computer Physics Communications*, 176(7):471–480.

Jiang, M., Leroueil, S., and Konrad, J. (2004). Insight into shear strength functions of unsaturated granulates by dem analyses. *Computers and Geotechnics*, 31(6):473–489.

Jiang, Z., Wu, K., Couples, G., Van Dijke, M., Sorbie, K., and Ma, J. (2007b). Efficient extraction of networks from three-dimensional porous media. *Water Resources Research*, 43(12).

Jing, L., Ma, Y., and Fang, Z. (2001). Modeling of fluid flow and solid deformation for fractured rocks with discontinuous deformation analysis (dda) method. *International Journal of Rock Mechanics and Mining Sciences*, 38(3):343–355.

Jivkov, A. P., Hollis, C., Etiese, F., McDonald, S. A., and Withers, P. J. (2013). A novel architecture for pore network modelling with applications to permeability of porous media. *Journal of Hydrology*, 486:246–258.

Joanny, J. and De Gennes, P.-G. (1984). A model for contact angle hysteresis. *The journal of chemical physics*, 81(1):552–562.

Joekar-Niasar, V. and Hassanizadeh, S. M. (2012). Analysis of fundamentals of two-phase flow in porous media using dynamic pore-network models: A review. *Critical Reviews in Environmental Science and Technology*, 42(18):1895–1976.

Joekar-Niasar, V., Hassanizadeh, S. M., and Dahle, H. K. (2010a). Non-equilibrium effects in capillarity and interfacial area in two-phase flow: dynamic pore-network modelling. *Journal of Fluid Mechanics*, 655:38–71.

Joekar-Niasar, V., Prodanović, M., Wildenschild, D., and Hassanizadeh, S. M. (2010b). Network model investigation of interfacial area, capillary pressure and saturation relationships in granular porous media. *Water Resources Research*, 46(6):n/a–n/a. W06526.

Kafui, K., Thornton, C., and Adams, M. (2002). Discrete particle-continuum fluid modelling of gas–solid fluidised beds. *Chemical Engineering Science*, 57(13):2395–2410.

Kamali, M., Gillissen, J., Sundaresan, S., and Van den Akker, H. (2011). Contact line motion without slip in lattice boltzmann simulations. *Chemical engineering science*, 66(14):3452–3458.

Kandhai, D., Koponen, A., Hoekstra, A. G., Kataja, M., Timonen, J., and Sloot, P. M. (1998). Lattice-boltzmann hydrodynamics on parallel systems. *Computer Physics Communications*, 111(1-3):14–26.

Kharaghani, A., Metzger, T., and Tsotsas, E. (2012). An irregular pore network model for convective drying and resulting damage of particle aggregates. *Chemical engineering science*, 75:267–278.

King, P. (1987). The fractal nature of viscous fingering in porous media. *Journal of Physics A: Mathematical and General*, 20(8):L529.

Kistler, S. F. and Schweizer, P. M. (1997). *Liquid film coating: scientific principles and their technological implications*. Springer.

Kohgo, Y., Nakano, M., and Miyazaki, T. (1993). Theoretical aspects of constitutive modelling for unsaturated soils. *Soils and foundations*, 33(4):49–63.

Koplik, J. and Lasseter, T. (1985). Two-phase flow in random network models of porous media. *Society of Petroleum Engineers Journal*, 25(01):89–100.

Koponen, A., Kataja, M., Timonen, J., and Kandhai, D. (1998). Simulations of single-fluid flow in porous media. *International Journal of Modern Physics C*, 9(08):1505–1521.

Krüger, T., Kusumaatmaja, H., Kuzmin, A., Shardt, O., Silva, G., and Viggen, E. M. (2017). *The Lattice Boltzmann Method*. Springer.

Kueper, B. H., Abbott, W., and Farquhar, G. (1989). Experimental observations of multiphase flow in heterogeneous porous media. *Journal of Contaminant Hydrology*, 5(1):83–95.

Ladd, A. J. (1994). Numerical simulations of particulate suspensions via a discretized boltzmann equation. part 1. theoretical foundation. *Journal of fluid mechanics*, 271:285–309.

Lambert, P. (2007). *Capillary forces in microassembly: modeling, simulation, experiments, and case study*. Springer Science & Business Media.

Lambert, P. and Valsamis, J.-B. (2013). Axial capillary forces. In *Surface Tension in Microsystems*, pages 19–44. Springer.

Laroche, C., Vizika, O., and Kalaydjian, F. (1999). Network modeling as a tool to predict three-phase gas injection in heterogeneous wettability porous media. *Journal of Petroleum Science and Engineering*, 24(2):155–168.

Latt, J. (2008). Choice of units in lattice boltzmann simulations. *Freely available online at http://lbmethod. org/_media/howtos: lbunits. pdf*.

Latt, J. (2009). Palabos, parallel lattice boltzmann solver.

Latt, J., Chopard, B., Malaspinas, O., Deville, M., and Michler, A. (2008). Straight velocity boundaries in the lattice boltzmann method. *Physical Review E*, 77(5):056703.

Lee, T. and Lin, C.-L. (2005). A stable discretization of the lattice boltzmann equation for simulation of incompressible two-phase flows at high density ratio. *Journal of Computational Physics*, 206(1):16–47.

Lenormand, R. (1986). Pattern growth and fluid displacements through porous media. *Physica A: Statistical Mechanics and its Applications*, 140(1-2):114–123.

Lenormand, R. (1990). Liquids in porous media. *Journal of Physics: Condensed Matter*, 2(S):SA79.

Lenormand, R., Touboul, E., and Zarcone, C. (1988). Numerical models and experiments on immiscible displacements in porous media. *Journal of Fluid Mechanics*, 189:165–187.

Lenormand, R., Zarcone, C., and Sarr, A. (1983). Mechanisms of the displacement of one fluid by another in a network of capillary ducts. *J. Fluid Mech*, 135(34):337–353.

Li, J. (2013). *Numerical investigations of the coupled DEM-LBM technique with application to leakage-soil interaction due to a leaking pipe.* PhD thesis, University of Birmingham.

Li, Q. and Luo, K. (2014). Thermodynamic consistency of the pseudopotential lattice boltzmann model for simulating liquid–vapor flows. *Applied Thermal Engineering*, 72(1):56–61.

Li, X., Chu, X., and Sheng, D. (2007). A saturated discrete particle model and characteristic-based sph method in granular materials. *International Journal for Numerical Methods in Engineering*, 72(7):858–882.

Lian, G. and Seville, J. (2016). The capillary bridge between two spheres: New closed-form equations in a two century old problem. *Advances in colloid and interface science*, 227:53–62.

Lian, G., Thornton, C., and Adams, M. J. (1993). A theoretical study of the liquid bridge forces between two rigid spherical bodies. *Journal of colloid and interface science*, 161(1):138–147.

Lindquist, W. B., Lee, S.-M., Coker, D. A., Jones, K. W., and Spanne, P. (1996). Medial axis analysis of void structure in three-dimensional tomographic images of porous media. *Journal of Geophysical Research: Solid Earth*, 101(B4):8297–8310.

Liu, H., Valocchi, A. J., Kang, Q., and Werth, C. (2013). Pore-scale simulations of gas displacing liquid in a homogeneous pore network using the lattice boltzmann method. *Transport in porous media*, 99(3):555–580.

Lominé, F., Scholtes, L., Sibille, L., and Poullain, P. (2013). Modeling of fluid–solid interaction in granular media with coupled lattice boltzmann/discrete element methods: application to piping erosion. *International Journal for Numerical and Analytical Methods in Geomechanics*, 37(6):577–596.

Lu, N., Wu, B., and Tan, C. P. (2007). Tensile strength characteristics of unsaturated sands. *Journal of Geotechnical and Geoenvironmental Engineering*, 133(2):144–154.

Lu, T., Nielsen, D., and Biggar, J. (1995). Water movement in glass bead porous media: 3. theoretical analyses of capillary rise into initially dry media. *Water Resources Research*, 31(1):11–18.

Lucy, L. B. (1977). A numerical approach to the testing of the fission hypothesis. *The astronomical journal*, 82:1013–1024.

Luo, L.-S. (1998). Unified theory of lattice boltzmann models for nonideal gases. *Physical review letters*, 81(8):1618.

Ma, S., Mason, G., and Morrow, N. R. (1996). Effect of contact angle on drainage and imbibition in regular polygonal tubes. *Colloids and Surfaces A: Physicochemical and Engineering Aspects*, 117(3):273–291.

Martin, E. A. (1962). Miscible fluid displacement in a porous medium.

Martys, N. S. and Chen, H. (1996). Simulation of multicomponent fluids in complex three-dimensional geometries by the lattice boltzmann method. *Physical review E*, 53(1):743.

Mason, G. and Morrow, N. R. (1984). Coexistence of menisci and the influence of neighboring pores on capillary displacement curvatures in sphere packings. *Journal of colloid and interface science*, 100(2):519–535.

Mason, G. and Morrow, N. R. (1991). Capillary behavior of a perfectly wetting liquid in irregular triangular tubes. *Journal of Colloid and Interface Science*, 141(1):262–274.

Mayer, R. P. and Stowe, R. A. (1965). Mercury porosimetry—breakthrough pressure for penetration between packed spheres. *Journal of Colloid Science*, 20(8):893 – 911.

Mei, R., Yu, D., Shyy, W., and Luo, L.-S. (2002). Force evaluation in the lattice boltzmann method involving curved geometry. *Physical Review E*, 65(4):041203.

Melnikov, K., Mani, R., Wittel, F. K., Thielmann, M., and Herrmann, H. J. (2015). Grain-scale modeling of arbitrary fluid saturation in random packings. *Physical Review E*, 92(2):022206.

Mitarai, N. and Nori, F. (2006). Wet granular materials. *Advances in Physics*, 55(1-2):1–45.

Mogensen, K. and Stenby, E. H. (1998). A dynamic two-phase pore-scale model of imbibition. *Transport in Porous Media*, 32(3):299–327.

Monaghan, J. and Kocharyan, A. (1995). Sph simulation of multi-phase flow. *Computer Physics Communications*, 87(1-2):225–235.

Monaghan, J. J. (2005). Smoothed particle hydrodynamics. *Reports on progress in physics*, 68(8):1703.

Montellà, E. (2019). Dataset of multiphase drainage of 40 sphere assembly with a multicomponent shan-chen lbm. `https://osf.io/24wnb/?view_only=4e55ca6e106848d9ab720068e075280d`.

Montellà, E., Toraldo, M., Chareyre, B., and Sibille, L. (2016). Localized fluidization in granular materials: Theoretical and numerical study. *Physical Review E*, 94(5):052905.

Nakase, H., Takeda, T., and Oda, M. (1999). A simulation study on liquefaction using dem. *Earthquake geotechnical engineering*, 3:637–642.

Newitt, D. and Conway-Jones, J. (1958). A contribution to the theory and practice of granulation. *Trans. Inst. Chem. Eng*, 36.

Olsson, E. and Kreiss, G. (2005). A conservative level set method for two phase flow. *Journal of computational physics*, 210(1):225–246.

Ono, S. and Kondo, S. (1960). Molecular theory of surface tension in liquids. In *Structure of Liquids/Struktur der Flüssigkeiten*, pages 134–280. Springer.

Oren, P., Bakke, S., Arntzen, O. J., et al. (1997). Extending predictive capabilities to network models. In *SPE Annual Technical Conference and Exhibition*. Society of Petroleum Engineers.

Øren, P. and Pinczewski, W. (1995). Fluid distribution and pore-scale displacement mechanisms in drainage dominated three-phase flow. In *Multiphase Flow in Porous Media*, pages 105–133. Springer.

Øren, P.-E. and Bakke, S. (2003). Reconstruction of berea sandstone and pore-scale modelling of wettability effects. *Journal of Petroleum Science and Engineering*, 39(3):177–199.

Orr, F., Scriven, L., and Rivas, A. P. (1975). Pendular rings between solids: meniscus properties and capillary force. *Journal of Fluid Mechanics*, 67(4):723–742.

Orr Jr, F., Brown, R., and Scriven, L. (1977). Three-dimensional menisci: Numerical simulation by finite elements. *Journal of Colloid and Interface Science*, 60(1):137–147.

Orr Jr, F., Scriven, L., and Rivas, A. (1975). Menisci in arrays of cylinders: numerical simulation by finite elements. *Journal of Colloid and Interface Science*, 52(3):602–610.

Osher, S. and Sethian, J. A. (1988). Fronts propagating with curvature-dependent speed: algorithms based on hamilton-jacobi formulations. *Journal of computational physics*, 79(1):12–49.

Otomo, H., Fan, H., Li, Y., Dressler, M., Staroselsky, I., Zhang, R., and Chen, H. (2016). Studies of accurate multi-component lattice boltzmann models on benchmark cases required for engineering applications. *Journal of Computational Science*, 17:334–339.

Pan, C., Hilpert, M., and Miller, C. (2004). Lattice-boltzmann simulation of two-phase flow in porous media. *Water Resources Research*, 40(1).

Patzek, T. W. et al. (2000). Verification of a complete pore network simulator of drainage and imbibition. In *SPE/DOE Improved Oil Recovery Symposium*. Society of Petroleum Engineers.

Piri, M. and Blunt, M. J. (2005). Three-dimensional mixed-wet random pore-scale network modeling of two-and three-phase flow in porous media. i. model description. *Physical Review E*, 71(2):026301.

Pooley, C. and Furtado, K. (2008). Eliminating spurious velocities in the free-energy lattice boltzmann method. *Physical Review E*, 77(4):046702.

Porter, M. L., Coon, E., Kang, Q., Moulton, J., and Carey, J. (2012). Multicomponent interparticle-potential lattice boltzmann model for fluids with large viscosity ratios. *Physical Review E*, 86(3):036701.

Porter, M. L., Schaap, M. G., and Wildenschild, D. (2009). Lattice-boltzmann simulations of the capillary pressure–saturation–interfacial area relationship for porous media. *Advances in Water Resources*, 32(11):1632–1640.

Potapov, A. V., Hunt, M. L., and Campbell, C. S. (2001). Liquid–solid flows using smoothed particle hydrodynamics and the discrete element method. *Powder Technology*, 116(2-3):204–213.

Princen, H. (1969). Capillary phenomena in assemblies of parallel cylinders: Ii. capillary rise in systems with more than two cylinders. *Journal of Colloid and Interface Science*, 30(3):359 – 371.

Prodanović, M. and Bryant, S. L. (2006). A level set method for determining critical curvatures for drainage and imbibition. *Journal of colloid and interface science*, 304(2):442–458.

Prodanović, M., Lindquist, W., and Seright, R. (2006). Porous structure and fluid partitioning in polyethylene cores from 3d x-ray microtomographic imaging. *Journal of Colloid and Interface Science*, 298(1):282 – 297.

Pruess, K. and Garcia, J. (2002). Multiphase flow dynamics during co 2 disposal into saline aquifers. *Environmental Geology*, 42(2):282–295.

Raeini, A. Q., Blunt, M. J., and Bijeljic, B. (2012). Modelling two-phase flow in porous media at the pore scale using the volume-of-fluid method. *Journal of Computational Physics*, 231(17):5653–5668.

Raoof, A. and Hassanizadeh, S. M. (2013). Saturation-dependent solute dispersivity in porous media: Pore-scale processes. *Water Resources Research*, 49(4):1943–1951.

Richefeu, V., El Youssoufi, M. S., Azéma, E., and Radjai, F. (2009). Force transmission in dry and wet granular media. *Powder Technology*, 190(1-2):258–263.

Richefeu, V., El Youssoufi, M. S., and Radjai, F. (2006). Shear strength properties of wet granular materials. *Physical Review E*, 73(5):051304.

Richefeu, V., Radjai, F., and Delenne, J.-Y. (2016). Lattice boltzmann modelling of liquid distribution in unsaturated granular media. *Computers and Geotechnics*, 80:353–359.

Rowlinson, J. S. and Widom, B. (2013). *Molecular theory of capillarity.* Courier Corporation.

Ruiz-Cabello, F. J. M., Kusumaatmaja, H., Rodríguez-Valverde, M. A., Yeomans, J., and Cabrerizo-Vílchez, M. A. (2009). Modeling the corrugation of the three-phase contact line perpendicular to a chemically striped substrate. *Langmuir*, 25(14):8357–8361.

Saito, M. and De Lemos, M. (2005). Convective heat transfer coefficient for turbulent flow in a porous medium formed by an array of square rods. *Latin American Journal of Solids and Structures*, 2(4):291–304.

Sakellariou, A., Sawkins, T., Senden, T., and Limaye, A. (2004). X-ray tomography for mesoscale physics applications. *Physica A: Statistical Mechanics and its Applications*, 339(1-2):152–158.

Sbragaglia, M. and Belardinelli, D. (2013). Interaction pressure tensor for a class of multicomponent lattice boltzmann models. *Physical Review E*, 88(1):013306.

Scheel, M., Seemann, R., Brinkmann, M., Di Michiel, M., Sheppard, A., Breidenbach, B., and Herminghaus, S. (2008). Morphological clues to wet granular pile stability. *Nature Materials*, 7(3):189.

Scheidegger, A. et al. (1958). *The physics of flow through porous media.* University Of Toronto Press: London.

Schmieschek, S. and Harting, J. (2009). Contact angle determination in multicomponent lattice boltzmann simulations. *arXiv preprint arXiv:0910.3915.*

Scholtès, L. (2008). *Modélisation micromécanique des milieux granulaires partiellement saturés.* PhD thesis, Institut National Polytechnique de Grenoble-INPG.

Scholtès, L., Chareyre, B., Michallet, H., Catalano, E., and Marzougui, D. (2015). Modeling wave-induced pore pressure and effective stress in a granular seabed. *Continuum Mechanics and Thermodynamics*, 27(1-2):305–323.

Scholtès, L., Chareyre, B., Nicot, F., and Darve, F. (2009). Micromechanics of granular materials with capillary effects. *International Journal of Engineering Science*, 47(1):64 – 75.

Scholtès, L., Hicher, P.-Y., Nicot, F., Chareyre, B., and Darve, F. (2009). On the capillary stress tensor in wet granular materials. *International Journal for Numerical and Analytical Methods in Geomechanics*, 33(10):1289–1313.

Schubert, H. (1984). Capillary forces-modeling and application in particulate technology. *Powder Technology*, 37(1):105–116.

Semprebon, C., Scheel, M., Herminghaus, S., Seemann, R., and Brinkmann, M. (2016). Liquid morphologies and capillary forces between three spherical beads. *Physical Review E*, 94(1):012907.

Shan, X. (2006). Analysis and reduction of the spurious current in a class of multiphase lattice boltzmann models. *Physical Review E*, 73(4):047701.

Shan, X. (2008). Pressure tensor calculation in a class of nonideal gas lattice boltzmann models. *Physical Review E*, 77(6):066702.

Shan, X. and Chen, H. (1993). Lattice boltzmann model for simulating flows with multiple phases and components. *Physical Review E*, 47(3):1815.

Shan, X. and Chen, H. (1994). Simulation of nonideal gases and liquid-gas phase transitions by the lattice boltzmann equation. *Physical Review E*, 49(4):2941.

Shan, X. and Doolen, G. (1995). Multicomponent lattice-boltzmann model with interparticle interaction. *Journal of Statistical Physics*, 81(1):379–393.

Sheng, D., Sloan, S., and Gens, A. (2004). A constitutive model for unsaturated soils: thermomechanical and computational aspects. *Computational Mechanics*, 33(6):453–465.

Sheppard, A., Sok, R., and Averdunk, H. (2005). Improved pore network extraction methods. In *International Symposium of the Society of Core Analysts*, pages 21–25.

Silin, D. and Patzek, T. (2006). Pore space morphology analysis using maximal inscribed spheres. *Physica A: Statistical Mechanics and its Applications*, 371(2):336 – 360.

Silin, D. B., Jin, G., and Patzek, T. W. (2003). Robust determination of the pore space morphology in sedimentary rocks. In *SPE Annual Technical Conference and Exhibition*. Society of Petroleum Engineers.

Singh, M. and Mohanty, K. K. (2003). Dynamic modeling of drainage through three-dimensional porous materials. *Chemical Engineering Science*, 58(1):1–18.

Sinha, P. K. and Wang, C.-Y. (2007). Pore-network modeling of liquid water transport in gas diffusion layer of a polymer electrolyte fuel cell. *Electrochimica Acta*, 52(28):7936–7945.

Šmilauer, V. and Chareyre, B. (2010). Yade dem formulation. *Yade Documentation*.

Son, S., Chen, L., Kang, Q., Derome, D., and Carmeliet, J. (2016). Contact angle effects on pore and corner arc menisci in polygonal capillary tubes studied with the pseudopotential multiphase lattice boltzmann model. *Computation*, 4(1):12.

Spaid, M. A. and Phelan Jr, F. R. (1997). Lattice boltzmann methods for modeling microscale flow in fibrous porous media. *Physics of fluids*, 9(9):2468–2474.

Sterling, J. D. and Chen, S. (1996). Stability analysis of lattice boltzmann methods. *Journal of Computational Physics*, 123(1):196–206.

Strauch, S. and Herminghaus, S. (2012). Wet granular matter: a truly complex fluid. *Soft Matter*, 8(32):8271–8280.

Succi, S. (2001). *The lattice Boltzmann equation: for fluid dynamics and beyond*. Oxford university press.

Suh, H. S. and Yun, T. S. (2018). Modification of capillary pressure by considering pore throat geometry with the effects of particle shape and packing features on water retention curves for uniformly graded sands. *Computers and Geotechnics*, 95:129–136.

Sukop, M. C., Huang, H., Lin, C. L., Deo, M. D., Oh, K., and Miller, J. D. (2008). Distribution of multiphase fluids in porous media: Comparison between lattice boltzmann modeling and micro-x-ray tomography. *Physical Review E*, 77(2):026710.

Sussman, M., Almgren, A. S., Bell, J. B., Colella, P., Howell, L. H., and Welcome, M. L. (1999). An adaptive level set approach for incompressible two-phase flows. *Journal of Computational Physics*, 148(1):81–124.

Sweijen, T., Aslannejad, H., and Hassanizadeh, S. M. (2017a). Capillary pressure–saturation relationships for porous granular materials: Pore morphology method vs. pore unit assembly method. *Advances in Water Resources*, 107:22–31.

Sweijen, T., Chareyre, B., Hassanizadeh, S., and Karadimitriou, N. (2017b). Grain-scale modelling of swelling granular materials; application to super absorbent polymers. *Powder Technology*, 318:411–422.

Sweijen, T., Hassanizadeh, S. M., Chareyre, B., and Zhuang, L. (2018). Dynamic pore-scale model of drainage in granular porous media: The pore-unit assembly method. *Water resources research*, 54(6):4193.

Sweijen, T., Nikooee, E., Hassanizadeh, S. M., and Chareyre, B. (2016). The effects of swelling and porosity change on capillarity: Dem coupled with a pore-unit assembly method. *Transport in porous media*, 113(1):207–226.

Swift, M. R., Orlandini, E., Osborn, W., and Yeomans, J. (1996). Lattice boltzmann simulations of liquid-gas and binary fluid systems. *Physical Review E*, 54(5):5041.

Swift, M. R., Osborn, W., and Yeomans, J. (1995). Lattice boltzmann simulation of nonideal fluids. *Physical review letters*, 75(5):830.

Tadmor, R. (2004). Line energy and the relation between advancing, receding, and young contact angles. *Langmuir*, 20(18):7659–7664.

Tartakovsky, A. M. and Meakin, P. (2005). Simulation of unsaturated flow in complex fractures using smoothed particle hydrodynamics. *Vadose Zone Journal*, 4(3):848–855.

Tartakovsky, A. M. and Meakin, P. (2006). Pore scale modeling of immiscible and miscible fluid flows using smoothed particle hydrodynamics. *Advances in Water Resources*, 29(10):1464–1478.

Tartakovsky, A. M., Ward, A. L., and Meakin, P. (2007). Pore-scale simulations of drainage of heterogeneous and anisotropic porous media. *Physics of Fluids*, 19(10):103301.

Tarumi, Y. and Hakuno, M. (1988). A granular assembly simulation for the dynamic liquefaction of sand. *Natural disaster science*, 10(1):45–59.

Terzaghi, v. K. (1936). The shearing resistance of saturated soils and the angle between the planes of shear. In *Proceedings of the 1st International Conference on Soil Mechanics and Foundation Engineering*, volume 1, pages 54–56. Harvard University Press Cambridge, MA.

Thompson, K. E. and Fogler, H. S. (1997). Modeling flow in disordered packed beds from pore-scale fluid mechanics. *AIChE Journal*, 43(6):1377–1389.

Thorne, D. T. and Michael, C. (2006). Lattice boltzmann modeling: an introduction for geoscientists and engineers. *2nd. ed.*

Thu, T. M., Rahardjo, H., and Leong, E.-C. (2007). Elastoplastic model for unsaturated soil with incorporation of the soil-water characteristic curve. *Canadian Geotechnical Journal*, 44(1):67–77.

Tölke, J., Freudiger, S., and Krafczyk, M. (2006). An adaptive scheme using hierarchical grids for lattice boltzmann multi-phase flow simulations. *Computers & fluids*, 35(8-9):820–830.

Tong, A.-T., Catalano, E., and Chareyre, B. (2012). Pore-scale flow simulations: model predictions compared with experiments on bi-dispersed granular assemblies. *Oil & Gas Science and Technology–Revue d'IFP Energies nouvelles*, 67(5):743–752.

Tsakiroglou, C. D. and Fleury, M. (1999). Resistivity index of fractional wettability porous media. *Journal of Petroleum Science and Engineering*, 22(4):253–274.

Tsakiroglou, C. D. and Payatakes, A. C. (2000). Characterization of the pore structure of reservoir rocks with the aid of serial sectioning analysis, mercury porosimetry and network simulation. *Advances in Water Resources*, 23(7):773–789.

Turner, M., Knuefing, L., Arns, C., Sakellariou, A., Senden, T., Sheppard, A., Sok, R., Limaye, A., Pinczewski, W. V., and Knackstedt, M. (2004). Three-dimensional imaging of multiphase flow in porous media. *Physica A: Statistical mechanics and its applications*, 339(1-2):166–172.

Turton, R. (2008). Challenges in the modeling and prediction of coating of pharmaceutical dosage forms. *Powder Technology*, 181(2):186–194.

Urso, M. E. D., Lawrence, C. J., and Adams, M. J. (1999). Pendular, funicular, and capillary bridges: Results for two dimensions. *Journal of colloid and interface science*, 220(1):42–56.

Urso, M. E. D., Lawrence, C. J., and Adams, M. J. (2002). A two-dimensional study of the rupture of funicular liquid bridges. *Chemical engineering science*, 57(4):677–692.

Van Dijke, M. and Sorbie, K. (2006). Existence of fluid layers in the corners of a capillary with non-uniform wettability. *Journal of colloid and interface science*, 293(2):455–463.

Van Kats, F. and Egberts, P. (1999). Simulation of three-phase displacement mechanisms using a 2d lattice-boltzmann model. *Transport in Porous Media*, 37(1):55–68.

Vogel, H.-J., Tölke, J., Schulz, V., Krafczyk, M., and Roth, K. (2005). Comparison of a lattice-boltzmann model, a full-morphology model, and a pore network model for determining capillary pressure–saturation relationships. *Vadose Zone Journal*, 4(2):380–388.

Šmilauer et al., V. (2015). *Yade Documentation 2nd ed.* The Yade Project. http://yade-dem.org/doc/.

Wagner, A. J. (2003). The origin of spurious velocities in lattice boltzmann. *International Journal of Modern Physics B*, 17(01n02):193–196.

Wang, C. and Cheng, P. (1997). Multiphase flow and heat transfer in porous media. *Advances in heat transfer*, 30:93–196.

Wang, J.-P., Gallo, E., François, B., Gabrieli, F., and Lambert, P. (2017). Capillary force and rupture of funicular liquid bridges between three spherical bodies. *Powder Technology*, 305:89–98.

Wang, L., Huang, H.-b., and Lu, X.-Y. (2013). Scheme for contact angle and its hysteresis in a multiphase lattice boltzmann method. *Physical Review E*, 87(1):013301.

Wang, Z.-B., Chen, R., Wang, H., Liao, Q., Zhu, X., and Li, S.-Z. (2016). An overview of smoothed particle hydrodynamics for simulating multiphase flow. *Applied Mathematical Modelling*, 40(23-24):9625–9655.

Wilkinson, D. and Willemsen, J. F. (1983). Invasion percolation: a new form of percolation theory. *Journal of Physics A: Mathematical and General*, 16(14):3365.

Willett, C., Adams, M., Johnson, S., and Seville, J. (2003). Effects of wetting hysteresis on pendular liquid bridges between rigid spheres. *Powder Technology*, 130(1-3):63–69.

Willett, C. D., Adams, M. J., Johnson, S. A., and Seville, J. P. (2000). Capillary bridges between two spherical bodies. *Langmuir*, 16(24):9396–9405.

Woodrow, J., Chilton, H., and Hawes, R. (1961). Forces between slurry particles due to surface tension. *Journal of Nuclear Energy. Part B. Reactor Technology*, 1(4):229–IN3.

Xiong, Q., Baychev, T. G., and Jivkov, A. P. (2016). Review of pore network modelling of porous media: experimental characterisations, network constructions and applications to reactive transport. *Journal of contaminant hydrology*, 192:101–117.

Yang, J. and Boek, E. S. (2013). A comparison study of multi-component lattice boltzmann models for flow in porous media applications. *Computers & Mathematics with Applications*, 65(6):882–890.

Yang, J. and Luo, X. (2015). Exploring the relationship between critical state and particle shape for granular materials. *Journal of the Mechanics and Physics of Solids*, 84:196–213.

Young, R. (1993). Two-phase brine mixtures in the geothermal context and the polymer flood model. *Transport in porous media*, 11(2):179–185.

Young, T. et al. (1805). Iii. an essay on the cohesion of fluids. *Philosophical transactions of the royal society of London*, 95:65–87.

Yu, L. and Wardlaw, N. C. (1986). Mechanisms of nonwetting phase trapping during imbibition at slow rates. *Journal of colloid and interface science*, 109(2):473–486.

Yuan, C. (2016). *Pore-scale modeling and hydromechanics of partially saturated granular materials*. PhD thesis, Université Grenoble Alpes.

Yuan, C. and Chareyre, B. (2017). A pore-scale method for hydromechanical coupling in deformable granular media. *Computer Methods in Applied Mechanics and Engineering*, 318:1066–1079.

Yuan, C., Chareyre, B., and Darve, F. (2016). Pore-scale simulations of drainage in granular materials: finite size effects and the representative elementary volume. *Advances in water resources*, 95:109–124.

Yuan, C., Chareyre, B., and Darve, F. (2018). Deformation and stresses upon drainage of an idealized granular material. *Acta Geotechnica*, 13(4):961–972.

Yuan, P. and Schaefer, L. (2006). Equations of state in a lattice boltzmann model. *Physics of Fluids*, 18(4):042101.

Yuan, Y. and Lee, T. R. (2013). Contact angle and wetting properties. In *Surface science techniques*, pages 3–34. Springer.

Zeghal, M. and El Shamy, U. (2004). A continuum-discrete hydromechanical analysis of granular deposit liquefaction. *International Journal for Numerical and Analytical Methods in Geomechanics*, 28(14):1361–1383.

Zhang, J. and Kwok, D. Y. (2004). Lattice boltzmann study on the contact angle and contact line dynamics of liquid- vapor interfaces. *Langmuir*, 20(19):8137–8141.

Zhao, H. Q., Macdonald, I. F., and Kwiecien, M. J. (1994). Multi-orientation scanning: A necessity in the identification of pore necks in porous media by 3-d computer reconstruction from serial section data. *Journal of Colloid and Interface Science*, 162(2):390 – 401.

Zheng, H., Shu, C., and Chew, Y.-T. (2006). A lattice boltzmann model for multiphase flows with large density ratio. *Journal of Computational Physics*, 218(1):353–371.

Résumé en français

Introduction Générale

Les écoulements multiphasiques couvrent un large éventail de phénomènes naturels et d'applications industrielles. Cela comprend les eaux de pluie infiltrées dans le sol, les glissements de terrain, la récupération du pétrole, l'industrie alimentaire, etc. Une meilleure compréhension des propriétés et des mécanismes des écoulements à travers un milieu poreux est essentiel pour prédire et modéliser le comportement de ces écoulements.

Les milieux multiphasiques sont étendus à plusieurs domaines scientifiques (chimie, mécanique, pharmacie, géosciences, biologie, science des matériaux, etc.). Cependant, il est important de signaler que les travaux développés dans cette thèse se concentrent sur les sols partiellement saturés. Ces sols sont des matériaux caractérisés par des grains solides et des vides (pores). L'espace poreux est généralement occupé par des fluides (par exemple, l'air et l'eau). Lorsque l'espace interstitiel est rempli d'une unique phase (l'eau, par exemple), la loi de Darcy et les équations de Navier-Stokes décrivent le mouvement du fluide dans le milieu poreux. Malheureusement, la description du flux devient beaucoup plus complexe dans les systèmes multiphasiques.

Des processus tels que l'érosion interne, dommages induits par des mouvements de terrain sur des structures et la réduction de la capacité portante des fondations superficielles causée par les fissures de désaturation au-dessus du niveau phréatique sont des exemples classiques de problèmes hydromécaniques qui démontrent l'intérêt de comprendre le comportement des sols non saturés.

Les méthodes expérimentales et numériques macroscopiques sont d'excellentes approches pour obtenir les propriétés physiques du sol. Néanmoins, la nature hétérogène et discontinue des matériaux granulaires peut éprouver certaines difficultés. Les propriétés locales sont inaccessibles ou décrites de manière inexacte par des tests expérimentaux ou des méthodes à l'échelle macroscopique.

Les progrès récents dans la technologie et l'informatique ont permis de développer nombreuses méthodes numériques capables de reproduire l'interaction hydromécanique complexe entre les phases à l'échelle des pores. Les méthodes numériques d'un point de vue microscopique, au contraire des approches classiques, nous permettent d'obtenir les propriétés locales qui seront ultérieurement utilisées pour récupérer les processus manifestés à l'échelle macroscopique.

Dans ce contexte, les méthodes numériques peuvent aider à mieux comprendre les structures liquides observées dans les milieux granulaires à faible saturation en liquide (ponts pendulaires, trimères et autres structures complexes). Le comportement hydromécanique du pont pendulaire a été étudié et implémenté dans de nombreux modèles numériques (Scholtès et al. (2009); Scholtès et al. (2009)). Cependant, moins d'attention a été consacrée à l'étude des matériaux humides pendant le régime funiculaire (il s'agit lorsque les ponts liquides se fusionnent pour former une phase liquide continue). Actuellement, les images tridimensionnelles générées par des techniques telles que la tomographie à rayons X, sont fréquemment pour caractériser la morphologie du fluide dans le milieu poreux (Scheel et al. (2008); Turner et al. (2004); Sakellariou et al. (2004)). Malgré ces développements, très peu de tentatives ont été effectuées pour obtenir les détails de la distribution du liquide dans le milieu poreux (Melnikov et al. (2015); Yuan et al. (2018)). Dans cette thèse, le comportement hydromécanique de la microstructure liquide est évalué afin de mieux comprendre les propriétés hydrostatiques et les forces capillaires dans le régime funiculaire. L'étude a été possible grâce à des simulations par la méthode de Boltzmann sur réseau (LBM) basées sur le modèle à plusieurs composants de Shan-Chen. La morphologie des structures liquides, les forces capillaires et la relation entre la pression capillaire et la saturation sont analysées pour différentes configurations des grains.

LBM est capable de gérer des géométries complexes. Par conséquent, LBM est adéquat pour décrire les écoulements multiphasiques dans des milieux poreux avec précision. Malheureusement, les simulations LBM d'échantillons de taille réaliste sont très coûteuses en temps de calcul. Ce travail, donc, explore la possibilité d'utiliser un modèle hybride basé sur une décomposition spatiale du milieu granulaire pour évaluer les propriétés hydromécaniques dans temps de computation acceptables.

Il convient de signaler qu'en raison de la nature discrète des milieux granulaires, les méthodes aux éléments discrets (DEM) sont largement utilisées pour la modélisation des interactions entre les particules solides qui constituent le milieu. Dans ce travail, on propose le couplage de la DEM avec un modèle réseau de gorges de pores (Throat-Network (TN), en anglais) en 2D inspiré par les modèles de réseau de pores. La représentation de l'espace des pores dans le modèle TN en 2D est basée sur une triangulation régulière d'un ensemble de disques. Les champs de pression et les flux sont évalués à l'aide de l'équation de continuité pour les fluides incompressibles afin de reproduire l'effet des fluides sur chaque particule solide.

Le modèle TN-DEM basé sur des solutions analytiques est limité à la deuxième dimension. Par conséquent, les algorithmes multiphasiques doivent être reformulés pour surmonter les complexités de la géométrie des pores dans la troisième dimension. Nous proposons un modèle Hybride qui combine l'efficacité de l'approche réseau de pores et la précision du LBM à l'échelle des pores. En d'autres termes, nous nous appuyons sur des simulations LBM pour déterminer les propriétés hydrostatiques (forces capillaires, pression capillaire d'entrée, courbes de pression capillaire-saturation, etc.) à l'échelle des pores pour évaluer le comportement global du milieu granulaire en intégrant les propriétés locales dans un modèle de réseau de pores. Même si le modèle hybride tire parti de l'approche réseau de pores en optimisant les ressources informatiques, le coût des calculs n'est pas négligeable. Par conséquent, on ajoute une révision des approximations et des solutions empiriques trouvées dans la littérature précédente afin d'améliorer et de valider les règles locales qui régissent l'écoulement multiphasique.

Modèles numériques pour les écoulements multiphasiques

Le comportement de milieux granulaires partiellement saturés peut être étudié d'un point de vue expérimental. En raison du coût élevé des appareils expérimentaux et de l'impossibilité de mesurer certaines propriétés mécaniques à échelles très locales, les méthodes numériques constituent une alternative intéressante pour obtenir des informations sur les mécanismes physiques de l'écoulement multiphasique dans les milieux poreux. Le développement de la technologie a créé de nouvelles possibilités pour étudier le domaine des écoulements multiphasiques avec des modèles numériques. Cependant, la géométrie complexe et la non-linéarité du problème compliquent encore l'analyse sans approximations grossières. En conséquence, les approches macroscopiques sont basées sur des simplifications géométriques et les propriétés de transport sont obtenues d'expériences en laboratoire. La principale difficulté rencontrée par les chercheurs pour modéliser les écoulements multiphasiques dans une perspective globale est liée aux fluctuations locales induites par les interactions microscopiques entre les fluides. Ces interactions modifient les conditions aux limites de l'autre fluide en modifiant la réponse globale. Le couplage hydromécanique devient encore plus complexe à étudier lorsque nous traitons de structures solides déformables.

Contrairement aux méthodes qui adoptent une perspective macroscopique, certains travaux (Kharaghani et al. (2012); Yuan and Chareyre (2017); Sweijen et al. (2018)) ont opté pour une approche à l'échelle microscopique. Ces modèles prennent en compte le couplage entre l'écoulement des fluides et la déformation de la phase solide pour étudier le comportement hydromécanique à l'échelle des pores. Le comportement mécanique du matériau granulaire est souvent basé sur la populaire méthode à éléments discrets (DEM) introduite par Cundall and Strack (1979). Bien que le DEM ait été conçu pour traiter les matériaux granulaires secs, certains travaux ont étendu le modèle aux milieux granulaires saturés et partiellement saturés. Les sections suivantes présentent différentes stratégies adoptées pour le couplage de la DEM avec des modèles d'écoulement des fluides.

- **Modèles continus**: La description macroscopique du système est possible en résolvant le moment cinétique et linéaire pour chaque particule solide et les équations de Navier-Stokes pour décrire le mouvement du fluide interstitiel. Ces modèles intègrent les fluctuations locales induites par les interactions microscopiques entre les fluides assurant la conservation de la masse. Les approches continues nécessitent des lois empiriques et des informations sur les propriétés constitutives. De plus, ces méthodes reposent sur maillage grossier pour la partie fluide (Kafui et al. (2002); Zeghal and El Shamy (2004)). Selon Catalano (2012), les modèles basés sur le continu sont incapables de décrire le comportement très local, cette limitation ajoute certaines difficultés pour les problèmes dans lesquels l'hétérogénéité joue un rôle important dans le comportement global (bandes de cisaillement dans les matériaux sans cohésion, microfissures dans les matériaux, etc). Bien que cet inconvénient limite l'applicabilité du modèle, les couplages continu-discrets effectuent des simulations numériques dans des temps de calcul raisonnables.

- **Modèles microscopiques**: Récemment, plusieurs méthodes ont été développées pour prédire l'écoulement dans les milieux poreux. La méthode de Boltzmann sur réseau (LBM) (Pan et al. (2004); Sukop et al. (2008)), la méthode du volume de fluide (VOF) (Raeini et al. (2012)) ou des méthodes sans maillage lagrangien (Tartakovsky et al. (2007)) sont des exemples de modèles microscopiques utilisés dans l'analyse des écoulements multiphasiques à travers des milieux poreux. Malgré le coût de calcul élevé, ces modèles permettent de reproduire les phénomènes physiques à différentes échelles. En outre, la nature de ces modèles les rend convenables dans géométries complexes et facilement parallélisables dans des clusters. Nous soulignons également que la plupart des modèles couplés entre DEM et écoulement des fluides résolu avec modèles microscopiques sont limités à la 2D en raison du élevé temps de calcul. Le couplage 2D DEM-LBM est généralement utilisé pour étudier le comportement d'un lit de sol soumis à un flux injecté localisé (Cui et al. (2012, 2014)). La méthode Smoothed Particle Hydrodynamics (SPH) a également été associée au DEM, fournissant des résultats prometteurs pour la simulation de mélanges solide-liquide (Potapov et al. (2001); Li et al. (2007)). D'autre part, SPH présente certaines difficultés pour appliquer la viscosité macroscopique (Li (2013)) et reproduire les écoulements turbulents.

- **Modèles Réseau de pores**: Afin d'avoir un coût de calcul acceptable, il est possible de décrire l'écoulement à travers un milieu poreux avec modèles de réseau de pores (Pore-Network (PN) en anglais). L'idéalisation de l'espace des pores en tant que réseau de pores et de gorges connectés entraîne une réduction du nombre d'inconnues par rapport aux modèles à l'échelle microscopique. Jusqu'à présent, très peu de travaux ont été consacrés aux modèles PN couplés à des modèles mécaniques. Pour un écoulement monophasique, Tarumi and Hakuno (1988) a été la première tentative d'incorporation des effets d'interaction des fluides dans la DEM. Leur technique a modifié la micromécanique du DEM afin d'inclure la loi de Darcy qui prend en compte la pression de l'eau dans les pores. Plus récemment, Jing et al. (2001) a analysé le comportement mécanique de l'interaction couplée contrainte-déformation et écoulement fluide dans la fracture de la roche. Malgré les résultats positifs, les simulations ont été limitées aux échantillons de disques 2D.

  Une approche tridimensionnelle à l'échelle des pores qui mérite d'être soulignée est la formulation en volume fini (Pore Finite Volume (PFV) en anglais) de l'écoulement visqueux d'un fluide interstitiel incompressible. La technique proposée par Chareyre et al. (2012) est basée sur une décomposition de l'espace des pores en éléments de pores et en conductances locales. La discrétisation de l'espace des pores est effectuée par des triangulations régulières et leurs graphes doubles de Voronoi appliqués à l'échantillon granulaire, comme illustré

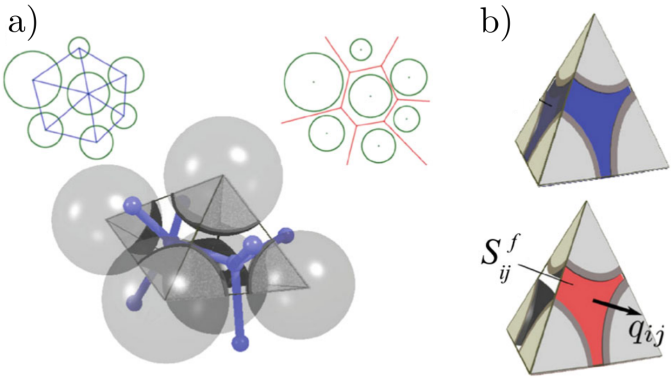

Figure 8.3: a) Une triangulation régulière et son graphe dual de Voronoi en deux et trois dimensions. b) Domaine fluide élémentaire (tétraèdre) à l'intérieur de sphères triangulées. Images extraites de Chareyre et al. (2012); Scholtès et al. (2015).

à la figure 8.3a. Le couplage PFV-DEM a donné de bons résultats dans les problèmes d'écoulement à une phase (Catalano et al. (2014); Scholtès et al. (2015); Montellà et al. (2016)). L'applicabilité du PFV-DEM est limitée au régime saturé. Par conséquent, le PFV-DEM a été étendu à un modèle capable de reproduire des écoulements de fluide à deux phases. Cette approche est appelée "Pore-scale two-phase flow - Discrete Element Method" (2PFV-DEM) et a été développée par Yuan et al. (2016). Des recherches récentes (Sweijen et al. (2017b); Yuan and Chareyre (2017)) montrent que les problèmes de fluide à deux phases sont efficacement résolus avec le 2PFV-DEM (voir l'exemple de la figure 8.4).

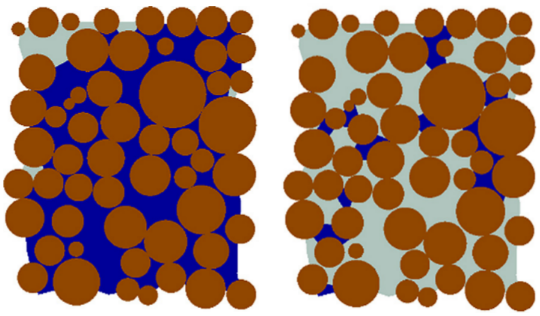

a) p_c^{*}=7.25 S_w=0.96 b) p_c^{*}=13.2 S_w=0.18

Figure 8.4: Drainage réalisé avec le 2PFV-DEM. Les sphères marrons représentent la phase solide, le bleu représente la phase mouillante et le gris, la phase non-mouillante. La phase non-mouillante envahit l'ensemble par le haut. La phase mouillante est piégée dans l'échantillon après le drainage. Image extraite de Yuan and Chareyre (2017).

Modèle 2PFV

Phase fluide

Considérons une unité de pore i. L'équation de continuité pour un fluide incompressible s'écrit:

$$V_i \frac{\partial S_{w,i}}{\partial t} + \sum_{j=1}^{4} q_{ij} = 0 \tag{8.1}$$

où V_i est le volume du pore et q_{ij} sont les flux de fluide du tétraèdre i vers les tétraèdres adjacents j_1 à j_4. Les flux et les gradients de pression ont une relation linéaire:

$$q_{ij} = g_{ij} \frac{\Delta_{ij}}{L_{ij}} \tag{8.2}$$

où Δ_{ij} est la chute de pression entre deux pores adjacents et c'est liée à la pression capillaire et aux pressions de fluide des pores voisins, L_{ij} est la distance entre les pores i et j , et g_{ij} est liée à la conductance hydraulique à travers la gorge des pores ij. Il faut noter que la pression capillaire (p_c) correspond à une différence entre la pression au sein du fluide mouillant (p^w) et celle de la phase non-mouillante (p^{nw}).

La définition suivante a été proposée avec des résultats satisfaisants pour g_{ij} dans le cas d'une gorge saturée (Tong et al. (2012)):

$$g_{ij} = \frac{S_{ij}^f R_{ij}^h}{L_{ij}^2} 2\mu \tag{8.3}$$

où S_{ij}^f est la surface occupée par le fluide dans la facette (voir figure 8.3) et R_{ij}^h est le rayon hydraulique (défini comme le rapport entre le volume occupé par le fluide et la surface solide-fluide).

Sur la base des configurations de fluide possibles dans deux pores voisins et une gorge de pore (Koplik and Lasseter (1985)), Δ_{ij} peut être exprimé par:

$$\Delta_{ij} = p_i^{nw} - p_j^{nw} + s_i^w (p_{c,ij} - p_{c,i}) - s_j^w (p_{c,ij} - p_{c,j}) \tag{8.4}$$

où $p_{c,i}$ et $p_{c,j}$ sont les pressions capillaires des éléments i et j, respectivement, et $p_{c,ij}$ est la pression capillaire d'entrée de la gorge du pore ij. Ainsi, le flux volumétrique (Éq. 8.2) est reformulé comme suit:

$$q_{ij} = g_{ij} \frac{(p_i^{nw} - p_j^{nw} + s_i^w (p_{c,ij} - p_{c,i}) - s_j^w (p_{c,ij} - p_{c,j}))}{l_{ij}} \tag{8.5}$$

Pression capillaire d'entrée

Supposons un pore rempli de la phase mouillante. La phase non-mouillante envahira le pore par la gorge lorsque la pression capillaire locale (p_c) sera supérieure à la pression capillaire d'entrée (p_c^e) de cette gorge. Plusieurs approches peuvent être envisagées pour calculer la pression capillaire d'entrée. Les approximations les plus courantes sont la méthode de Haines (Sweijen et al. (2016)) et la méthode de Mayer-Stowe-Princen (MS-P) (Joekar-Niasar et al. (2010b); Yuan et al. (2016)). L'approximation de Haines (Haines (1930)), "Méthode Incircle" ci-après, propose que la courbure de l'interface passant à travers la gorge des pores puisse être assumée comme une sphère en contact avec les grains sphériques définissant la gorge. D'autre part, la méthode MS-P repose sur un équilibre des forces pour les lignes de contact lors de l'invasion. Le modèle MS-P prédit la pression capillaire du ménisque de l'arc d'une goutte de fluide de longueur infinie à l'intérieur d'un tube cylindrique (Princen (1969); Mayer and Stowe (1965); Ma et al. (1996)).

Connaitre les pressions capillaires d'entrée pour chaque gorge est essentiel pour étudier le drainage dans un milieu granulaire. Au début, l'échantillon est totalement saturé avec la phase mouillante. Le drainage commence en diminuant la pression de la phase mouillante (p^w) tandis que la pression p^{nw} du réservoir de la phase non-mouillante est maintenue constante. Dès qu'un pore est envahi ($p_c^e \leq p_c$), la phase non-mouillante atteint de nouveaux points d'étranglement, déclenchant éventuellement une cascade récursive de sauts de Haines (Yuan (2016)), et envahissant plus d'un pore pour une seule valeur de p^w appliquée. En plus, la phase mouillante peut être déconnectée pendant le drainage.

Phase solide

La force totale $\mathbf{F}_k^f$ exercée sur une particule solide k par deux phases fluides inclut la contribution de la pression tenant compte des phases mouillante et non-mouillante ($\mathbf{F}_k^p$) et l'effet de la tension superficielle à l'interface solide - mouillant - non-mouillant $\mathbf{F}_k^t$.

$$\mathbf{F}_k^f = \mathbf{F}_k^p + \mathbf{F}_k^t \tag{8.6}$$

Méthode de Boltzmann sur réseau (LBM)

LBM est un modèle mésoscopique capable de simuler la dynamique des fluides dans des géométries complexes (Chen and Doolen (1998)). Alors que les méthodes numériques classiques reposent sur la discrétisation des équations de continuité macroscopique, le LBM est basé sur des modèles microscopiques et des équations cinétiques mésoscopiques des fluides. En raison de sa simplicité et de sa capacité à modéliser le mouvement des fluides dans des limites complexes, le LBM est très approprié pour simuler un écoulement multiphasique à travers un milieu poreux.

Le LBM résout une équation cinétique discrète (équation de Boltzmann) pour une fonction de distribution de particules $f^\sigma(\mathbf{x},t)$. Où l'exposant σ indique le composant fluide, $\mathbf{x}$ fait référence au nœud du réseau et t est le temps. Dans le LBM, le mouvement du fluide est décrit par l'équation de Boltzmann en réseau. Basée sur le simple et populaire opérateur de collision de Bhatnagar-Gross-Krook (BGK) (Bhatnagar et al. (1954)), l'équation standard de LBM peut être exprimée comme suit:

$$f_k^\sigma(\mathbf{x_k} + \mathbf{e_k}\Delta t, t + \Delta t) - f_k^\sigma(\mathbf{x_k}, t) = \frac{-\Delta t}{\tau^\sigma}(f_k^\sigma(\mathbf{x_k}, t) - f_k^{\sigma,eq}(\mathbf{x_k}, t)) \tag{8.7}$$

où τ^{σ} est le temps de relaxation vers l'équilibre local, $f_k^{\sigma,eq}$ est la fonction de distribution d'équilibre, Δt est l'incrément de temps, $\mathbf{e_k}$ sont les vitesses discrètes qui dépendent du modèle de vitesse particulier. Dans ce travail, le modèle utilisé est D3Q19 (espace tridimensionnel et 19 vitesses), et k varie de 0 à $Q-1$, ce qui représente les directions dans le réseau. Le côté gauche de l'équation 8.7 décrit l'étape de propagation (les particules se déplacent vers le nœud le plus proche en suivant la direction de leur vitesse) alors que le côté droit représente l'opérateur de collision (les particules arrivant au nœud le plus proche modifient leur vitesse vers un équilibre local). L'opérateur de collision correspond au terme visqueux dans l'équation de Navier-Stokes.

L'équilibre local $f_k^{\sigma,eq}$ dépend du type de réseau, de la densité et de la quantité de mouvement (Latt et al. (2008)). Les variables macroscopiques à chaque nœud du réseau sont récupérées utilisant les moments des fonctions de distribution:

- Densité:
$$\rho^{\sigma} = \sum_k f_k^{\sigma} \tag{8.8}$$
- Quantité de mouvement:
$$\rho^{\sigma}\mathbf{u}^{\sigma} = \sum_k f_k^{\sigma}\mathbf{e_k} \tag{8.9}$$

La distribution d'équilibre peut être vue comme une extension de la fonction de distribution de Maxwell-Boltzmann pour faibles nombres de Mach:

$$f_k^{\sigma,eq} = \rho^{\sigma} w_k \left[1 + \frac{1}{c_s^2}(\mathbf{e_k}\cdot\mathbf{u}^{\sigma,\mathbf{eq}}) - \frac{1}{2c_s^2}(\mathbf{u}^{\sigma,\mathbf{eq}}\cdot\mathbf{u}^{\sigma,\mathbf{eq}}) + \frac{1}{2c_s^4}(\mathbf{e_k}\cdot\mathbf{u}^{\sigma,\mathbf{eq}})^2\right] \tag{8.10}$$

où $c_s = \dfrac{1}{\sqrt{3}}$ est la vitesse du son et $\mathbf{u}^{\sigma,\mathbf{eq}}$ est la vitesse d'équilibre définie par Shan and Chen (1993, 1994):

$$\mathbf{u}^{\sigma,\mathbf{eq}} = \mathbf{u}' + \frac{\tau^{\sigma}\mathbf{F}_{\sigma}}{\rho^{\sigma}} \tag{8.11}$$

où $\mathbf{u}' = \dfrac{\sum_{\sigma} \dfrac{\rho^{\sigma}\mathbf{u}^{\sigma}}{\tau^{\sigma}}}{\sum_{\sigma} \dfrac{\rho^{\sigma}}{\tau^{\sigma}}}$ est une vitesse effective et $\mathbf{F}_{\sigma}$ est la force totale agissant sur chaque composant.

Modèle Shan-Chen

Dans le modèle de Shan-Chen, une force d'interaction entre composants (ou phases) est introduite pour décrire les écoulements multiphasiques. Cette force modifie l'opérateur de collision à travers d'une vitesse d'équilibre produisant un effet répulsif entre les phases.

Dans ce travail, nous nous concentrons sur les écoulements biphasiques ($\sigma = 2$). Ainsi, on considère que deux $f_k^{\sigma}(\mathbf{x},t)$ modélisent des écoulements avec deux composants fluides. Ci-après, ρ^w et ρ^{nw} feront référence aux phases mouillante et de non-mouillante.

Dans le modèle de Shan-Chen, la force non locale responsable de l'interaction fluide-fluide peut être exprimée comme suit:

$$\mathbf{F}_\sigma(\mathbf{x}) = -\Psi(\mathbf{x})\sum_{\bar{\sigma}} G_{\sigma\bar{\sigma}} \sum_k \Psi_{\bar{k}}(\mathbf{x}+\mathbf{e_k})\mathbf{e_k} \tag{8.12}$$

où Ψ_k est le potentiel inter-particule qui induit la séparation de phases et $G_{\sigma\bar{\sigma}}$ est la force d'interaction entre les composants σ, $\bar{\sigma}$.

Les travaux précédents (Shan and Chen (1994); Yuan and Schaefer (2006); Huang et al. (2011); Porter et al. (2012)) ont utilisé plusieurs potentiels inter-particule. Par des raisons de simplicité, nous considérons $\Psi_k = \rho_k$, comme le fait Pan et al. (2004). Les interactions entre les composants, $G_{12} = G_{21}$, sont définies comme positives afin d'induire une force de répulsion entre les phases. Les faibles valeurs de G_{12} conduisent à des processus de dissolution observés dans des mélanges miscibles. Au contraire, des valeurs significativement élevées de G_{12} provoquent des systèmes binaires presque immiscibles avec des interfaces pointues sujettes à des instabilités numérique. Par conséquent, une attention particulière doit être portée lors du choix de la force d'interaction car elle contrôle la tension superficielle et l'immiscibilité du système.

Finalement, l'équation d'état des gaz non idéaux peut être déterminée comme suit:

$$p = c_s^2 \sum_\sigma \rho^\sigma + c_s^2 \sum_{\sigma\bar{\sigma}} G_{\sigma\bar{\sigma}} \Psi_\sigma \Psi_{\bar{\sigma}} \tag{8.13}$$

Forces capillaires

Les forces capillaires exercées sur les particules de matériaux granulaires ont un impact important sur le comportement macroscopique. Les faibles teneurs en eau dans les sols humides confèrent des forces capillaires importantes qui augmentent la cohésion du matériau (Hornbaker et al. (1997)). En effet, l'action capillaire est fortement influencée par la quantité de contenu en eau. En conséquence, la compréhension des propriétés hydromécaniques des matériaux granulaires humides présente un intérêt majeur.

Dans le modèle Shan-Chen, des propriétés d'interaction similaires à celles d'un fluide sont attribuées aux nœuds solides (Huang et al. (2007)). Cette configuration aboutit à une couche non physique entre le fluide et le solide (Chen et al. (2014)). Par conséquent, des contraintes hétérogènes et non réelles se retrouvent dans les proximités solides. Pour surmonter les complexités présentées près des objets solides, nous proposons d'analyser les contraintes à l'intérieur d'un élément de volume éloigné de l'interface solide-fluide (voir élément Ω' dans la figure 8.5). La plupart de nos recherches sont conduites avec des particules sphériques, ce qui permet de prendre en compte les éléments de volume sphériques. Cependant, d'autres éléments, tels que des cubes, des tétraèdres, des plans, des ellipsoïdes peuvent être pris en compte.

La force agissant sur les grains sphériques est évaluée par l'intégrale suivante:

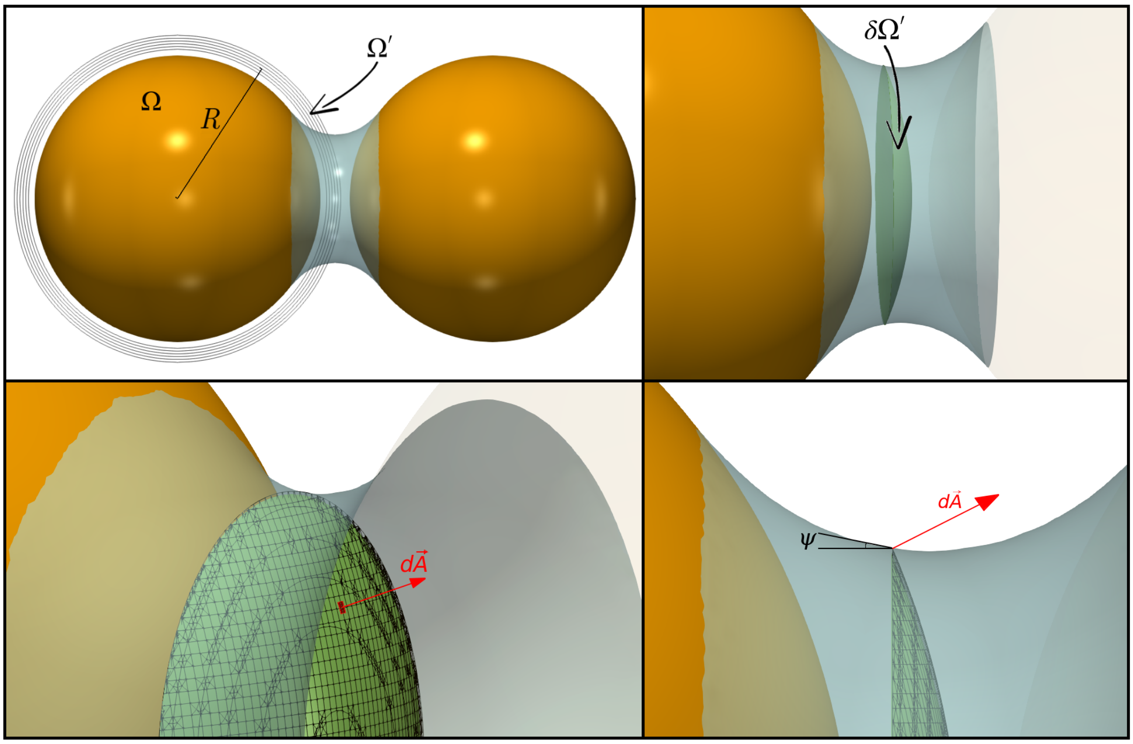

Figure 8.5: Dans le coin supérieur gauche, plusieurs éléments de volume sphériques (**Ω′**s) entourent le grain sphérique indiqué par **Ω**. Les autres images illustrent la surface obtenue à la suite de l'intersection (**δΩ′**) entre le pont liquide capillaire et l'élément de volume sphérique. Les contraintes sont intégrées sur tous les points de **δΩ′**.

$$\mathbf{F_c} = \int_{\delta\Omega'} -[p\delta_{ij} - c_s^2(2\tau - 1)S_{ij}]\mathbf{dA} \tag{8.14}$$

où **δΩ′** est la surface résultant de l'intersection de l'élément de volume sphérique et du pont liquide (voir les schémas dans la figure 8.5), S_{ij} est le tenseur déviateur et **dA** est le vecteur d'aire normal affiché au bas de la figure 8.5.

Simulations avec la méthode de Boltzmann sur réseau

Ponts capillaires et autres structures liquides plus complexes sont simulés avec LBM dans des conditions de drainage. Les forces capillaires, le volume et la morphologie des liquides obtenus sont comparés avec les solutions théoriques, approximations et résultats expérimentaux.

Pont capillaire

Le profil d'un pont capillaire peut être décrit par l'équation de Young-Laplace, comme le montre De Bisschop and Rigole (1982). La courbure moyenne (H_m) d'un pont pendulaire peut être écrite sous la forme suivante:

$$2H_m = \frac{r''}{(1+r'^2)^{3/2}} - \frac{1}{r(1+r'^2)^{1/2}} = \frac{p_c}{\gamma} \tag{8.15}$$

où $r = r(x)$ spécifie le rayon du col du pont capillaire à la position x. En raison de l'impossibilité d'intégrer Éq. 8.15 analytiquement, plusieurs études ont utilisé des approches numériques pour le résoudre. (Lian et al. (1993); Willett et al. (2000); Lian and Seville (2016); Scholtès et al. (2009)).

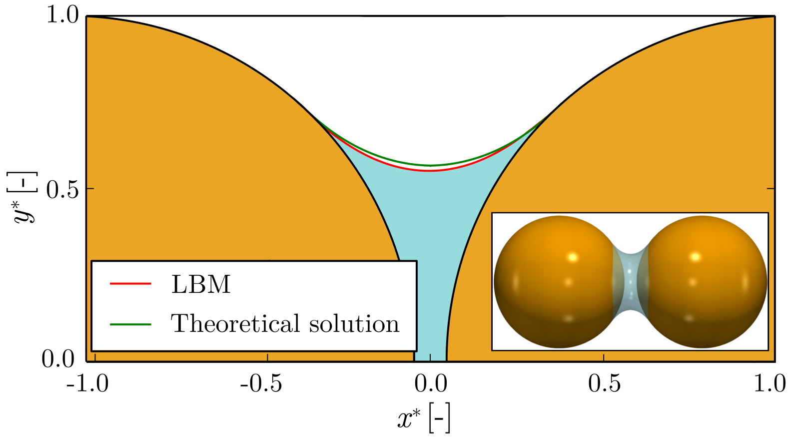

Figure 8.6: Profils de ponts capillaires superposés obtenus numériquement et analytiquement pour une pression capillaire $p_c^* = 0.6$.

La forme du pont pendulaire lorsque $p_c^* = 0.6$ est comparée à la solution de l'équation de Young-Laplace (Lian et al. (1993)) dans la figure 8.6. Après, la simulation LBM a été poursuivie en réduisant la quantité de phase mouillante et en enregistrant le volume du pont simulé pour une comparaison quantitative avec la solution de Young-Laplace.

La figure 8.7 montre la relation volume-pression jusqu'à la rupture du pont. La simulation LBM et la solution Laplace-Young suivent une tendance très similaire où l'erreur relative est généralement inférieure à 10 $^{-2}$.

En ce qui concerne les forces capillaires, la comparaison entre le LBM et la solution théorique confirme la validité de la méthode d'évaluation de la force. Nous observons des chemins similaires entre la simulation LBM et la solution Laplace-Young dans la figure 8.8 lorsque le liquide du pont est progressivement sucé. La figure 8.8a illustre des courbes presque coïncidentes pour des volumes relativement importants. Cependant, l'erreur augmente rapidement lorsque la pression capillaire est élevée et nous nous approchons au point de rupture. Les écarts élevés observés à $p_c^* \approx 15$ de la figure 8.8) sont attribués aux courants fausses (Shan (2006); Pooley and Furtado (2008)). Ces courants sont des vitesses non physiques qui apparaissent près des interfaces courbes en raison de la discrétisation de l'espace. Près de la rupture du pont, l'interface se rapproche d'un événement instable. A ce moment, la courbure de l'interface est considérablement élevée et la contribution de la contrainte déviatorique dans l'Éq. 8.14 devient la partie la plus importante. Au cours des étapes précédentes, des vitesses fausses étaient toujours présentes. Cependant, leur action n'a pas eu une grande influence sur l'analyse de la force, en effet, l'action hydrostatique dans

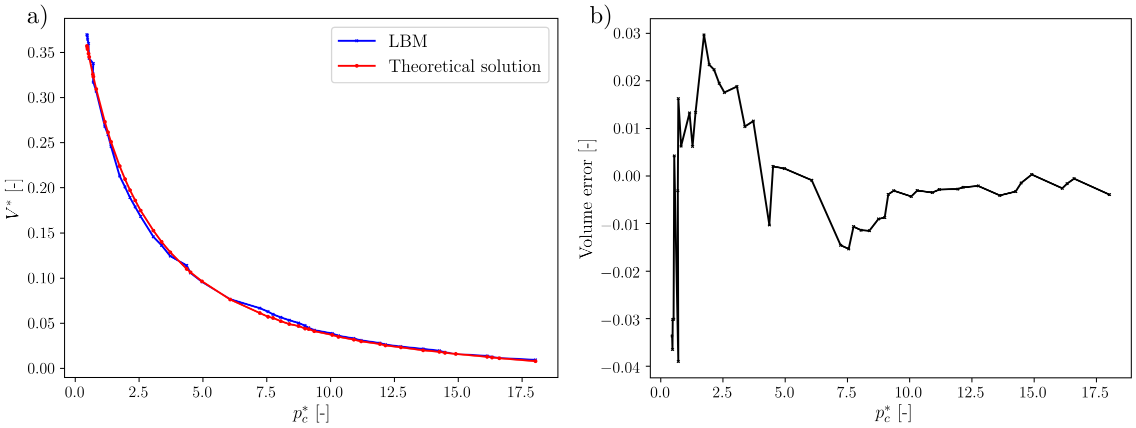

Figure 8.7: a) Volume en fonction de la pression capillaire pour un pont pendulaire simulé avec LBM et la solution numérique de l'équation de Laplace-Young. b) L'erreur relative est la différence entre le volume simulé et le volume théorique normalisé en tant que $V^* = V/R^3$, où V est le volume du pont et R le rayon des sphères.

l'Éq. 8.14 (qui implique des résultats plus précis) était prédominant. Malgré l'erreur introduite par les vitesses fausses, la méthode actuelle est capable de suivre la force pendant le processus de drainage avec une bonne précision.

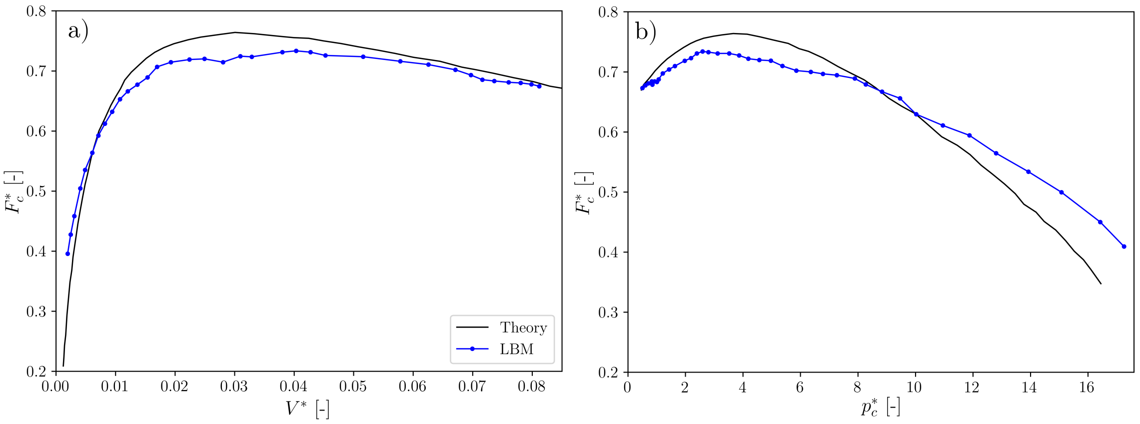

Figure 8.8: Évolution de la force capillaire en fonction du volume (a) et de la force capillaire en fonction de la pression capillaire (b) lors de drainage d'un pont capillaire. Les résultats sont obtenus pour un pont pendulaire entre deux grains séparés d'une distance $S^* = \dfrac{d}{R} = 0.1$, où d est la séparation entre les grains sphériques.

Trimère

Les trimères sont les configurations liquides obtenues après la fusion de trois ponts pendulaires formés entre trois particules adjacentes. Cette structure liquide est l'une des plus courantes durant le régime funiculaire (Scheel et al. (2008); Semprebon et al. (2016)). L'évolution de ces microstructures est évaluée dans des conditions de drainage avec LBM. Les résultats sont comparés aux données expérimentales et numériques fournies par Wang et al. (2017) en utilisant l'outil Surface Evolver (SE).

Tous les paramètres géométriques et les propriétés hydrostatiques sont ajustés pour reproduire le test de Wang et al. (2017).

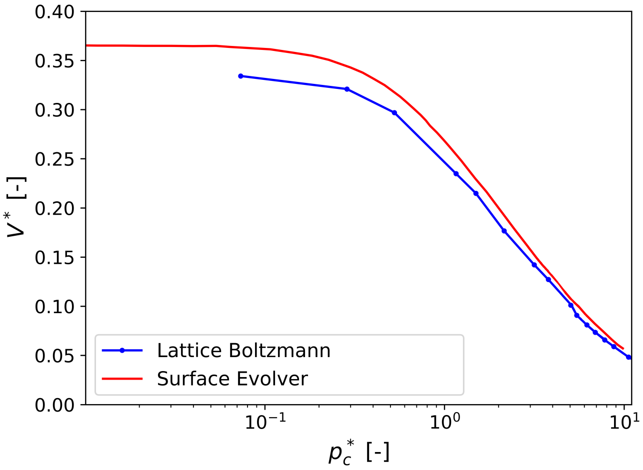

Figure 8.9: Volume en fonction de la pression capillaire pour les sphères en contact dans des conditions de drainage. Comparaison entre LBM et les résultats pour SE extraits de Wang et al. (2017).

L'effet de drainage en termes de pression capillaire est illustré à la figure 8.9 à l'échelle logarithmique. La diminution du contenu en liquide induit une augmentation de la pression capillaire. Nous soulignons le bon accord entre Surface Evolver et LBM dans la figure 8.9.

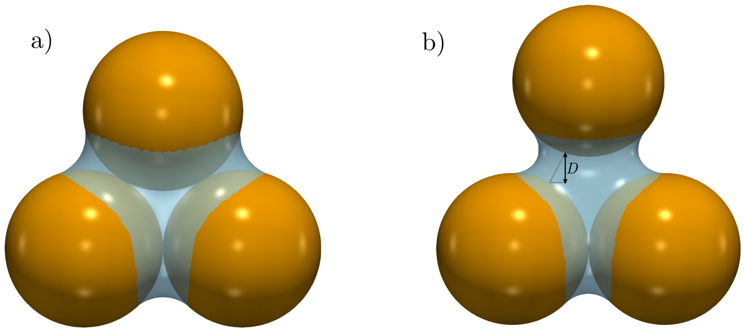

Figure 8.10: Évolution du régime funiculaire pour différents déplacements. Les images sont obtenues après des simulations LBM dans des conditions de volume contrôlé. À gauche, la sphère supérieure présente un déplacement vertical de $D^* = 0$. La figure de droite montre la configuration du fluide correspondant à un déplacement vertical de $D^* = 0.39$.

L'effet de la séparation d'une particule éloignée des autres est également étudié. Initialement, les trois sphères sont en contact et le volume de liquide est fixe. Ensuite, une des sphères est déplacée et la séparation augmente progressivement tout en maintenant le volume constant. La figure 8.10 montre la configuration des 3 sphères à l'état initial à gauche. La configuration après l'augmentation de la distance entre particules est illustrée à droite de la figure 8.10. Le déplacement de la sphère supérieure est défini comme suit: $D^* = \dfrac{D}{R}$, où D est la distance indiquée à la figure 8.10.

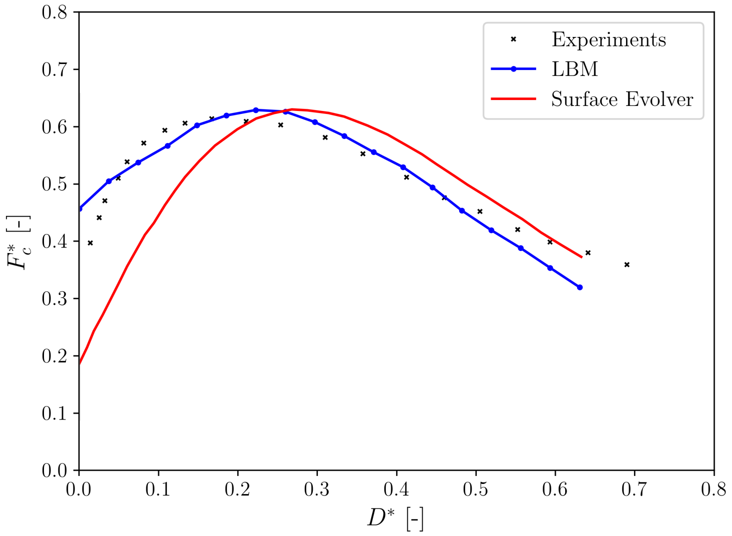

Figure 8.11: Comparaison de forces capillaires entre les résultats expérimentaux et les approches numériques pour $V^* = \dfrac{V}{\frac{4}{3}\pi R^3} = 0.178$. Les résultats expérimentaux et les données Surface Evolver ont été obtenus à partir de Wang et al. (2017). Trois sphères de diamètre égal en contact sont définies comme configuration initiale. L'un des grains sphériques est progressivement déplacé du reste.

La figure 8.11 montre la comparaison de LBM, SE et les résultats expérimentaux. La force capillaire augmente au début de l'essai en raison de l'effet d'épinglage. Comme le résume Willett et al. (2003), ce que l'on appelle l'effet d'épinglage se manifeste lorsqu'une force agit sur le liquide et que la ligne de contact triphasée reste entre les valeurs intermédiaires des limites de l'angle de contact. Lorsque l'une de ces limites est atteinte, la ligne de contact triphasique glisse. Une fois le pic est atteint, le test se déroule dans des conditions de glissement, ce qui entraîne une diminution de la force capillaire lorsque la distance de séparation augmente. La figure 8.11 montre des chemins similaires pour toutes les approches. Nous soulignons la bonne précision de la force capillaire maximale (des valeurs de pic similaires sont observées à la figure 3.12a). D'autre part, la courbe SE est décalée par rapport aux résultats expérimentaux et la courbe LBM n'est pas capable de reproduire avec précision l'effet d'épinglage (c'est pertinent à dire qu'en LBM, l'angle de contact est fixé à $\theta \approx 0^o$). Même si les effets des angles de contact en progression/recul ne sont pas intégrés, nous constatons que la solution LBM offre une prédiction précise des forces capillaires.

Modèle de réseau de gorge 2D

De nombreux articles ont étudié l'écoulement multiphasique contrôlé par capillarité Bakke et al. (1997); Hilpert and Miller (2001) en idéalisant la géométrie du milieu poreux. Néanmoins, les simplifications de la nature complexe peuvent entraver la description des phénomènes. De plus, certains travaux Gao et al. (2012) ont choisi d'enlever les structures liquides isolées (trimères, pentamères et autres grappes) car elles sont sujettes aux erreurs numériques. Afin de surmonter les difficultés liées à l'idéalisation géométrique, nous proposons un modèle numérique en 2D basé sur des solutions analytiques et un réseau extrait de la géométrie des pores comme détaillé dans Gladkikh and Bryant (2005); Yuan et al. (2016). La présente approche souligne l'importance de simuler à l'échelle du ménisque/gorge (plutôt qu'à l'échelle du pore) pour éviter les limitations associées à l'imbibition dans un milieu poreux (Vogel et al. (2005); Patzek et al. (2000)).

L'objectif principal de ce travail est mettre en place une étude préliminaire pour la réalisation d'un modèle numérique permettant de mieux prédire le déplacement multiphasique à travers un milieu poreux. Cette méthode s'appelle réseau de gorges de pores (Throat-Network (TN), en anglais). Ainsi, cette méthode est une démonstration pour ultérieur modèles hybrides basés sur des approches de réseau de pores et des expressions semi-analytiques (Chareyre et al. (2017)). La précision du modèle est testée avec les résultats fournis par la méthode de Boltzmann sur réseau à plusieurs composants de Shan-Chen (Shan and Chen (1993)).

Suivant l'idée de Blunt et al. (2002); Sinha and Wang (2007), le présent modèle évalue la position de l'interface fluide-fluide à travers de l'équation de Young-Laplace et du champ de pression dans le réseau. Deux phases non miscibles sont considérées (généralement l'air et l'eau). De plus, la conservation de la masse est supposée dans chaque pore.

Décomposition à l'échelle des pores

On considère qu'une triangulation régulière représente la topologie de l'espace des pores (Helba et al. (1992); Thompson and Fogler (1997); Bryant and Johnson (2003)). Dans ce cas particulier, les trois sommets du triangle correspondent aux trois centres de particules. Ce schéma est adopté car le domaine est divisé en groupes de trois disques les plus proches voisins. Dans un milieu granulaire dense, chaque groupe définit un pore. Puis, deux triangles adjacents forment une gorge de pore (voir figure 8.13). Par conséquent, cette décomposition conduit à un modèle de réseau de gorges où les caractéristiques géométriques sont bien représentées.

Équations gouvernantes

Selon l'équation de Young-Laplace (Blunt et al. (2002); Young et al. (1805)), le saut de pression à travers une interface fluide-fluide est proportionnel au produit de la tension superficielle et de la courbure de l'interface (voir figure 8.12):

$$p_c = p^{nw} - p^{w} = \gamma \left(\frac{1}{R_1} + \frac{1}{R_2} \right) \tag{8.16}$$

où p_c est la pression capillaire, p^{nw} et p^{w} sont respectivement les pressions des phases non-mouillante et mouillante, γ est la tension superficielle, et R_1 et R_2 sont

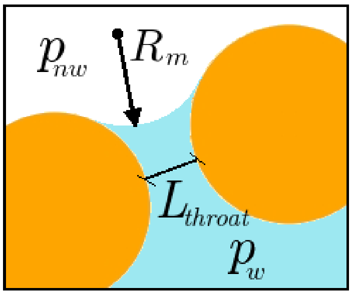

Figure 8.12: Selon l'équation de Young-Laplace (Éq. 8.17), le saut de pression $(p^{nw}-p^{w})$ à travers une interface fluide-fluide est proportionnel au produit de la tension superficielle et la courbure de l'interface $\left(k=\dfrac{1}{R_m}\right)$.

les principaux rayons de courbure. Puisque notre recherche est limitée à la 2D, nous adoptons l'expression de Young-Laplace suivante:

$$p_c = p^{nw} - p^{w} = \gamma \frac{1}{R_m} cos\theta \tag{8.17}$$

où θ est l'angle de contact et R_m est le rayon du ménisque. Nous supposons désormais un angle de contact de $\theta \approx 0$, mais le modèle peut être étendu de manière triviale à $\theta \neq 0$.

Au cours du déplacement d'interface dû au drainage, p_c est augmenté et les rayons du ménisque sont réduits en fonction de l'Éq. 8.17. La phase non-mouillante commence à envahir les pores lorsque le diamètre du ménisque est égal à la longueur de la gorge des pores (distance minimale entre deux grains solides), c'est-à-dire $2 \cdot R_m = L_{throat}$, voir la figure 8.12 pour une explication graphique. A ce moment, la pression capillaire est appelée pression capillaire d'entrée:

$$p_c^e = \frac{2\gamma}{L_{throat}} \tag{8.18}$$

En réalité (un espace tridimensionnel), le déplacement de fluide est assez complexe à simuler en raison de la difficulté à déterminer la pression d'entrée p_c^e. En effet, p_c^e se trouve généralement après quelques simplifications (Haines (1927) et Mayer and Stowe (1965); Princen (1969)). En ce qui concerne les simulations 2D, la complexité du problème est commodément réduite. Les problèmes tridimensionnels peuvent être simplifiés en 2D dans des cas particuliers tels que l'étude de l'écoulement perpendiculaire à des éléments cylindriques (Saito and De Lemos (2005)) ou l'évaluation de la perméabilité en milieu poreux fibreux (Spaid and Phelan Jr (1997)).

Par souci de simplicité, nous considérons des échantillons contenant des fluides incompressibles et particules statiques. Ainsi, Éq. 8.1 devient:

$$\sum_{j=1}^{3} q_{ij} = 0 \tag{8.19}$$

où q_{ij} est le flux entre les pores i et j (voir la figure 8.13a).

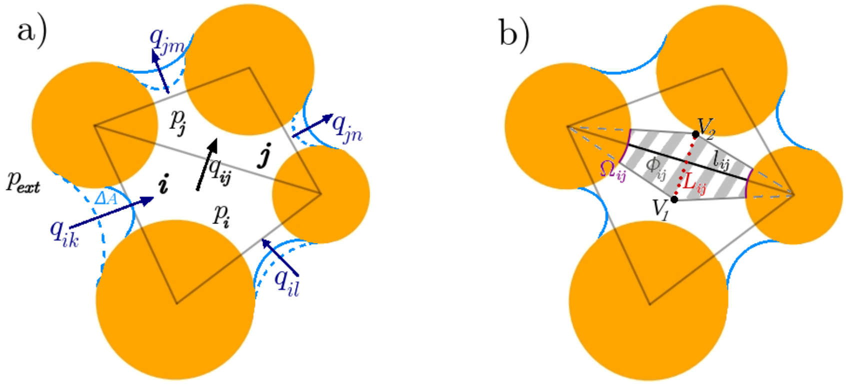

Figure 8.13: a) Éléments triangulaires après la décomposition. q_{ij} est le flux entre les pores i et j. L'interface fluide au temps t est affichée avec une ligne en pointillé. Au temps $t+\Delta t$, le flux vers l'élément j mène à une nouvelle configuration représentée par une ligne continue. b) les quantités géométriques de la gorge selon Chareyre et al. (2012)

Le flux q_{ij} peut être exprimé, avec un nombre de Reynolds bas, en termes de gradient inter-pores:

$$q_{ij} = g_{ij} \frac{p_i - p_j}{L_{ij}} \tag{8.20}$$

où $p_i - p_j$ est la différence de pression entre deux triangles adjacents, L_{ij} est la longueur de la gorge des pores définie comme la distance entre les sommets de Voronoi (le diagramme de Voronoi est double de la triangulation de Delaunay), et g_{ij} est la conductance locale qui peut être évaluée comme suit:

$$g_{ij} = \chi \frac{l_{ij} {R^h_{ij}}^2}{\mu} \tag{8.21}$$

où l_{ij} est la longueur de l'ouverture de la gorge, μ est la viscosité dynamique du fluide, R^h_{ij} est le rayon hydraulique du pore défini par $R^h_{ij} = \frac{\phi_{ij}}{\Omega_{ij}}$ (ϕ_{ij} est la zone ombrée occupée par le fluide dans la figure 8.13b et Ω_{ij} le périmètre de l'interface solide-fluide affiché dans la figure 8.13b), et χ est le facteur de conductance non dimensionnel, supposé égal à 0.5 comme dans Chareyre et al. (2012). Voir la figure 8.13b pour avoir une meilleure idée des quantités géométriques.

Éq. 8.20 est modifié pour les gorges qui ont au moins une interface fluide-fluide (elles seront désormais appelées gorges "ouvertes"). Dans ce cas particulier, l'expression Éq. 8.20 est remplacé par:

$$q_{i,ext} = g_{i,ext} \frac{p_{ext} - p_i + p_c}{L_{i,ext}} \tag{8.22}$$

Afin de reproduire le déplacement de l'interface, une source est introduite dans Éq. 8.19:

$$\sum_{j=1}^{3} q_{ij} = \Theta \tag{8.23}$$

où Θ adopte des valeurs positives pour les processus d'imbibition ou de condensation et des valeurs négatives pour le drainage et l'évaporation. Si $\Theta = 0$, aucune source n'est prise en compte.

En suivant les étapes de Bakke et al. (1997) et de Sinha and Wang (2007), nous pouvons déterminer le champ de pression de notre réseau après avoir résolu l'ensemble des équations linéaires suivantes:

$$\mathbf{QP} = \mathbf{f} \tag{8.24}$$

où **Q** est une matrice comprenant les informations sur les conductivités, **P** est la matrice contenant les valeurs de pression des cellules triangulaires (**P** est inconnu) et **f** représente les sources. Les valeurs internes de **f** sont non nulles pour les gorges d'interface dans lesquelles une source est imposée.

Indépendamment de l'existence d'une "source", la procédure suivante est effectuée pour chaque pas de temps:

1. Le champ de pression est déterminé après résolution de l'Éq. 8.24. Chaque cellule a une certaine pression.

2. La pression capillaire, p_c, est calculée pour toutes les interfaces (donc, les gorges "ouvertes"). Si p_c atteint la pression d'entrée ($p_c = p_c^e$), le liquide pénètre dans la gorge et commence à envahir le pore.

3. Les flux sont évalués avec Éq. 8.20 et 8.22 pour chaque gorge.

4. La position de l'interface est trouvée en fonction de la pression capillaire. Le rayon du ménisque est trouvé après l'Éq. 8.17, donc $R_m = \dfrac{\gamma}{p_c}$. L'interface correspond à l'arc de cercle tangent aux deux disques qui forment la gorge.

5. Le mécanisme est répété pour chaque pas de temps.

Résultats

Imbibition d'un macropore

Cette section illustre un phénomène typique observé dans les milieux poreux: la fusion de ménisques. Plus particulièrement, nous simulons un macropore dans des conditions d'imbibition en aspirant la phase non-mouillante, donc, la pression capillaire diminue. Par conséquent, les ménisques grossissent et se fusionnent une fois qu'ils touchent d'autres ménisques (voir la figure 8.14). Le nombre de ménisques est réduit (à mesure que les rayons augmentent) jusqu'à ce que le macropore soit presque complètement saturé (voir la figure 8.14c).

Des conditions quasi-statiques sont assurées tout au long de la simulation. En effet, le manque d'événements dynamiques conduit à une correspondance presque parfaite entre les profils LBM et TN (voir la figure 8.14). Il convient de souligner que les courbes de pression capillaire - saturation (voir la figure 8.14) sont également en bon accord avec LBM. Cependant, de légères divergences sont observées à cause de faibles pertes de charge. Ces sauts correspondent à des événements mineurs de Haines qui se produisent lorsque la phase mouillante traverse la gorge et commence à occuper un espace plus vaste. Globalement, les résultats de LBM et de TN coïncident, ce qui suggère que TN est capable de reproduire le mécanisme de fusion de ménisques.

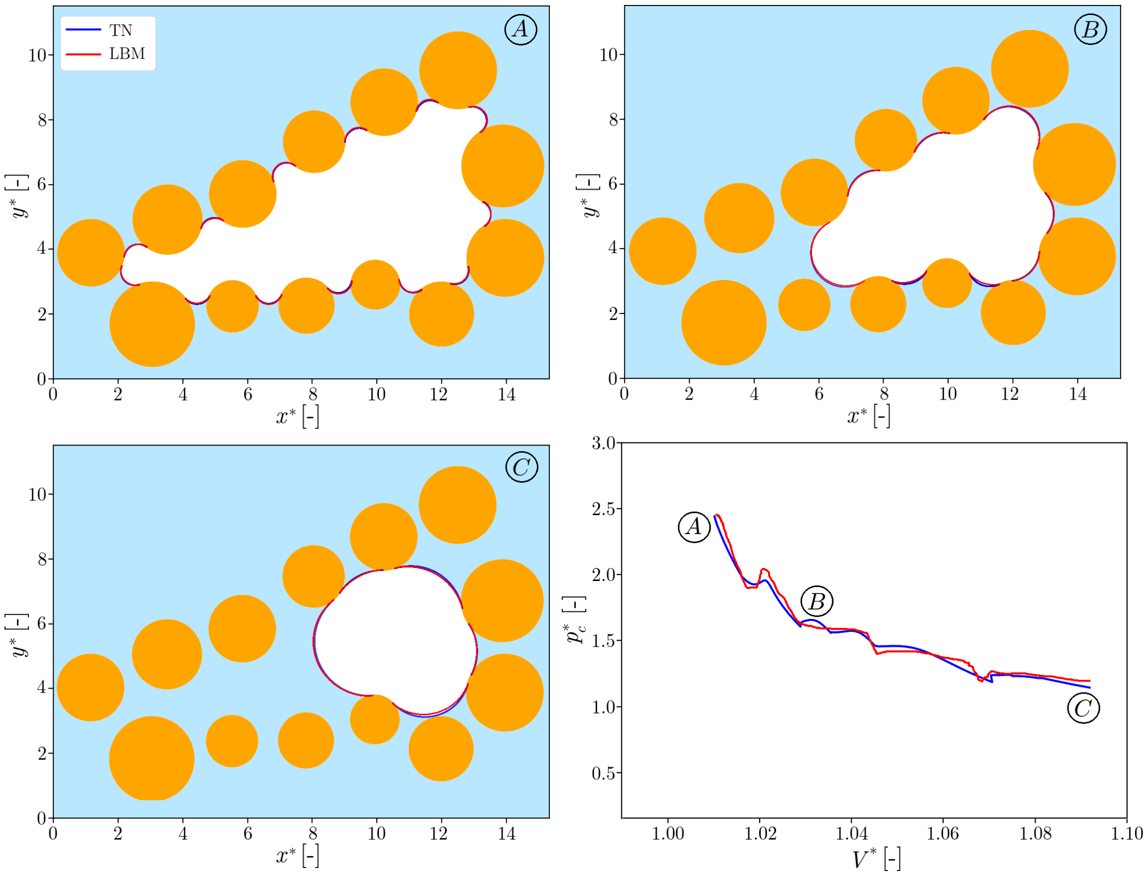

Figure 8.14: Comparaison de la position de l'interface entre les modèles LBM et TN. La pression capillaire est volontairement réduite pour forcer l'imbibition du macropore. Les ménisques commencent à se fusionner avec les autres ménisques à mesure qu'ils augmentent les rayons. Progressivement, le système devient plus saturé. Différents volumes sont considérés: Ⓐ $V^* = 1.01$, Ⓑ $V^* = 1.03$ et Ⓒ $V^* = 1.09$.

Remplissage d'un pore

Cet exemple prétend reproduire le mécanisme de "remplissage des pores". Le mouvement de l'interface fluide entre une gorge étroite et un pore plus large entraîne un saut de Haines et, par la suite, une redistribution rapide du fluide. Techniquement, un fort événement dynamique peut conduire au remplissage d'une gorge déjà vide. Afin de reproduire ce phénomène, nous avons adopté la configuration de disques présentée dans la figure 8.15. Des conditions quasi-statiques ont été supposées pour assurer la cinétique du drainage. Les événements les plus remarquables de la procédure sont énumérés ci-dessous:

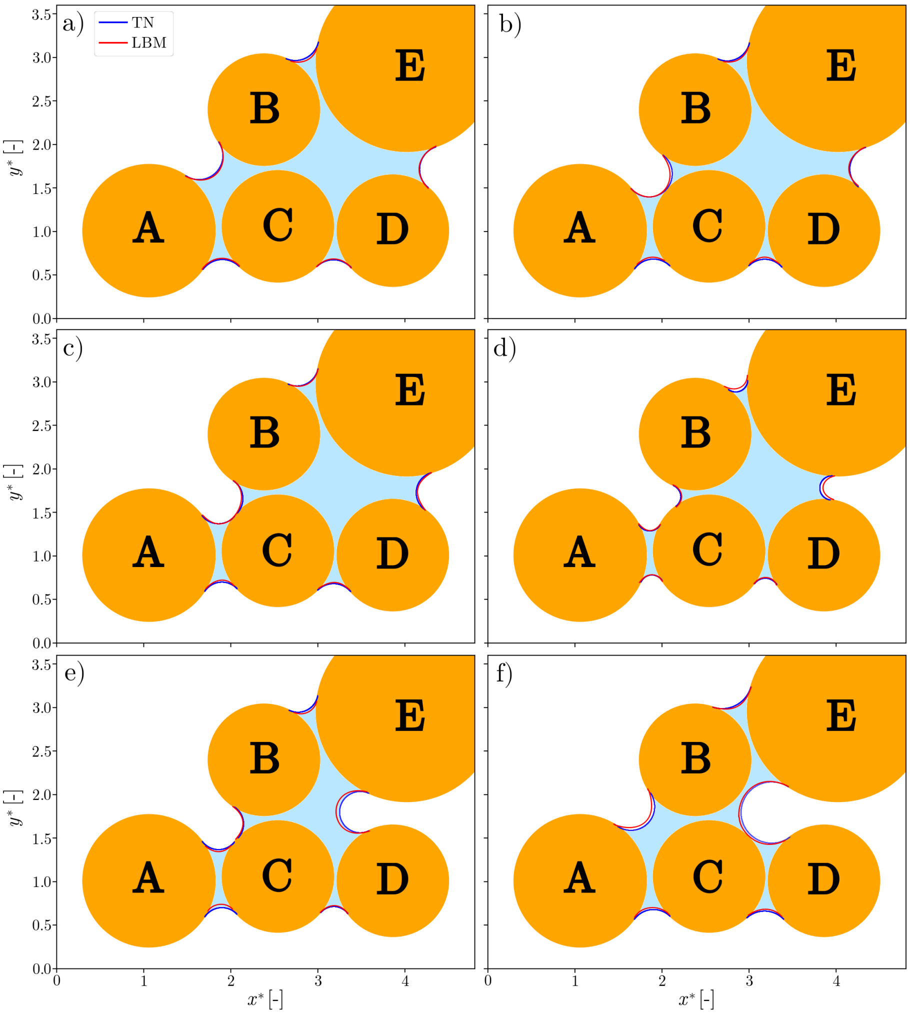

Figure 8.15: Comparaison de la position de l'interface entre les modèles LBM et TN. Différents volumes sont considérés: a) $V^* = 0.97$, b) $V^* = 0.82$, c) $V^* = 0.80$, d) $V^* = 0.69$, e) $V^* = 0.58$ et f) $V^* = 0.54$.

- a) L'ensemble des 5 disques est initialement complètement saturé, comme indiqué dans la figure 8.15a.
- b) La phase non-mouillante pénètre à travers la gorge A-B. Le ménisque A-B croît légèrement jusqu'à rencontrer le disque C. La figure 8.15b montre que le pore ABC n'est pas beaucoup plus large que la gorge A-B. Par conséquent, la pression capillaire est marginalement réduite (aucune chute de pression significative n'est observée) après avoir atteint la pression capillaire d'entrée de la gorge A-B (voir figure 8.16).
- c) Le ménisque A-B se scinde en deux ménisques lorsque le disque C est atteint. La nouvelle configuration est une microstructure liquide formée de 4 disques

(B-C-D-E) et d'un pont isolé (A-C). L'avancée de l'interface se poursuit avec l'augmentation de la pression capillaire (voir figure 8.16).

- d) L'interface du ménisque D-E continue d'augmenter sa courbure jusqu'à envahir la gorge des pores. À ce moment, la pression capillaire (pression capillaire d'entrée pour la gorge D-E) atteint son maximum sur la figure 8.16.
- e) Le ménisque d'arc D-E déplace la phase mouillante remplissant le pore contenu par les particules B-C-D-E. L'invasion rapide provoque un remplissage des pores. Tous les ménisques réduisent leur courbure. Le déplacement de fluide le plus remarquable se trouve au niveau de la gorge B-C. L'action dynamique induite par le saut de Haines commence à remplir le pore ABC. Outre le mécanisme de remplissage illustré dans 8.15e, nous observons la chute de pression importante qui déclenche le phénomène de remplissage de la figure 8.16.
- f) Le pore ABC est complètement rempli avec la phase mouillante. À partir des trois dernières images de la séquence (figures 8.15d, 8.15e et 8.15f), nous observons que la phase non-mouillante pénètre dans le groupe par la gorge D-E et pousse la phase mouillante vers le côté gauche, remplissant éventuellement le pore constitué par les particules ABC. La simulation a été arrêtée lorsque le ménisque de l'arc D-E touche le disque C.

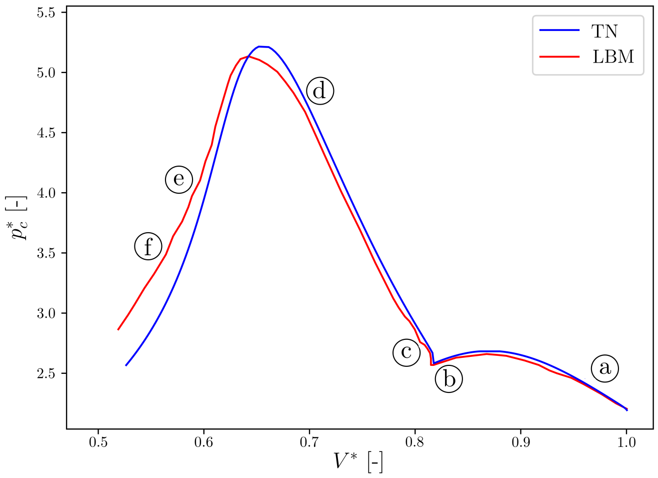

Figure 8.16: Comparaison de la courbe pression capillaire - saturation entre les modèles LBM et TN. Les volumes de la phase mouillante de la figure 8.15 sont inclus dans cette image.

Modèle hybride multi-échelle

Globalement, la pression capillaire augmente progressivement pendant le procès de drainage. Cependant, de brusques pertes de pression apparaissent lorsque la phase non-mouillante traverse une gorge étroite pour pénétrer dans un pore plus large

(Haines (1930)). Cette instabilité est provoquée quand la pression capillaire locale dépasse la pression capillaire d'entrée ($p_c^e < p_c$). Comme indiqué dans les sections précédentes, p_c^e peut être approché par la méthode Incircle (Sweijen et al. (2016)), la méthode de Mayer-Stowe-Princen (MS-P) (Joekar-Niasar et al. (2010b); Yuan et al. (2016)), ou des simulations directes de fluide.

Les simulations des modèles microscopiques permettent de reproduire le mouvement des écoulements multiphasiques avec une excellente précision à l'échelle des pores. Cependant, ces modèles présentent limitations de calcul à l'échelle macroscopique. Plusieurs études basées sur la méthode de Boltzmann sur réseau (Pan et al. (2004); Van Kats and Egberts (1999); Ahrenholz et al. (2008)) ont décrit avec succès le déplacement de l'interface dans des géométries complexes. Bien que la méthode soit facile à mettre en parallèle, les simulations sont limitées à des domaines relativement petits en raison des coûts de calcul élevés.

En revanche, actuellement il y a des méthodes très efficaces qui reposent sur des estimations et des approximations qui prédisent le comportement d'un écoulement multiphasique dans un temps de calcul acceptable, au détriment de la précision. Un exemple de ces méthodes sont les modèles de réseau de pores (PN), ces méthodes ont été largement utilisées pour prédire le mouvement de fluides à travers un milieu poreux (Fatt et al. (1956); Fenwick et al. (1998); Blunt (2001)).

Nous présentons un modèle hybride basé sur une approche de réseau de pores qui décompose l'échantillon granulaire en petits sous-domaines. Puis, des simulations LBM sont effectuées pour chaque gorge des pores afin de déterminer les propriétés hydrodynamiques (pression capillaire d'entrée, courbe de drainage primaire, morphologie du liquide, etc.) à l'échelle microscopique. Les propriétés locales obtenues avec LBM sont incorporées au réseau pour effectuer la simulation à plus grande échelle. Cette stratégie conduit à une réduction significative du temps de calcul à l'échantillon par rapport à une méthode totalement résolue. Par conséquent, la méthode hybride combine l'efficacité de l'approche par réseau de pores et la précision du LBM.

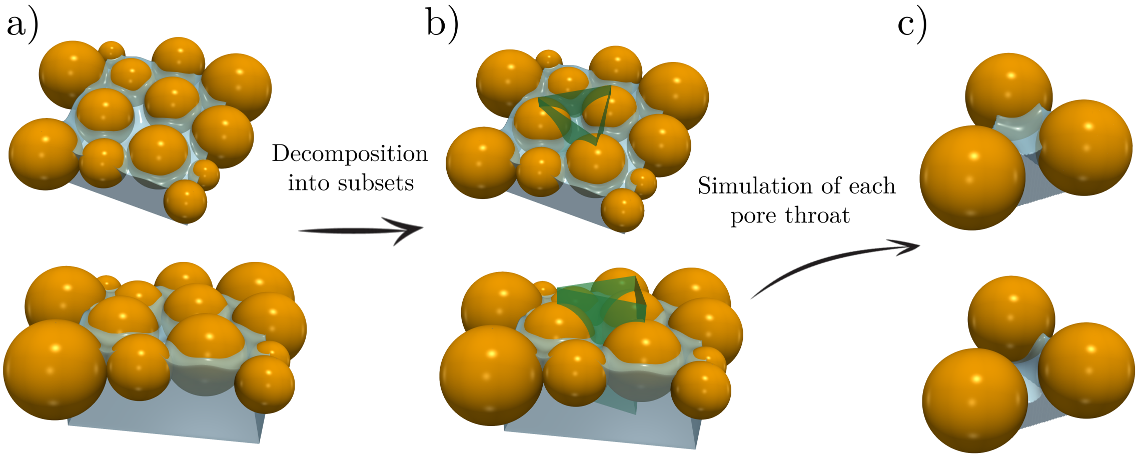

Figure 8.17: Décomposition de l'échantillon granulaire (a) en petits sous-domaines (b). Chaque sous-domaines est composé de 3 sphères (c).

Approximations à l'échelle des pores

Suivant le schéma de triangulation décrit au début de ce résumé (voir figure 8.3), un ensemble de sphères peut être décomposé comme indiqué dans la figure 8.17. La topologie des gorges des pores est décrite par chaque sous-domaine élémentaire. En particulier, la forme d'une gorge de pore est définie par la surface de la section transversale qui s'étend au sein d'une facette tétraédrique (voir figure 8.18).

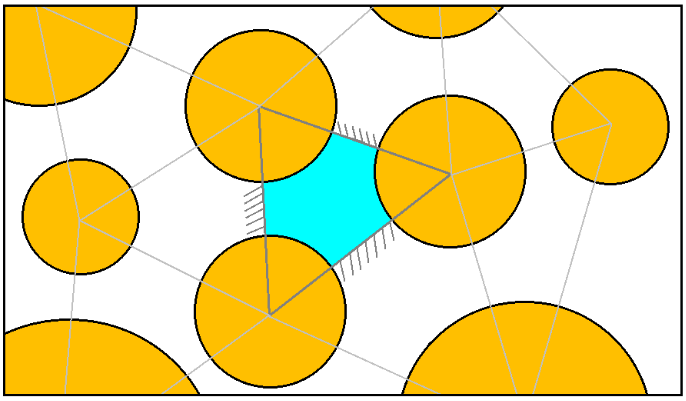

Figure 8.18: Domaine (en 2D) après la décomposition.

Comme détaillé dans la section **"Pression capillaire d'entrée"**, p_c^e est l'un des principaux facteurs contrôlant le drainage. Nous suivons un critère d'invasion similaire au schéma 2PFV-DEM. Ainsi, le déplacement de la phase non-mouillante est directement lié à la pression capillaire. En outre, l'invasion par la gorge des pores se produit lorsque la pression capillaire locale est supérieure à la pression capillaire d'entrée.

Lors du déplacement de fluide dans un sous-domaine, l'interface adopte des formes très complexes. En fait, les ménisques de l'interface observés dans la figure 8.17c ne montrent aucune symétrie de translation ou de rotation. L'analyse de la forme du ménisque nécessite la solution de l'équation de Laplace-Young, une équation différentielle partielle de deuxième ordre non linéaire pouvant être résolue numériquement en temps de calcul très élevés. En raison de cette limitation, il semble raisonnable d'envisager d'autres approches permettant de prédire la pression capillaire d'entrée et la forme du ménisque. Nous utilisons des simulations directes basées sur le LBM pour déterminer les principales propriétés hydromécaniques. Néanmoins, pour des raisons pratiques, lorsque les ressources de calcul sont limitées, une expression semi-analytique peut être utilisée pour prédire la pression capillaire d'entrée. Les approximations les plus courantes sont la méthode de Haines Incircle (Sweijen et al. (2016)) et la méthode de Mayer-Stowe-Princen (MS-P) (Joekar-Niasar et al. (2010b); Yuan et al. (2016)).

MS-P

Le modèle Mayer-Stowe-Princen (MS-P) prédit la pression capillaire du ménisque de l'arc d'une goutte de fluide de longueur infinie à l'intérieur d'un tube cylindrique (Princen (1969); Mayer and Stowe (1965); Ma et al. (1996)).

Dans le schéma 2PFV-DEM, la pression capillaire d'entrée (p_c^e) de la gorge interstitielle est calculée en suivant la méthode MS-P, qui utilise l'équilibre des forces sur l'interface non-mouillante - mouillante à l'état transitoire. La balance sur une gorge spécifique s'écrit:

$$\sum \mathbf{F}(p_c) = \mathbf{F^p}(p_c) + \mathbf{F^t}(p_c) = 0 \tag{8.25}$$

où $\mathbf{F^p}$ est la force capillaire agissant sur le domaine de la section de gorge des pores; $\mathbf{F^t}$ est la force de tension totale au long des lignes de contact multiphasiques, et p_c^e est la valeur de p_c telle que $\sum \mathbf{F}(p_c) = 0$.

Approximation de "Haines Incircle"

L'approximation de Haines Incircle (Haines (1930)), "Méthode Incircle" ci-après, propose que la courbure de l'interface traversant la gorge des pores puisse être assumée comme une sphère en contact avec les grains sphériques définissant la gorge des pores. Par conséquent, la pression capillaire d'entrée est $p_c^e = 2\gamma/r_{ins}$, où γ est la tension superficielle et r_{ins} est le rayon du cercle inscrit dans la gorge des pores.

Simulation directe d'une sole gorge avec LBM

Cette section fournit une méthode alternative pour déterminer p_c^e pour chaque gorge. Au lieu d'utiliser les approximations MS-P ou Incircle, les propriétés hydrostatiques sont obtenues à partir de simulations directes. L'espace des pores est décomposé en une série de domaines de la gorge suivant une triangulation régulière (voir figure 8.17). La décomposition mène à une liste de gorges de pores résolues indépendamment. Simulations LBM avec le modèle Shan-Chen sont utilisées pour évaluer le mouvement des fluides et estimer la courbe de drainage primaire et la pression capillaire d'entrée pour chaque gorge. Le domaine de calcul est un prisme de forme triangulaire défini par trois parois solides orthogonales à la gorge des pores (plan défini par les trois sphères, comme indiqué sur la figure 8.17b). Chacune de ces parois traverse deux des centres des sphères (deux sommets du triangle défini par les centres des 3 sphères). Le lecteur est dirigé vers les figures 8.17 et 8.18 pour une compréhension plus complète. Un angle de contact de 90 degrés est imposé aux limites pour imiter les conditions symétriques de chaque paroi solide. De plus, le domaine est entouré de deux triangles en haut et en bas du prisme représentant les sections d'entrée et de sortie des simulations LBM.

Initialement, les phases mouillante et non-mouillante sont en équilibre pour chaque problème élémentaire. La figure 8.19 montre l'évolution d'une configuration de sous-domaine typique. Dans ce cas, la gorge des pores est formée de trois sphères de même taille en contact. La densité des nœuds situés dans les sections d'entrée et de sortie est ajustée pour augmenter progressivement la pression capillaire. L'incrément déclenche le déplacement de l'interface fluide-fluide (voir figures 8.17c et figure 8.19). La courbure du ménisque d'interface augmente à mesure que la pression capillaire monte.

L'évolution de la pression capillaire normalisée ($p_c^* = \dfrac{2p_cR}{\gamma}$, où γ est la tension superficielle, R est le rayon des sphères et p_c est la pression capillaire) pendant

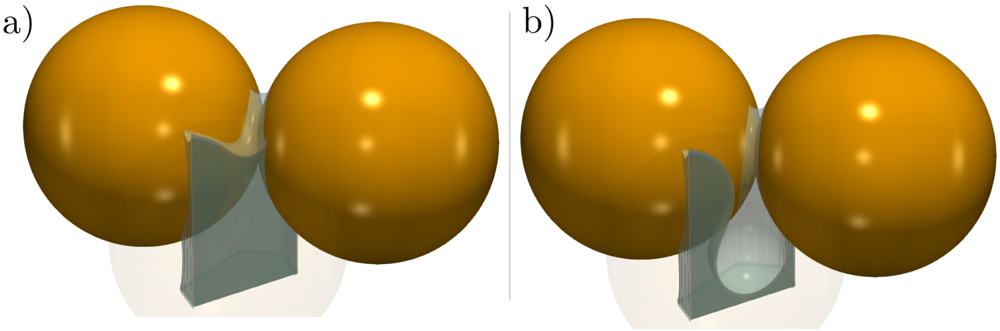

Figure 8.19: Invasion par une phase non-mouillante d'une gorge de pore formée par trois sphères. Remarquez la troisième sphère translucide devant les autres sphères.

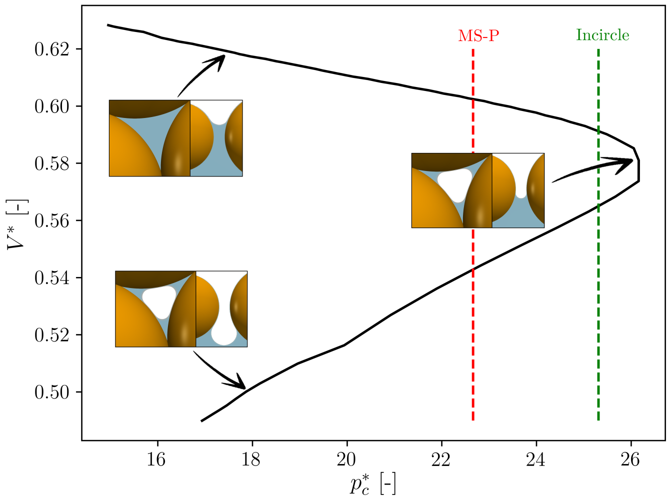

Figure 8.20: Changement de volume et pression capillaire lors de l'invasion de la gorge, superposés à la pression capillaire d'entrée prédite par les méthodes MS-P et Incircle. Trois instantanés affichant des tranches verticales et horizontales de la simulation montrent la morphologie du liquide avant, pendant et après l'invasion des pores.

l'invasion est liée au changement de volume de la phase mouillante dans la figure 8.20. Le volume adimensionnel est défini comme:

$$V^* = \frac{V(t)}{\frac{4}{3}\pi R^3}, \text{ où } V(t) \text{ est le volume au temps } t.$$

La pression capillaire d'entrée p_c^e est définie comme la valeur maximale atteinte par p_c pendant le processus d'invasion. Lorsque la pression capillaire atteint la pression capillaire d'entrée ($p_c = p_c^e$), la phase non-mouillante pénètre dans le pore (voir figures 8.19 et 8.20). Immédiatement après l'invasion, le ménisque d'interface élargi, entraînant une réduction de la pression capillaire. Cette procédure est répétée pour toutes les gorges de l'échantillon. Ainsi, p_c^e est déterminé pour tous les sous-domaines et intégré au problème global traité par le réseau de pores.

Drainage dans un échantillon granulaire à 40 sphères

Cette section présente les résultats d'un processus de drainage dans un échantillon granulaire à 40 sphères. Une simulation LBM entièrement résolue a été réalisée et supposée comme donnée de référence. Ensuite, les résultats sont comparés au modèle hybride. Un pack de sphères aléatoires est créé par le code source ouvert YADE. Une boîte cubique de 10 mm x 10 mm x 10 mm est définie avec 40 sphères polydispersées. Le rayon moyen de la sphère est de 1.26 mm. Les hypothèses suivantes sont formulées lors des simulations numériques:

- Le drainage est évalué sous un flux quasi-statique ($Ca \approx 0.0001$).
- Mouillage parfait du solide par la phase mouillante.
- Les régions déconnectées restent saturées.

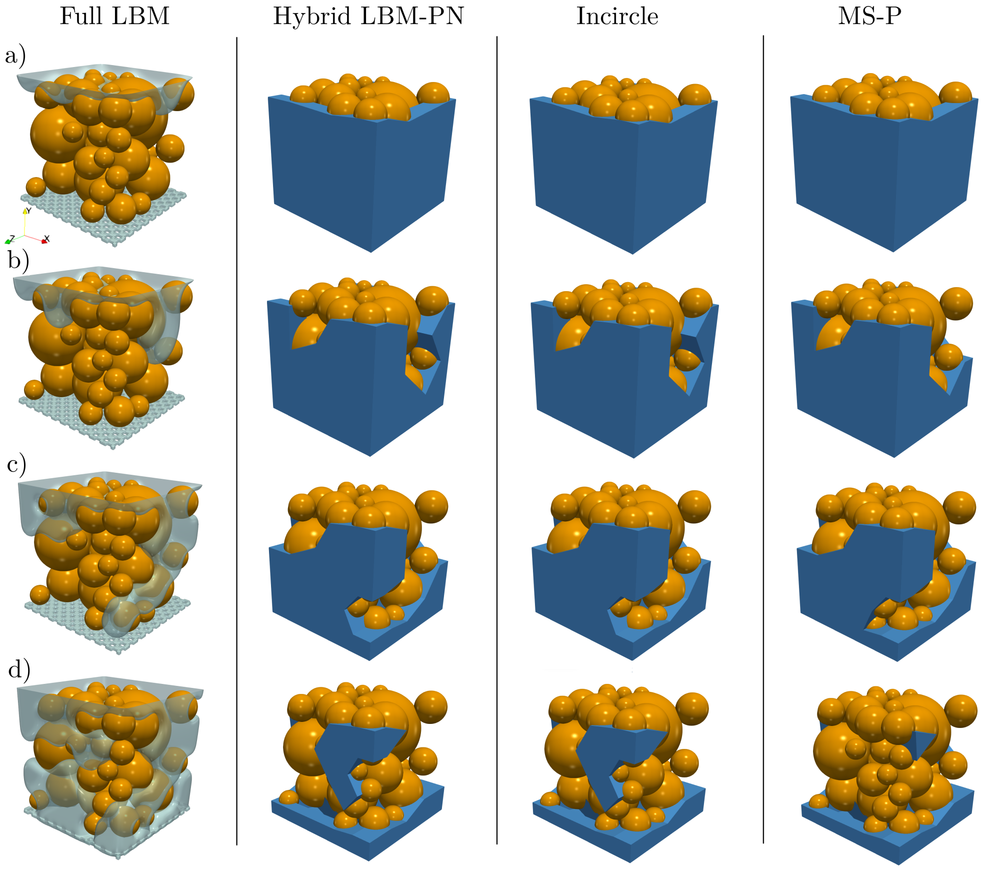

Figure 8.21: Comparaison du chemin d'invasion entre la simulation LBM complète (interface translucide) et les méthodes Hybride, Incircle et MS-P (phase mouillante illustrée en bleu).

Initialement, l'échantillon granulaire est complètement saturé (voir figure 8.21a - Full LBM). Une membrane poreuse est située au bas de l'échantillon afin d'empêcher la phase non-mouillante d'atteindre la sortie et d'assurer un drainage complet. Le déplacement de l'interface est effectué par un flux fixe contrôlé par une différence de pression entre le réservoir non-mouillant (haut de l'échantillon) et le réservoir mouillant (bas de l'ensemble granulaire). L'interface s'écoule vers le bas, entraînée par le gradient de pression envahissant d'abord les pores les plus grands, puis la phase non-mouillante occupe progressivement les espaces de pores de l'échantillon. La pression capillaire est augmentée et enregistrée jusqu'à ce que tous les nœuds au-dessus de la membrane poreuse soient remplis avec la phase non-mouillante (voir figure 8.21d- Full LBM). À ce moment, la phase mouillante restante est piégée dans l'assemblage granulaire sous forme de microstructures liquides. La figure 8.22 met en évidence la présence de ponts pendulaires et de trimères dans le milieu granulaire après le drainage.

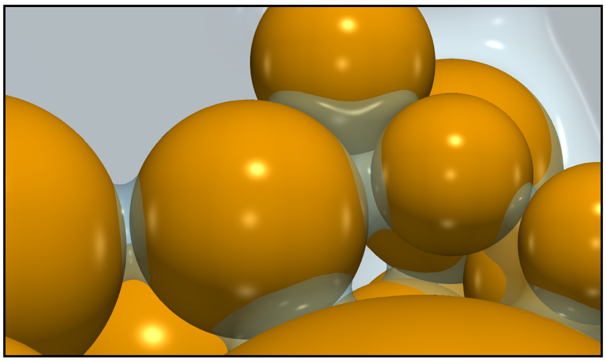

Figure 8.22: Distribution de la phase mouillante après la simulation du drainage. La phase mouillante est piégée dans certaines régions de l'échantillon sous la forme de ponts pendulaires ou autres structures liquides.

La figure 8.21 capture les chemins parcours par la phase non-mouillantes pour différents pas de temps pour chaque méthode. L'interface de la simulation LBM complètement résolue est représentée par une isosurface bleue translucide et la phase mouillante est représentée en bleu foncé pour les modèles Hybride, Incircle et MS-P dans la figure 8.21. Nous remarquons la capacité du modèle Hybride et Incircle à prédire le premier chemin préférentiel (une intrusion identique est observée dans les figures 8.21b et 8.21c). Au fur et à mesure du drainage, la phase non-mouillante continue d'occuper l'échantillon en laissant liquide déconnectée (voir figure 8.21d). Même si la méthode hybride représente bien la phase mouillante piégée dans l'assemblage, la figure 8.21d suggère qu'il existe une certaine divergence de phases entre les modèles dans certaines régions.

Il est à noter que le temps CPU pour un drainage complet correspond à 29.6 jours pour lea simulation LBM complètement résolue. D'autre part, en utilisant le modèle hybride, le coût de calcul est réduit à 11.2 jours.

Conclusions

L'objectif principal de cette thèse était d'évaluer les propriétés hydrostatiques et le comportement mécanique des microstructures liquides au-delà du régime pendulaire. Nous nous sommes concentrés sur différentes approches pour décrire la morphologie des liquides et les forces capillaires à l'échelle des pores. De plus, nous avons développé de nouvelles techniques pour étudier les écoulements multiphasiques à travers des milieux poreux.

La première partie de cette thèse (chapitres 2 et 3) était consacrée à l'examen de la précision de la méthode de Boltzmann sur réseau basée sur le modèle à plusieurs composants de Shan-Chen (SC-LBM) et de la possibilité de reproduire un écoulement multiphasique à la micro-échelle. L'étude sur les forces capillaires pendant le régime funiculaire a suggéré que la forme de l'interface a un impact plus fort sur les forces que la pression capillaire loin des transitions régime / forme.

En raison des coûts de calcul élevés associés aux simulations LBM, les chapitres 4, 5 et 6 explorent la possibilité d'utiliser modèles hybrides basés sur la décomposition de l'échantillon granulaire afin d'évaluer les propriétés hydromécaniques avec un temps de calcul acceptable.

Le chapitre 4 présente un modèle de réseau de gorge 2D appelée Throat-Network (TN) inspiré des modèles de réseau de pores précédents. TN est basé sur des solutions analytiques et capable de reproduire un flux triphasique dans un milieu poreux 2D constitué par particules circulaires tassées. La position de l'interface fluide-fluide a été bien décrite et s'est avérée presque identique au profil LBM dans les exemples élémentaires. Au cours des simulations, il est devenu évident que le modèle TN peut gérer plusieurs événements locaux: saut de Haines, rupture du ménisque en ménisques indépendants, fusion de deux ménisques et remplissage des pores en raison d'effets dynamiques. La polyvalence et la précision du modèle rendent le TN comme une alternative attrayante pour reproduire des problèmes multiphasiques 2D. Par exemple, l'écoulement à travers des éléments cylindriques ou l'évaluation de la perméabilité dans des milieux poreux fibreux.

Aux chapitres 5 et 6, nous avons proposé un modèle hybride qui tire parti à la fois de l'efficacité des modèles de réseau de pores et de la précision des simulations directes obtenues avec le LBM. La méthode hybride a été capable de reproduire avec précision les mouvements de l'interface pendant le processus de drainage. Les ponts liquides ont été facilement identifiés et bien décrits après l'invasion de chaque gorge des pores. Les ressources de calcul ont été optimisées en remplaçant les gorges avec configurations géométriques complexes par de simples approximations. Compter exclusivement sur des méthodes approximatives (méthodes MS-P et Incircle) est une autre alternative qui permette de prédire les principales propriétés hydrostatiques sans coûts de calcul importants. En fait, le modèle hybride n'offrait pas une solution bien meilleure que l'approximation Incircle lors de l'étude de chemins d'invasion ou de la courbe de drainage primaire. En revanche, le modèle hybride est le seul capable de déterminer la relation entre la pression capillaire et le contenu de la phase mouillante pour chaque gorge des pores et la morphologie du liquide après l'invasion de la phase non-mouillante. L'identification des interfaces restantes est une caractéristique importante si l'on veut évaluer les forces capillaires entre particules. Par conséquent, l'adoption du modèle hybride fait une différence par rapport au reste des approximations à l'échelle des pores pour comprendre le comportement hydromécanique à l'échelle microscopique.

Resum en català

Introducció general

Els fluxos multifàsics cobreixen un ample ventall de fenòmens naturals i d'aplicacions industrials. Alguns exemples són les aigües de pluja infiltrades al sòl, els lliscaments de terreny, la recuperació del petroli, la indústria alimentària, etc. Una millor comprensió de les propietats i dels mecanismes dels fluxos a través d'un entorn porós és essencial per predir i modelar el comportament dels fluxos multifàsics.

Els fluxos multifàsics es troben en diversos àmbits científics (química, mecànica, farmàcia, geociències, biologia, ciència dels materials, etc.). Tanmateix, és important fer èmfasi que els treballs desenvolupats a aquesta tesi es centren en els sòls parcialment saturats. Aquests sòls són materials caracteritzats per partícules sòlides i buits (porus). L'espai porós està generalment ocupat per fluids (per exemple, l'aire i l'aigua). Quan l'espai intersticial s'omple d'una única fase (l'aigua, per exemple), la llei de Darcy i les equacions de Navier-Stokes permeten descriure el moviment del fluid dins el medi porós. Malauradament, la descripció del flux esdevé molt més complexa als sistemes que inclouen més d'una fase.

Processos tals com l'erosió interna, danys induïts per sòls expansius sobre estructures i la reducció de la capacitat portant de les fundacions superficials degut a les fissures de desaturació a sobre del nivell freàtic són exemples clàssics de problemes hidromecànics que demostren l'interès d'entendre el comportament dels sòls no saturats.

Els mètodes experimentals i numèrics que adopten una perspectiva macroscòpica són excel · lents per obtenir les propietats físiques del sòl. Tanmateix, la naturalesa heterogènia i discontínua dels materials granulars pot donar lloc a certes dificultats. Per exemple, les propietats locals són inaccessibles o descrites de manera inexacta.

Els recents avenços en la tecnologia i la informàtica han permès l'aparició de nombrosos mètodes numèrics capaços de reproduir la interacció hidromecànica complexa entre les fases a l'escala dels porus. Aquests tipus de mètodes numèrics, a diferència dels enfocaments clàssics, permeten obtenir les propietats locals que, posteriorment, s'utilitzaran per estudiar els processos manifestats a l'escala macroscòpica.

Així doncs, els mètodes numèrics poden ajudar a comprendre millor les estructures líquides observades als medis granulars a baixa saturació (ponts pendulars, trimers i altres estructures complexes). El comportament hidromecànic del pont pendular ha estat estudiat i implementat a molts models numèrics (Scholtès et al. (2009); Scholtès et al. (2009)). En canvi, l'estudi dels materials humits durant el règim funicular (quan els ponts líquids es fusionen per formar una fase líquida continua) ha rebut un interès menor. Actualment, les imatges tridimensionals generades per tècniques com ara la tomografia a radis X, són freqüentment utilitzades per caracteritzar la morfologia del fluid a l'entorn porós (Scheel et al. (2008); Turner et al. (2004); Sakellariou et al. (2004)). Malgrat aquests desenvolupaments tecnològics, els estudis per obtenir informació detallada sobre la distribució del líquid al medi porós són escassos (Melnikov et al. (2015); Yuan et al. (2018)). A aquesta tesi, el comportament hidromecànic de la microestructura líquida s'avalua per tal de comprendre millor les propietats hidroestàtiques i les forces capil · lars durant el règim funicular. L'estudi ha estat possible gràcies a simulacions realitzades amb el lattice Boltzmann method (LBM) basades en el model de diversos components de Shan-Chen. La morfologia de les estructures líquides, les forces capil · lars i la relació entre la pressió capil · lar i la saturació s'analitzen per a diferents configuracions de les partícules sòlides.

El LBM és capaç de reproduir el moviment dels fluids dins de geometries complexes. Per tant, el LBM és una bona eina per descriure els fluxos multifàsics a través de medis porosos amb precisió. Desgraciadament, les simulacions realistes amb el LBM són molt costoses en quant a temps de càlcul. Aquest treball, doncs, explora la possibilitat d'emprar un model Híbrid basat en una descomposició espacial del medi granular per avaluar les propietats hidromecàniques amb temps de computació acceptables.

Convé indicar que degut a la naturalesa discreta dels medis granulars, els mètodes d'elements discrets (DEM) són àmpliament utilitzats per a la modelització de les interaccions entre les partícules sòlides que constitueixen el medi. A aquest treball es proposa un acoblament entre el DEM i un model de xarxa de goles de porus (Throat-Network (TN), en anglès) en 2D. La representació de l'espai dels porus al model TN en 2D es basa en una triangulació regular d'un conjunt de discos. El camp de pressió i els fluxos es determinen amb l'ajuda de l'equació de continuïtat per als fluids incompressibles per tal de reproduir l'efecte dels fluids sobre cada partícula sòlida.

El model TN-DEM basat en solucions analítiques presenta diverses limitacions quan s'estén a la tercera dimensió. Per consegüent, els algoritmes multifàsics han de ser reformulats per superar les complexitats de la geometria dels porus. Finalment, proposem un model Híbrid que combina l'eficàcia de l'enfocament de la xarxa porus i la precisió del LBM a l'escala dels porus. En altres paraules, utilitzem simulacions LBM per tal de determinar les propietats hidroestàtiques (forces capil · lars, pressió capil · lar d'entrada, corbes de pressió capil · lar-saturació, etc.) a l'escala dels porus per posteriorment avaluar el comportament global del medi granular integrant les propietats locals a un model de xarxa de porus. Tot i que el model Híbrid es beneficia de l'enfocament xarxa de porus optimitzant els recursos informàtics, el cost computacional no és negligible. Per tant, a l'estudi s'inclou una revisió de les aproximacions i de les solucions empíriques utilitzades en treballs precedents per tal de millorar i validar les regles locals que prediuen el flux multifàsic.

Models numèrics per a fluxos multifàsics

El comportament de sòls parcialment saturats pot ser estudiat des d'un punt de vista experimental. No obstant, l'elevat cost dels aparells i la impossibilitat de mesurar certes propietats mecàniques a escales molt locals fan que els mètodes numèrics siguin una alternativa interessant per obtenir informacions detallades sobre els mecanismes físics del flux multifàsic dins de medis porosos. La constant innovació i avenços en les ciències de la computació fan possible un estudi exhaustiu i realista dels fluxos multifàsics. Tanmateix, la complexa geometria i la no-linealitat dels problemes compliquen una anàlisi sense recórrer a les aproximacions. En conseqüència, els mètodes macroscòpics es basen en simplificacions geomètriques i propietats físiques obtingudes en experiments realitzats al laboratori. La principal dificultat trobada pels investigadors per a modelar els fluxos multifàsics des d'una perspectiva global està lligada a les fluctuacions locals induïdes per les interaccions microscòpiques entre els fluids. A més, l'acoblament hidromecànic esdevé encara més complex a l'hora d'estudiar estructures sòlides deformables.

A diferència dels mètodes que adopten una perspectiva macroscòpica, certs treballs (Kharaghani et al. (2012); Yuan and Chareyre (2017); Sweijen et al. (2018)) han optat per un enfocament a l'escala microscòpica. Aquests models prenen en compte l'acoblament entre el flux dels fluids i la deformació de la fase sòlida per estudiar el comportament hidromecànic a l'escala dels porus. El comportament mecànic del material granular sovint es descriu amb el popular mètode a elements discrets (DEM) introduït per Cundall and Strack (1979). Encara que el DEM hagi estat concebut per tractar els materials granulars secs, certs treballs han estès el model a medis granulars saturats i parcialment saturats, incloent-hi els efectes viscosos. Les seccions següents presenten diferents estratègies adoptades per a l'acoblament de la DEM amb models de flux dels fluids.

- **Models continus**: La descripció macroscòpica del sistema és possible resolent el moment cinètic i lineal per a cada partícula i les equacions de Navier-Stokes per descriure el moviment del fluid intersticial. Aquests models integren les fluctuacions locals induïdes per les interaccions microscòpiques entre els fluids assegurant la conservació de la massa. Els models continus depenen de lleis empíriques i les propietats extretes de models constitutius. A més a més, aquests mètodes es basen en un mallatge groller per a la part fluida (Kafui et al. (2002); Zeghal and El Shamy (2004)). Segons Catalano (2012), els models continus són incapaços de descriure el comportament local. Aquesta limitació comporta certes dificultats pels problemes en els quals l'heterogeneïtat juga un paper important al comportament global (bandes de cisallament als materials sense cohesió, microfissures, etc). Encara que aquest inconvenient limita l'aplicabilitat del model, els acoblaments continu-discrets efectuen simulacions numèriques amb temps de càlcul molt raonable.

- **Models microscòpics**: Recentment, diversos mètodes han estat desenvolupats per predir el flux als medis porosos. El mètode de "lattice Boltzmann" (LBM) (Pan et al. (2004); Sukop et al. (2008)), el mètode del "Volume of fluid" (VOF) (Raeini et al. (2012)) o els mètodes sense mallatge lagrangià

(Tartakovsky et al. (2007)) són exemples de models microscòpics utilitzats a l'anàlisi dels fluxos multifàsics a través dels medis porosos. Malgrat l'elevat cost computacional, aquests models permeten reproduir els fenòmens físics a diferents escales. A més, la naturalesa d'aquests models els fa adequats per a geometries complexes i fàcilment paral · lelitzables a clústers. Ressaltem que la majoria dels models acoblats entre DEM i models microscòpics per a la simulació de fluids es limiten a la 2D a causa de l'elevat temps de càlcul. L'acoblament DEM-LBM en 2D s'utilitza generalment per estudiar el comportament d'un llit granular subjecte a un flux injectat localitzat (Cui et al. (2012, 2014)). El mètode "Smoothed Particle Hydrodynamics" (SPH) també ha estat acoblat al DEM proporcionant resultats prometedors per a la simulació de barreges multifàsiques (Potapov et al. (2001); Li et al. (2007)). D'altra banda, SPH presenta certes dificultats per aplicar la viscositat macroscòpica (Li (2013)) i reproduir fluxos turbulents.

- **Models xarxa de porus**: Per tal d'aconseguir un temps computacional acceptable, el flux a través d'un medi porós es pot descriure amb models de xarxa de porus (Porus-Network (PN) en anglès). Aquests models idealitzen l'espai dels porus com una xarxa de porus i de goles connectades. Fins ara, molt pocs treballs han utilitzat els models PN acoblats a models mecànics. Tarumi and Hakuno (1988) va ser el primer intent d'incorporar els efectes d'interacció dels fluids a la DEM modificant la micromecànica de la DEM per tal d'incloure la llei de Darcy que pren en compte la pressió de l'aigua als porus. Més recentment, Jing et al. (2001) va analitzar el comportament hidromecànic en la fracturació de roques. Malgrat els resultats positius, les simulacions han estat limitades a mostres granulars en 2D.

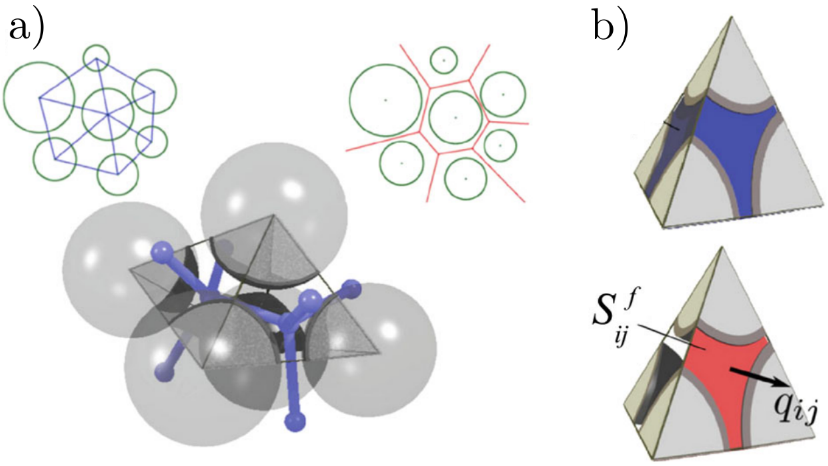

Figure 8.23: a) Una triangulació regular i el seu dual de Voronoi en dos i tres dimensions. b) Domini fluid elemental (tetraedre) a l'interior d'esferes triangulades. Imatges extretes de Chareyre et al. (2012); Scholtès et al. (2015).

Un model tridimensional a l'escala dels porus que mereix ser destacat és la formulació en volum finit (Porus Finite Volum (PFV) en anglès) del flux viscós d'un fluid incompressible. La tècnica proposada per Chareyre et al. (2012)

es basa en una descomposició de l'espai dels porus en elements tetraèdrics i en conductàncies locals. La discretització de l'espai dels porus s'efectua per triangulacions regulars i els dobles de Voronoi aplicats a la mostra granular, tal com s'il · lustra a la figura 8.23a. L'acoblament PFV-DEM ha donat lloc a bons resultats als problemes de flux monofàsics (Catalano et al. (2014); Scholtès et al. (2015); Montellà et al. (2016)) atès que la seva aplicabilitat es limita al règim saturat. Per consegüent, el PFV-DEM va ser estès a un model capaç de reproduir fluxos bifàsics. Aquest enfocament s'anomena "Porus-scale two-fase flow - Discrete Element Method" (2PFV-DEM) i ha estat desenvolupat per Yuan et al. (2016). Investigacions recents (Sweijen et al. (2017b); Yuan and Chareyre (2017)) mostren que els problemes de flux a dues fases són eficaçment resolts amb el 2PFV-DEM (veure l'exemple de la figura 8.24).

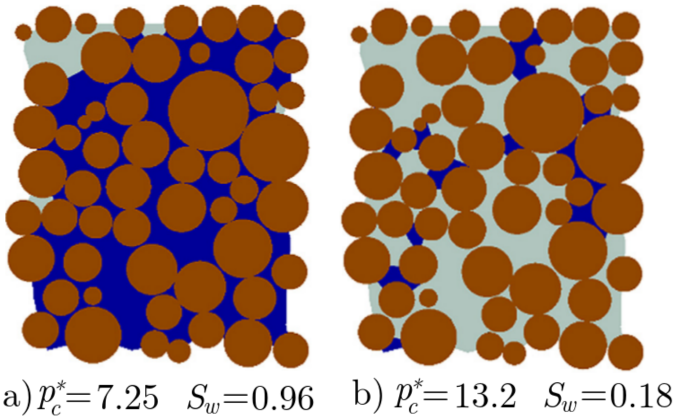

Figure 8.24: Drenatge realitzat amb el 2PFV-DEM. Les esferes marrons representen la fase sòlida, el blau representa la fase mullant i el gris, la fase no-mullant. La fase no-mullant envaeix la mostra granular des de dalt. La fase mullant queda atrapada dins el medi porós després del drenatge. Imatge extreta de Yuan and Chareyre (2017).

Model 2PFV

Fase fluida

Considerem una unitat de porus i. L'equació de continuïtat per a un fluid incompressible s'expressa com:

$$V_i \frac{\partial S_{w,i}}{\partial t} + \sum_{j=1}^{4} q_{ij} = 0 \tag{8.26}$$

on V_i és el volum del porus i q_{ij} són els fluxos de fluid del tetraedre i cap als tetraedres adjacents j_1 a j_4. Els fluxos i els gradients de pressió tenen una relació lineal tal que:

$$q_{ij} = g_{ij} \frac{\Delta_{ij}}{L_{ij}} \tag{8.27}$$

on Δ_{ij} és la caiguda de pressió entre dos porus adjacents i està relacionada amb la pressió capil · lar i les pressions de fluid dels porus veïns, L_{ij} és la distància entre els porus i i j , i g_{ij} depèn de la conductància hidràulica a través de la gola dels porus ij. Cal mencionar que la pressió capil · lar (p_c) correspon a la diferència de pressió entre el fluid mullant (p^w) i la fase no-mullant (p^{nw}).

La següent definició per a g_{ij} ha estat proposada amb resultats satisfactoris pel cas de goles de porus saturades (Tong et al. (2012)):

$$g_{ij} = \frac{S^f_{ij} R^h_{ij}}{L^2_{ij}} 2\mu \tag{8.28}$$

on S^f_{ij} és la superfície ocupada pel fluid a la cara del porus (veure la figura 8.23) i R^h_{ij} és el radi hidràulic (definit com la relació entre el volum ocupat pel fluid i la superfície sòlid-fluid).

Segons les possibles configuracions entre dos porus veïns i la gola de porus respecte a la presència de fluids (Koplik and Lasseter (1985)), Δ_{ij} es pot expressar de la següent manera:

$$\Delta_{ij} = p^{nw}_i - p^{nw}_j + s^w_i (p_{c,ij} - p_{c,i}) - s^w_j (p_{c,ij} - p_{c,j}) \tag{8.29}$$

on $p_{c,i}$ i $p_{c,j}$ són les pressions capil · lars dels elements i i j, respectivament, i $p_{c,ij}$ és la pressió capil · lar d'entrada de la gola del porus ij. Així doncs, el flux volumètric (Eq. 8.27) queda reformulat com:

$$q_{ij} = g_{ij} \frac{(p^{nw}_i - p^{nw}_j + s^w_i (p_{c,ij} - p_{c,i}) - s^w_j (p_{c,ij} - p_{c,j}))}{l_{ij}} \tag{8.30}$$

Pressió capil · lar d'entrada

Suposem un porus completament ple de la fase mullant. La fase no-mullant envairà el porus per la gola quan la pressió capil · lar local (p_c) sigui superior a la pressió capil · lar d'entrada (p^e_c) d'aquesta gola. Diverses tècniques ens permeten calcular la pressió capil · lar d'entrada. Les aproximacions més corrents són el mètode d'Haines (Sweijen et al. (2016)) i el mètode de Mayer-Stowe-Princen (MS-P) (Joekar-Niasar et al. (2010b); Yuan et al. (2016)). L'aproximació d'Haines (Haines (1930)), "Mètode Incircle" d'ara endavant, proposa que la curvatura de la interfície a través de la gola dels porus es pot considerar com una esfera en contacte amb les partícules esfèriques que defineixen la gola. D'altra banda, el mètode MS-P es basa en un equilibri de les forces que actuen sobre les línies de contacte en el moment de la invasió. El model MS-P prediu la pressió capil · lar d'una gota de fluid de longitud infinita a l'interior d'un tub cilíndric (Princen (1969); Mayer and Stowe (1965); Ma et al. (1996)).

Conèixer les pressions capil · lars d'entrada per a cada gola és essencial per estudiar el drenatge a un medi granular. Al començament de les simulacions, les mostres estan totalment saturades amb la fase mullant. El drenatge comença disminuint la pressió de la fase mullant (p^w) mentre la pressió p^{nw} del dipòsit de la fase no-mullant es manté constant. Quan un porus és envaït ($p^e_c \leq p_c$), la fase no-mullant avança cap a noves goles, desencadenant eventualment una cascada recursiva de salts d'Haines (Yuan (2016)), i envaint més d'un porus per a un únic valor de p^w. A més, la fase mullant pot quedar desconnectada durant el drenatge formant ponts capil · lars o altres microestructures líquides.

Fase sòlida

La força total $\mathbf{F}_k^f$ exercida sobre una partícula sòlida k per dues fases fluides inclou la contribució de la pressió tenint compte les fases mullant i no-mullant ($\mathbf{F}_k^p$) i l'efecte de la tensió superficial a la interfície sòlida - mullant - no-mullant $\mathbf{F}_k^t$.

$$\mathbf{F}_k^f = \mathbf{F}_k^p + \mathbf{F}_k^t \tag{8.31}$$

Mètode Lattice Boltzmann (LBM)

El LBM és un model mesoscòpic capaç de simular la dinàmica dels fluids a través de geometries complexes (Chen and Doolen (1998)). Mentre que els mètodes numèrics clàssics es basen en la discretització de les equacions de continuïtat macroscòpica, el LBM estableix equacions cinètiques mesoscòpiques dels fluids. Degut a la seva senzillesa i la seva capacitat per a modelar el moviment dels fluids en entorns geomètrics complexos, el LBM és molt apropiat per simular un flux multifàsic a través d'un medi porós.

En els nodes de la xarxa hi resideixen funcions de distribució de partícules $f^\sigma(\mathbf{x},t)$ que viatgen en un conjunt discret de direccions de moviment. L'exponent σ indica el component fluid, $\mathbf{x}$ la posició a la xarxa i t és el temps. El moviment del fluid queda descrit per l'equació discreta de Boltzmann. Mitjançant el simple i popular operador de col · lisió de Bhatnagar-Gross-Krook (BGK) (Bhatnagar et al. (1954)), l'equació estàndard de LBM s'expressa de la següent manera:

$$f_k^\sigma(\mathbf{x_k} + \mathbf{e_k}\Delta t, t + \Delta t) - f_k^\sigma(\mathbf{x_k}, t) = \frac{-\Delta t}{\tau^\sigma}(f_k^\sigma(\mathbf{x_k}, t) - f_k^{\sigma,eq}(\mathbf{x_k}, t)) \tag{8.32}$$

on τ^σ és el temps de relaxació cap a l'equilibri local, $f_k^{\sigma,eq}$ és la funció de distribució d'equilibri, Δt és l'increment de temps, $\mathbf{e_k}$ són les velocitats discretes que depenen del model de velocitat particular. A aquest treball, el model utilitzat és D3Q19 (espai tridimensional amb 19 direccions possibles), i k varia de 0 a $Q-1$, representant les direccions a la xarxa. La banda esquerra de l'equació 8.32 descriu l'etapa de propagació (les partícules es desplacen cap al node més pròxim seguint la direcció de la seva velocitat) mentre que el costat dret representa l'operador de col · lisió (les partícules arribant al node més pròxim modifiquen la seva velocitat cap a un equilibri local). L'operador de col · lisió correspon al terme viscós a l'equació de Navier-Stokes.

L'equilibri local $f_k^{\sigma,eq}$ depèn del tipus de xarxa, de la densitat i de la quantitat de moviment (Latt et al. (2008)). Les variables macroscòpiques a cada node de la xarxa es poden determinar utilitzant els moments de les funcions de distribució:

- Densitat:

$$\rho^{\sigma} = \sum_{k} f_k^{\sigma} \tag{8.33}$$

- Quantitat de moviment:

$$\rho^{\sigma}\mathbf{u}^{\sigma} = \sum_{k} f_k^{\sigma}\mathbf{e_k} \tag{8.34}$$

La distribució d'equilibri pot ser vista com una extensió de la funció de distribució de Maxwell-Boltzmann per a baixos nombres de Mach:

$$f_k^{\sigma,eq} = \rho^{\sigma} w_k \left[1 + \frac{1}{c_s^2}(\mathbf{e_k}\cdot\mathbf{u}^{\sigma,\mathbf{eq}}) - \frac{1}{2c_s^2}(\mathbf{u}^{\sigma,\mathbf{eq}}\cdot\mathbf{u}^{\sigma,\mathbf{eq}}) + \frac{1}{2c_s^4}(\mathbf{e_k}\cdot\mathbf{u}^{\sigma,\mathbf{eq}})^2\right] \tag{8.35}$$

on $c_s = \dfrac{1}{\sqrt{3}}$ és la velocitat del so i $\mathbf{u}^{\sigma,\mathbf{eq}}$ és la velocitat d'equilibri definida per Shan and Chen (1993, 1994):

$$\mathbf{u}^{\sigma,\mathbf{eq}} = \mathbf{u}^{'} + \frac{\tau^{\sigma}\mathbf{F}_{\sigma}}{\rho^{\sigma}} \tag{8.36}$$

on $\mathbf{u}^{'} = \dfrac{\sum_{\sigma} \dfrac{\rho^{\sigma}\mathbf{u}^{\sigma}}{\tau^{\sigma}}}{\sum_{\sigma} \dfrac{\rho^{\sigma}}{\tau^{\sigma}}}$ és una velocitat efectiva i $\mathbf{F}_{\sigma}$ és la força total que actua en cada fase.

Model Shan-Chen

El model de Shan-Chen introdueix una força d'interacció entre els components (o fases) per tal de descriure els fluxos multifàsics. Aquesta força modifica l'operador de col · lisió a través d'una velocitat d'equilibri produint un efecte repulsiu entre les fases.

A aquest treball, ens centrem en els fluxos bifàsics ($\sigma = 2$). Així doncs, es considera que dos $f_k^{\sigma}(\mathbf{x},t)$ modelitzen els fluxos amb dos components fluids. D'ara endavant, ρ^{w} i ρ^{nw} faran referència a les fases mullant i de no-mullant.

Al model de Shan-Chen, la força no local responsable de la interacció fluid-fluid s'expressa com:

$$\mathbf{F}_{\sigma}(\mathbf{x}) = -\Psi(\mathbf{x})\sum_{\bar{\sigma}} G_{\sigma\bar{\sigma}} \sum_{k} \Psi_{\bar{k}}(\mathbf{x}+\mathbf{e_k})\mathbf{e_k} \tag{8.37}$$

on Ψ_k és el potencial inter-partícula que indueix la separació de fases i $G_{\sigma\bar{\sigma}}$ és la força d'interacció entre els components σ, $\bar{\sigma}$

Treballs precedents (Shan and Chen (1994); Yuan and Schaefer (2006); Huang et al. (2011); Porter et al. (2012)) han utilitzat diversos potencials inter-partícula. Per raons de senzillesa, considerem $\Psi_k = \rho_k$, tal com es fa a Pan et al. (2004). Les interaccions entre els components, $G_{12} = G_{21}$, es defineixen com positives per tal d'induir una força de repulsió entre les fases. Valors baixos de G_{12} condueixen a un procés de dissolució observat a barreges miscibles. En canvi, valors significativament elevats de G_{12} provoquen sistemes binaris gairebé immiscibles amb interfícies de poca espessor subjectes a inestabilitats numèriques. Per conseqüent, cal fer especial atenció a l'hora de triar la força d'interacció que controla la tensió superficial i la immiscibilitat del sistema.

Finalment, l'equació d'estat dels gasos no ideals es pot escriure com:

$$p = c_s^2 \sum_{\sigma} \rho^{\sigma} + c_s^2 \sum_{\sigma\bar{\sigma}} G_{\sigma\bar{\sigma}} \Psi_{\sigma} \Psi_{\bar{\sigma}} \tag{8.38}$$

Les forces capil · lars exercides sobre les partícules de materials granulars tenen un impacte important en el comportament macroscòpic. Els baixos continguts en aigua als sòls humits confereixen forces capil · lars significatives que augmenten la cohesió del material (Hornbaker et al. (1997)). De fet, els efectes capil · lars estan fortament influenciats pel contingut d'aigua. En conseqüència, comprendre les propietats hidromecàniques és essencial per estudiar el comportament dels materials granulars parcialment saturats.

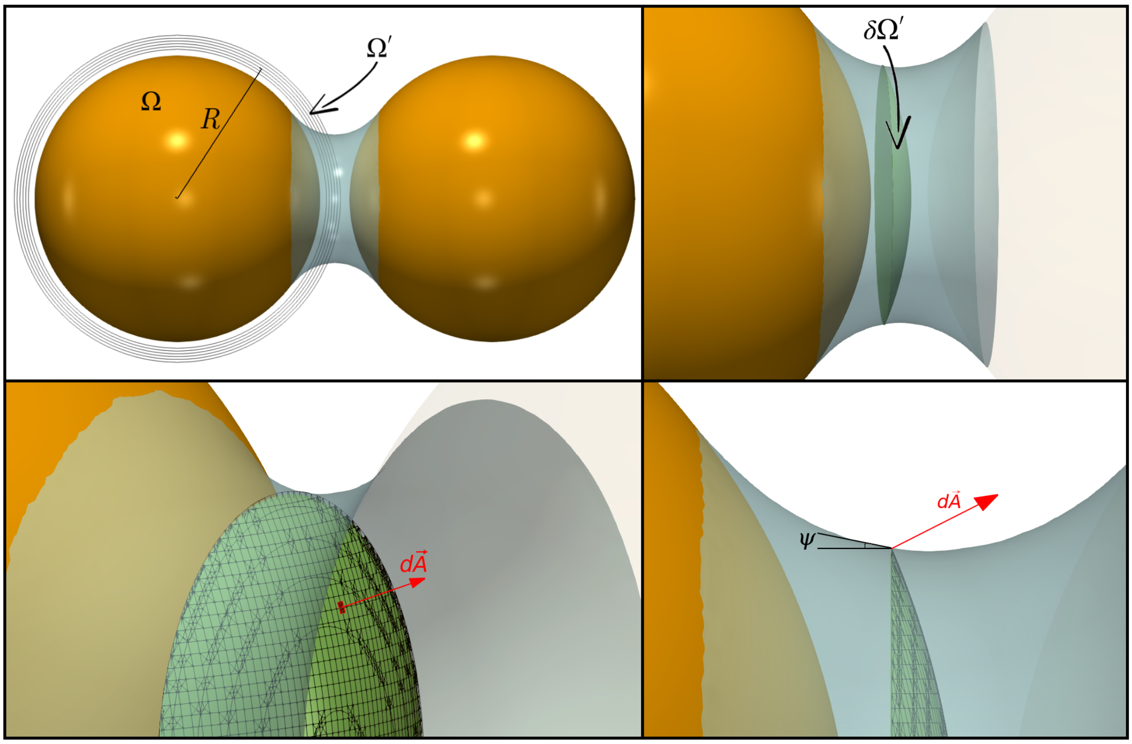

Figure 8.25: A la part superior esquerra, diversos elements de volum esfèrics (Ω's) envolten la partícula esfèrica indicada per Ω. Les altres imatges il · lustren la superfície obtinguda després de la intersecció ($\delta\Omega'$) entre el pont líquid capil · lar i l'element de volum esfèric. Les tensions s'integren sobre tots els punts de $\delta\Omega'$.

En el model Shan-Chen, les propietats dels nodes sòlids s'atribueixen de manera semblant a aquelles dels nodes que corresponen als fluids (Huang et al. (2007)). Aquesta configuració comporta una capa amb una espessor numèrica que no coincideix amb el gruix real entre el fluid i el sòlid (Chen et al. (2014)). Per superar les complexitats i irregularitats observades a prop dels objectes sòlids, proposem analitzar les tensions a l'interior d'un element de volum allunyat de la interfície sòlid-fluid (veure l'element $\mathbf{\Omega'}$ a la figura 8.25). La majoria de les nostres investigacions es duen a terme amb partícules esfèriques, per tant, prenem en compte elements de volum esfèrics. Tanmateix, altres elements, tals com cubs, tetraedres, plans, el · lipsoides, entre altres formes, poden ser considerats.

Així doncs, la força capil · lar que actua sobre els grans esfèrics ve determinada per la següent integral:

$$\mathbf{F_c} = \int_{\delta\Omega'} -[p\delta_{ij} - c_s^2(2\tau-1)S_{ij}]\mathbf{dA} \tag{8.39}$$

on $\boldsymbol{\delta\Omega'}$ és la superfície resultant de la intersecció de l'element de volum esfèric i del pont líquid (veure els esquemes a la figura 8.25), S_{ij} és el tensor desviador i $\mathbf{dA}$ és el vector d'àrea normal representat a la part inferior de la figura 8.25.

Simulacions amb el mètode lattice Boltzmann

Ponts capil · lars i altres estructures líquides més complexes han estat reproduïdes amb el LBM sota condicions de drenatge. Les forces capil · lars, el volum i la morfologia dels líquids obtinguts s'han comparat amb les solucions teòriques, aproximacions i resultats provinents d'experiments.

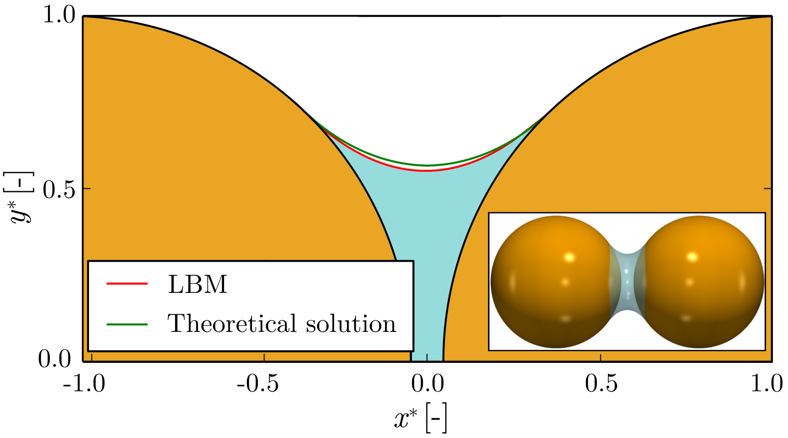

Figure 8.26: Perfils de ponts capil · lars superposats obtinguts numèricament i analíticament per una pressió capil · lar de $p_c^* = 0.6$.

Pont capil · lar

El perfil d'un pont capil · lar es pot descriure mitjançant l'equació de Young-Laplace, tal com es mostra a De Bisschop and Rigole (1982). A més, la curvatura mitjana (H_m) d'un pont pendular es determina com:

$$2H_m = \frac{r''}{(1+r'^2)^{3/2}} - \frac{1}{r(1+r'^2)^{1/2}} = \frac{p_c}{\gamma} \tag{8.40}$$

on $r = r(x)$ especifica el radi del coll del pont capil · lar a la posició x. Degut a la impossibilitat d'integrar Eq. 8.40 analíticament, diversos estudis han utilitzat mètodes numèrics per resoldre l'Eq. 8.40 (Lian et al. (1993); Willett et al. (2000); Lian and Seville (2016); Scholtès et al. (2009)).

La forma del pont pendular quan $p_c^* = 0.6$ ha estat comparada amb la solució directa de l'equació de Young-Laplace (Lian et al. (1993)) a la figura 8.26. Tot seguit, la simulació LBM ha continuat reduint la quantitat de fase mullant i enregistrant el volum del pont simulat per tal de fer una comparació quantitativa amb la solució de Young-Laplace.

La figura 8.27 mostra la relació volum-pressió fins a la ruptura del pont. La simulació LBM i la solució Laplace-Young segueixen una tendència molt similar on l'error relatiu és generalment inferior a 10^{-2}.

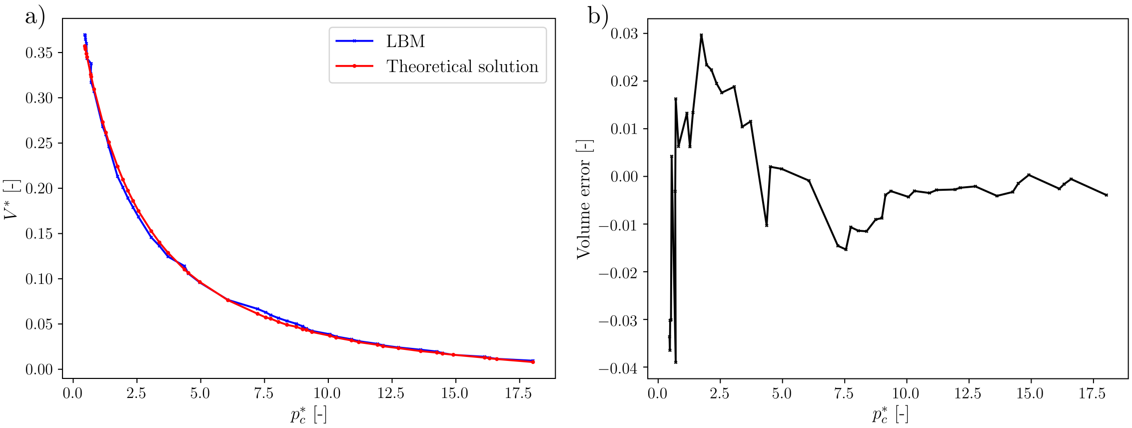

Figure 8.27: a) Volum en funció de la pressió capil · lar per a un pont pendular de LBM i de la solució numèrica de l'equació de Laplace-Young. b) L'error relatiu és la diferència entre el volum simulat i el volum teòric normalitzat en tant que $V^{=}V/R^3$, on V és el volum del pont i R el radi de les esferes.

Pel que fa a les forces capil · lars, la comparació entre el LBM i la solució teòrica confirma la validesa del mètode d'avaluació de la força. Observem corbes similars entre la simulació LBM i la solució Laplace-Young a la figura 8.28 quan el volum líquid del pont es redueix progressivament. La figura 8.28a il · lustra corbes gairebé coincidents per a volums relativament grans. Tanmateix, l'error augmenta ràpidament quan la pressió capil · lar és elevada i ens apropem al punt de ruptura. La divergència entre corbes observada a $p_c^* \approx 15$ de la figura 8.28) s'atribueix als corrents falsos (Shan (2006); Pooley and Furtado (2008)). Aquests corrents són velocitats no físiques que apareixen a prop de les interfícies corbes degut a la discretització de l'espai. A prop de la ruptura del pont, la interfície esdevé inestable. En aquest moment, la curvatura de la interfície és considerablement elevada i la contribució de la part desviadora a Eq. 8.39 és la part més important. En el transcurs del drenatge, les velocitats falses eren sempre presents. Tanmateix, la seva acció no tenia una gran influència sobre l'anàlisi de la força. De fet, l'acció hidroestàtica a la Eq. 8.39 (que implica resultats més precisos) era la part predominant. Malgrat l'error introduït per aquestes velocitats, el mètode actual és capaç de determinar la força capil · lar durant el procés de drenatge amb una bona precisió.

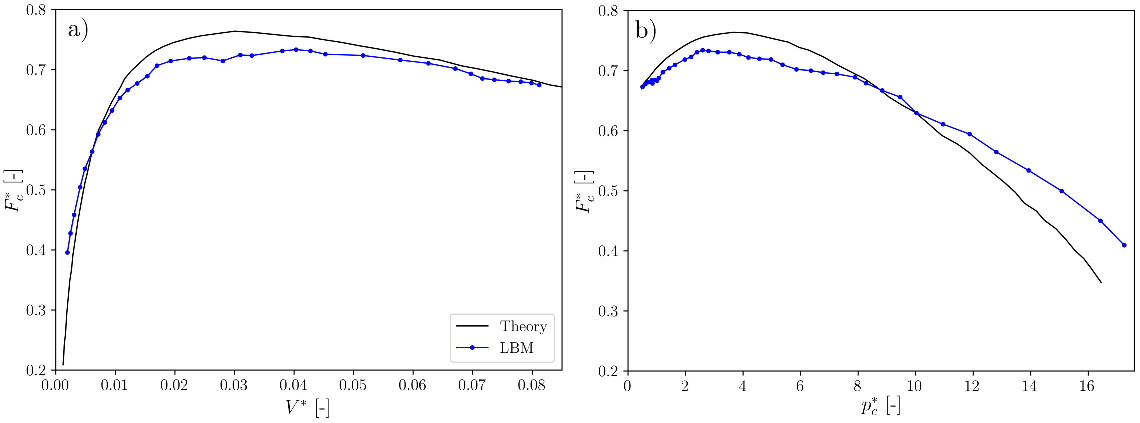

Figure 8.28: Evolució de la força capil · lar en funció del volum (a) i de la força capil · lar en funció de la pressió capil · lar (b) en el moment de drenatge d'un pont capil · lar. Els resultats han estat obtinguts per a un pont pendular entre dues esferes separades una distància $S^* = \dfrac{d}{R} = 0.1$, on d és la separació entre les partícules.

Trimer

Els trimers són configuracions líquides obtingudes després de la fusió de tres ponts pendulars formats entre tres partícules adjacents. Aquesta estructura líquida és una de les més habituals durant el règim funicular (Scheel et al. (2008); Semprebon et al. (2016)). L'evolució d'aquestes microestructures ha estat avaluada sota condicions de drenatge amb el LBM. Els resultats han estat contrastats amb les dades experimentals i numèriques proporcionades per Wang et al. (2017) utilitzant l'eina Surface Evolver (SE). Tots els paràmetres geomètrics i les propietats hidroestàtiques han estat ajustades per reproduir el test de Wang et al. (2017).

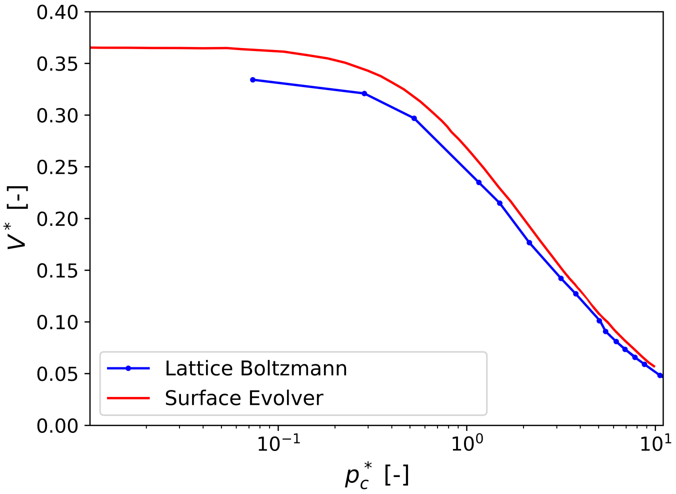

Figure 8.29: Volum en funció de la pressió capil · lar per a tres esferes en contacte sota condicions de drenatge. Comparació entre LBM i els resultats SE extrets de Wang et al. (2017)

.

L'efecte de drenatge en funció de pressió capil · lar s'il · lustra a la figura 8.29 mitjançant una escala logarítmica. La disminució del contingut del líquid indueix un augment de la pressió capil · lar. Ressaltem la semblança entre Surface Evolver i LBM a la figura 8.29.

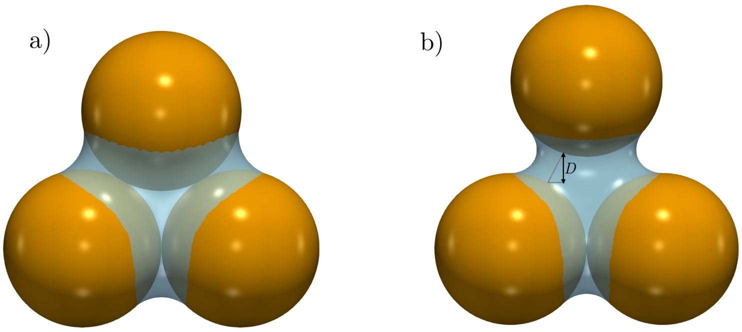

Figure 8.30: Evolució del règim funicular per a diferents desplaçaments. Les imatges han estat obtingudes a partir de simulacions LBM on el volum era el paràmetre controlat. A l'esquerra, l'esfera superior presenta un desplaçament vertical de $D^* = 0$. La figura de la dreta mostra la configuració del fluid corresponent a un desplaçament vertical de $D^* = 0.39$.

A continuació, hem estudiat l'efecte de la separació d'una partícula que s'allunya de les altres dues. Inicialment, les tres esferes estan en contacte i el volum de líquid es manté constant. Tot seguit, desplacem una de les esferes augmentant progressivament la separació i mantenint sempre el volum constant. La figura 8.30 mostra la configuració de les 3 esferes a l'estat inicial a l'esquerre. La configuració després de l'augment de la distància entre partícules s'il · lustra a la dreta de la figura 8.30. El desplaçament de l'esfera superior es defineix com: $D^* = \dfrac{D}{R}$, on D és la distància indicada a la figura 8.30.

La figura 8.31 mostra la comparació de LBM, SE i els resultats experimentals. La força capil · lar augmenta al començament de l'assaig degut a l'efecte d'enganxament. Tal com es detalla a Willett et al. (2003), l'efecte d'enganxament es manifesta quan una força actua sobre el líquid i la línia de contacte trifàsica es manté entre valors intermedis dels límits de l'angle de contacte. Quan s'arriba a un d'aquests límits, la línia de contacte trifàsica rellisca. Una vegada s'arriba al pic de la força capil · lar, el test prossegueix sota condicions de lliscament, fet que comporta una disminució de la força capil · lar quan la distància de separació augmenta. La figura 8.31 mostra corbes similars per a tots els tests. Subratllem la bona precisió de la força capil · lar màxima (els valors màxims de les forces són similars per a tots els casos). D'altra banda, la corba SE està desplaçada respecte als resultats experimentals, i la corba LBM no és capaç de reproduir amb precisió l'efecte d'enganxament (convé dir que en el LBM, l'angle de contacte està fixat a $\theta \approx 0^o$). Tot i que els efectes dels angles de contacte en progressió/retrocés no estan integrats, comprovem que les solucions LBM ofereixen una predicció precisa de les forces capil · lars.

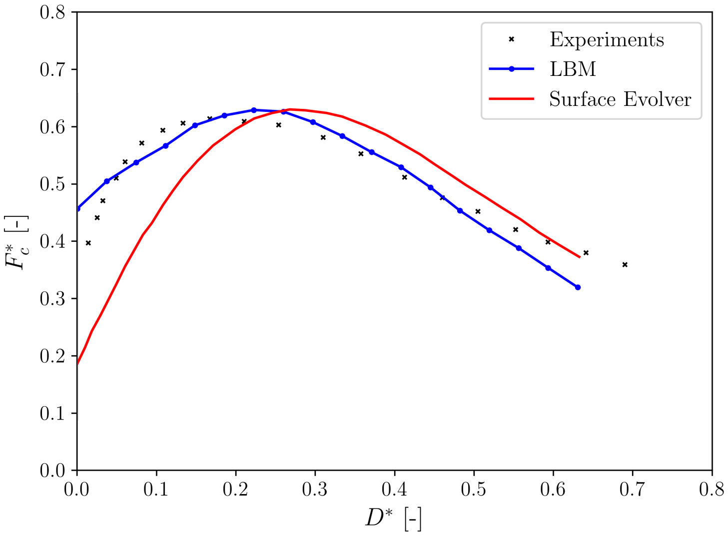

Figure 8.31: Comparació de forces capil · lars entre els resultats experimentals i els models numèrics per a $V^* = \dfrac{V}{\dfrac{4}{3}\pi R^3} = 0.178$. Les dades experimentals i els resultats obtinguts amb Surface Evolver han estat extrets de Wang et al. (2017). Tres esferes d'igual diàmetre i en contacte constitueixen la configuració inicial. A continuació, una de les esferes s'allunya progressivament de la resta.

Model reticular de goles de porus 2D

Diversos articles han estudiat el flux multifàsic controlat per capil · laritat Bakke et al. (1997); Hilpert and Miller (2001) idealitzant la geometria del medi porós. Tanmateix, les simplificacions d'una naturalesa complexa poden obstaculitzar la descripció d'alguns fenòmens locals. Per tal de superar les dificultats lligades a la idealització geomètrica, proposem un model numèric en 2D basat en solucions analítiques i una xarxa extreta de la geometria dels porus com es detalla a Gladkikh and Bryant (2005); Yuan et al. (2016). La present proposta subratlla la importància de simular a l'escala del menisc/gola (en lloc de l'escala del porus) per evitar les limitacions associades a la imbibició d'un medi porós (Vogel et al. (2005); Patzek et al. (2000)).

L'objectiu principal d'aquest treball és dur a terme un estudi preliminar per a la realització d'un model numèric que permeti predir el desplaçament multifàsic a través d'un medi porós en 3D. Aquest mètode s'anomena xarxa de goles de porus (Throat-Network (TN), en anglès). Així doncs, aquest mètode assenta les bases per a futurs models Híbrids bastats en xarxes de porus i expressions semianalítiques (Chareyre et al. (2017)). La precisió del model s'avalua amb els resultats proporcionats pel LBM basat en el model Shan-Chen (Shan and Chen (1993)).

Seguint la idea de Blunt et al. (2002); Sinha and Wang (2007), el present model avalua la posició de la interfície fluid-fluid a través de l'equació de Young-Laplace i del camp de pressió a la xarxa. En concret, es consideren dues fases no miscibles (generalment l'aire i l'aigua). A més, la conservació de la massa s'assegura per a cada porus.

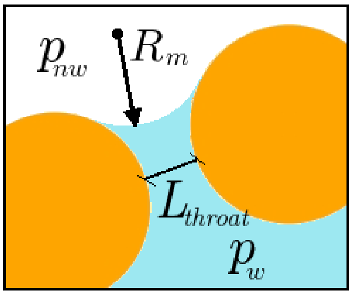

Figure 8.32: Segons l'equació de Young-Laplace (Eq. 8.42), el salt de pressió ($p^{nw} - p^{w}$) a través d'una interfície fluid-fluid és proporcional al producte de la tensió superficial i la curvatura de la interfície $\left(k = \frac{1}{R_m}\right)$.

Descomposició a l'escala dels porus

Es considera que una triangulació regular representa la topologia de l'espai dels porus (Helba et al. (1992); Thompson and Fogler (1997); Bryant and Johnson (2003)). Els vèrtexs del triangle corresponen als tres centres de les partícules. Aquest esquema s'adopta de manera que la mostra granular es divideix en grups de tres discos sòlids. A un medi granular dens, cada grup defineix un porus. A continuació, dos triangles adjacents formen la gola d'un porus (veure la figura 8.33). Per consegüent, aquesta descomposició dóna lloc a un model de xarxa de goles on les característiques geomètriques estan ben representades.

Equacions governants

Segons l'equació de Young-Laplace (Blunt et al. (2002); Young et al. (1805)), el salt de pressió a través d'una interfície fluid-fluid és proporcional al producte de la tensió superficial i la curvatura de la interfície (veure figura 8.32):

$$p_c = p^{nw} - p^{w} = \gamma\left(\frac{1}{R_1} + \frac{1}{R_2}\right) \tag{8.41}$$

on p_c és la pressió capil · lar, p^{nw} i p^{w} són respectivament les pressions de les fases no-mullant i mullant, γ és la tensió superficial, i R_1 i R_2 són els principals radis de curvatura. Ja que la nostra investigació es limita a la 2D, adoptem l'expressió següent:

$$p_c = p^{nw} - p^{w} = \gamma\frac{1}{R_m}cos\theta \tag{8.42}$$

on θ és l'angle de contacte i R_m és el radi del menisc. Suposem, d'ara endavant, un angle de contacte de $\theta \approx 0$, tot i que el model pot ser extens de manera trivial a $\theta \neq 0$.

En el transcurs del drenatge, p_c augmenta i els radis del menisc disminueixen en funció de l'Eq. 8.42. La fase no-mullant comença a envair els porus quan el diàmetre del menisc és igual a la longitud de la gola dels porus (distància mínima entre dos grans sòlids), és a dir $2 \cdot R_m = L_{throat}$. Convidem al lector veure la figura 8.32 per a

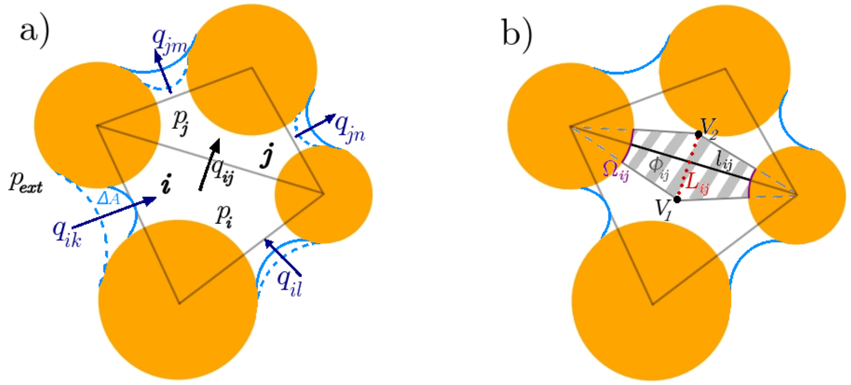

Figure 8.33: a) Elements triangulars després de la descomposició. q_{ij} és el flux entre els porus i i j. La interfície fluida al temps t es mostra amb una línia discontinua. Al temps $t+\Delta t$, el flux cap a l'element j dóna lloc a una nova configuració representada per una línia continua. b) les quantitats geomètriques de la gola segons Chareyre et al. (2012)

.

una explicació gràfica. En aquest moment, la pressió capil · lar correspon a la pressió capil · lar d'entrada:

$$p_c^e = \frac{2\gamma}{L_{throat}} \tag{8.43}$$

En realitat (un espai tridimensional), el desplaçament del fluid esdevé més complex degut a la dificultat per determinar la pressió d'entrada p_c^e. En efecte, p_c^e es determina, generalment, a partir de simplificacions (Haines (1927) i Mayer and Stowe (1965); Princen (1969)). Pel que fa a les simulacions 2D, la complexitat del problema es redueix considerablement. Els problemes tridimensionals poden ser simplificats a 2D en casos particulars tals com l'estudi del flux perpendicular a elements cilíndrics (Saito and De Lemos (2005)) o l'avaluació de la permeabilitat en un medi porós fibrós (Spaid and Phelan Jr (1997)).

Per simplicitat, considerem mostres amb fluids incompressibles i partícules estàtiques. Així, Eq. 8.26 esdevé:

$$\sum_{j=1}^{3} q_{ij} = 0 \tag{8.44}$$

on q_{ij} és el flux entre els porus i i j (veure la figura 8.33a).

El flux q_{ij} es pot expressar en funció del gradient inter-porus quan el nombre de Reynolds és baix:

$$q_{ij} = g_{ij}\frac{p_i - p_j}{L_{ij}} \tag{8.45}$$

on $p_i - p_j$ és la diferència de pressió entre dos triangles adjacents, L_{ij} és la longitud de la gola dels porus definida com la distància entre els vèrtexs de Voronoi (el diagrama de Voronoi és el doble de la triangulació de Delaunay), i g_{ij} és la conductància local que es determina com:

$$g_{ij} = \chi \frac{l_{ij} {R^h_{ij}}^2}{\mu} \tag{8.46}$$

on l_{ij} és la longitud de l'obertura de la gola, μ és la viscositat dinàmica del fluid, R^h_{ij} és el radi hidràulic del porus definit per $R^h_{ij} = \frac{\phi_{ij}}{\Omega_{ij}}$ (ϕ_{ij} és la zona ombrejada ocupada pel fluid a la figura 8.33b i Ω_{ij} el perímetre de la interfície sòlid-fluid il · lustrat a la figura 8.33b), i χ és el factor de conductància no dimensional, considerat igual a 0.5 com a Chareyre et al. (2012). Convidem al lector a veure la figura 8.33b per tenir una millor idea de les propietats geomètriques.

Eq. 8.45 es modifica per a les goles que tenen almenys una interfície fluid-fluid (seran d'ara endavant anomenades goles "obertes"). En aquest cas particular, l'expressió Eq. 8.45 es reemplaça per:

$$q_{i,ext} = g_{i,ext} \frac{p_{ext} - p_i + p_c}{L_{i,ext}} \tag{8.47}$$

Per tal de reproduir el desplaçament de la interfície, una "font" és introduïda a l'Eq. 8.44:

$$\sum_{j=1}^{3} q_{ij} = \Theta \tag{8.48}$$

on Θ adopta valors positius per als processos d'imbibició o de condensació i valors negatius per al drenatge i l'evaporació. Quan $\Theta = 0$, cap "font" és considerada.

Seguint els passos de Bakke et al. (1997) i Sinha and Wang (2007), podem determinar el camp de pressió de la nostra xarxa després d'haver resolt el conjunt d'equacions lineals següents:

$$\mathbf{QP} = \mathbf{f} \tag{8.49}$$

on **Q** és una matriu que inclou les informacions sobre les conductivitats, **P** és la matriu que conté els valors de pressió de les cèl · lules triangulars (**P** és la incògnita) i **f** representa les "fonts". Els valors interns de **f** són diferents de zero per a les goles obertes a les quals s'imposa una font.

Independentment de l'existència d'una "font", el següent procediment s'efectua per a cada pas de temps:

1. El camp de pressió es determina després de resoldre l'Eq. 8.49. Cada cèl · lula té una pressió assignada.

2. La pressió capil · lar, p_c, es calcula per a totes les interfícies (les goles "obertes"). Si p_c iguala a la pressió d'entrada ($p_c = p_c^e$), el líquid penetra a la gola i comença a envair el porus.

3. Els fluxos s'avaluen amb Eq. 8.45 i 8.47 per a cada gola.

4. La posició de la interfície es determina en funció de la pressió capil · lar. El radi del menisc es troba mitjançant l'Eq. 8.42, per tant, $R_m = \dfrac{\gamma}{p_c}$. La interfície correspon a l'arc de cercle tangent als dos discos que formen la gola.

5. El mecanisme es repeteix per a cada pas de temps.

Resultats

Imbibició d'un macro-porus

Aquesta secció il · lustra un fenomen observat als medis porosos: la fusió de meniscs. Més concretament, simulem un macro-porus sota condicions d'imbibició aspirant la fase no-mullant, en conseqüent, la pressió capil · lar disminueix. Per tant, els meniscs creixen i es fusionen quan entren en contacte amb altres meniscs (veure la figura 8.34). El nombre de meniscs es redueix (a mesura que els radis augmenten) fins que el macro-porus queda gairebé saturat (veure la figura 8.34c).

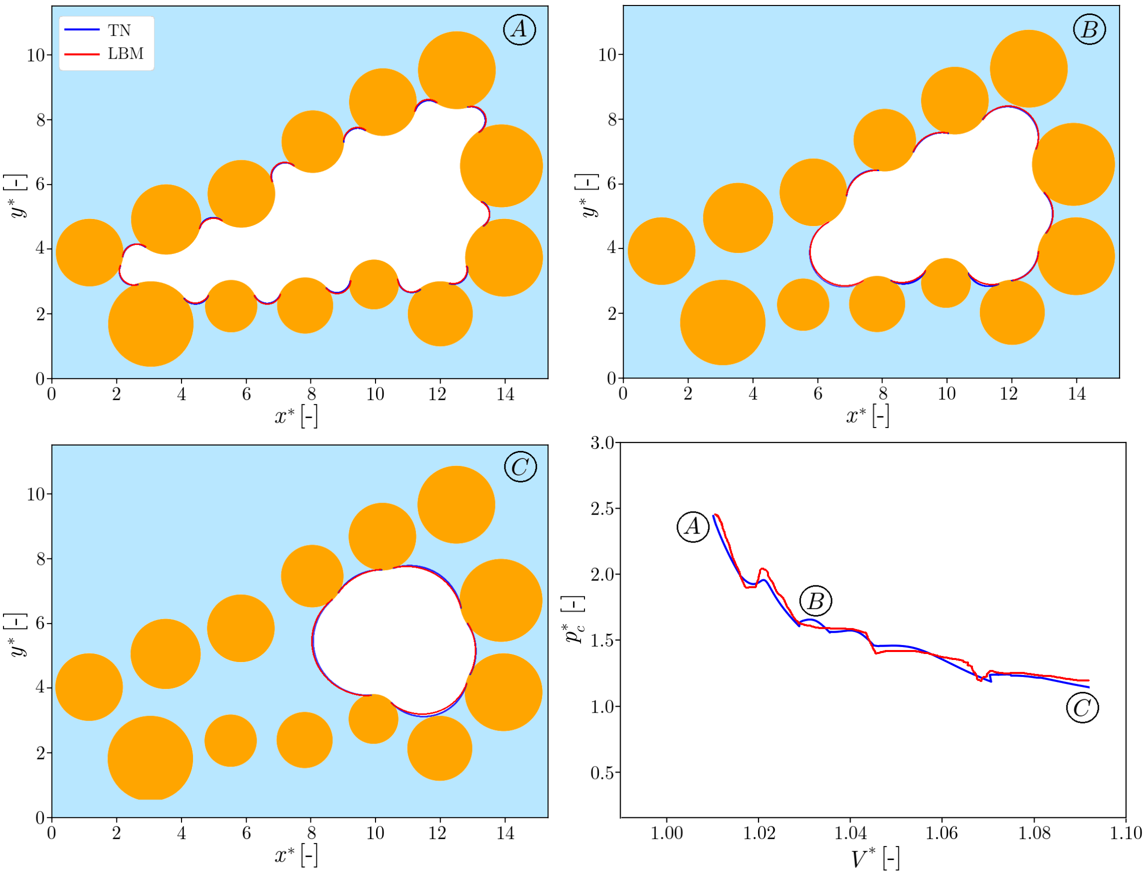

Figure 8.34: Comparació de la posició de la interfície entre els models LBM i TN. La pressió capil · lar es redueix per tal de forçar la imbibició del macro-porus. Els meniscs comencen a fusionar-se amb els altres meniscs a mesura que augmenten els radis. Progressivament, el sistema esdevé saturat. Es mostren diferents graus de saturació: Ⓐ $V^* = 1.01$, Ⓑ $V^* = 1.03$ i Ⓒ $V^* = 1.09$.

En aquesta simulació, la falta d'esdeveniments dinàmics dóna lloc a una semblança gairebé perfecta entre els perfils LBM i TN (veure la figura 8.34). Convé subratllar que les corbes de pressió capil · lar - saturació (veure la figura 8.34) també segueixen recorreguts similars. Tanmateix, lleugeres discrepàncies s'observen degut a petites pèrdues de càrrega. Aquests salts corresponen a esdeveniments menors d'Haines que es produeixen quan la fase mullant travessa la gola i comença a ocupar un espai més extens. Globalment, els resultats de LBM i de TN són força coincidents, fet que suggereix que el TN és capaç de reproduir el mecanisme de fusió de meniscs.

Ompliment d'un porus

Aquest exemple pretén reproduir el mecanisme d'"ompliment dels porus". El moviment de la interfície fluid-fluid entre una gola estreta i un porus més ample provoca un salt d'Haines i, tot seguit, hi ha una ràpida redistribució del fluid. Tècnicament, un esdeveniment fort i dinàmic pot comportar l'ompliment d'una gola ja buida. Per tal de reproduir aquest fenomen, hem adoptat la configuració de discs de la figura 8.35. Els esdeveniments més rellevants del procediment es detallen a continuació:

- a) El conjunt dels 5 discos està inicialment saturat, com s'aprecia a la figura 8.35a.
- b) La fase no-mullant penetra a través de la gola A-B. El menisc A-B creix lleugerament fins a trobar el disc C. La figura 8.35b mostra que el porus ABC no és gaire més ample que la gola A-B. Per consegüent, la pressió capil · lar disminueix marginalement (no observem cap caiguda de pressió significativa) després d'haver arribat a la pressió capil · lar d'entrada de la gola A-B (veure la figura 8.36).
- c) El menisc A-B s'escindeix en dos meniscs quan entra en contacte amb el disc C. La nova configuració és una microestructura líquida formada per 4 discs (B-C-D-E) i un pont aïllat (A-C). L'avenç de la interfície prossegueix amb l'augment de la pressió capil · lar (veure la figura 8.36).
- d) La interfície del menisc D-E continua augmentant la seva curvatura fins a envair la gola dels porus. En aquest moment, la pressió capil · lar (pressió capil · lar d'entrada per a la gola D-E) arriba al seu màxim tal com s'observa a la figura 8.36.
- e) El menisc d'arc D-E desplaça la fase mullant tot omplint el porus contingut per les partícules B-C-D-E. La ràpida invasió provoca l'ompliment dels porus per part de la fase no-mullant. Tots els meniscs redueixen la seva curvatura. El desplaçament de fluid més rellevant es troba a la gola B-C. L'acció dinàmica induïda pel salt d'Haines comença a omplir el porus ABC. A més del mecanisme d'ompliment il · lustrat a 8.35e, la figura 8.36 mostra una important caiguda de pressió que desencadena el fenomen d'ompliment.
- f) El porus ABC queda reomplert amb la fase mullant. A partir de les tres últimes imatges de la seqüència (figures 8.35d, 8.35e i 8.35f), observem que la

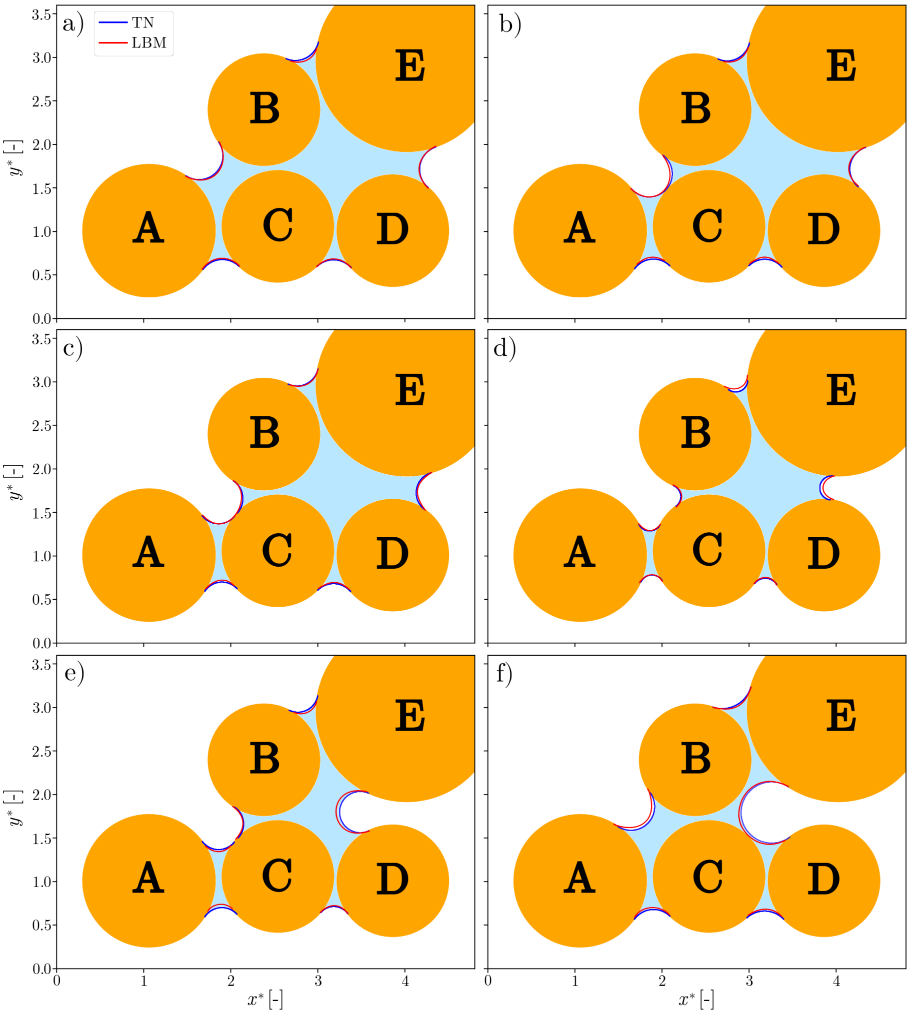

Figure 8.35: Comparació de la posició de la interfície entre els models LBM i TN. Es mostren diferents graus de saturació: a) $V^* = 0.97$, b) $V^* = 0.82$, c) $V^* = 0.80$, d) $V^* = 0.69$, e) $V^* = 0.58$ i f) $V^* = 0.54$.

fase no-mullant penetra a dins de la microestructura per la gola D-E i empeny la fase mullant cap al costat esquerre, omplint eventualment el porus constituït per les partícules ABC. La simulació s'atura quan el menisc de l'arc D-E entra en contacte amb el disc C.

Model Híbrid multi-escala

Globalment, la pressió capil · lar augmenta progressivament durant el drenatge. Tanmateix, observem brusques pèrdues de pressió quan la fase no-mullant travessa una gola estreta per penetrar a un porus més ample (Haines (1930)). Aquesta inestabilitat es manifesta quan la pressió capil · lar local sobrepassa la pressió capil · lar d'entrada ($p_c^e < p_c$). Tal com s'ha indicat a les seccions precedents, p_c^e es pot estimar pel mètode Incircle (Sweijen et al. (2016)), el mètode de Mayer-Stowe-Princen (MS-P) (Joekar-Niasar et al. (2010b); Yuan et al. (2016)), o mitjançant simulacions

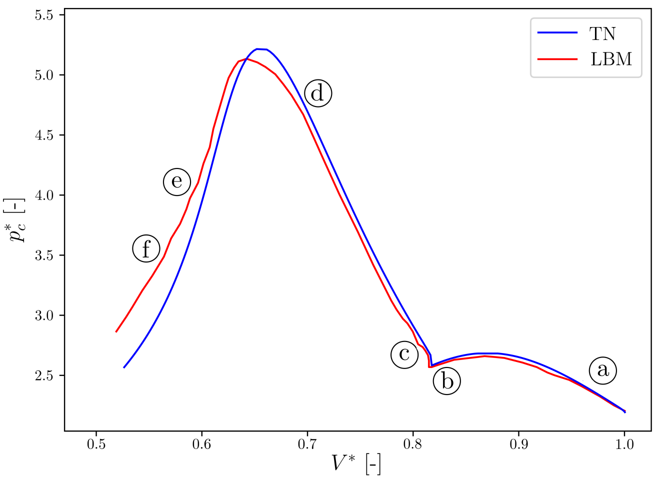

Figure 8.36: Comparació de la corba pressió capil · lar - saturació entre els models LBM i TN. Els continguts del líquid de la figura 8.35 s'inclouen en aquesta imatge.

directes.

Les simulacions de la dinàmica dels fluids des d'una perspectiva microscòpica permeten reproduir el moviment dels fluxos multifàsics amb una excel · lent precisió a l'escala dels porus. Tanmateix, aquests models presenten limitacions respecte al temps de computació a l'escala macroscòpica. Diversos estudis basats en el LBM (Pan et al. (2004); Van Kats and Egberts (1999); Ahrenholz et al. (2008)) descriuen amb èxit el desplaçament de la interfície a través de geometries complexes. Encara que el mètode sigui fàcil de paral · lelitzar, les simulacions estan limitades a dominis relativament petits degut als elevats costos de càlcul.

Per altra banda, actualment hi ha mètodes basats en estimacions i aproximacions que prediuen el comportament d'un flux multifàsic amb un temps de càlcul acceptable, en detriment de la precisió. Un bon exemple són els models de xarxa de porus (PN), els quals han estat àmpliament utilitzats per predir el moviment de fluids a través d'un medi porós (Fatt et al. (1956); Fenwick et al. (1998); Blunt (2001)).

En aquesta tesi, proposem un model Híbrid basat en una xarxa de porus que descompon la mostra granular en petits subdominis. Tot seguit, simulacions LBM s'efectuen per a cada gola dels porus per tal de determinar les propietats hidrodinàmiques (pressió capil · lar d'entrada, corba de drenatge, morfologia del líquid, etc.) a l'escala microscòpica. Les propietats locals obtingudes amb LBM s'incorporen a la xarxa per efectuar la simulació a una escala global. Aquesta estratègia dóna lloc a una reducció significativa del temps de càlcul respecte a un mètode que resol tot el domini mitjançant un model de simulació de fluids. Per consegüent, el mètode Híbrid combina l'eficàcia de la xarxa de porus i la precisió del LBM.

Aproximacions a l'escala dels porus

Segons l'esquema sobre triangulació d'una mostra granular detallat al començament d'aquest resum (veure la figura 8.23), un conjunt d'esferes es pot descompondre tal com s'indica a la figura 8.37. La topologia de les goles dels porus ve descrita per

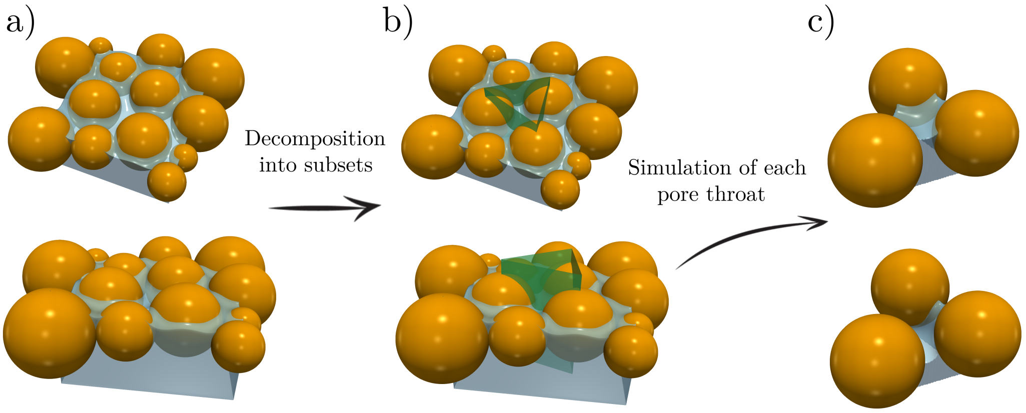

Figure 8.37: Descomposició de la mostra granular (a) en petits subdominis (b). Cada sub-domini està format per 3 esferes (c).

cada sub-domini elemental. En particular, la forma d'una gola de porus es defineix per la superfície de la secció transversal que s'estén en el si d'una cara tetraèdrica (veure la figura 8.38).

Tal com s'explica a la secció **"Pressió capil · lar d'entrada"**, p_c^e és un dels principals factors que controla el drenatge. Aquest treball segueix un criteri d'invasió semblant a l'esquema 2PFV-DEM. Així doncs, el desplaçament de la fase no-mullant està directament relacionat a la pressió capil · lar. A més, la invasió per la gola dels porus es produeix quan la pressió capil · lar local és superior a la pressió capil · lar d'entrada.

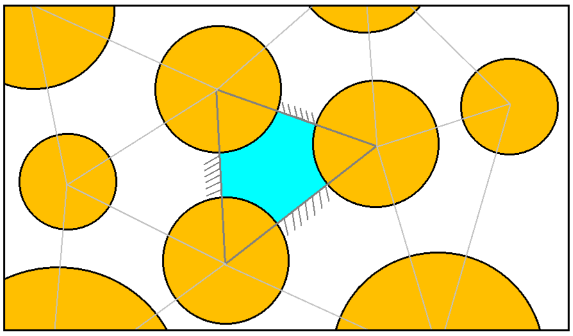

Figure 8.38: Domini (en 2D) després de la descomposició.

En el moment del desplaçament de fluid dins un sub-domini, la interfície adopta formes molt complexes. De fet, els meniscs de la interfície observats a la figura 8.37c no mostren cap simetria de translació o de rotació. L'anàlisi de la forma del menisc requereix la solució de l'equació de Laplace-Young, una equació diferencial parcial de segon ordre no lineal que pot ser resolta numèricament amb un cost computacional molt elevat. Degut a aquesta limitació, sembla raonable considerar altres mètodes que permetin predir la pressió capil · lar d'entrada i la forma del menisc. Concretament, utilitzem simulacions directes basades en el LBM per determinar les principals propietats hidromecàniques. Tanmateix, per a raons pràctiques, quan els recursos computacionals són limitats, es poden emprar expressions semi-analítiques per predir la pressió capil · lar d'entrada. Les aproximacions més corrents són el mètode d'Haines Incircle (Sweijen et al. (2016)) i el mètode de Mayer-Stowe-Princen (MS-P) (Joekar-Niasar et al. (2010b); Yuan et al. (2016)).

MS-P

El model Mayer-Stowe-Princen (MS-P) prediu la pressió capil · lar d'una gota de fluid de longitud infinita a l'interior d'un tub cilíndric (Princen (1969); Mayer and Stowe (1965); Ma et al. (1996)).

A l'esquema 2PFV-DEM, la pressió capil · lar d'entrada p_c^e de la gola es calcula seguint el mètode MS-P, que utilitza l'equilibri de les forces sobre la interfície no-mullant - mullant a l'estat transitori. L'equilibri de forces sobre una gola específica s'escriu com:

$$\sum \mathbf{F}(p_c) = \mathbf{F^p}(p_c) + \mathbf{F^t}(p_c) = 0 \tag{8.50}$$

on $\mathbf{F^p}$ és la força capil · lar actuant sobre el domini de la secció de gola dels porus; $\mathbf{F^t}$ és la força de tensió total al llarg de les línies de contacte multifàsics, i p_c^e és el valor de p_c tal que $\sum \mathbf{F}(p_c) = 0$.

Aproximació d'"Haines Incircle"

L'aproximació d'Haines Incircle (Haines (1930)), "Mètode Incircle" d'ara endavant, proposa que la curvatura de la interfície que travessa la gola dels porus és una esfera en contacte amb les partícules que defineixen la gola dels porus. Per consegüent, la pressió capil · lar d'entrada és $p_c^e = 2\gamma/r_{ins}$, on γ és la tensió superficial i r_{ins} és el radi del cercle inscrit a la gola dels porus.

Simulació directa d'una sola gola de porus amb LBM

Aquesta secció proporciona un mètode alternatiu per determinar p_c^e per a cada gola. En comptes d'utilitzar les aproximacions MS-P o Incircle, les propietats hidroestàtiques s'obtenen a partir de simulacions directes. L'espai dels porus es descompon en una sèrie de dominis seguint una triangulació regular (veure figura 8.37). La descomposició dóna lloc a una llista de goles de porus que es resolen independentment. Mitjançant simulacions LBM amb el model Shan-Chen s'avalua el moviment dels fluids i s'estima la corba de drenatge i la pressió capil · lar d'entrada per a cada gola. El domini computacional és un prisma de forma triangular definit per tres parets sòlides ortogonals a la gola dels porus (pla definit per les tres esferes, com s'indica a la figura 8.37b). Cadascun d'aquests límits sòlids travessa dos dels centres de les esferes (dos vèrtexs del triangle definit pels centres de les 3 esferes). Recomanem al lector dirigir-se a les figures 8.37 i 8.38 per a una comprensió més completa. Un angle de contacte de 90 graus s'imposa als límits per imitar les condicions simètriques de cada paret sòlida. A més, el domini queda envoltat de dos triangles (amunt i a baix del prisma) representant les seccions d'entrada i sortida de les simulacions LBM.

Inicialment, les fases mullant i no-mullant estan en equilibri per a cada problema elemental. La figura 8.39 mostra l'evolució d'una configuració típica d'un

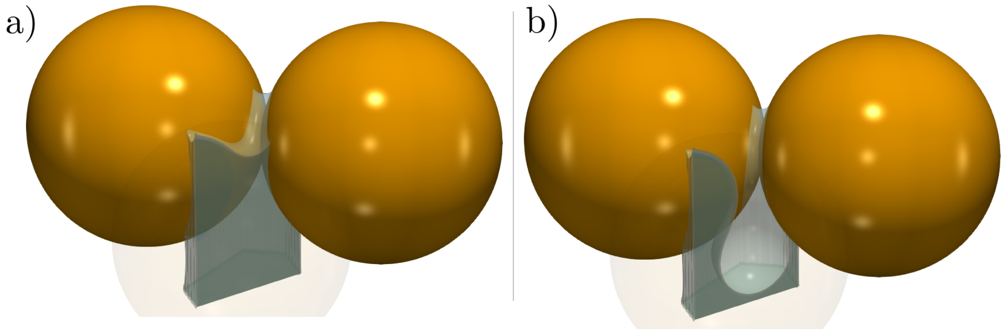

Figure 8.39: Invasió de la fase no-mullant d'una gola de porus formada per tres esferes. Observeu la tercera esfera translúcida davant de les altres esferes.

sub-domini. En aquest cas, la gola dels porus està formada per tres esferes en contacte amb el mateix radi. La densitat dels nodes situats a les seccions d'entrada i sortida s'ajusta per tal d'augmentar progressivament la pressió capil · lar. L'increment de p_c desencadena el desplaçament de la interfície fluid-fluid (veure les figures 8.37c i figura 8.39). La curvatura del menisc d'interfície augmenta a mesura que la pressió capil · lar creix.

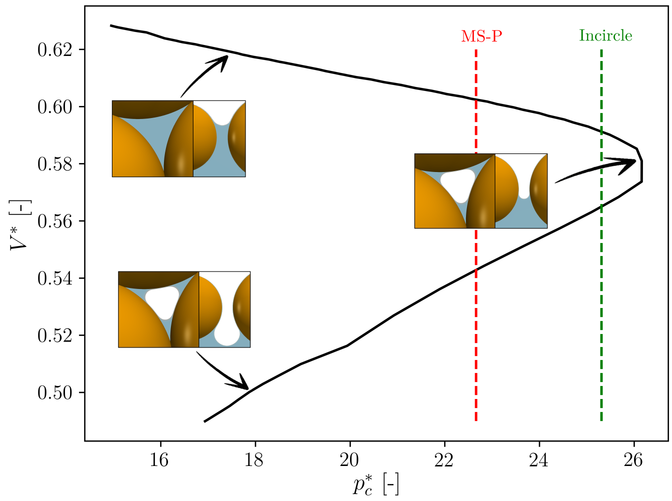

Figure 8.40: Canvi de volum i pressió capil · lar en el moment de la invasió de la gola. A la imatge hi ha superposades les pressions capil · lars d'entrada obtingudes amb els mètodes MS-P i Incircle. Tres instants il · lustrats amb talls verticals i horitzontals de la simulació mostren la morfologia del líquid abans, durant i després de la invasió dels porus.

L'evolució de la pressió capil · lar normalitzada ($p_c^* = \dfrac{2p_cR}{\gamma}$, on γ és la tensió superficial, R és el radi de les esferes i p_c és la pressió capil · lar) durant la invasió està relacionada amb el canvi de volum de la fase mullant tal com s'aprecia a la figura 8.40. El volum adimensional es defineix com:

$V^* = \dfrac{V(t)}{\dfrac{4}{3}\pi R^3}$, on $V(t)$ és el volum a l'instant t.

La pressió capil · lar d'entrada p_c^e es defineix com el valor màxim obtingut per p_c durant el procés d'invasió. Quan la pressió capil · lar arriba a la pressió capil · lar d'entrada ($p_c = p_c^e$), la fase no-mullant penetra al porus (veure figures 8.39 i 8.40). Immediatament després de la invasió, el menisc de la interfície creix, fet que comporta una reducció de la pressió capil · lar. Aquest procediment es repeteix per a totes les goles de la mostra. Així doncs, p_c^e es determina per a tots els subdominis i s'integra al problema global tractat per la xarxa de porus.

Drenatge d'una mostra granular de 40 esferes

Aquesta secció presenta els resultats d'un procés de drenatge d'una mostra granular de 40 esferes. Una simulació LBM totalment resolta ha estat realitzada i es considera de referència. A continuació, els resultats es comparen amb el model Híbrid. El pack d'esferes aleatòries ha estat creat mitjançant el codi obert YADE. La mostra correspon a un cub de 10 mm x 10 mm x 10 mm amb 40 esferes polidisperses. El radi mitjà de les esferes és d'1.26 mm. Les següents hipòtesis es prenen en compte:

- El drenatge és avaluat sota un flux quasi-estàtic ($Ca \approx 0.0001$).
- Mullatge perfecte del sòlid per la fase mullant.
- Les regions desconnectades queden saturades.

Inicialment, la mostra granular està completament saturada (veure la figura 8.41a - Full LBM). Una membrana porosa es situa a baix de la mostra per tal d'impedir que la fase no-mullant arribi a la sortida i s'asseguri un drenatge complet. El desplaçament de la interfície s'efectua a través d'un flux fix controlat per una diferència de pressió entre el dipòsit no-mullant (dalt de la mostra) i el dipòsit mullant (a baix del medi granular). La interfície es desplaça cap avall, degut al gradient de pressió, envaint primer els porus més grans. A continuació, la fase no-mullant ocupa progressivament la resta d'espais de la mostra. La pressió capil · lar augmenta i s'enregistra fins que tots els nodes situats sobre de la membrana porosa corresponen a la fase no-mullant (veure figura 8.41d- Full LBM). En aquest moment, la fase mullant restant queda atrapada dins la mostra granular en forma d'estructures líquides. La figura 8.42 evidencia la presència de ponts pendulars i trimers dins el medi granular després del drenatge.

La figura 8.41 captura els recorreguts de la fase no-mullant en diferents instants per a cada mètode. La interfície de la simulació LBM completa està representada per una iso-superfície blava translúcida, mentre que la fase mullant s'il · lustra en blau fosc per als models Híbrid, Incircle i MS-P a la figura 8.41. Observem la capacitat del model Híbrid i Incircle per predir el primer camí preferent (una intrusió idèntica s'observa a les figures 8.41b i 8.41c). Al llarg del drenatge, la fase no-mullant continua ocupant la mostra deixant líquid desconnectat (veure la figura 8.41d). Tot i que el mètode Híbrid representa bé la fase mullant atrapada dins la mostra, la figura 8.41d suggereix que existeix una certa discrepància de fases entre els models a algunes regions.

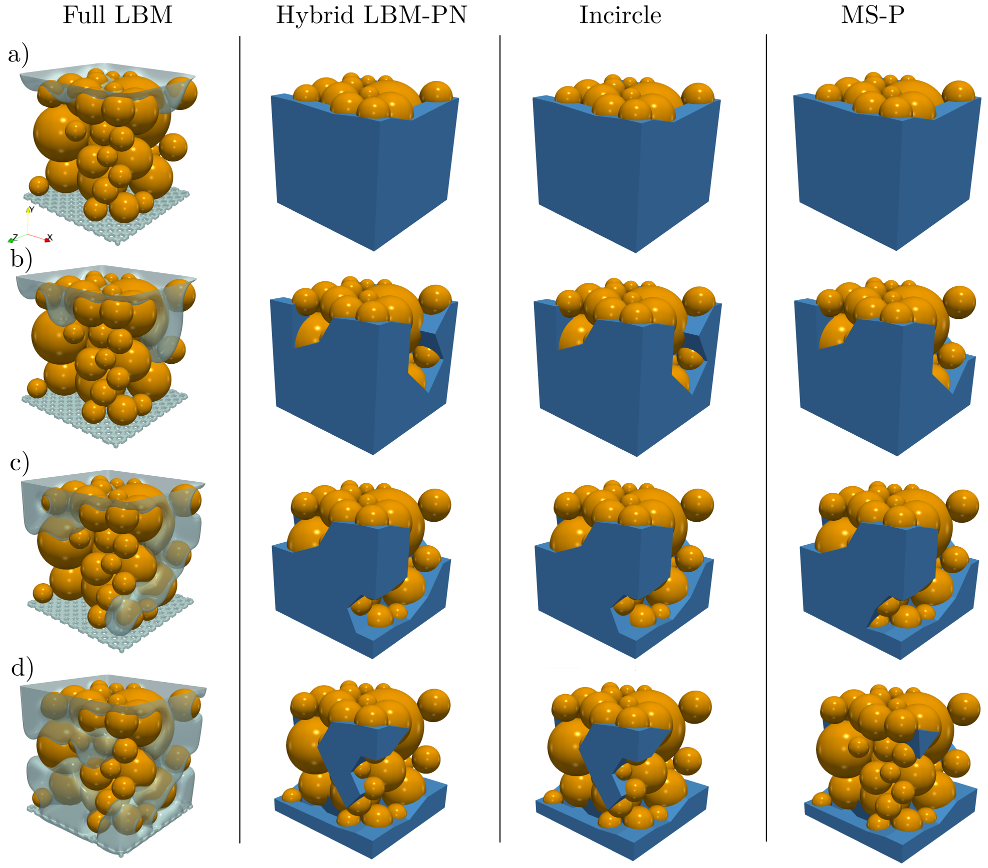

Figure 8.41: Comparació dels camins d'invasió entre la simulació LBM completa (interfície translúcida) i els mètodes Híbrid, Incircle i MS-P (fase mullant il · lustrada en blau).

És important mencionar que el temps CPU pel drenatge d'aquesta mostra correspon a 29.6 dies per a la simulació LBM completa. D'altra part, utilitzant el model Híbrid, el cost de càlcul es redueix a 11.2 dies.

Conclusions

L'objectiu principal d'aquesta tesi ha consistit en avaluar les propietats hidroestàtiques i el comportament mecànic de les microestructures líquides més enllà del règim pendular. Ens hem concentrat en diferents mètodes per descriure la morfologia dels líquids i les forces capil · lars a l'escala dels porus. A més, hem desenvolupat noves tècniques per estudiar els fluxos multifàsics a través dels medis porosos.

La primera part d'aquesta tesi (capítols 2 i 3) està dedicada a la calibració i validació del mètode lattice Boltzmann basat en el model a diversos components de Shan-Chen (SC-LBM), així com l'estudi preliminar per reproduir fluxos multifàsics a nivell meso i microscòpic. L'anàlisi sobre les forces capil · lars sota el règim funicular suggereix que la forma de la interfície té un impacte molt significatiu sobre les forces. Conseqüentment, els canvis més substancials en les forces capil · lars es produeixen durant les transicions de règim. En canvi, les variacions de la pressió capil · lar

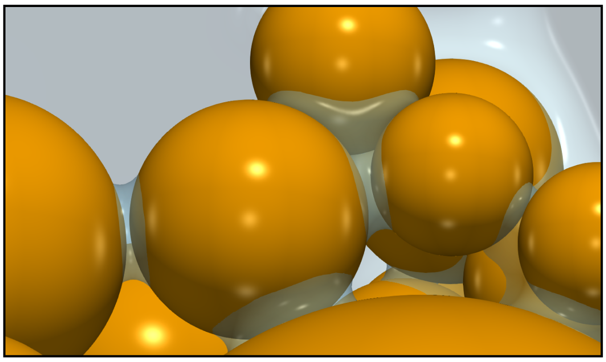

Figure 8.42: Distribució de la fase mullant després de la simulació del drenatge. La fase mullant queda desconnectada a certes zones de la mostra en forma de ponts pendulars o altres estructures líquides.

lluny de les transicions comporten alteracions menys accentuades sobre les forces capil · lars.

Degut als elevats costos de càlcul associats a les simulacions LBM, els capítols 4, 5 i 6 exploren la possibilitat d'emprar models Híbrids basats en la descomposició de la mostra granular per tal d'avaluar les propietats hidromecàniques amb un temps computacional acceptable.

Al capítol 4 presentem un model reticular de gola dels porus en 2D anomenat Throat-Network (TN) inspirat en models de xarxa de porus precedents. El TN es basa en solucions analítiques i és capaç de reproduir un flux trifàsic dins un medi porós 2D constituït de partícules circulars comprimides. La posició de la interfície fluid-fluid ha estat ben descrita i resulta gairebé idèntica al perfil LBM pels exemples elementals. En el transcurs de les simulacions, s'evidencia que el model TN pot reproduir diversos esdeveniments locals tals com: salt d'Haines, ruptura del menisc en meniscs independents, fusió de dos meniscs i ompliment dels porus degut a efectes dinàmics. La polivalència i la precisió del model, fan que el TN sigui una alternativa atractiva per reproduir problemes multifàsics en 2D. Per exemple, el flux a través d'elements cilíndrics o l'avaluació de la permeabilitat a medis porosos fibrosos.

Per acabar, en els capítols 5 i 6, proposem un model Híbrid que es beneficia de l'eficàcia dels models de xarxa de porus i de la precisió de les simulacions directes obtingudes amb el LBM. El mètode Híbrid és capaç de reproduir amb precisió els moviments de la interfície durant el procés de drenatge. A més a més, els ponts líquids desconnectats en acabar la invasió de cada gola dels porus queden ben descrits i identificats. Els recursos de càlcul es poden optimitzar reemplaçant les goles amb configuracions geomètriques complexes per simples aproximacions. Fer un ús exclusiu dels mètodes aproximats (MS-P i Incircle) és una altra alternativa que permet predir les principals propietats hidroestàtiques sense costos computacionals importants. De fet, el model Híbrid no ofereix una solució gaire més precisa que l'aproximació Incircle pel que fa als recorreguts d'invasió o corba de drenatge. Per contra, el model Híbrid és l'únic capaç de determinar la relació entre la pressió capil · lar i el contingut de la fase mullant per a cada gola dels porus i la morfologia del líquid després de la invasió de la fase no-mullant. La identificació de les interfícies restants és una característica essencial si es volen avaluar les forces capil · lars entre partícules. Per consegüent, l'adopció del model Híbrid marca una diferència respecte a la resta de les aproximacions a l'escala dels porus per comprendre el comportament hidromecànic dels sòls no saturats.